Green Materials in Civil Engineering

Woodhead Publishing Series in Civil and Structural Engineering

Green Materials in Civil Engineering

Edited by

Anasua GuhaRay

Toshiro Hata

Nagesh R. Iyer

Pijush Samui

Sanjay Kumar

ELSEVIER

WP
WOODHEAD PUBLISHING
An imprint of Elsevier

Woodhead Publishing is an imprint of Elsevier
50 Hampshire Street, 5th Floor, Cambridge, MA 02139, United States
125 London Wall, London EC2Y 5AS, United Kingdom

Notices

Knowledge and best practice in this field are constantly changing. As new research and experience broaden our understanding, changes in research methods, professional practices, or medical treatment may become necessary.

Practitioners and researchers must always rely on their own experience and knowledge in evaluating and using any information, methods, compounds, or experiments described herein. In using such information or methods they should be mindful of their own safety and the safety of others, including parties for whom they have a professional responsibility.

To the fullest extent of the law, neither the Publisher nor the authors, contributors, or editors, assume any liability for any injury and/or damage to persons or property as a matter of products liability, negligence or otherwise, or from any use or operation of any methods, products, instructions, or ideas contained in the material herein.

ISBN: 978-0-443-19106-0 (print)
ISBN: 978-0-443-19107-7 (online)

For information on all Woodhead Publishing publications visit our website at https://www.elsevier.com/books-and-journals

Publisher: Matthew Deans
Acquisitions Editor: Gwen Jones
Editorial Project Manager: Sara Greco
Production Project Manager: Sharmila Kirouchenadassou
Cover Designer: Christian Bilbow

Typeset by MPS Limited, Chennai, India

Dedication

Dedicated to my grandmother Pratima Pal

–Pijush Samui

Contents

List of contributors **xiii**
Preface **xvii**

1 A model to predict water retention characteristic curve of fly ash **1**
Ammavajjala Sesha Sai Raghuram
1.1 Introduction 1
1.2 Previous studies on water retention characteristic curve of fly ash 1
1.3 Objectives of the present study 2
1.4 Experimental program 2
1.5 Measurement of suction 2
1.6 Results and discussion 3
1.7 Validation with published study 8
1.8 Conclusion 10
Acknowledgments 10
References 10

2 Experimental study of the parameter for predicting the strength of geopolymer concretes based on ground granulated blast furnace slag and fly ash **13**
Sumanth Kumar Bandaru and Rama Seshu D.
2.1 Introduction 13
2.2 Experimental program 14
2.3 Cast and curing of geopolymer concrete specimens 15
2.4 Test results and discussions 17
2.5 Conclusion 24
References 25

3 Mitigating the environmental impacts of conventional concrete—a quantitative sustainable concrete approach **27**
Suchith Reddy Arukala
3.1 Introduction 27
3.2 Autodesk Revit 28
3.3 Literature review 29
3.4 Methodology 30
3.5 Case study 31
3.6 Results and discussion 32

3.7 Conclusion 38
References 39

4 Consistency, setting, and strength properties of fly ash and slag based geopolymer mortar activated with water glass 41
Rajashekar Sangi, B. Sesha Sreenivas and K. Shanker
4.1 Introduction 41
4.2 Materials used 42
4.3 Experimental program 43
4.4 Results and discussion 45
4.5 Conclusion 51
References 51

5 Developing flyash and slagbased high-strength geopolymer concrete 53
Krupansh Patel and Bhargav R. Tewar
5.1 Introduction 53
5.2 Experimental program 56
5.3 Conclusion 63
Abbreviations 64
References 64

6 Interfacial direct shear behavior of aluminum slag and uniaxial geogrids 67
Bhargav Kumar Karnamprabhakara, Umashankar Balunaini and Arul Arulrajah
6.1 Introduction 67
6.2 Materials used 68
6.3 Experimental program 70
6.4 Results and discussion 70
6.5 Conclusion 77
References 77

7 Fly ash-granulated blast furnace slag: better replacement materials for subbase flexible pavement construction 81
Manjula Devi Balasundar and Hemant Chore
7.1 Introduction 81
7.2 Properties of materials 82
7.3 Methodology 85
7.4 Model pavement 86
7.5 Sample preparation of model pavement 86
7.6 Results and discussion 90
7.7 Summary and conclusions 92
References 92

8 High performance concrete using fly ash 95
Sekar Saya Kanappan and Punitha Kumar Akhas
8.1 Introduction 95
8.2 Mix design of high performance concrete 96
8.3 High performance green concrete 97
8.4 Role of superplasticizer in high performance green concrete 100
8.5 Mix proportion 100
8.6 Strength development 101
8.7 Transporting and placing of high performance green concrete 103
8.8 Curing of high performance green concrete 104
8.9 Conclusion 105
References 105

9 Engineering green concrete for sustainable infrastructure 109
Nagesh R. Iyer
9.1 Introduction 109
9.2 Engineering green concrete strategies for sustainability 114
9.3 Engineered concretes 128
References 150

10 Behavior assessment of poor subgrade soil using natural coir geotextile under static and repeated load condition 153
D. Harinder and S. Shankar
10.1 Introduction 153
10.2 Materials used for the study 155
10.3 Experimental setup 155
10.4 Results and discussion 157
10.5 Conclusion 162
References 163

11 Utilization of higher percentage of reclaimed asphalt pavement material in bituminous mixtures 165
Sridhar Raju and Bhanuprasad Katla
11.1 Introduction 165
11.2 Material 166
11.3 Marshall mixture design 169
11.4 Test method 170
11.5 Result and discussion 173
11.6 Conclusions 178
References 178

12 Mineral wastes 181
O. Kehinde, D. Hughes and E.H. Amalu
12.1 Introduction 181
12.2 Mineral waste 181

12.3 Utilization of mineral wastes 184
12.4 Optimal utilization of mineral wastes 190
12.5 Conclusions 191
References 192

13 Morphology and strength of concrete incorporating natural rubber latex and plastic fibers 201
Paul O. Awoyera, Folashayo Oluyemi, Naraindas Bheel, Oluwatobi Aluko, Afonso R.G. de Azevedo and Oladimeji B. Olalusi
13.1 Introduction 201
13.2 Materials and method 204
13.3 Conclusion 214
Funding 215
Data availability 215
Competing interests 215
References 215

14 Fiber-reinforced polymer nanocomposites for structural retrofitting applications 219
Bhuvaneshwari Balasubramaniam and Nagesh R. Iyer
14.1 Introduction 219
14.2 Characteristics of fiber-reinforced polymers 221
14.3 Fiber-reinforced polymer nanocomposites 222
14.4 Standard practices and codes involved in fiber-reinforced polymer-structural retrofit 224
14.5 Summary and conclusion 225
Acknowledgments 225
References 225

15 Biological materials for geotechnical engineering 229
Toshiro Hata
15.1 Introduction 229
15.2 Overview of mechanisms of crystal precipitation by microbial functions and their engineering applications 229
15.3 Development of preservation materials with self-healing and environmental preservation functions based on the microbial functions 233
15.4 Summary 238
References 238

16 A review on microstructural characteristics of bacterial concrete 241
Sk Rahaman, Arkamitra Kar, Jayati Ray Dutta and Mohna Bandyopadhyay
16.1 Introduction 241
16.2 Methodology adopted for the study 243

16.3 Background of microstructural and chemical analyses 243
16.4 Microstructure of bio-concrete 245
16.5 Conclusions 257
Acknowledgments 258
References 258

17 Geoenvironmental evaluation on coal gangue: greener alternative to existing fill materials 263
Mohammed Ashfaq and Arif Ali Baig Moghal
17.1 Introduction 263
17.2 Materials and methods 264
17.3 Results and discussion 266
17.4 Conclusions 274
17.5 Practical relevance of the study 274
References 274

18 Utilization of Sustainable Material: Ferrock for Stabilization of Subgrade Soil 279
Mayuri Makwana Nirav and Santosh Shah G.
18.1 Introduction 279
18.2 An understanding of important technologies 280
18.3 Potential applications 280
18.4 Testing procedures 280
18.5 Findings and conclusion 281
18.6 Conclusion 291
References 293

Index 295

List of contributors

Punitha Kumar Akhas School of Civil Engineering, Vellore Institute of Technology, Vellore, Tamil Nadu, India

Oluwatobi Aluko Civil Engineering Department, School of Civil Engineering, Universiti Teknologi Malaysia, Skudai, Johor, Malaysia

E.H. Amalu Department of Engineering, School of Computing, Engineering and Digital Technologies, Teesside University, Middlesbrough, United Kingdom

Suchith Reddy Arukala Department of Civil Engineering, Kakatiya Institute of Technology and Science, Warangal, Telangana, India

Arul Arulrajah Department of Civil and Construction Engineering, Swinburne University of Technology, Hawthorn, Melbourne, Australia

Mohammed Ashfaq Osaimi Geotechnic Company, Tabuk, Saudi Arabia

Paul O. Awoyera Department of Civil Engineering, Covenant University, Ogun State, Nigeria

Bhuvaneshwari Balasubramaniam Department of Chemistry, Indian Institute of Technology (BHU), Varanasi, Uttar Pradesh, India

Manjula Devi Balasundar Department of Civil Engineering, Datta Meghe College of Engineering, Airoli, Navi Mumbai, Maharashtra, India

Umashankar Balunaini Department of Civil Engineering, Indian Institute of Technology Hyderabad, Sangareddy, Telangana, India

Sumanth Kumar Bandaru Civil Engineering Department, Kakatiya Institute of Technology and Science, Warangal, Telangana, India

Mohna Bandyopadhyay Sharp Edge Labs, Pittsburgh, PA, United States

Naraindas Bheel Department of Civil Engineering, Universiti Teknologi Petronas, Bandar Seri Iskandar, Tronoh, Perak, Malaysia

Hemant Chore Department of Civil Engineering, Dr. B.R. Ambedkar National Institute of Technology, Jalandhar, Punjab, India

Afonso R.G. de Azevedo Civil Engineering Laboratory – LECIV, State University of the Northern Rio de Janeiro—UENF, Alberto Lamego, Campos dos Goytacazes, Rio De Janeiro, Brazil

D. Harinder Civil Engineering, Vallurupalli Nageswara Rao Vignana Jyothi Institute of Engineering and Technology, Hyderabad, Telangana, India

Toshiro Hata Geotechnical Laboratory, Department of Civil and Environmental Engineering, Graduate School of Advanced Science and Engineering, Hiroshima University, Hiroshima, Japan

D. Hughes Department of Engineering, School of Computing, Engineering and Digital Technologies, Teesside University, Middlesbrough, United Kingdom

Nagesh R. Iyer Department of Mechanical Engineering, Indian Institute of Technology, Dharwad, Karnataka, India; Indian National Academy of Engineering, New Delhi, India; Department of Civil & Infrastructure Engineering, IIT Dharwad, Dharwad, Karnataka, India

Arkamitra Kar Department of Civil Engineering, Birla Institute of Technology and Science-Pilani, Hyderabad Campus, Hyderabad, Telangana, India

Bhargav Kumar Karnamprabhakara Department of Civil Engineering, Indian Institute of Technology Hyderabad, Sangareddy, Telangana, India

Bhanuprasad Katla Department of Civil Engineering, Birla Institute of Technology and Science, Pilani Hyderabad Campus, Hyderabad, Telangana, India

O. Kehinde Department of Engineering, School of Computing, Engineering and Digital Technologies, Teesside University, Middlesbrough, United Kingdom

Mayuri Makwana Nirav Civil Engineering Department, Gujarat Technological University, Chandkheda, Gandhinagar, Gujarat, India

Arif Ali Baig Moghal National Institute of Technology Warangal, Warangal, Telangana, India

Oladimeji B. Olalusi Department of Civil Engineering, Structural Engineering & Computational Mechanics Group (SECM), University of KwaZulu-Natal, Durban, South Africa

Folashayo Oluyemi Department of Civil Engineering, Covenant University, Ogun State, Nigeria

Krupansh Patel Faculty of Technology, CEPT University, Ahmedabad, Gujarat, India

Ammavajjala Sesha Sai Raghuram Department of Civil Engineering, Birla Institute of Technology and Science (BITS) - Pilani, Hyderabad, Telangana, India

Sk Rahaman Department of Civil Engineering, Birla Institute of Technology and Science-Pilani, Hyderabad Campus, Hyderabad, Telangana, India

Sridhar Raju Department of Civil Engineering, Birla Institute of Technology and Science, Pilani Hyderabad Campus, Hyderabad, Telangana, India

Jayati Ray Dutta Biological Sciences Department, Birla Institute of Technology and Science-Pilani, Hyderabad Campus, Hyderabad, Telangana, India

Rajashekar Sangi Department of Civil Engineering, Kakatiya University, Warangal, Telangana, India; Department of Civil Engineering, Kamala Institute of Technology & Science, Singapur, Telangana, India

Sekar Saya Kanappan School of Civil Engineering, Vellore Institute of Technology, Vellore, Tamil Nadu, India

Rama Seshu D. Civil Engineering Department, National Institute of Technology, Warangal, Telangana, India

Santosh Shah G. Civil Engineering Department, Centre for Research & Innovation, Sankalchand Patel University, Visnagar, Mehsana District, Gujarat, India

S. Shankar National Institute of Technology, Civil Engineering Department, Warangal, Telangana, India

K. Shanker Department of Civil Engineering, Kamala Institute of Technology & Science, Singapur, Telangana, India

B. Sesha Sreenivas Department of Civil Engineering, Kakatiya University, Warangal, Telangana, India

Bhargav R. Tewar Faculty of Technology, CEPT University, Ahmedabad, Gujarat, India

Preface

In the pursuit of sustainable development and environmental responsibility, the emergence of green materials has revolutionized the field of civil engineering. This book serves as a central resource, offering an easy-to-understand exploration of various green materials and their practical applications through insightful case studies. Our mission is to empower practitioners, researchers, and newcomers alike with a comprehensive understanding of these environmentally friendly alternatives.

With a strong emphasis on clarity and practicality, we bridge the gap between technical literature and accessible knowledge, enabling readers to grasp the concepts and embrace the potential of green materials. Through on-site models tailored to different regions and scenarios, we illuminate the seamless integration of these materials into real-world projects.

Within its pages lies a treasure trove of knowledge, meticulously crafted to empower engineers, researchers, and novices alike. Written in an approachable style without compromising on depth, this literary marvel breathes life into the essence of practicality.

Green Materials in Civil Engineering fosters a profound understanding of the significant impact that these novel materials can have on achieving sustainable development goals. As a guiding star in academia, postgraduate scholars, early-career researchers, and mid-career engineers will find solace within the pages of this treasured volume.

Each chapter orchestrates a harmonious chorus of possibilities, celebrating the versatility and promise of environmentally friendly alternatives. From the emerald embrace of green concrete to the resourceful prowess of agricultural waste, from biologically inspired wonders to the brilliance of smart materials, and even the artistry found in repurposed waste materials—all are showcased in their grandeur. Moreover, this book unlocks the gates to the realm of material science research, inviting readers to witness the dawn of a new era in engineering materials.

Within these profound chapters, the heart of civil engineering beats with newfound vigor. As the demand for green materials continues to surge, this book stands as a timeless testament to innovation, sustainability, and the unified spirit of a field marching towards a brighter, greener, and more harmonious future.

Anasua GuhaRay
Toshiro Hata
Nagesh R. Iyer
Pijush Samui
Sanjay Kumar

A model to predict water retention characteristic curve of fly ash

1

Ammavajjala Sesha Sai Raghuram
Department of Civil Engineering, Birla Institute of Technology and Science (BITS) - Pilani, Hyderabad, Telangana, India

1.1 Introduction

Fly ash (FA), a by-product of thermal power plants, is utilized in a variety of geoenvironmental applications, including embankments, backfill, hydraulic barriers, and pavements. The FA exhibits distinct characteristics in its saturated and unsaturated conditions. Therefore mechanical and hydraulic behavior of FA in unsaturated conditions becomes more essential in such projects. A water retention characteristic curve (WRCC) provides essential information for this purpose. WRCC shows the relation between water content and suction. The accuracy of the suction measurement and the resulting WRCC are critical for modeling the unsaturated behavior (Raghuram et al., 2021). WRCC can be obtained through experiments and empirical correlations. However, obtaining WRCC through experiments is cumbersome and time taking. Several empirical models exist to compute the WRCC of soils. Nevertheless, there are none for geomaterials like FA. Hence, the current study aimed to propose a set of nonlinear regression equations to estimate the WRCC of FA.

1.2 Previous studies on water retention characteristic curve of fly ash

Many researchers have utilized FA in the past for construction and geological projects (Horiuchi et al., 2000; Sivapullaiah & Baig, 2011). Some researchers have also investigated FA's utility as a hydraulic barrier (Nhan et al., 1996; Prashanth et al., 2001). Deka (2015) examined the range of suction for FA. The author collected four FA samples and estimated the WRCC of FA using four different methods.

Puppala et al. (2006) evaluated the WRCC of expansive soil stabilized with FA, bottom ash and fibers. They concluded that the volumetric water content reduced as the percentage of FA increased. Yang et al. (2011) estimated the WRCCs of expansive soil stabilized with lime and FA. Wen et al. (2015) studied the WRCC behavior of silt and clay stabilized with FA. They presented the WRCC for drying and wetting cycles and reported the WRCC fitting parameters of the stabilized soils

Green Materials in Civil Engineering. DOI: https://doi.org/10.1016/B978-0-443-19106-0.00001-4

under drying and wetting conditions. Abhijit and Sreedeep (2015) and Deka and Sekharan (2021) estimated the WRCC of FA using tensiometer (TM), a matric potential sensor (MPS), an equitensiometer (EQT), and a dew point potentiometer (WP4). They concluded that the WRCC fitting parameters of FA computed using various techniques cannot be unique. However, their study is limited to four FA samples only. Prakash et al. (2017, 2019) quantified the uncertainties associated with WRCC of FA using Gaussian copula approach.

It is evident from the above studies that there are numerous applications of FA in geotechnical engineering. Nonetheless, investigations on the water retention behavior of FA are limited, particularly for Indian FA. Therefore in this study, a total of 22 FA samples are collected from three different sources and the WRCCs of the FA samples are estimated.

1.3 Objectives of the present study

The WRCC of FA was evaluated experimentally using the filter paper technique for all 22 samples. A set of nonlinear regression equations are provided in terms of particle size diameter D60 to estimate the WRCC fitting parameters for the Fredlund & Xing (1994) (FX) model. Furthermore, an existing WRCC of FA is used to validate the authenticity of the proposed model.

1.4 Experimental program

A total of 22 FA samples were collected from three different sources in Andhra Pradesh and Telangana. Out of which eight samples were obtained from Vijayawada thermal power station (VTPS), Andhra Pradesh. Another eight samples were collected from Ramagundam thermal power station (RTPS), Telangana. The remaining six samples were obtained from Kakatiya thermal power station (KTPS), Telangana. The specific gravity (G), moisture content (OMC), and maximum dry density (γ_d) of FA samples are presented in Table 1.1. The grain size distribution of the VTPS fly ash (VFA), RTPS fly ash (RFA), and KTPS fly ash (KFA) samples are presented in Fig. 1.1A–C, respectively. WRCC of FA was collected from Abhijit and Sreedeep (2015) to validate the proposed nonlinear equations. This study adopted the filter paper suggested by Han et al. (2019). All FA samples are compacted at optimum conditions. The drying WRCC procedure adopted by Raghuram et al. (2020) is used to obtain the WRCC of FA.

1.5 Measurement of suction

The matric suction of the FA samples was obtained using the contact filter paper technique suggested by ASTM D5298 (ASTM, 2016). The samples of FA were uniformly divided into four equally sized portions. Three filter papers were sandwiched and wrapped with insulating tape between two samples of FA. Power et al. (2008)

Table 1.1 Properties of fly ash from three different sources.

Fly ash source	Sample no.	*G*	Unit weight (kN/m^3)	OMC (%)
VTPS	VFA-1	2.00	13.2	23.4
	VFA-2	2.02	12.7	25.0
	VFA-3	2.01	13.8	18.0
	VFA-4	1.97	13.0	21.7
	VFA-5	2.04	13.3	22.2
	VFA-6	1.99	12.9	23.4
	VFA-7	2.01	13.2	23.1
	VFA-8	2.03	13.0	21.5
RTPS	RFA-1	2.03	14.6	24.3
	RFA-2	2.19	13.9	21.4
	RFA-3	2.19	14.2	23.6
	RFA-4	2.14	14.0	21.9
	RFA-5	2.18	13.7	20.3
	RFA-6	2.19	13.9	21.1
	RFA-7	2.18	14.1	24.0
	RFA-8	2.20	14.0	23.6
KTPS	KFA-1	2.32	13.0	20.6
	KFA-2	2.28	12.8	21.2
	KFA-3	2.24	13.2	20.4
	KFA-4	2.28	12.6	21.7
	KFA-5	2.26	12.9	21.0
	KFA-6	2.24	13.1	21.1

proposed applying a pressure of 1 kPa to the filter paper and FA slice to ensure proper contact. The entire set up was sealed for 7 days to allow equilibrium conditions to prevail. Finally, the middle filter paper's water content (w) was determined to get the matric suction (ψ) value as indicated in Eq. (1.1).

$$\log\psi = \begin{cases} 5.327 - 0.0779ww < 45.3\% \\ 2.412 - 0.0135ww \geq 45.3\% \end{cases} \tag{1.1}$$

Similarly, the water content of each slice of FA was determined. The average water content and suction of two FA slices out of four were estimated. The WRCC was then plotted with the known values of the suction and water content for each sample of FA.

1.6 Results and discussion

1.6.1 Water retention characteristic curves of fly ash

The measured WRCC of FA samples were represented by FX WRCC model. The FX model can be given as follows:

$$\theta_w = c\psi \frac{\theta_s}{\left\{\ln\left[e + \left(\frac{\psi}{a_f}\right)^{n_f}\right]\right\}^{m_f}} \tag{1.2}$$

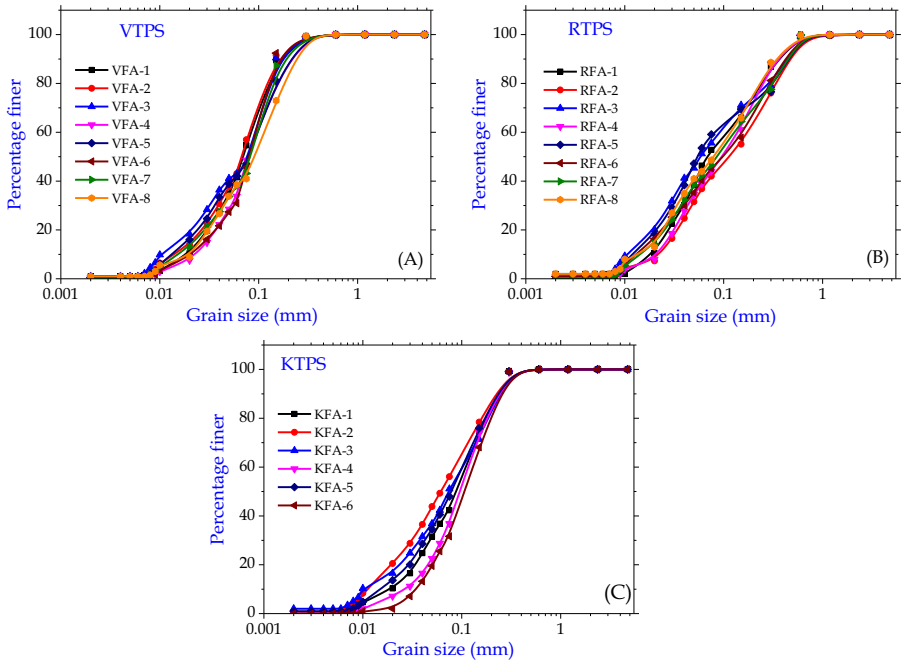

Figure 1.1 Particle size distributions of (A) Vijayawada fly ash, (B) Ramagundam fly ash, and (C) Kakatiya fly ash.

where a_f, n_f, and m_f are the fitting parameters of WRCC and are related to air entry value (AEV), slope of WRCC and water holding capacity, respectively; and are the volumetric, saturated, and residual water contents, respectively; = correction factor (is equal to 1 as recommended by Leong & Rahardjo, 1997).

Fig. 1.2A–H shows the WRCC of FX model for eight different Ramagundam fly ash samples. It may be noted from Fig. 1.2A–H that RFA-2 desaturates quickly and RFA-5 desaturates slowly when compared to rest of RFA samples. This could be attributed to the more number of fines in RFA-5 and low amount of fines in RFA-2 samples which contributed to higher and lower suction values in RFA-5 and RFA-2 samples, respectively. The results presented in Fig. 1.3A–H depicts the WRCC of FX model for Vijayawada fly ash for eight various samples. Similarly, the WRCC of FX model for Kakatiya fly ash is presented in Fig. 1.4A–F for six different FA samples. The results depicted in Fig. 1.5A–C show the WRCCs of RTPS, VTPS, and KTPS fly ash samples, respectively, for FX model. It may be observed from Fig. 1.5A–C that there is significant difference in WRCC especially for RTPS and KTPS fly ash samples.

Table 1.2 summarizes the values of particle size diameter D60 and the corresponding WRCC fitting parameters. It can be noted from Table 1.2 that particle size diameter D60 is inversely proportional to the WRCC fitting parameter a_f. This could be attributed to parameter a_f, which is directly proportional to AEV. AEV is

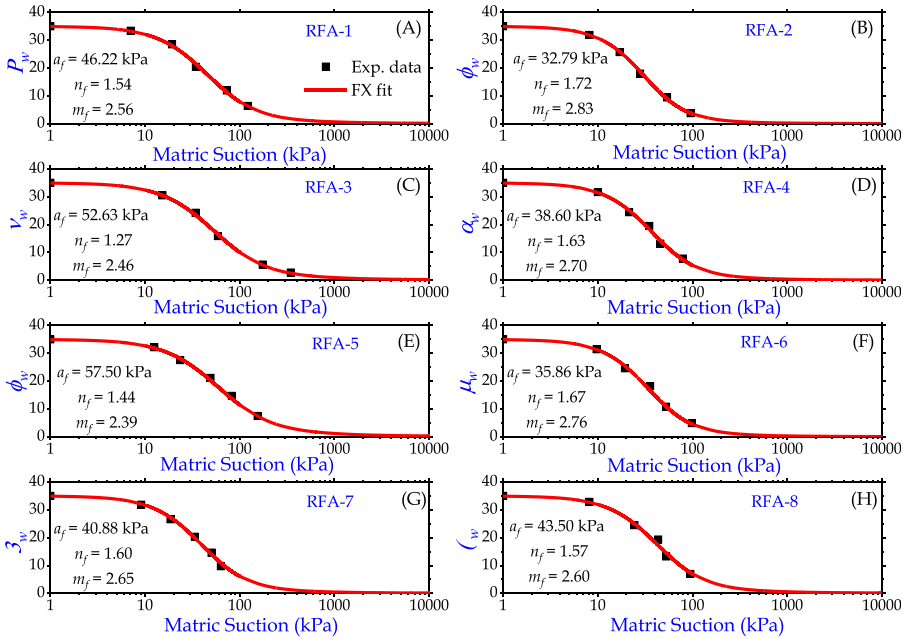

Figure 1.2 Estimated water retention characteristic curve (WRCC) of FX model for Ramagundam thermal power station (RTPS) fly ash: (A) sample 1, (B) sample 2, (C) sample 3, (D) sample 4, (E) sample 5, (F) sample 6, (G) sample 7, and (H) sample 8.

the suction value at which air enters the FA from the larger pores. The larger value of D60 indicates the presence of high number of coarser particles when compared to lower values of D60. Therefore a greater number of larger voids may present for a FA with higher D60 and hence the air can easily enter the FA leading to lower a_f values.

Furthermore, it may be observed from Table 1.2 that D60 is directly proportional to fitting parameters, n_f and m_f. This is because the fitting n_f is related to particle size distribution. The higher value of n_f signifies the presence of coarse size particles and steeper WRCC. Hence, increase in the D60 increases the n_f value. The fitting parameter m_f is related to water retention capacity and is low for coarse grain particles when compared to fine particles. Therefore with increase in D60, the fitting parameter m_f increases.

1.6.2 Regression models for water retention characteristic curve of fly ash

Zapata et al. (2000) experimented with several functions of gradation parameters to propose correlations for nonplastic soils and determined that the particle diameter D60 performed well. Therefore in this study, nonlinear equations are recommended to estimate the WRCC fitting parameters in terms of particle diameter D60 on the

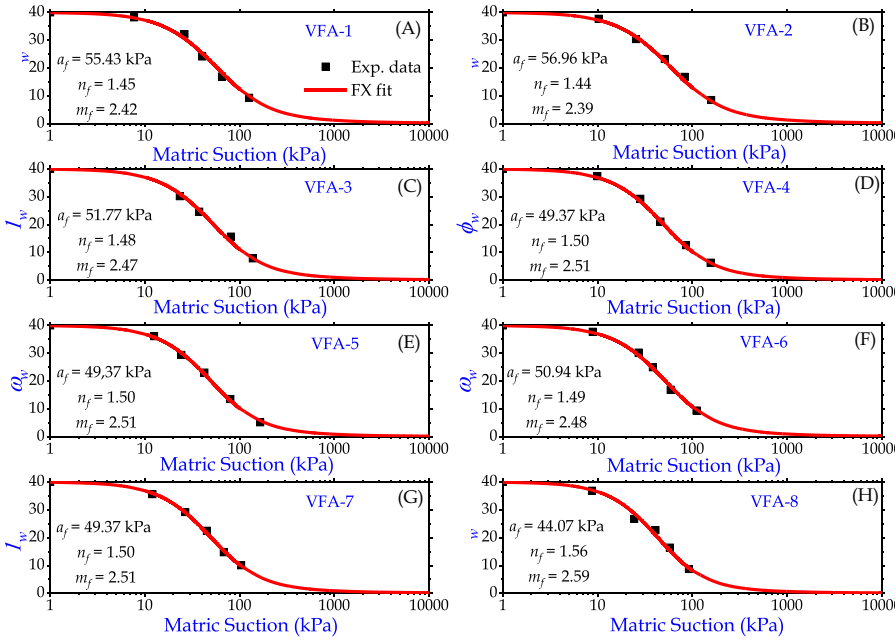

Figure 1.3 Computed water retention characteristic curve (WRCC) of FX model for Vijayawada thermal power station (VTPS) fly ash: (A) sample 1, (B) sample 2, (C) sample 3, (D) sample 4, (E) sample 5, (F) sample 6, (G) sample 7, and (H) sample 8.

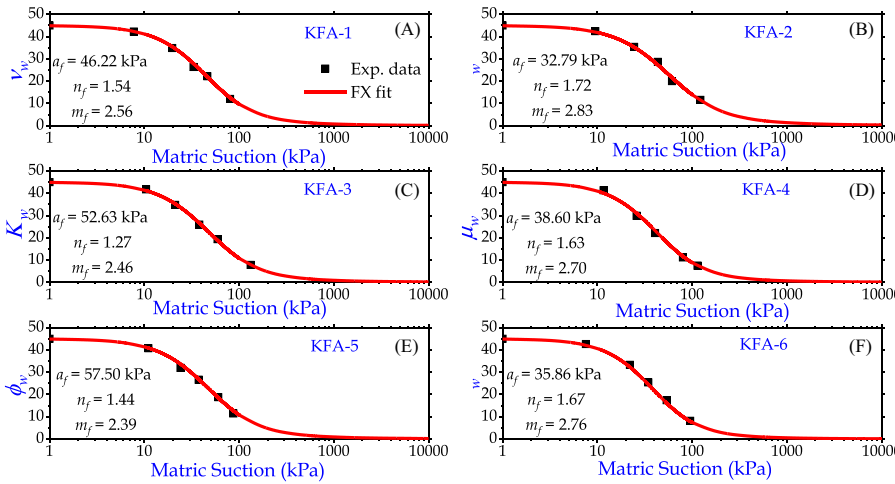

Figure 1.4 Estimated water retention characteristic curve (WRCC) of FX model for Kakatiya thermal power station (KTPS) fly ash: (A) sample 1, (B) sample 2, (C) sample 3, (D) sample 4, (E) sample 5, and (F) sample 6.

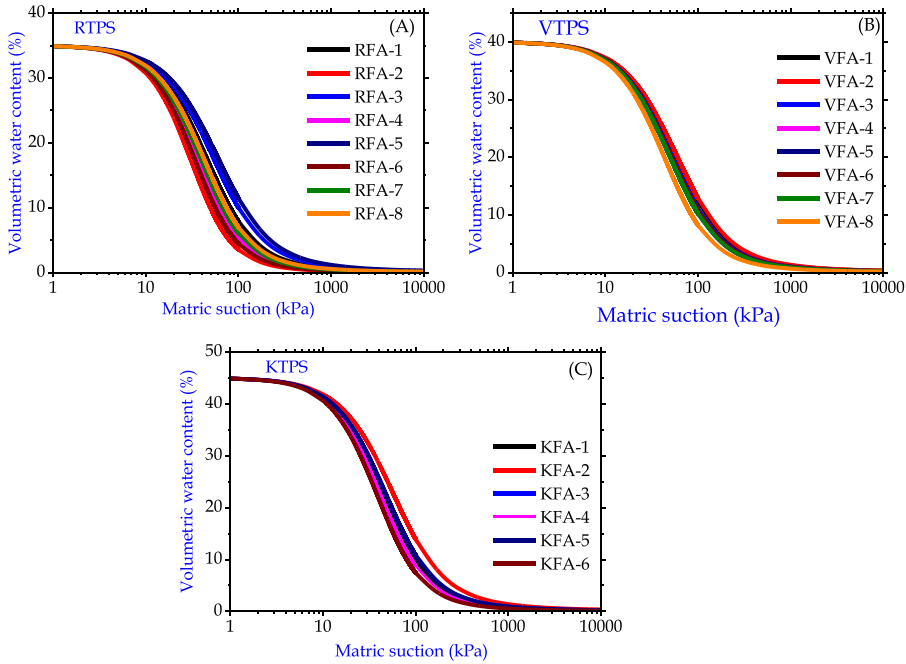

Figure 1.5 Water retention characteristic curves (WRCCs) of (A) Ramagundam thermal power station (RTPS) fly ash, (B) Vijayawada thermal power station (VTPS) fly ash, and (C) Kakatiya thermal power station (KTPS) fly ash for FX model.

Table 1.2 Particle size diameter and water retention characteristic curve (WRCC) fitting parameters of various fly ash samples.

Source	Sample no.	D60 (mm)	a_f (kPa)	n_f	m_f
VTPS	VFA-1	0.084	55.43	1.45	2.42
	VFA-2	0.081	56.96	1.44	2.39
	VFA-3	0.092	51.77	1.48	2.47
	VFA-4	0.098	49.37	1.50	2.51
	VFA-5	0.098	49.37	1.50	2.51
	VFA-6	0.094	50.94	1.49	2.48
	VFA-7	0.098	49.37	1.50	2.51
	VFA-8	0.114	44.07	1.56	2.59
RTPS	RFA-1	0.107	46.22	1.54	2.56
	RFA-2	0.169	32.79	1.72	2.83
	RFA-3	0.090	52.63	1.47	2.46
	RFA-4	0.136	38.60	1.63	2.70
	RFA-5	0.080	57.50	1.44	2.39
	RFA-6	0.150	35.86	1.67	2.76
	RFA-7	0.126	40.88	1.60	2.65
	RFA-8	0.116	43.50	1.57	2.60

(*Continued*)

Table 1.2 (Continued)

Source	Sample no.	D60 (mm)	a_f (kPa)	n_f	m_f
KTPS	KFA-1	0.110	45.27	1.55	2.57
	KFA-2	0.084	55.43	1.45	2.42
	KFA-3	0.102	47.91	1.52	2.53
	KFA-4	0.117	43.22	1.57	2.61
	KFA-5	0.102	47.91	1.52	2.53
	KFA-6	0.130	39.93	1.61	2.67

basis of the acquired experimental data. The regression analysis was performed using DATAFIT (Oakdale Engineering, Pennsylvania). The regression equations to estimate the WRCC fitting parameters of FX model can be represented as follows:

$$a_f = \exp\left(2.154 - \frac{9.624 \times 10^{-11}}{D60} - 0.751\ln(D60)\right) \tag{1.3}$$

$$n_f = 2.303 - \frac{0.164}{D60} + \frac{2.675 \times 10^{-2}}{(D60)^{1.5}} \tag{1.4}$$

$$m_f = 6.364 - \frac{9.798 \times 10^{-4}}{(D60)^2} - 4.14\exp(-D60) \tag{1.5}$$

The R^2 value of Eqs. (1.3)−(1.5) is 0.998.

Fig. 1.6 shows the WRCC for the estimated experimental FX model and proposed regression fits for three different FA namely VFA-1, KFA-1, and RFA-1. The results demonstrated in Fig. 1.6 signifies that the proposed regression fit equations to compute WRCC of FA using FX model are in good match with the experimental FX model.

1.7 Validation with published study

The proposed equations (Eqs. 1.3−1.5) were validated with existing studies of Abhijit and Sreedeep (2015). Fig. 1.7 depicts the WRCC obtained from proposed regression fits and WRCCs presented by Abhijit and Sreedeep (2015) for NTPC Badarpur fly ash, New Delhi, India. The particle size diameter D60 of the FA is 0.07 (Deka, 2015). Abhijit and Sreedeep (2015) presented the WRCC of FA obtained from NTPC Badarpur using four different suction measuring equipment. Suction and WRCCs of FA are estimated using TM, an MPS, an EQT, and a WP4. An important observation is that the WRCC of FA obtained through various measuring equipment are significantly different. It can be noted from Fig. 1.7 that the

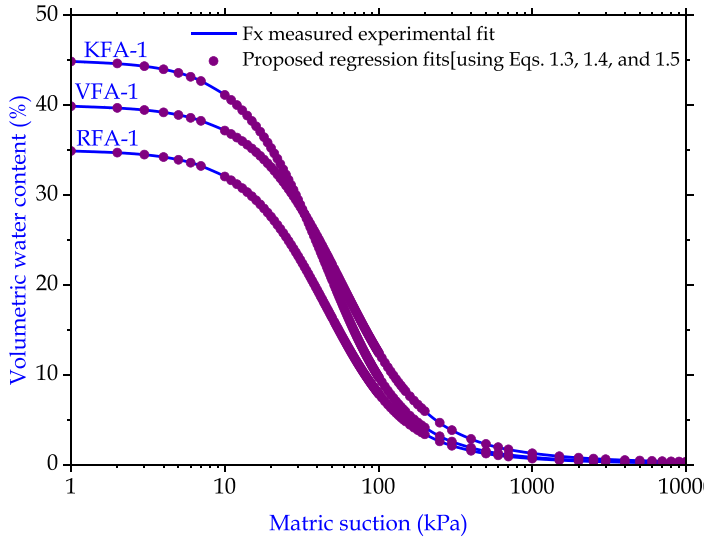

Figure 1.6 Comparison of proposed water retention characteristic curve (WRCC) regression model with experimental data.

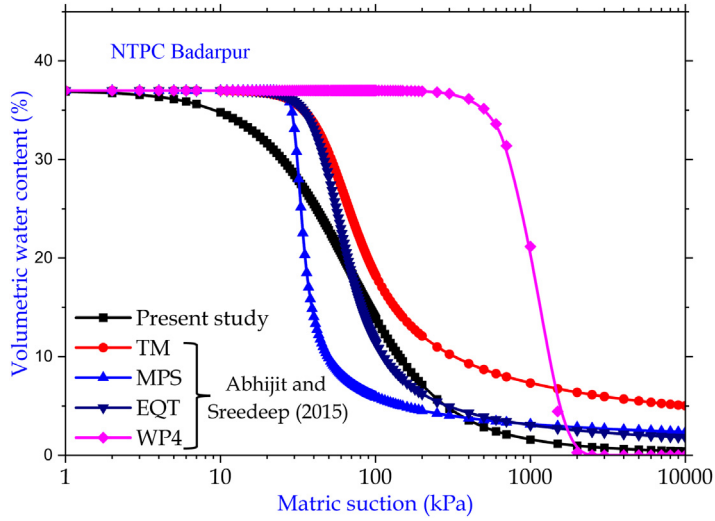

Figure 1.7 Comparison of proposed FX water retention characteristic curve (WRCC) regression fit with Abhijit and Sreedeep (2015).

WRCC estimated from the proposed regression fits is in good agreement with the WRCCs obtained from various suction measuring equipment. This clearly signifies that the proposed regression equations can estimate the WRCC of FA accurately.

1.8 Conclusion

The WRCC of FA samples obtained from three different sources namely VTPS, RTPS, and KTPS is estimated using filter paper method. A total of 22 FA samples were collected from the above sources and WRCCs were computed. A set of non-linear regression equations were developed and proposed to estimate the WRCC of FA in terms of particle size diameter D60. The proposed equations were validated with the published studies to find the authenticity of the proposed equations. The key outcomes of the present study are summarized below:

- The particle size diameter D60 is inversely proportional to the WRCC fitting parameter a_f. Parameter a_f is proportional to AEV. AEV is the suction at which air enters FA pores from larger pores. Larger D60 values signify a high number of coarser particles. FA with a higher D60 may have more larger voids, allowing air to easily enter.
- Furthermore, it may be observed that D60 is directly proportional to fitting parameters n_f and m_f.
- n_f is related to particle size distribution, a greater n_f value indicates the presence of coarser particles. Therefore higher D60 signifies higher n_f value.
- The fitting parameter m_f is related to water retention capacity and is low for coarse grain particles when compared to fine particles. Therefore with increase in D60, the fitting parameter m_f increases.

The practitioners and researchers will find the provided regression equations useful for determining WRCC of FA using particle size diameter D60.

Acknowledgments

The author gratefully acknowledges Skanda Material Testing Laboratory Private Limited, Hyderabad for providing FA from three different sources, which made laboratory research possible.

References

ASTM. (2016). *Standard test method for measurement of soil potential (suction) using filter paper*. ASTM D5298.

Abhijit, D., & Sreedeep, S. (2015). Evaluation of measurement methodologies used for establishing water retention characteristic curve of fly ash. *Journal of Testing and Evaluation*, *43*(5), 1066−1077. Available from https://doi.org/10.1520/JTE20130091, http://compass.astm.org/download/JTE20130091.18295.pdf.

Deka, A. (2015). *A study on the water retention and contaminant retention behavior of fly ash, bentonite and its mixes*. Ph.D. Thesis. Department of Civil Engineering, Indian Institute of Technology Guwahati.

Deka, A., & Sekharan, S. (2021). Influence of water retention curves model fitting parameters on unsaturated seepage modeling of fly ashes and pond ashes. *Indian Geotechnical Journal*, *51*(6), 1249−1262. Available from https://doi.org/10.1007/

s40098-021-00513-y, http://www.springer.com/engineering/civil + engineering/journal/40098.

Han, Z., Vanapalli, S. K., & Zou, W. L. (2019). Simple approaches for modeling hysteretic soil water retention behavior. *Journal of Geotechnical and Geoenvironmental Engineering*, *145*(10). Available from https://doi.org/10.1061/(ASCE)GT.1943-5606.0002148, http://ojps.aip.org/gto/.

Horiuchi, S., Kawaguchi, M., & Yasuhara, K. (2000). Effective use of fly ash slurry as fill material. *Journal of Hazardous Materials*, *76*(2−3), 301−337. Available from https://doi.org/10.1016/S0304-3894(00)00205-3.

Leong, E. C., & Rahardjo, H. (1997). Review of soil-water characteristic curve equations. *Journal of Geotechnical and Geoenvironmental Engineering*, *123*(12).

Nhan, C. T., Graydon, J. W., & Kirk, D. W. (1996). Utilizing coal fly ash as a landfill barrier material. *Waste Management*, *16*(7), 587−595. Available from https://doi.org/10.1016/S0956-053X(96)00108-0.

Power, K. C., Vanapalli, S. K., & Garga, V. K. (2008). A revised contact filter paper method. *Geotechnical Testing Journal*, *31*(6), 461−469.

Prakash, A., Hazra, B., Deka, A., & Sreedeep, S. (2017). Probabilistic analysis of water retention characteristic curve of fly ash. *International Journal of Geomechanics*, *17*(12). Available from https://doi.org/10.1061/(ASCE)GM.1943-5622.0001024, https://ascelibrary.org/journal/ijgnai.

Prakash, A., Hazra, B., & Sreedeep, S. (2019). Probabilistic analysis of unsaturated fly ash slope. *Journal of Hazardous, Toxic, and Radioactive Waste*, *23*(1). Available from https://doi.org/10.1061/(ASCE)HZ.2153-5515.0000428, http://ascelibrary.org/hzo/.

Prashanth, J. P., Sivapullaiah, P. V., & Sridharan, A. (2001). Pozzolanic fly ash as a hydraulic barrier in land fills. *Engineering Geology*, *60*(1−4), 245−252. Available from https://doi.org/10.1016/S0013-7952(00)00105-8.

Puppala, A. J., Punthutaecha, K., & Vanapalli, S. K. (2006). Soil-water characteristic curves of stabilized expansive soils. *Journal of Geotechnical and Geoenvironmental Engineering*, *132*(6), 736−751. Available from https://doi.org/10.1061/(ASCE)1090-0241(2006)132:6(736).

Raghuram, A. S. S., Basha, B. M., & Moghal, A. A. B. (2020). Effect of fines content on the hysteretic behavior of water-retention characteristic curves of reconstituted soils. *Journal of Materials in Civil Engineering*, *32*(4). Available from https://doi.org/10.1061/(ASCE)MT.1943-5533.0003114, http://ascelibrary.org/mto/resource/1/jmcee7/.

Raghuram, A. S. S., Basha, B. M., & Raviteja, K. V. N. S. (2021). Variability characterization of SWCC for clay and silt and its application to infinite slope reliability. *Journal of Materials in Civil Engineering*, *33*(8). Available from https://doi.org/10.1061/(ASCE)MT.1943-5533.0003809, http://ascelibrary.org/mto/resource/1/jmcee7/.

Sivapullaiah, P. V., & Baig, M. A. A. (2011). Gypsum treated fly ash as a liner for waste disposal facilities. *Waste Management*, *31*(2), 359−369. Available from https://doi.org/10.1016/j.wasman.2010.07.017.

Wen, H., Wang, J., Wen, V. F. W., & Muhunthan, B. (2015). Soil−water characteristic curves for soils stabilized with class C fly ash. *Transportation Research Record*, *2473*(1), 147−154. Available from https://doi.org/10.3141/2473-17, https://journals.sagepub.com/home/TRR.

Yang, H., He, C., Xiao, J., & Zhan, W. (2011). Analysis on improvement effect of expansive soil by soil-water characteristic curve. *Journal of Highway and Transportation Research and Development (English Edition)*, *6*(4), 272−279.

Zapata, C. E., Houston, W. N., Houston, S. L., & Walsh, K. D. (2000). Soil-water characteristic curve variability. *Geotechnical Special Publication*, *287*(99), 84−124.

Experimental study of the parameter for predicting the strength of geopolymer concretes based on ground granulated blast furnace slag and fly ash

2

Sumanth Kumar Bandaru [1] *and Rama Seshu D.* [2]
[1]Civil Engineering Department, Kakatiya Institute of Technology and Science, Warangal, Telangana, India, [2]Civil Engineering Department, National Institute of Technology, Warangal, Telangana, India

2.1 Introduction

From the standpoint of sustainability, geopolymer concrete (GPC) is considered an alternative to conventional cement concrete as a building material (Davidovits, 1994; Wang et al., 1995). It consumes less energy during the manufacturing process and also gets cured under ambient conditions without any need for water curing. The production of GPC involves the use of source materials such as fly ash (FA), ground granulated blast furnace slag (GGBS), which are rich in silicon and aluminum, along with alkaline liquids such as sodium hydroxide and/or sodium silicate solution.

In recent past, several investigations reported various parameters affecting the strength of geopolymer concrete, such as sodium hydroxide solution concentration, that is, molarity of NaOH solution, the ratio of sodium silicate to sodium hydroxide, alkaline activator solution to binder (FA + GGBS), binder content, curing temperature, the content of coarse and fine aggregate (Anuradha et al., 2012; Hardjito et al., 2004; Kotwal et al., 2015; Lloyd & Rangan, 2009; Lzrescu, 2017; Rangan, 2008).

The combination of various parameters effects the strength of GGBS- and FA-based GPC and is represented by the proposed parameter called "Binder Index (Bi)" (Rama Seshu et al., 2017). Earlier, effect of molarity and ratio of source material were considered in evaluating binder index. Nevertheless, the suggested binder index takes into account variations in several parameters such as molarity, alkaline solution, ratio of source materials, and a modified binder index for GPC has been proposed (2019).

Green Materials in Civil Engineering. DOI: https://doi.org/10.1016/B978-0-443-19106-0.00002-6

2.2 Experimental program

The experimental program consisted of cast and testing cubes of size $150 \times 150 \times 150$ mm and prisms of size $100 \times 100 \times 400$ mm for determining the compressive strength and flexural strength, that is, modulus of rupture (tensile strength in bending) of FA- and GGBS-based GPC. Fig. 2.1 gives the flow chart of the experimental program conducted on GPC.

2.2.1 Materials used

FA and GGBS were used as binders and these were obtained from NTPC Ramagundam thermal power plant, Ramagundam, India, and JSW Cements Pvt Ltd, Bilakalagudur, India with a specific gravity of 2.17 and 2.90, respectively. Table 2.1 shows the details of chemical compositions of the binders.

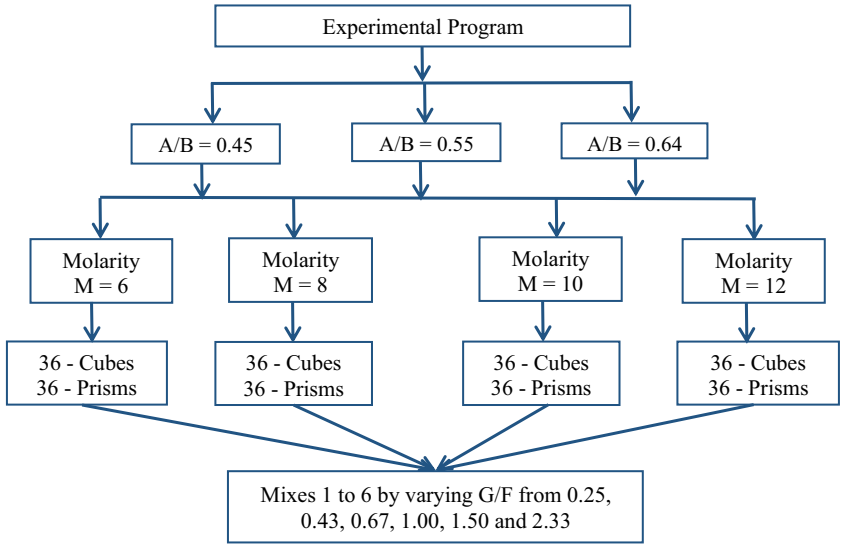

Figure 2.1 Schematic diagram of the experimental program.

Table 2.1 Chemical composition of fly ash and ground granulated blast furnace slag (GGBS) (% by mass).

Binder material	SiO_2	Al_2O_3	Fe_2O_3	SO_3	CaO	MgO	Na_2O	LOI
Fly ash	60.11	26.53	4.25	0.35	4.00	1.25	0.22	0.88
GGBS	37.73	14.42	1.11	0.39	37.34	8.71	–	1.41

Aggregates like river sand conforming to Zone-II of IS 383, 2016 was used as fine aggregate. The specific gravity and bulk density of sand are 2.65 and 1.45 g/cm^3, respectively. Well-graded aggregate conforming to IS 383, 2016 with 20 mm nominal size of granite was used as coarse aggregate of 2.80 and 1.5 g/cm^3 with specific gravity and bulk density, respectively.

Alkaline activator solution is a combination of sodium hydroxide and sodium silicate solutions. Sodium hydroxide in the form of pellets with 98% purify was used for the study. Sodium hydroxide pellets were dissolved in portable water to prepare solutions of different molarity (M = 6, 8, 10, and 12). After cooling, sodium hydroxide solution was mixed with sodium silicate in the form of liquid with a mixing ratio of 1:2.5, and the prepared alkaline activator solution thus prepared was stored at an ambient temperature for 24 hours at a relative humidity of 65%−75% before using it in the casting of GPC specimens.

Sulphonated napthalene polymers (Conplast SP 430 Fosroc make) were used as a superplasticizer.

2.2.2 Mix proportions

The GPC mix proportions adopted in the study are shown in Table 2.2. These mixes were designed to facilitate the study of the effect of various parameters on FA- and GGBS-based GPC. Molarity of sodium hydroxide varied from 6M, 8M, 10M, and 12M, while sodium silicate to sodium hydroxide ratio was fixed at 2.5.

2.3 Cast and curing of geopolymer concrete specimens

For evaluating the compressive and flexural strength of GPC, around 72 cubes and prisms with six different mixes with varying ratios of GGBS to FA (0.25, 0.43, 0.67, 1.0, 1.5, and 2.3), four different molarities (6, 8, 10, and 12) of NaOH alkaline solution were considered. In all the above specimens, the alkaline activator solution to binder content ratio was maintained constant at 0.64.

Additionally, to study the effect of alkaline activator solution to binder content ratio on the compressive and flexural strength of GPC, 72 cubes and 72 prism specimens were cast and tested. The parameters varied include two different alkaline activator solution to binder content ratios (0.55 and 0.45), three varying ratios of GGBS to FA of 0.25, 0.67, and 1.5, and four different molarities (6, 8, 10, and 12) of NaOH alkaline solution. Three specimens were cast and tested for each variation.

A rotating drum-type pan mixer of 100 kg capacity was used to mix the dry materials. After uniform mixing of dry materials, an alkaline activator solution of a specified quantity and a superplasticizer (Conplast SP 430 Fosroc make) at optimal dosage were added. A consistent mixture was obtained after mixing it for about 5−7 minutes. The fresh mixes that were prepared were cohesive and there was no

Table 2.2 Mix proportions of geopolymer concrete.

A/B	G/F	Fly ash (kg/m^3) (F)	GGBS (kg/m^3) (G)	Coarse aggregate (kg/m^3)	Fine aggregate (kg/m^3)	NaOH (kg/m^3)	Na_2SiO_3 (kg/m^3)	Alkaline liquid (kg/m^3) (A)
0.64	0.25	354.80	90.40	813.56	596.61	81.36	203.39	284.75
	0.43	311.86	133.33	813.56	596.61	81.36	203.39	284.75
	0.67	267.12	178.08	813.56	596.61	81.36	203.39	284.75
	1.00	222.82	222.37	813.56	596.61	81.36	203.39	284.75
	1.50	178.08	267.12	813.56	596.61	81.36	203.39	284.75
	2.3	133.33	311.86	813.56	596.61	81.36	203.39	284.75
0.55	0.25	354.80	90.40	813.56	596.61	69.96	174.90	244.86
	0.43	311.86	133.33	813.56	596.61	69.96	174.90	244.86
	0.67	267.12	178.08	813.56	596.61	69.96	174.90	244.86
	1.00	222.82	222.37	813.56	596.61	69.96	174.90	244.86
	1.50	178.08	267.12	813.56	596.61	69.96	174.90	244.86
	2.3	133.33	311.86	813.56	596.61	69.96	174.90	244.86
0.45	0.25	354.80	90.40	813.56	596.61	57.24	143.10	200.34
	0.43	311.86	133.33	813.56	596.61	57.24	143.10	200.34
	0.67	267.12	178.08	813.56	596.61	57.24	143.10	200.34
	1.00	222.82	222.37	813.56	596.61	57.24	143.10	200.34
	1.50	178.08	267.12	813.56	596.61	57.24	143.10	200.34
	2.3	133.33	311.86	813.56	596.61	57.24	143.10	200.34

segregation of the mix. The mixture was placed in cubes and prism molds and compacted by placing it on the jolted table. After compaction, the top surface of the molds was leveled with a trowel. The cubes and prisms were demolded after 24 hours of casting. The specimens are air-cured at room temperature of 35°C ± 2°C and relative humidity of 75% for 28 days.

2.3.1 Testing procedure for compressive strength test

The GPC cube specimens of size $150 \times 150 \times 150$ mm and prisms of size $100 \times 100 \times 400$ mm that were cast were tested on a 2000 kN Tinius Olsen Testing machine and failure loads were recorded and tabulated in Table 2.3. The testing of cube and prism specimens was carried out at the end of 28 days of curing outdoors. The testing was done conforming to IS 516, 1959.

2.3.1.1 Compressive strength of geopolymer concrete

From the recorded maximum load or failure loads of three identical cube specimens, the average compression strength of GPC for different GGBS to FA ratios and for different molarities of NaOH alkaline activator were calculated and tabulated in Table 2.3.

2.3.2 Flexural strength or modulus of rupture (tensile strength in bending) of geopolymer concrete

After outdoor curing for 28 days, the prism samples were tested in accordance with IS 516, 1959 (IS 516, 1956). The load was applied at an increasing constant rate until the specimen's resistance to the increasing load broke down and could no longer be maintained. The maximum load applied to the specimen was recorded. From the recorded maximum load or failure loads of three identical prism specimens, the average flexural strength of GPC for different GGBS to FA ratios and for different molarities of the NaOH alkaline activator was tabulated. These data are presented in Table 2.3.

2.4 Test results and discussions

Compressive and flexural strength for different mix proportions and the corresponding average binder index are tabulated in Table 2.3.

The variation in compressive strength, flexural strength with different molarity of NaOH, alkaline to binder ratio, GGBS to FA ratio, and binder index of GPC is plotted and discussed in the following sections.

Table 2.3 Test results on geopolymer specimens.

Molarity of NaOH solution (M)	GGBS/ Fly ash (G/F)	A/B = 0.64			A/B = 0.55			A/B = 0.45		
		Binder index (Bi)	Comp. strength (MPa)	Flex. strength (MPa)	Binder index (Bi)	Comp. strength (MPa)	Flex. strength (MPa)	Binder index (Bi)	Comp. strength (MPa)	Flex. strength (MPa)
6	0.25	0.96	16.62	1.77	0.83	13.33	1.65	0.68	12.62	1.50
6	0.43	1.65	18.14	2.10	–	–	–	–	–	–
6	0.67	2.57	24.97	2.48	2.21	20.00	2.40	1.81	17.11	2.25
6	1.00	3.84	37.82	2.70	–	–	–	–	–	–
6	1.50	5.76	41.69	3.00	4.95	33.33	2.73	4.05	28.44	2.55
6	2.33	8.95	45.67	3.36	–	–	–	–	–	–
8	0.25	1.28	19.27	1.83	1.10	19.10	1.71	0.90	19.02	1.59
8	0.43	2.20	23.45	2.19	–	–	–	–	–	–
8	0.67	3.43	30.17	2.55	2.95	28.88	2.46	2.41	25.77	2.40
8	1.00	5.12	38.53	2.93	–	–	–	–	–	–
8	1.50	7.68	42.71	3.09	6.60	35.55	2.92	5.40	28.88	2.85
8	2.33	11.93	49.34	3.59	–	–	–	–	–	–
10	0.25	1.60	22.53	2.06	1.38	21.33	1.80	1.13	20.08	1.74
10	0.43	2.75	25.99	2.29	–	–	–	–	–	–
10	0.67	4.29	37.41	2.61	3.69	33.33	2.55	3.02	28.44	2.46
10	1.00	6.40	39.55	2.99	–	–	–	–	–	–
10	1.50	9.60	43.83	3.12	8.25	37.33	3.00	6.75	30.53	2.92
10	2.33	14.91	53.92	3.66	–	–	–	–	–	–
12	0.25	1.92	27.93	2.16	1.65	25.77	2.10	1.35	24.44	1.95
12	0.43	3.30	30.07	2.36	–	–	–	–	–	–
12	0.67	5.15	39.65	2.64	4.42	34.22	2.58	3.62	31.11	2.52
12	1.00	7.68	41.08	3.05	–	–	–	–	–	–
12	1.50	11.52	44.75	3.36	9.90	40.44	3.27	8.10	36.13	3.15
12	2.33	17.89	58.00	3.75	–	–	–	–	–	–

Note: Binder index (Bi) = M × (G/F) × (A/B), where A/B is the alkaline-activator-to-binder ratio; binder B is the sum quantity of GGBS and fly ash (G + F).

2.4.1 Effect of molarity (M)/concentration of sodium hydroxide (NaOH) solution

2.4.1.1 On the compressive strength of geopolymer concrete

The effect of molarity of NaOH solution on different GGBS to FA ratios on the compressive strength of GPC is shown in Fig. 2.2. It was observed that as molarity increased, the compressive strength of GPC also increased. However, the increase in strength was not in proportion to increase in molarity. For a particular alkaline activator to binder ratio (i.e., A/B = 0.64), as the GGBS to FA ratio increased from 0.25 to 2.3, the compressive strength of GPC increased by 175%, 156%, 139%, and 107% for molarity of NaOH solution of 6M, 8M, 10M, and 12M, respectively.

2.4.1.2 On the flexural strength of geopolymer concrete

The effect of the molarity of NaOH solution for the different GGBS to FA ratios on the flexural strength of GPC is shown in Fig. 2.3. It was observed that as the molarity increased, the flexural strength of GPC also increased. However, the increase in strength was not in proportion to the increase in molarity. For a particular alkaline activator to binder ratio (i.e., A/B = 0.64), as the GGBS to FA ratio increased from 0.25 to 2.3, the flexural strength of GPC increased by 89.8%, 96.1%, 77.6%, and 73.6% for a molarity of 6M, 8M, 10M, and 12M, respectively, of the NaOH solution.

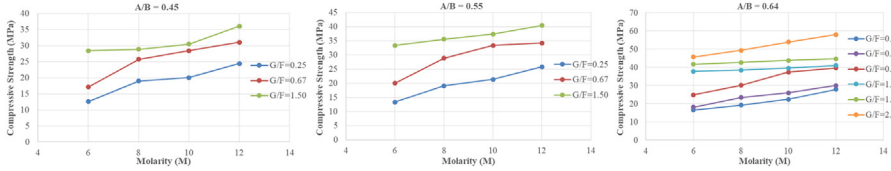

Figure 2.2 Compression strength of the geopolymer concrete (GPC) versus molarity of NaOH for different ground granulated blast furnace slag (GGBS) to fly ash ratio and different alkaline activator to binder ratio.

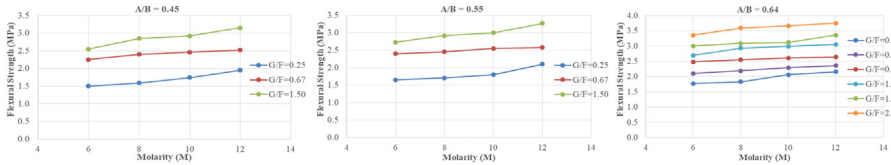

Figure 2.3 Flexural strength of the geopolymer concrete (GPC) versus molarity of NaOH for different ground granulated blast furnace slag (GGBS) to fly ash ratio and different alkaline activator to binder ratio.

2.4.2 Effect of the alkaline activator to binder ratio (A/B)

2.4.2.1 On the compressive strength of geopolymer concrete

The effect of alkaline activator to binder ratio (A/B) and molarity of the NaOH solution on the compressive strength of GPC for a particular GGBS to FA ratio is shown in Fig. 2.4. From the figure, it can be observed that the compression strength of GPC increased with an increase in the alkaline activator to binder content ratio. However, the rate of increase of the compressive strength was higher for higher GGBS to FA ratios. For a particular GGBS to FA ratio (i.e., G/F = 0.67), as the alkaline activator to binder ratio increased from 0.25 to 1.50, the compressive strength of GPC increased by 150%, 121%, 94%, and 60% for a molarity 6M, 8M, 10M, and 12M, respectively, of the alkaline activator.

For a constant value of low molarity (6M) and GGBS to FA ratio (0.67), increasing the alkaline activator to binder content ratio from 0.45 to 0.64, the compressive strength of GPC increased from 125% to 150%. However, in the case of high molarity (12M) and GGBS to FA ratio (0.67), increasing the alkaline activator to binder content ratio from 0.45 to 0.64 increased the compressive strength of GPC from 48% to 60%. Hence the use of a stronger alkaline activator to binder content ratio is beneficial in increasing the strength of GPC prepared with low molarity NaOH solution.

2.4.2.2 On the flexural strength of geopolymer concrete

The effect of alkaline activator to binder content ratio (A/B) and molarity of NaOH solution on the flexural strength of GPC for a particular GGBS to FA ratio is shown in Fig. 2.5. From the figure, it can be seen that the flexural strength of GPC increases with an increase in the alkaline activator to binder content ratio. However, the rate of increase of flexural strength is more or less uniform as the alkaline activator to binder content ratio (A/B) increased for the same molarity of NaOH solution. For a particular GGBS to FA ratio (i.e., G/F = 0.67), as the alkaline activator solution to binder ratio increased from 0.25 to 1.50, the flexural strength of GPC increased by 70%, 69%, 51%, and 55% for the molarity of NaOH solutions of 6M, 8M, 10M, and 12M, respectively. However, in the case of constant low or

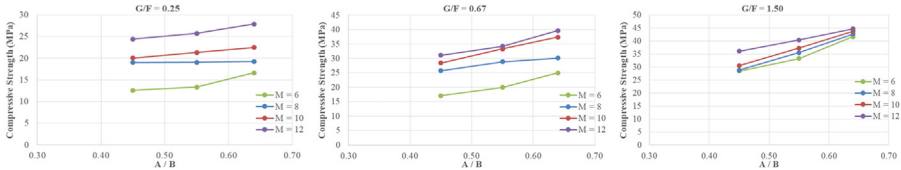

Figure 2.4 Compression strength of the geopolymer concrete (GPC) versus alkaline activator to binder ratio for different molarity of NaOH and different ground granulated blast furnace slag (GGBS) to fly ash ratios.

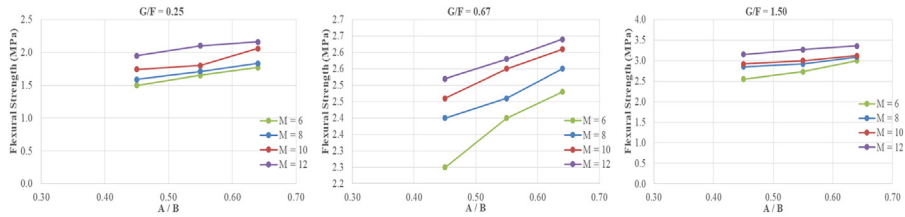

Figure 2.5 Flexural strength of the geopolymer concrete (GPC) versus alkaline activator to binder ratio for different molarity of NaOH and different ground granulated blast furnace slag (GGBS) to fly ash ratios.

high molarity (6M or 12M) and for constant GGBS to FA ratio (0.67), increasing A/B ratio from 0.45 to 0.64 led to percent increase in flexural strength of GPC and this varied from 51% to 70%.

2.4.3 Effect of ground granulated blast furnace slag to fly ash ratio (G/F)

2.4.3.1 On the compressive strength of geopolymer concrete

The GGBS to FA ratio and molarity of the alkaline activator effects the compressive strength of GPC for a alkaline activator solution to binder content ratio constant is shown in Fig. 2.6. From the figure, it can be observed that the compression strength of GPC increases with increase in ratio of GGBS to FA. Nevertheless, the rate of rise in the compressive strength was higher for GGBS to FA ratios lower than 1.0, as indicated by larger rise of compressive strength when there was a change in molarity.

2.4.3.2 On the flexural strength of geopolymer concrete

The effect of GGBS to FA ratio and molarity of the alkaline activator on the flexural strength of GPC for a particular alkaline activator to binder ratio is shown in Fig. 2.7. From the figure, it can be observed that the flexural strength of GPC increased with an increase in GGBS to FA ratio. However, the rate of increase of flexural strength was lower compared to that of the compression strength of GPC for all GGBS to FA ratios considered in the investigation.

2.4.4 Validation of binder index

The concept of a unified parameter called “Binder Index (Bi)” is proposed which includes the effect of GGBS to FA ratio (G/F), alkaline activator solution to binder

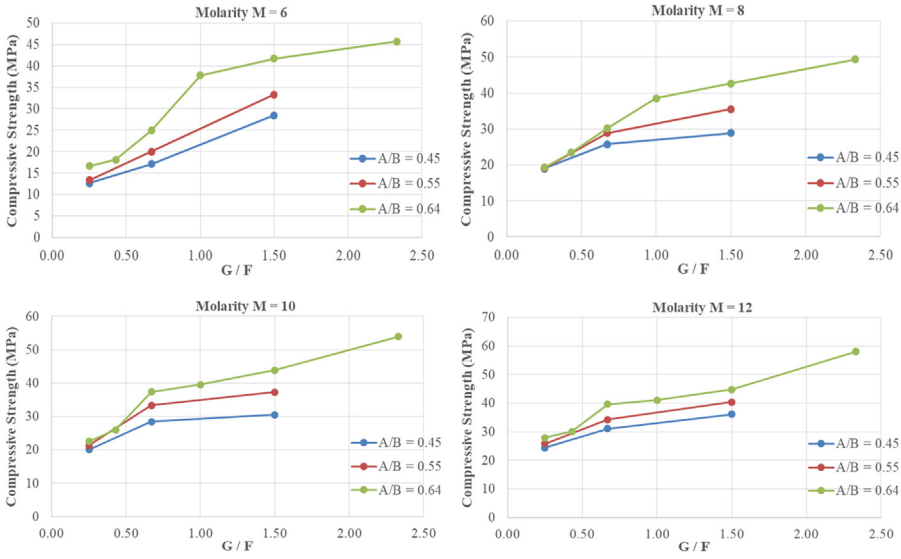

Figure 2.6 Compression strength of the geopolymer concrete (GPC) versus ground granulated blast furnace slag (GGBS) to fly ash ratios for the different alkaline activator to binder ratio and different molarity of NaOH.

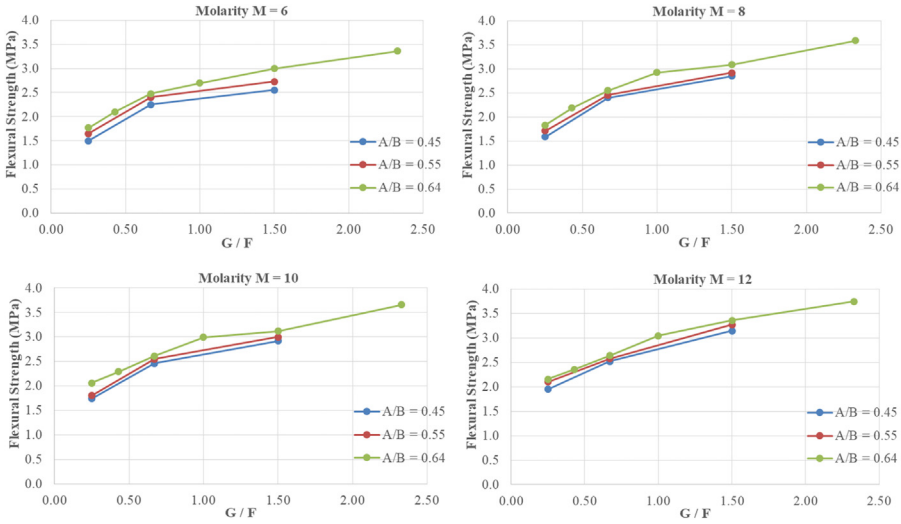

Figure 2.7 Flexural strength of the geopolymer concrete (GPC) versus ground granulated blast furnace slag (GGBS) to fly ash ratios for the different alkaline activator to binder ratio and different molarity of NaOH.

content ratio (A/B), and the molarity of NaOH solution (M) controlling the strength of GGBS- and FA-based GPC.

$$\mathbf{Bi} = \frac{\mathbf{MA}}{(\mathbf{G}+\mathbf{F})}\left[\frac{\mathrm{G}}{\mathrm{F}}\right] \tag{2.1}$$

The values of the compressive strength of GPC at 28 days (f_{gpc}) and the corresponding binder index (Bi) are given in Table 2.3, and a variation between them is shown in Fig. 2.8. This variation indicates that the compressive strength of GPC increases with an increase of binder index. Nevertheless, the increases in strength was not in proportion to an increase in binder index. A nonlinear variation exists between the binder index and the compressive strength of GPC. The following best-fit equation gives the relation between the compressive strength of the FA- and GGBS-based GPC at 28 days with binder index. The equation was represented by a single power equation with an acceptable correlation with the experimental values (Rama Seshu and Sumanth Kumar, 2019).

Where f_{gpc} is the compressive strength of geopolymer concrete at 28 days and Bi is binder index. The values of the flexural strength of GPC at 28 days and corresponding binder index (Bi) are given in Table 2.3, and the variation between them is shown in Fig. 2.9. This variation indicates that the flexural strength of GPC increased with an increase in the binder index and is along similar lines to the compressive strength of GPC. The following best-fit equation gives the relation between the flexural strength of the FA- and GGBS-based GPC at 28 days with the binder index (Bi).

$$f_{gpc} = 17.70[Bi]^{0.41} \tag{2.2}$$

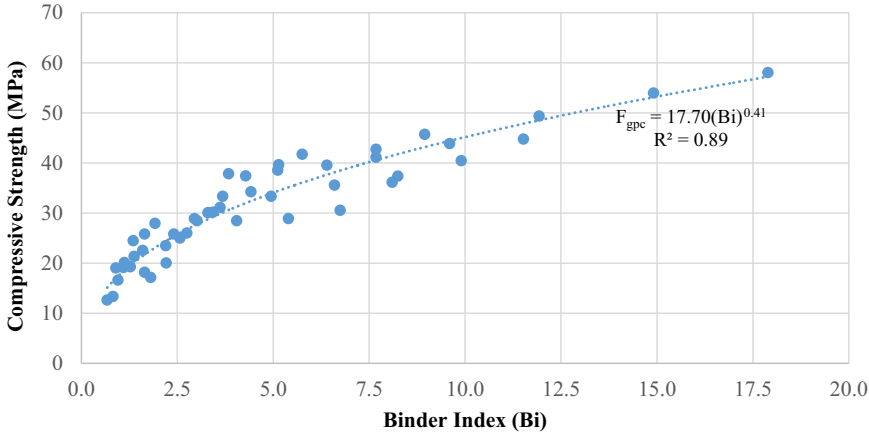

Figure 2.8 Variation of compressive strength w.r.t binder index.

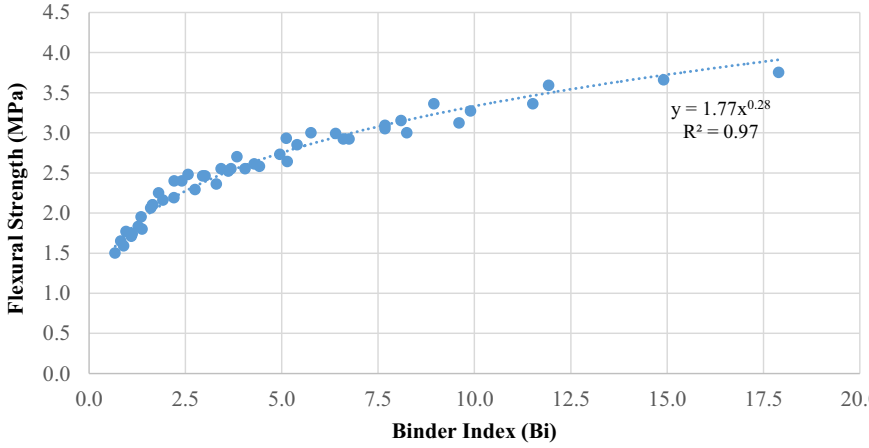

Figure 2.9 Variation of flexural strength w.r.t binder index.

Where $f_{flexural}$ is the flexural strength of GPC at 28 days and Bi is binder index.

$$f_{flexural} = 1.77[Bi]^{0.28} \tag{2.3}$$

It can be noted that the variation of strengths with binder index is in line with the proposed equation (Rama Seshu and Sumanth Kumar, 2019) for geopolymer mixes and follows the nonlinear power equation. Given the above discussions, the newly proposed parameter called "Binder Index (Bi)" combines the effects of alkaline to binder content ratio, GGBS to FA ratio, and molarity of sodium hydroxide and can be considered a single unique parameter to control the compressive strength of GPC.

2.5 Conclusion

The following conclusions are drawn from the experimental investigation presented:

1. The compression strength of the FA- and GGBS-based GPC increases with an increase in GGBS to FA ratio. However, the rate of increase of the compressive strength is higher for the GGBS to FA ratios lower than 1.0.
2. Flexural strength of the FA- and GGBS-based GPC increases with an increase in the GGBS to FA ratio. However, the rate of increase of flexural strength is lower compared to that of the compression strength of GPC.
3. The compression strength of GPC increases with an increase in the alkaline activator to binder content ratio. However, the rate of increase of the compressive strength is higher for higher GGBS to FA ratios for constant molarity of NaOH solution in an alkaline activator.
4. The use of a higher alkaline activator to binder content ratio (A/B) is beneficial in increasing the strength of GPC prepared with low molarity NaOH.

5. The flexural strength of GPC increases with an increase in alkaline activator to binder content ratio (A/B). However, the rate of increase of the flexural strength is more or less uniform with increase in alkaline activator to binder ratio (A/B) for a constant molarity of the alkaline activator.
6. The strength of GPC (both compression and flexural strengths) increases with an increase of binder index.

References

Anuradha, R., Sreevidya, V., Venkatasubramani, R., & Rangan, B. V. (2012). Modified guidelines for geopolymer concrete mix design using Indian standard. *Asian Journal of Civil Engineering*, *13*(3), 353−364. Available from http://www.bhrc.ac.ir/portal/LinkClick.aspx?fileticket = Z0FB0JorcN8%3d&tabid = 1102.

Davidovits, J. (1994). Geopolymers: Man-made geosynthetics and the resulting development of very early high strength cement. *Journal of Materials Education*, *16*(2&3), 91−139.

Hardjito, D., Wallah, S. E., Sumajouw, D. M. J., & Rangan, B. V. (2004). On the development of fly ash-based geopolymer concrete. *ACI Materials Journal*, *101*(6), 467−472.

Kotwal, A. R., Kim, Y. J., Hu, J., & Sriraman, V. (2015). Characterization and early age physical properties of ambient cured geopolymer mortar based on class C fly ash. *International Journal of Concrete Structures and Materials*, *9*(1), 35−43. Available from https://doi.org/10.1007/s40069-014-0085-0.

IS 516 (1956). *Methods of Tests for Strength of Concrete Reaffirmed 1999*.

Lloyd, N., & Rangan, V. (2009). *Australia geopolymer concrete - sustainable cementless concrete*. American Concrete Institute, ACI special publication, 01932527. 261. pp. 33−53.

Lzrescu, A. (2017). The effect of alkaline activator ratio on the compressive strength of fly ash based geopolymer paste. *IOP Conference Series: Materials Science and Engineering*.

Rama Seshu, D., Shankaraiah, R., & Sesha Srinivas, B. (2017). Wpływ wskaźnika spoiwowego na wytrzymałość na ściskanie betonu geopolimerowego. *Cement, Wapno, Beton*, *2017*(3), 211−218. Available from http://www.cementwapnobeton.pl.

Rama Seshu, D., & Sumanth Kumar, B. (2019). Binder index as criterian for assessing the strength of geopolymer concrete. *Journal of Structural Engineering*, *46*(1), 12−16.

Rangan, B. V. (2008). Mix design and production of flyash based geopolymer concrete. *Indian Concrete Journal*, *82*(5), 7−15.

Wang, S. D., Pu, X. C., Scrivener, K. L., & Pratt, P. L. (1995). Alkali-activated slag cement and concrete: A review of properties and problems. *Advances in Cement Research*, *7* (27), 93−102. Available from https://doi.org/10.1680/adcr.1995.7.27.93.

Mitigating the environmental impacts of conventional concrete—a quantitative sustainable concrete approach

3

Suchith Reddy Arukala
Department of Civil Engineering, Kakatiya Institute of Technology and Science, Warangal, Telangana, India

3.1 Introduction

Construction makes up 6% of the global GDP and is a significant business that affects all other industries. It makes up one-third of the waste that is disposed of in landfills (Mastrucci et al., 2017). Real estate developers and buyers now prioritize sustainable environment and surroundings (Reddy et al., 2019). Buildings have a significant negative impact on the environment, from the design stage through to the demolition stage. Buildings use nearly 30%−40% of the primary energy globally during their full life cycle and emit 40% of GHG emissions (Bansal, 2007). In developing countries like India, the demand for electrical energy was 30% more than the demand for primary energy (24%). India, which produces 4% of the world's electricity, is the sixth largest power producer and user. About 22% of the CO_2 emissions in India's economy are produced by the building sector, and 80% of those emissions come from the production of cement, steel, lime, and bricks. To lessen the negative environmental effects of construction processes, there is an urgent need for change (Spence & Mulligan, 1995). True progress toward a sustainable built environment requires a life cycle thinking approach, which entails a thorough analysis of every stage of the building life cycle (Horvath, 2004). Mineral extraction from their natural ores is still a labor-intensive process that uses energy, generates waste, and contributes to environmental pollution. This contamination has negative effects on the environment, including resource depletion, biological losses, and other emissions that contribute to global warming and acid rain.

To reduce construction's negative environmental effects and move the community closer to sustainable advancement, modifications to typical cement concrete are now required. One of the urban locations where the effects of development on the environment should be considered is the space occupied by buildings. They provide the necessary framework for productive endeavors and meet essential human needs. However, because of this advantage held by the structures, stakeholders can fail to recognize the environmental impact of developing nations. In this aspect, life cycle assessment

Green Materials in Civil Engineering. DOI: https://doi.org/10.1016/B978-0-443-19106-0.00003-8

(LCA) is a useful tool since it provides an account of the resources and energy needed to create a system or product and evaluates the resulting environmental effects (ISO 14040). LCA provides the required data to systemically reduce the impacts and create a sustainable environment through the thorough study. The current study attempts to assess and estimate the environmental effects of a residential structure with a 60-year service life while taking numerous concrete variants into consideration. Numerous earlier case studies have examined life cycle energy (LCE) and offered suggestions for how to lower LCE consumption on different materials considering a few life cycle stages. The present study focused on impacts caused by basic concrete with mostly used supplementary cementitious materials (SCMs) (i.e., fly ash [FA] and ground granulated blast furnace [GGBS]) with varying percentages and without compromising strength and durability properties. The novelty of the study lies in considering an existing building in a particular location and suggesting various impacts caused, energy consumed, and variability of usage in selecting a particular proportion for further and future design perspectives and constructions. The aim of the current study is to determine how the effects of replacing cement with various pozzolanic materials at different percentages can change the performance of the cement industry's sustainability.

3.2 Autodesk Revit

It is a well-known Building Information Modeling (BIM) software application mostly utilized by designers, contractors, engineers, and architects. The BIM is an advancement that enables the creation of a real-time visual depiction of an infrastructure. It will ultimately make planning, designing, building, and operating easier. To ensure project success, the BIM model will offer a precise geometrical view and associated data, to support the project's acquisition, installation, fabrication, and construction activities.

3.2.1 Tally

Tally is an add-on for the Autodesk Revit software that enables users to do LCA on buildings and determine the environmental effects of BIM models that have materials assigned to them. When the building materials are assigned to BIM elements in Tally's database, the LCA of the BIM model will be performed. It is simple to use and does not call for any advanced modeling abilities. In order to evaluate two or more design options, it offers a design option comparison. Eutrophication potential (EP), acidification potential (AP), global warming potential (GWP), smog formation potential (SFP), ozone depletion potential (ODP), and primary energy demand (PED) are the six impact categories that are assessed.

3.2.2 Life cycle assessment

By examining the life cycle of raw materials, production, and disposal, as well as the life cycle of the product itself, the LCA approach is one of the systems for

measuring the environmental effects of products, processes, and activities. "LCA is a strategy for analyzing the potential environmental characteristics associated with a product (or service) by collecting an inventory of relevant inputs and outputs," according to ISO 14040,040 (1997). It examines the outcomes of the inventory and impact stages and assesses any potential environmental effects linked to these inputs and outputs. Four steps comprise the LCA process: planning, reviewing the inventory, evaluating the impact, and analyzing improvements.

- Planning: An LCA planning framework that outlines the study's goals, objectives, boundaries, breadth, and scope outlines how the investigation will progress.
- Inventory analysis: The measurement of energy, air pollutants, raw materials, water-borne effluent, and solid and liquid waste forms the basis of an analysis of the system's inputs and outputs.
- Impact assessment: The application of qualitative and quantitative techniques that examine the usage of energy and production, raw materials, water consumption, air pollutants, and solid waste production allows for the assessment of the product's environmental impact.
- Improvement analysis: Improvement analysis involves taking a thorough look at a product or system's complete cycle and examining the effects of some modifications on the environment. The goal is to lower the environmental burdens connected with the product or system.

3.3 Literature review

The energy efficiency of several residential structures (one, two, and multistory) was assessed by the authors. Nearly 10 homes were used for testing of double glass windows (DGW) and thermal insulation (TI) on roofs and walls. It is noted that the LCE of a building varies from 240 to 380 kWh/m^2 per year, depending on the type of building and climatic location (Ramesh et al., 2012). One of the buildings underwent additional inspection in order to evaluate performance of LCE with on-site power generation. It was also observed that approximately 5%−30% of LCE was preserved (Ramesh et al., 2012). In one study, the LCE of a building was made up of different energies like constructional energy (CE), operational energy (OE), and demolition energy (DE). This study is a case study on the LCE analysis of residential progress and consists of 96 identical apartment-style homes located in Southern India. It was discovered that CE is a crucial part of the LCE of residential buildings with partial or no air conditioning. The CE becomes crucial as the OE due to shorter building service lifespans and more energy efficiency in the operations phase (Devi & Palaniappan, 2014). The largest contributors to GHG emissions are RCC framework and steel, which use 59% of all energy solely during their operational period, according to accurate data. It is clear that fiber emits the most carbon, followed by ceramics, metals, elastomers, and polymers (Ansari, 2017). The importance of choosing the right materials for sustainability has been demonstrated by authors (Arukala et al., 2020). By incorporating BSA techniques into BIM platforms, a more sustainable environment can be created (Carvalho et al., 2021).

BIM offers creative ways to use e-procurement in construction, which helps the construction procurement process (Costa & Grilo, 2015). BIM is a tool that allows for the storing and reuse of knowledge over the course of a project. This document properly explains the BIM idea (Yadav & Kanade, 2018). Understanding the potential and continuing constraints of the BIM-based LCA tools under development requires a comparison of practical tool applications that is clearly significant (Bueno & Fabricio, 2018).

3.3.1 Life cycle assessment integrated building information modeling software

The literature review on the integration of BIM with LCA identified three key factors. Identifying information regarding LCA tools and the requirement for BIM integration comes first. Finding the data that could be incorporated into the BIM model is the second step. The final step is to compare the energy and environmental performance of two different structures in order to understand the effects of the designer's decisions on the building's performance. The environmental product declaration (EPD), which was enacted and harmonized with EN 15942:2011, serves as the main source for LCA tool databases (Reddy et al., 2019). For business-to-business transactions, this makes the product's environmental performance easier (BSI, 2011). Tally is one of the few tools that directly operate as a plug-in for Autodesk Revit, and it is used in this study to conduct the LCA.

3.4 Methodology

The environmental impact of residential construction is assessed quantitatively in the current study and contrasted with various concrete mixtures. It covers all the steps from "cradle to grave," starting with the extraction of raw materials and continuing through manufacturing, shipment, installation, and deconstruction. The study's narrow focus is on contrasting how different concrete mixtures for residential buildings affect the environment. The percentages of FA and GGBS in the concrete mixtures were changed in seven different ways. To perform the effect assessment, a building with a built-up size of 650 square feet is modeled in Revit and exported to Tally using the TRACI 2.1 impact evaluation method. In the current study, a case study of a building composed of FA- and GGBS-based concrete in varied percentages was used to examine the impact categories over the building's life cycle.

The study took into account six main categories of environmental impact: AP, EP, GWP, ODP, SFP, and PED. The following schematic diagram shows the detailed methodology of the study undertaken for assessing the environmental performance of buildings considering the varied concrete SCMs percentages in different stages of the building life cycle and impact categories (Fig. 3.1).

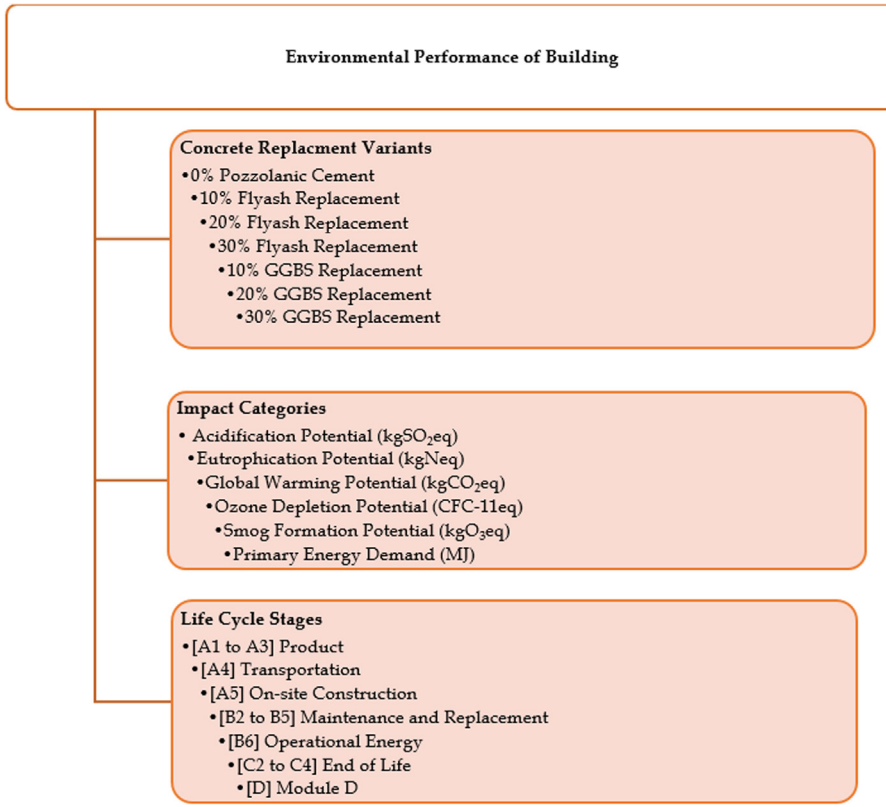

Figure 3.1 The schematic diagram for methodology adopted in assessing the environmental performance of a building work flow for assessing impacts.

3.5 Case study

The study considered the existing building specifications, structural components, and building elements. The following are detailed descriptions of the specification considered while constructing the building (Fig. 3.2):

3.5.1 System boundaries

The four stages of construction—product/manufacturing, on-site construction, operating, and demolition—are all included within the system limits. Transportation effects are also taken into account, and the material's transport distance from the closest vendor was picked. The system boundaries covered water use and on-site building. Assessment of indoor air quality was not included in the evaluation. The building's service life is estimated to be 60 years.

Building Element	Description of buildings system
Internal and External walls	External walls: Brick (190x190x10) with mortar. Edge brick sealed with cement. Exterior acrylic latex Internal walls: 10 mm finish Gypsum board on stud, acrylic paint exterior finish.
Foundation	Reinforced concrete isolated footing of 450mm thickness
Floors	Ceramic tiles(8mm) unglazed with cement grout and cement mortar
Column	RCC column of size 450x300mm
Roof	RCC slab of 100mm thickness
Doors	External doors: Timber frame, double door with dead bolt with gloss finish. Internal doors and laundry: Timber frame, Single door with gloss finish.
Windows	Timber frame with Curtain wall system (Glazing)

Figure 3.2 Building elements and specifications of building components.

3.5.2 Functional unit

Functional units are defined as units of reference in ISO 14040, which is used to calculate the systematic variable performance in LCA technology. "m^2" has been chosen as the functional unit for this assessment.

3.5.3 Life cycle inventory

Tally has created a unique LCA database that combines details on material qualities, structural information, and construction information with data on the environmental effects produced via a partnership between Kieran Timberlake and the thinking step. Using databases from GaBI 2018 and according to GaBI's database and modeling standards, the LCA modeling was finished in GaBI 8.5.

3.6 Results and discussion

This section lists the LCA consequences for the residential building. The four life cycle phases, namely the manufacturing/product, construction, operating, and demolition phases, were evaluated. The results show that the operational stage has dominated the other life cycle modules, accounting for 90% of impacts across all impact categories. Table 3.1 shows that if the operational phase (B6) is omitted, the product/manufacturing stage (A1 to A3) will become a critical module with 70%−90% of life cycle impacts, making it an obvious and crucial category for resource utilization.

Note: Modules A1 to A3 negative GWP values are coproduct allocation credits. According to EN15804, Module D does not perform credit allocation (Gervasio & Dimova, 2018).

Table 6.2 displays the effects of various concrete mixtures in the study. B6 has been the scenario's main influencer, as has already been established (operational stage). However, cement considerably improved in the A1 to A3 (product stage)

Table 3.1 Impacts of RCC considering life cycle phases without the addition of pozzolanic material.

Row labels	Acidification potential total ($kgSO_2$-eq)	Eutrophication potential total (kgN-eq)	Ozone depletion potential total (CFC-11-eq)	Global warming potential total ($kgCO_2$-eq)	Smog formation potential total (kgO_3-eq)	Primary energy demand total (MJ)
[A1−A3] Product	135.43	6.21	43,687	−1.82E-05	2034.87	502,254.11
[A4] Transportation	1.96	0.16	423.79	1.45E-11	64.89	6,162.78
[A5] On-site construction	2.57	4.42	879.00	1.39E-09	22.73	15,551.00
[B2-B5] Maintenance and replacement	9.61	0.23	694.28	3.47E-06	54.53	14,903.83
[B6] Operational energy	5490	318.60	2,340,000	3.96E-06	58,500.00	44,100,000.00
[C2-C4] End of life	14.71	0.78	4935.78	1.28E-08	290.45	53,834.31
[D] Module D	−7.88	−0.21	−2912.36	1.70E-05	−64.15	−29,446.77
Grand total	5646.41	330.19	2,387,708.36	6.28E-06	60,903.32	44,663,259.25

Table 3.2 Impacts of concrete incorporated with pozzolanic materials with varying percentages.

S. no.	Environmental impact indicators	0% Pozzolanic	10% Fly ash	20% Fly ash	30% Fly ash	10% GGBS	20% GGBS	30% GGBS
1.	AP ($kgSO_2$ eq)	5646.41	5643.91	5641.40	5638.85	5643.42	5640.41	5637.42
2.	EP (kgN-eq)	330.19	330.01	329.82	329.62	329.96	329.72	329.42
3.	GWP ($kgCO_2$eq)	2,387,708.36	2,386,596.10	2,385,483.83	2,384,345.67	2,386,323.86	2,384,434.06	2,383,548.22
4.	ODP (CFC-11-eq)	6.28E-06	6.28E-06	6.28E-06	6.28E-06	6.28E-06	6.28E-06	6.28E-06
5.	SFP (kgO_3-eq)	60,903.32	60,848.26	60,793.20	60,737.17	60,840.89	60,776.51	60,713.28
6.	PED (MJ)	44,663,259.25	44,656,635.64	44,650,012.03	44,643,129.05	44,653,861.46	44,644,423.38	44,635,017.74

module when pozzolanic ingredients were substituted. Pozzolanic materials have no impact on the remaining modules, such as A5 (on-site construction) and B6 (operational), because the impacts of these modules are determined by consumption units regardless of the type of material used in the construction. The addition of pozzolanic elements also had an impact on the A4 (transportation) module, which involved with end of life stage in Table 3.2.

The potential effects of the product/manufacturing stage (i.e., A1 to A3) of varying cement on acidification are shown in Fig. 3.3. When 10% FA was used, about 1.8% of impacts were reduced. This pattern persisted as 20%, 30%, and 3.72% and 5.62%, respectively, were replaced.

Due to the fact that GGBS had less of an impact than FA, the impact of FA was further diminished. When 10% of GGBS is substituted with cement, the effects are found to be 2.24%; when 20% and 30% are added, the impacts are found to be 4.48% and 6.73%, respectively. A similar linear variation is presented in Fig. 3.4.

With the incremental replacement of FA, the impacts were reduced by 3.05%, 6.11%, and 9.33% for 10%, 20%, and 30%, respectively, whereas those of GGBS were 3.8%, 7.7%, and 11.5%. With 32% of the overall emissions (excluding the operational stage), cement is the main impact-producing material for eutrophication potential, and this further reduces the impacts compared to acidification potential. According to Fig. 6.5, the GWP of the FA mixes decreased by 2.6%, 5.09%, and 7.69%, and the GGBS variations by 3.14%, 6.29%, and 9.56%, respectively. Brick masonry is the second-largest producer of negative impacts at 23%, despite cement

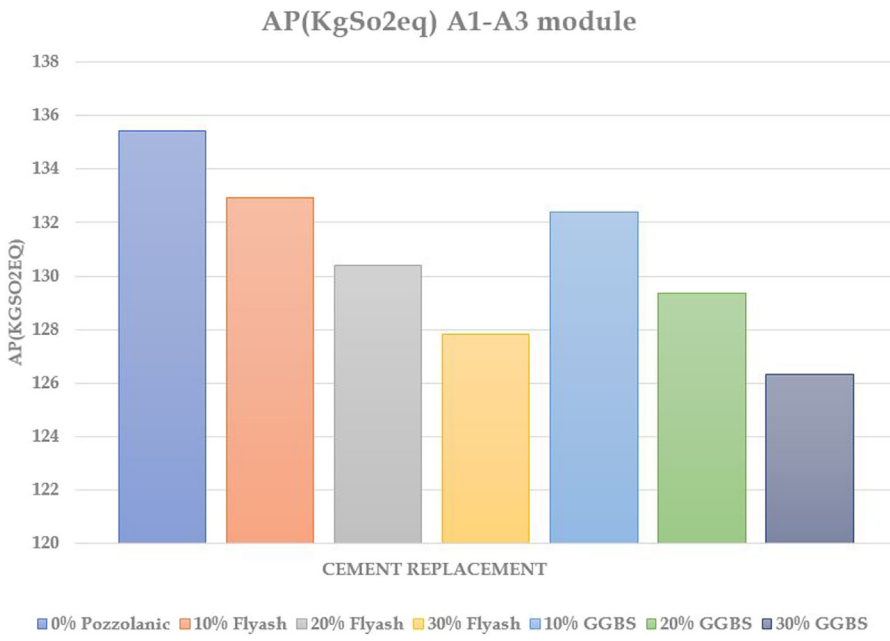

Figure 3.3 A1 to A3 module acidification potential (AP) comparison.

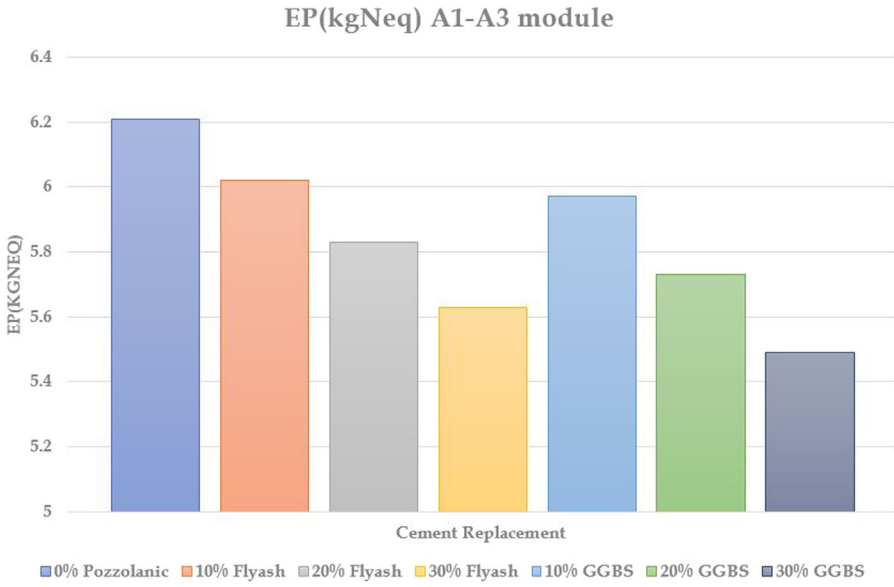

Figure 3.4 A1 to A3 module eutrophication potential (EP) comparison.

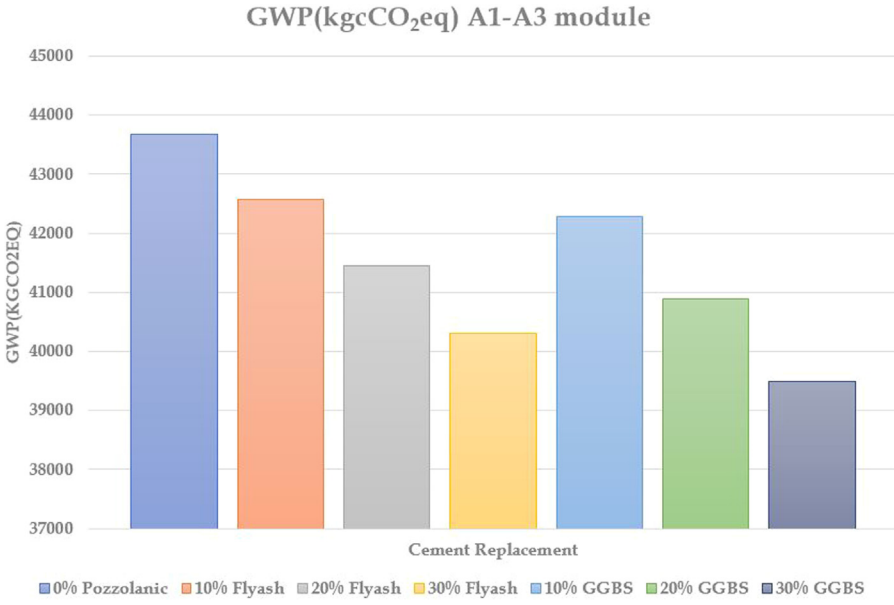

Figure 3.5 A1 to A3 module global warming potential (GWP) comparison.

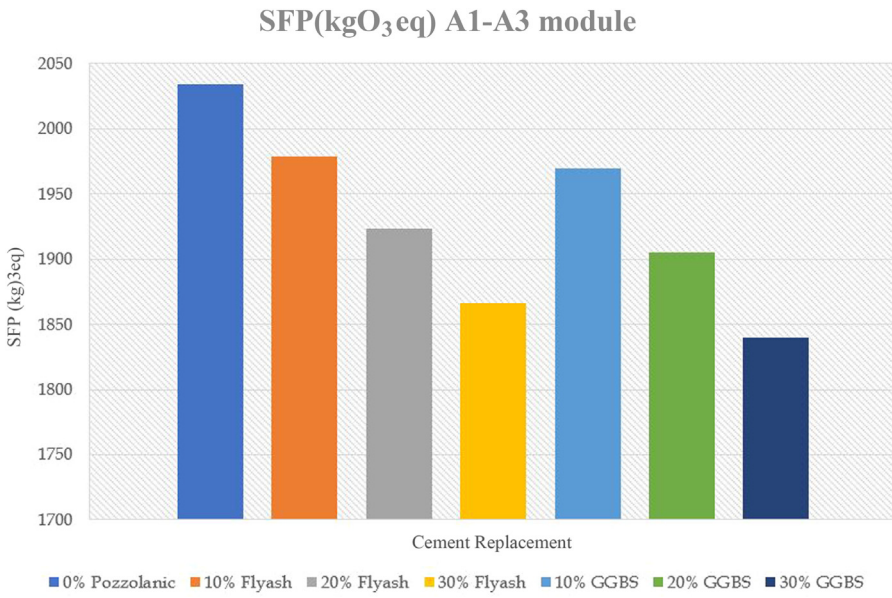

Figure 3.6 A1 to A3 module smog formation potential (SFP) comparison.

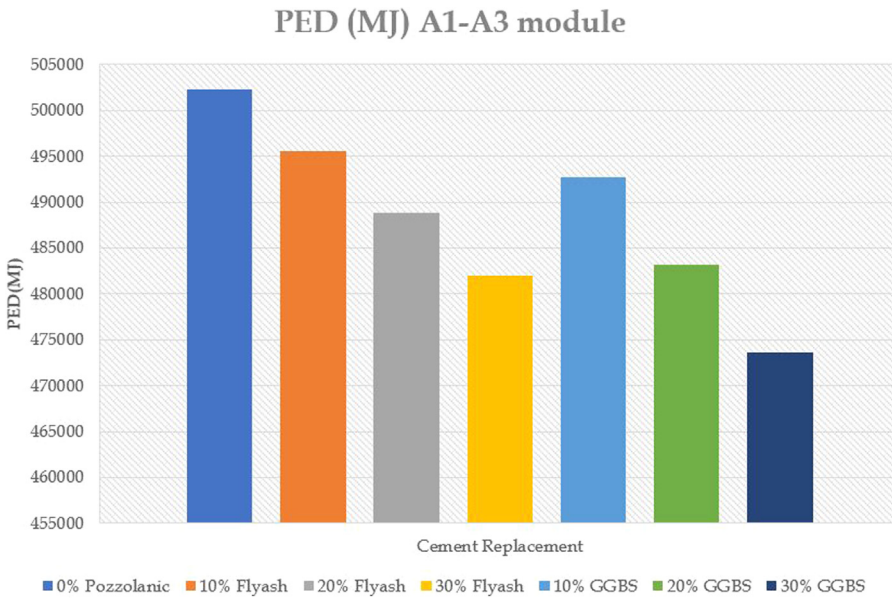

Figure 3.7 A1 to A3 module primary energy demand (PED) comparison.

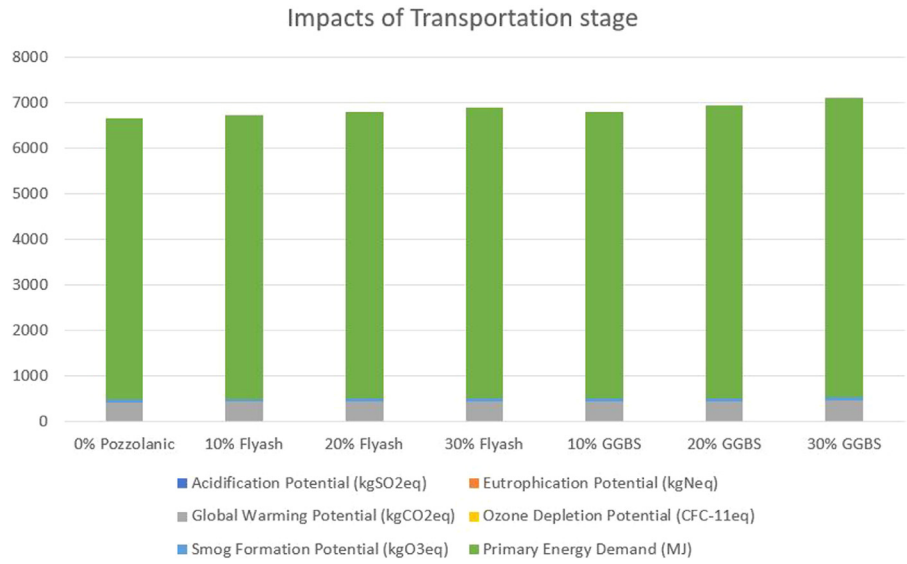

Figure 3.8 Transportation module (A4) impacts comparison.

having the highest impact-producing potential of any material (29%) as shown in Fig. 3.5.

From Fig. 3.6, it can be seen that the potential for smog formation, the replacement impacts of FA, and the replacement impacts of GGBS are as follows: 2.7%, 5.4%, and 8.26%, respectively. Cement was the primary impact producer with 28% of smog formation. The primary energy demand decreased by 1.33%, 2.66%, and 4.04% for 10%, 20%, and 30% FA replacement, respectively. Fig. 3.7 depicts that impacts are observed to be reduced by 1.9%, 3.8%, and 5.7% for GGBS versions, respectively. Based on the analyses, it can be concluded that primary energy consumption for masonry bricks is a large consumer at 33%, 17% for steel, and 16% for cement.

Table 6.4 shows the impacts of the A4 transportation module. From the results, it is clear that the transportation of pozzolanas from long distances has an increased impact on the environment. The FA and GGBS have been collected from 70 and 550 km distances, the nearest thermal plant locations (see Fig. 3.8).

3.7 Conclusion

This study gives a broad overview of a residential structure's life cycle effects throughout all life cycle stages. Autodesk Revit was used for BIM, while the Plug-in Tally was used for LCA. The study has evaluated building performance considering varying FA and GGBS content toward sustainability considering four life cycle phases, namely the manufacturing/product, construction, operating, and demolition

phases. The results show that the operational stage has dominated the other life cycle modules, accounting for 90% of impacts acros*s all impact categories*. The analysis yields the following specific findings:

- FA and GBBS lessen life cycle impacts, and the impact categories change linearly when cement is substituted.
- With every 10% substitution of cement, the effects of cement are reduced drastically from 5% to 8%.
- The GWP of the incremental FA variants decreased by 2.5%, 5.11%, and 7.72%, and similarly for the GGBS variations by 3.12%, 6.3%, and 9.58%, respectively.
- It is also observed that with 30% FA and 30% GGBS cement replacement variations, concrete is more environmentally friendly than other types.
- EP was the category with the lowest impact, and A1−A3 was the module with the highest sustainability.

Despite the fact that GGBS was seven times more difficult to get than FA, these data support the claim that it is a more environmentally friendly pozzolana. In India, where 1.6 million new homes are built annually, despite the fact that the variation in percentage was often less than 5%, these figures have the potential to be game-changers and can solve a variety of concerns in the long run with regard to the sustainability of the environment.

References

Ansari, A. (2017). Life cycle assessment of residential villa. *IOSR Journal of Mechanical and Civil Engineering*, *14*, 50−59. Available from https://doi.org/10.9790/1684-1403015059.

Arukala, S. R., Kalpande, V. P., & Pancharathi, R. K. (2020). *Evaluation of sustainable material through life cycle assessment using PSI method. Advances in sustainable construction materials* (pp. 87−101). Singapore: Springer.

Bansal, N. K. (2007). *Energy security, climate change and sustainable development. Science, technology and society: Energy security for India* (pp. 15−23). *New Delhi*: *Anamaya Publishers*.

BSI. (2011). BS EN 15942:2011 - Sustainability of construction works − Environmental Product Declarations - Communication format business-to-business. BSI, ed.

Bueno, C., & Fabricio, M. (2018). Comparative analysis between a complete LCA study and results from a BIM-LCA plug-in. *Automation in Construction*, *90*, 188−200. Available from https://doi.org/10.1016/j.autcon.2018.02.028.

Carvalho, J. P., Bragança, L., & Mateus, R. (2021). Sustainable building design: Analysing the feasibility of BIM platforms to support practical building sustainability assessment. *Computers in Industry*, *127*103400. Available from https://doi.org/10.1016/j.compind.2021.103400.

Costa, A. A., & Grilo, A. (2015). BIM-based E-procurement: An innovative approach to construction E-procurement. *The Scientific World Journal*, *2015*. Available from https://doi.org/10.1155/2015/905390.

Devi, L., & Palaniappan, S. (2014). A case study on life cycle energy use of residential building in Southern India. *Energy and Buildings*, *80*, 247−259. Available from https://doi.org/10.1016/j.enbuild.2014.05.034.

Gervasio, H., & Dimova, S. (2018). *Model for life cycle assessment (LCA) of buildings. Brussels, Belgium*: *Publications Office of the European Union*.

Horvath, A. (2004). Construction materials and the environment. *Annual Review of Environment and Resources*, *29*, 181−204. Available from https://doi.org/10.1146/annurev.energy.29.062403.102215.

Mastrucci, A., Marvuglia, A., Leopold, U., & Benetto, E. (2017). Life cycle assessment of building stocks from urban to transnational scales: A review. *Renewable and Sustainable Energy Reviews*, *74*, 316−332.

Ramesh, T., Prakash, R., & Shukla, K. K. (2012). Life cycle approach in evaluating energy performance of residential buildings in Indian context. *Energy and Buildings*, *54*, 259−265. Available from https://doi.org/10.1016/j.enbuild.2012.07.016.

Reddy, A. S., Kumar, P. R., & Raj, P. A. (2019). Preference based multi-criteria framework for developing a Sustainable Material Performance Index (SMPI). *International Journal of Sustainable Engineering*, *12*(6), 390−403.

Spence, R., & Mulligan, H. (1995). Sustainable development and the construction industry. *Habitat International*, *19*(3), 279−292. Available from https://doi.org/10.1016/0197-3975(94)00071.

Yadav, S., & Kanade, G. (2018). Application of revit as building information modeling (BIM) for integrated project delivery (IPD) to building construction project-A review. *International Research Journal of Engineering and Technology*, *5*(10).

Consistency, setting, and strength properties of fly ash and slag based geopolymer mortar activated with water glass

4

Rajashekar Sangi[1,2], *B. Sesha Sreenivas*[1] *and K. Shanker*[2]
[1]Department of Civil Engineering, Kakatiya University, Warangal, Telangana, India,
[2]Department of Civil Engineering, Kamala Institute of Technology & Science, Singapur, Telangana, India

4.1 Introduction

Globally most commonly used material for construction is cement, and its utilization is rising with increasing urbanization. The cement manufacturing industry is the second-largest emitter of greenhouse gas. Cement production adversely affects the environment. Cement industry emission is 8% of universal CO_2 emissions. To enhance the strength properties, reduce the environmental impact and also reduce the disposal problems of industrial waste. The utilization of industrial waste as supplementary cementitious materials in concrete along with cement has been well-recognized. Geopolymer is a new binder that can be a sustainable binding material. It is produced with industrial waste products such as fly ash and GGBS by replacing 100% cement in concrete. Geopolymer is an alumina-silicate polymer produced from the activation of various alumina-silicate source materials such as fly ash and GGBS. The polymerization reaction of alumina-silicate material under alkaline conditions results in a three-dimensional polymeric chain, the final products of geopolymer are mainly influenced by the chemical composition of the activator and source materials.

Geopolymer concrete (GPC) is a potential material for structural application as an alternative to ordinary Portland cement (OPC) concrete. It can play a significant role in green concrete technology by eliminating cement and utilizing various by-product materials such as fly ash and blast furnace slag (Vikas & Rao, 2021). Studies conducted over the last decades indicated the potential benefits of fly ash-based geopolymer over OPC concrete (Dineshkumar & Umarani, 2020; Jindal, 2019). It has been reported that low calcium fly ash-based geopolymer concrete achieved excellent mechanical and durability properties, when cured in high temperatures (Connie et al., 2018; Haloob Al Majidia et al., 2016; Zhanga et al., 2018). Geopolymer is an inorganic polymer, which is produced from various alumina-silicate materials reacted by alkaline solutions. The alumina-silicate source

Green Materials in Civil Engineering. DOI: https://doi.org/10.1016/B978-0-443-19106-0.00004-X

materials include by-product materials like fly ash and blast furnace slag, and materials of geological origin such as metakaolin (Topark-Ngarm et al., 2015). The general concept of polymerization can be explained with three distinct reactions: (1) destruction-coagulation; (2) coagulation-condensation; and (3) condensation-crystallization (Mallikarjuna Rao & Gunneswara Rao, 2015; Nath & Kumar Sarker, 2014). The polymerization reaction is dependent on many factors such as the chemical composition of the binder and the alkaline solution, curing condition, and water content. Curing temperature has a significant effect on the microstructural and mechanical strength development of the geopolymer system. Generally, the polymerization is accelerated at a higher temperature than the ambient. Since fly ash-based geopolymer paste reacts slowly at low ambient temperature as compared to heat-cured samples (Gökhan & Gökhan, 2014). These mixtures are usually subjected to mild curing temperatures ranging from 30°C to 85°C and high relative humidity of about 95% (Hardjito, 2005; Juenger et al., 2011). Curing time also varied from several hours to several days and requires additional conditioning at ambient temperature. The amount of calcium content in the fly ash was found to have a significant impact on the resulting hardened geopolymer. Calcium oxide is believed to form calcium silicate hydrate (CSH), along with the aluminosilicate geopolymer gel (Rangan, 2007, 2008; Wallah & Rangan, 2006). Notable studies reported on the fly ash geopolymer blended with some additional materials (Fernandez-Jimenez et al., 2006). The amount of internal and external calcium in the fly ash was found to have a significant impact on the resulting geopolymer (Davidovits, 2008). The suitability of fly ash-based geopolymers mixed with silica fume, metakaolin (Wallah et al., 2006), and blast furnace slag (Rangan, 2008) has been studied by several researchers. The addition of calcium oxide and calcium hydroxide as a replacement for fly ash improved mechanical properties for ambient cured samples and decreased properties for the 70°C cured samples. Fly ash-based geopolymer has also been reported to improve by enhancing the reactivity of fly ash, that is, by increasing the fineness (Duxson et al., 2007). The polymerization process and the resulting products may also be influenced by other factors such as the type and properties of aluminosilicate sources and the composition of alkaline solution (Nath & Kumar Sarker, 2014; Rangan, 2007; Vijai et al., 2010).

4.2 Materials used

In this study, GGBS and low calcium fly ash were used as binders (Table 4.1). Fly ash was collected from Ramagundam thermal power plant, Telangana, India and GGBS was collected from JSW Cement, Telangana, India. The chemical composition of GGBS and fly ash is shown in Table 4.1.

The fine aggregate used for the study, river sand, was collected from the Godavari river of specific gravity 2.6. Sieve analysis was done according to IS 383-2016, sand confined to zone II and the fineness modulus was 2.73. Crushed granite used as a coarse aggregate angular shape with a nominal maximum size of

Table 4.1 Chemical composition of GGBS and fly ash (% by mass).

Chemical composition	SiO_2	Al_2O_3	Cao	MgO	Fe_2O_3	Na_2O	SO_3	LOI
Flay ash	60.12	26.35	4.21	1.26	4.17	0.23	0.35	3.25
GGBS	34.29	20.15	32.45	7.39	0.87	Nil	0.91	3.85

aggregate is 12.5 mm and specific gravity of 2.7. Activator used for the study, "Water-Glass," was collected from KIRAN GLOBAL SOLUTIONS, India. It is the impure form of sodium silicate (Sangi et al., 2023). Its grade is represented by SiO_2/Na_2O ratio. Water glass is alkaline if the SiO_2/Na_2O ratio is less than 2.85, in this present instigation water glass with a SiO_2/Na_2O ratio of 2.0 was used as an activator. It chemical composition SiO_2-29.95%, Na_2O-14.95%, and solids 44.90, it P^H-12.6 and density 1.56 g/cc.

4.3 Experimental program

To study the fresh behavior of geopolymer paste, that is, consistency, setting time, and strength of geopolymer paste, the following experimental program was adopted.

4.3.1 Consistency of geopolymer paste

A Vicat apparatus was used to measure the consistency of the geopolymer paste. Vicat's apparatus contains a 10 mm dia steel plunger that penetrates into the paste with 300 g of weight. Test was conducted at a temperature of $20 \pm 2°C$. Consistency of geopolymer paste carried for various combinations of fly ash-GGBS and water-to-water glass (W/WG) ratios, the procedure used for finding the consistency is similar to the standard consistency of cement as per IS 4031 (part 4).

4.3.2 Setting time

The setting behavior of geopolymer paste was evaluated based on IS 4031 (part 5) by considering GGBS and fly ash content as 500 g and activator content as 0.85P, where P is the percentage of an activator required to produce a paste of consistency for that specific geopolymer mix (Table 4.2). Geopolymer mix M1G0F100 activated with water glass for different W/WG ratios 0, 0.1, 0.2, 0.3 consistency was 34, 33, 32, 32 percentage, respectively.

4.3.3 Compressive strength of mortar

The compressive strength testing was executed according to IS 4031 (part 6). Different combinations of fly ash to GGBS and W/WG ratios were used to make

Table 4.2 Quantity of water glass and water required for testing setting time and compressive strength of geopolymer mortar cubes.

Mix proportion	W/WG ratio	Standard consistency (%)	Quantity of water glass and water required for testing setting time		Quantity of water glass and water required for testing compressive strength of mortar cubes	
			Water glass (g)	Water (g)	Water glass (g)	Water (g)
F100-G0	0	34	145	0	92	0
	0.1	33	128	13	82	8
	0.2	32	113	23	73	15
	0.3	32	105	31	68	20
F90-G10	0	33	140	0	90	0
	0.1	32	124	12	80	8
	0.2	31	110	22	72	14
	0.3	30	98	29	65	19
F80-G20	0	34	145	0	92	0
	0.1	33	128	13	82	8
	0.2	32	113	23	73	15
	0.3	32	105	31	68	20
F70-G30	0	36	153	0	96	0
	0.1	34	131	13	84	8
	0.2	32	113	23	73	15
	0.3	32	105	31	68	20
F60-G40	0	38	162	0	100	0
	0.1	36	139	14	87	9
	0.2	34	120	24	77	15
	0.3	34	111	33	71	21
F50-G50	0	40	170	0	104	0
	0.1	39	151	15	93	9
	0.2	37	131	26	82	16
	0.3	36	118	35	74	22
F40-G60	0	42	179	0	108	0
	0.1	39	151	15	93	9
	0.2	38	135	27	83	17
	0.3	37	121	36	75	23
F30-G70	0	42	179	0	108	0
	0.1	40	155	15	95	9
	0.2	40	142	28	87	17
	0.3	37	121	36	75	23
F20-G80	0	43	183	0	110	0
	0.1	41	158	16	96	10
	0.2	40	142	28	87	17
	0.3	38	124	37	77	23

(*Continued*)

Table 4.2 (Continued)

Mix proportion	W/WG ratio	Standard consistency (%)	Quantity of water glass and water required for testing setting time		Quantity of water glass and water required for testing compressive strength of mortar cubes	
			Water glass (g)	Water (g)	Water glass (g)	Water (g)
F10-G90	0	43	183	0	110	0
	0.1	42	162	16	98	10
	0.2	41	145	29	88	18
	0.3	38	124	37	77	23
F0-G100	0	45	191	0	114	0
	0.1	43	166	17	100	10
	0.2	43	152	30	92	18
	0.3	41	134	40	82	24

70.6 mm mortar cubes, and aviator content was calculated as ((P/4) + 3)% of the combined mass of binding material and sand. P is the percentage of an activator required to produce a paste of consistency. A total of 200 g binding material and 600 g sand was used for the preparation of mortar cubes (i.e., mix 1:3 ratios).

4.4 Results and discussion

Eleven combinations of fly ash to GGBS ratios are designed to study the effect of consistency, setting time, and compressive strength of geopolymer mortar (GPM) cubes cured at ambient temperature.

4.4.1 Consistency of geopolymer paste

In this constituency test, water glass of different (W/WC) ratios is used instead of water. Consistency was reported as the activator percentage that can be sufficient to penetrate a 10 mm diameter plunger to a depth of 33−35 mm from the top of the Vicat's mold. The Mix ID of geopolymer from M1G0F100 to M11G100F0 indicates GGBS-fly ash proportions. It is identified that consistency of the geopolymer pastes M1G0F100 mix requires less activator than M11G100F0. Consistency of geopolymer paste increased with increase in GGBS content. This is because fly ash particles have low internal friction and their shape is spherical, but GGBS particles are flaky, have sharp-edged elongated shape and rough surface texture. It has higher internal friction. Geopolymer activated with water glass with W/WG ratio zero (i.e., without water) for mix M1G0F100 consistency was observed to be 32% and for

mix, M11G100F0 consistency will be 45%. It was observed that W/WC ratio of geopolymer did not much affect the consistency. Detailed consistency results are shown in Table 4.3.

4.4.2 Setting time geopolymer past

Setting time of geopolymer was done as per IS 4031 (part 5) for different GGBS and fly ash combinations and W/WG ratios. Vicat's apparatus was used to determine the setting time of the geopolymer paste. Activator with W/WG ratios 0, 0.1, 0.2, and 0.3 and 11 combinations of fly ash-GGBS was used to make geopolymer paste. A total of 500 g of binding material and activator 0.85P were considered to find the setting time of the geopolymer paste. The setting behavior of the geopolymer paste is presented in Table 3.2. For the geopolymer mix ID-M1G0F100 activated with W/WG ratio 0, 0.1, 0.2, 0.3, its initial setting time is 980, 1020, 1050, 1080 and its final setting time is 1620, 1680, 1710, 1760, respectively. It is observed that as the W/WG ratio increases, the setting time is also increasing for the same mix. For the mix, M11G100F0 activated with W/WG ratio 0, 0.1, 0.2, 0.3, initial setting time is 35, 37, 38, 42 and its final setting time is 40, 55, 63, 67, respectively. It was clear that GGBS quickly reacts with the WG than fly ash. It was observed that GGBS-based geopolymer binders M11G100F0 activated with water glass of W/WG ratio 0.2 and 0.3 increased final setting time, which normally has a final setting time of 45 minutes when activated with water glass without water, that is, W/WG ratio 0. As GGBS is replaced with fly ash, initial setting time and the final setting time increase. Detailed setting times of geopolymer paste for various binder proportions results are shown in Table 4.4 (Figs. 4.1 and 4.2).

4.4.3 Variation of compressive strength of geopolymer mortar for different water-to-water glass ratios

Compressive strength of GPM cube having various combinations of fly ash to GGBS and different W/WG ratios is shown in Table 7.5. The compressive strength of GPM after 28 days of curing at ambient temperature compressive strength ranges from 26 to 77 MPa. It was witnessed that with an increase in the W/WG ratio of water glass, there was an increase in the compressive strength up to the W/WG ratio 0.2 after 0.2 compressive strength decreased for flash replaced with GGBS up to 50%. After 50% replacement of GGBS, strength decrement percentage is less.

With increasing the GGBS percentage in the geopolymer mortar, the strengths gap very less for different W/WG ratios, it is representing that the replacement of GGBS of more than 50% with fly ash was producing high strength even for a W/WG ratio of 0.3. The maximum strength at 100% GGBS is 77 MPa with a W/WG ratio of 0.2. Minimum compressive strength of GPM 26 MPa was obtained for 100% fly ash and W/WG ratio 0.3. For the same mix proportion and W/WG ratio for 50% fly ash and 50% GGBS, the strength of GPM is about 42 MPa. The percentage of GGBS content increased from 0% to 50%. Strength has increased by

Table 4.3 Consistency of geopolymer paste for different proportions of fly ash-GGBS.

W/WG	M1 G0 F100	M2 G10 F90	M3 G20 F80	M4 G30 F70	M5 G40 F60	M6 G50 F50	M7 G60 F40	M8 G70 F30	M9 G80 F20	M9 G90 F10	M10 G100 F0
0	34	33	34	36	38	40	42	42	43	43	45
0.1	33	32	33	34	36	39	39	40	41	42	43
0.2	32	31	32	32	34	37	38	40	40	41	43
0.3	32	30	32	32	34	36	37	37	38	38	39

Table 4.4 Initial and final setting time of geopolymer pastes activated with different water-to-water-glass ratios and various combinations of fly ash and GGBS.

Mix ID	(W/WG) = 0		(W/WG) = 0.1		(W/WG) = 0.2		(W/WG) = 0.3	
	Initial setting time	Final setting time	Initial setting time	Final setting time	Initial setting time	Final setting time	Initial setting time	Final setting time
M1G0F100	980	1620	1020	1680	1050	1710	1080	1760
M2G10F90	890	1540	920	1560	970	1620	1010	1680
M3G20F80	780	1220	880	1430	930	1470	970	1530
M4G30F70	560	980	870	1090	890	1120	920	1230
M5G40F60	480	860	520	890	570	930	590	970
M6G50F50	370	720	340	760	360	830	410	870
M7G60F40	290	560	310	590	340	610	380	650
M8G70F30	230	420	240	430	260	450	290	490
M9G80F20	170	280	190	310	210	320	230	340
M10G90F10	90	155	110	170	130	185	140	190
M11G100F0	35	45	37	55	38	63	42	67

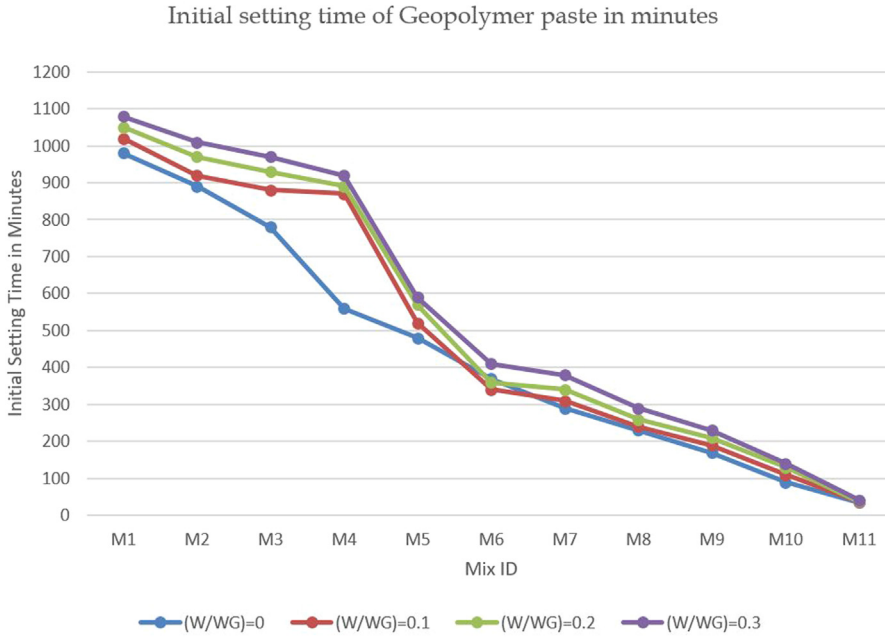

Figure 4.1 Initial setting time of geopolymer paste. Initial setting time for different proportions of fly ash-GGBS and water-to-water glass ratio.

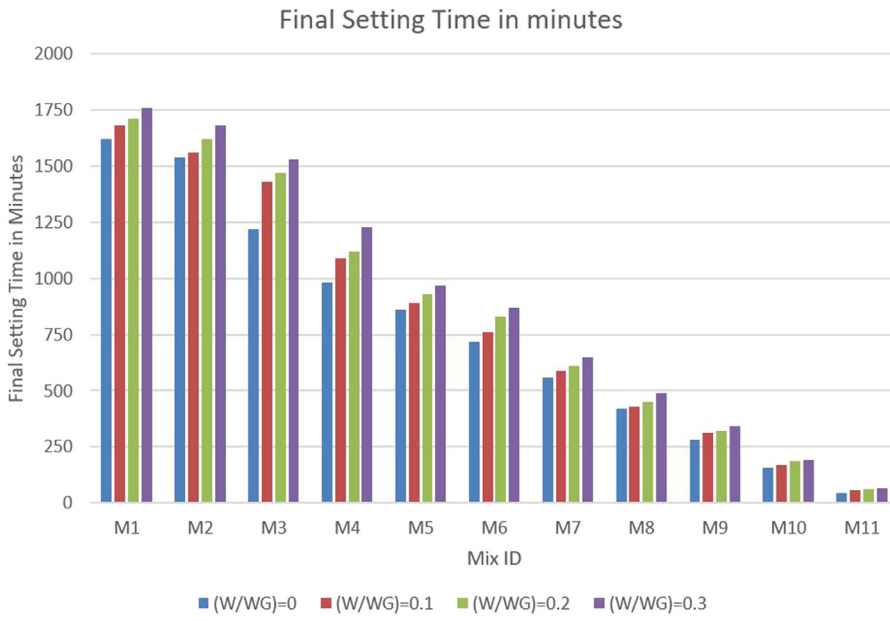

Figure 4.2 Final setting time of geopolymer concrete. Variation of final setting for different proportions of fly ash-GGBS and water-to-water glass ratio.

Table 4.5 Compressive strength of geopolymer mortar (GPM) cubes activated with different water-to-water glass ratios and different proportions of fly ash to GGBS.

Mix ID	Compressive strength of mortar cube in (N/mm^2)			
	(W/WG) = 0	(W/WG) = 0.1	(W/WG) = 0.2	(W/WG) = 0.3
M1G0F100	32	35	32	26
M2G10F90	34	37	33	29
M3G20F80	39	42	41	33
M4G30F70	44	46	46	34
M5G40F60	48	52	49	37
M6G50F50	52	54	56	42
M7G60F40	55	56	59	43
M8G70F30	58	58	63	56
M9G80F20	63	63	65	67
M10G90F10	67	69	72	77
M11G100F0	73	74	77	79

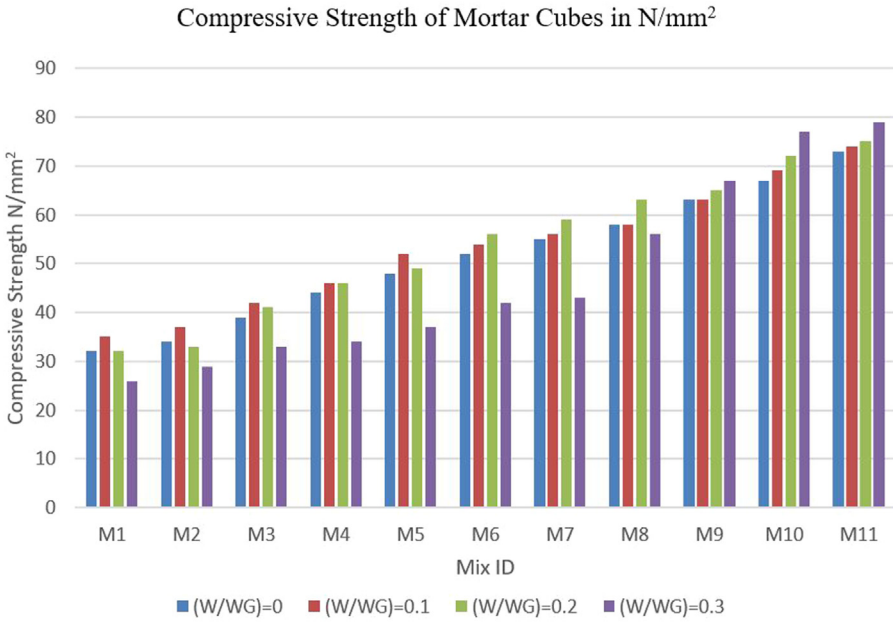

Figure 4.3 Compressive strength of geopolymer mortar (GPM). Compressive strength of GPM cubes activated with different water-to-water glass ratios and different proportions of fly ash to GGBS.

16 MPa. For some mix and W/WG ratios, for 100% GGBS content, the compressive strength of GPM is 69 MPa. The reason for an increase in the compressive strength of GPM is due to the higher calcium content present in GGBS (Table 4.5; Fig. 4.3).

4.5 Conclusion

It was observed that with an increase in W/WG ratio, there was a slight decrease in the compressive strength of GPM after 0.1. The compressive strength for the mix M1G0F100 with for W/WG ratio 0, 0.1, 0.2, 0.3,was 32, 35, 32, 30 respectively. For the M1G0F100 and M2G10F90 mixes, the compressive strength is maximum at a W/WG ratio of 0.1. For M3G20F80 to M8G70F30, strength is maximum at a W/WG ratio 0.2. For the M9G80F20 to M11G100F0, strength is maximum at W/WG ratio 0.3.

1. The consistency of geopolymer is not considerably affected by different W/WG ratios for the same mix (e.g., 50% fly ash and 50% GGBS). But consistency increase with the increase in GGBS percentage in the mix.
2. Initial and final setting time of the geopolymer paste increases with an increase in the W/WG ratio. This is because the increase in the water content slows down the rate of the polymerization reaction, therefore, the setting time was increased as compared with other W/WG ratios.
3. The initial and final setting times of geopolymer paste are decreased when fly ash is replaced with GGBS. The reason for this was the majority of elements present in GGBS: calcium and silica. Compared to other elements, calcium reacts with activator quickly.
4. The compressive strength of GPM after 0.1 compressive strength for the mix M1G0F100 was 32, 35, 32, 30 for W/WG ratio 0, 0.1, 0.2, 0.3, respectively. For the M1G0F100 and M2G10F90 mixes, the compressive strength is maximum at a W/WG ratio of 0.1. For the M3G20F80 to M8G70F30, strength is maximum at a W/WG ratio 0.2. For the M9G80F20 to M11G100F0, strength is maximum at W/WG ratio 0.3.
5. Replacement of fly ash with GGBS in GPM increases the compressive strength of GPM for all combinations of W/WG ratios. This is because the calcium content of the GGBS results in an increase in the rate of reaction and increases the compressive strength.

References

Connie, N. g., Johnson Alengarama, U., Wong, L. S., Hung Moa, K., Jumaata, M. Z., & Ramesh, S. (2018). A review on microstructural study and compressive strength of geopolymer mortar, paste and concrete. *Construction and Building Materials*, *186*, 550−576.

Davidovits, J. (2008). *Geopolymer chemistry and application* (2nd ed.). Saint-Quentin, France: Institut Géopolymère.

Dineshkumar, M., & Umarani, C. (2020). Effect of alkali activator on the standard consistency and setting times of fly ash and GGBS-based sustainable geopolymer paste. *Hindawi Advances in Civil Engineering*, *2020*, 2593207.

Duxson, P., Fernández-Jiménez, A. M., Provis, J. L., Lukey, G. C., Palomo, A., & Van Deventer, J. S. J. (2007). Geopolymer technology: The current state of the art. *Journal of Materials Science*, *42*, 2917−2933.

Fernandez-Jimenez, A. M., Palomo, A., & Hombrados, C. L. (2006). Engineering properties of alkali-activated fly ash concrete. *ACI Materials Journal*, *103*, 106−112.

Gökhan, G., & Gökhan, K. (2014). The influence of the NaOH solution on the properties of the fly ash-based geopolymer mortar cured at different temperatures. *Composites Part B: Engineering*, *58*, 371−377.

Haloob Al Majidia, M., Lampropoulosa, A., Cundya, A., & Meikleb, S. (2016). Development of geopolymer mortar under ambient temperature for in situ applications. *Construction and Building Materials*, *120*, 198−211.

Hardjito, D. (2005). *Studies of fly ash-based geopolymer concrete*. Doctoral Dissertation. Curtin University of Technology, Perth, Australia.

Jindal, B. B. (2019). Investigations on the properties of geopolymer mortar and concrete with mineral admixtures: A review. *Construction and Building Materials*, *227*, 116644.

Juenger, M. C. G., Winnefeld, F., Provis, J. L., & Ideker, J. H. (2011). Advances in alternative cementitious binders. *Cement and Concrete Research*, *41*(12), 1232−1243.

Mallikarjuna Rao, G., & Gunneswara Rao, T. D. (2015). Final setting time and compressive strength of fly ash and GGBS-based geopolymer paste and mortar. *Arabian Journal for Science and Engineering*, *40*(11), 3067−3074.

Nath, P., & Kumar Sarker, P. (2014). Effect of GGBFS on setting, workability and early strength properties of fly ash geopolymer concrete cured in ambient condition. *Construction and Building Materials*, *66*(2014), 163−171.

Rangan, B. V. (2007). Low-calcium fly ash-based geopolymer concrete. In E. G. Nawy (Ed.), *Concrete construction engineering handbook* (2nd ed). New York: CRC Press.

Rangan, B. V. (2008). *Fly ash-based geopolymer concrete*, Research report GC 4, Curtin University of Technology, Perth, Australia.

Sangi, R., Bollapragada, S. S., & Kandukuri, S. (2023). Mix design of fly ash and GGBS based geopolymer concrete activated with water glass. *Engineering, Technology & Applied Science Research (ETASR)*, *13*(5), 11884−11889, Submitted for publication.

Topark-Ngarm, P., Chindaprasirt, P., & Sata, V. (2015). Setting time, strength, and bond of high-calcium fly ash geopolymerconcrete. *Journal of Materials in Civil Engineering @ASCE*, *27*(7), 04014198-2.

Vijai, K., Kumutha, R., & Vishnuram, B. G. (2010). Effect of types of curing on strength of geopolymer concrete. *International Journal of Physical Sciences*, *5*, 1419−1423.

Vikas, G., & Rao, T. D. G. (2021). Setting time, workability and strength properties of alkali activated fly ash and slag based geopolymer concrete activated with high silica modulus water glass. *Iranian Journal of Science and Technology, Transactions of Civil Engineering*, *2021*, 1483−1492.

Wallah, S. E., & Rangan, B. V. (2006). Low-calcium fly ash-based geopolymer concrete: Long-term properties. Research Report GC 2, Faculty of Engineering, Curtin University of Technology, Perth, Australia.

Zhanga, P., Zhenga, Y., Wangb, K., & Zhanga, J. (2018). A review on properties of fresh and hardened geopolymer mortar. *Composites Part B: Engineering*, *152*, 79−95. Available from https://doi.org/10.1016/j.compositesb.2018.06.031.

Developing flyash and slagbased high-strength geopolymer concrete

5

Krupansh Patel and Bhargav R. Tewar
Faculty of Technology, CEPT University, Ahmedabad, Gujarat, India

5.1 Introduction

With current urbanization and the upcoming boost and focus on infrastructure and sustainable development, using sustainable materials is the need of the hour. Since Portland cement manufacturing led to high levels of CO_2 emissions. The development of cementless geopolymer concrete is a step closer to our goal. In order to produce substantially greener concrete, the utilization of wastes like blast furnace slag and fly ash has expanded due to the need for sustainable building materials. High-strength geopolymer concrete can be produced with blast furnace slag and fly ash in the presence of alkaline solution/activators such as NaOH and Na_2SiO_3.

5.1.1 The objective of the study

1. Developing high-strength cementless geopolymer concrete using fly ash and GGBS.
2. Analyzing the effect of different percentages of GGBS and fly ash on compressive strength of geopolymer concrete.
3. Analyzing the effect of water/solid ratio on the compressive strength of geopolymer concrete.
4. Studying the compressive strength increment pattern over the period of 28 days.

5.1.2 Scope of work

1. To develop a quantitative research methodology to carry out the research.
2. To develop formulae for fly ash and GGBS-based M70 grade high-strength geopolymer concrete.
3. To compare and analyze the effect of fly ash and GGBS on the compressive strength of high-strength geopolymer concrete.

Green Materials in Civil Engineering. DOI: https://doi.org/10.1016/B978-0-443-19106-0.00005-1

5.1.3 Literature study

5.1.3.1 Geopolymerization

Geopolymers are inorganic polymers produced through the process of geopolymerization. It is a chemical reaction that occurs when solid alumina-silicate oxides react with alkali silicates at alkaline temperatures of 30°C−100°C. Due to the presence of Si^{4+} and Al^{3+} in IV-fold coordination with oxygen, it produces a 3D amorphous to semicrystalline polymer structure (Davidovits, 1991). The alkaline solution's effect from the precursor material aluminate and silicate is formed by the coagulation of Al and Si atoms from an aluminosilicate source. In the solution, the molecules of silicon, aluminum, and aluminosilicate reach equilibrium. As aluminum oxide dissolves rapidly, nearby Si or Al molecules go through a condensation reaction in which the molecules' surrounding OH ions condense to create an oxygen bond that links them and releases a free molecule of water (H_2O). After the gel has been formed, the structure continues to reorganize, and the heat produced during the process combined with the surrounding temperature (preferred to be above 30°C) induces the polymerization of these monomers, together with additional Si and Al hydroxide molecules, to produce the rigid or 3D network known as N-(A)-S-H gel. Crystallization results from undissolved solid particles bonding within the final geopolymeric structure (Davidovits, 2016). For source materials (such as GGBS) containing a higher amount of CaO, Palomo et al. showed that the activation of these types of materials results in the formation of the [$(Na, K)_2O$-CaO-Al_2O_3-SiO_2-H_2O] system. It requires a relatively low alkaline concentration. C-S-H gel is the main reaction outcome, with a small percentage of aluminum in its structure to form C-(A)-S-H gel (Duxson et al., 2007).

An increase in compressive strength is observed when a certain amount of GGBS is added to the source material. Geopolymerization for such mixtures involves the chemical reaction of aluminosilicate oxides with alkali and calcium polysilicates. Research also supports that the presence of CaO in binder decreases the porosity and thereby increases the compressive strength. However, the kinetics of the reactions still depend on temperature, curing time, and concentration of NaOH solution (Škvára et al., 2006).

Research has also reported that the mixture with fly ash as a source material hardens at room temperature by the addition of a small amount of calcium and hence does not need any thermal activation. With the addition of an alkaline solution and also with the release of the heat of hydration due to calcium and silica content, the process of formation of aluminosilicate gel is accelerated, thereby reducing the setting time. Even when heat is not applied, the polymerization continues at a lower rate, and hence gradual but continuous increase in strength is observed at a later stage as well. This type of material can gain strength under the mechanism of pure polymerization. The addition of Ca source to this type of material also increases the compressive strength and diminishes the use of oven curing. Thus the C-S-H gel could be considered a self-catalyst for subsequent reactions. The possibilities of different gel formations in the mixture arise due to this complex mechanism. C-S-H and C-A-S-H gel might result in the mixture having a higher content of Ca and Si, whereas higher

Al and Si may be associated with the formation of N-A-S-H or (N, C)-A-S-H gel structures. Ultimately it depends on CaO/SiO_2 or SiO_2/Al_2O_3 ratio. The compatibility of different gels and their kinetics are still under study (Lodiero et al., 2015; Obonyo et al., 2011; Sanchez-Herrero et al., 2015).

Polymerization is an instant process, hence if it governs, an immediate rise in strength is observed. In polymerization-governed processes, there is not much strength gain at later stages. This type of behavior was seen in a mixture having only fly ash as the source material. If hydration governs, then it is a continuous process, which reflects the mechanism of strength gain at the later stage also but at a slower rate. This type of behavior was seen in a mixture having only GGBS as the source material. But the formation of hydrated products disturbs the process of polymerization and changes the microstructure of the resultant gel. If there is an overlap of polymerization and hydration, initial strength gain is observed, and subsequent strength gain after 28 days is also observed. This type of behavior was seen in cubes having a mixture of fly ash and GGBS. The ultimate gel results from a mixture of polymerization and hydration and have a complex microstructure.

5.1.3.2 Raw materials for geopolymer concrete

There are numerous materials with significant silicon and aluminum content that can be converted into geopolymers. Natural minerals, industrial wastes, calcined clays, and by-products such as fly ash, blast furnace slag, red mud, and waste glass can also be used (Hammond et al., 2011). Blast furnace slag and fly ash are extensively used by-products. Both are heterogeneous, and they both have impurities, such as Ca and Fe in fly ash and blast furnace slag, affecting the initial and final setting times, slump, strength, and shrinkage of the final product (Davidovits, 2016). The main components of fly ash are SiO_2 and Al_2O_3, with minor components such as CaO, Fe_2O_3, MgO, and others. Owing to the presence of alumina-silicate content, low water consumption, good workability, and ease of availability, fly ash is a highly preferred material. The embodied energy and embodied carbon of fly ash are 0.10 MJ/kg and 0.008 $kgCO_2e/kg$.

GGBS is a by-product of iron production that becomes a glassy, granular material with increased reactivity after quick cooling and grinding. SiO_2, CaO, Al_2O_3, and MgO make up this mineral. The addition of blast furnace slag to geopolymers improves their strength development. The embodied energy and embodied carbon of GGBS is 1.60 MJ/kg and 0.083 $kgCO_2e/kg$ (Hardjito et al., 2004).

When these source materials are combined with alkaline liquids like sodium or potassium silicate, which act as an alkaline solution and promote the reaction between the source materials and the solution (Kumar et al., 2010).

5.1.3.3 Factors influencing geopolymer concrete properties

One of the most important elements determining the qualities of fresh and hardened concrete is the initial and final setting time that steadily grew as the amount of fly ash in the mixture increased and dropped as the amount of GGBS in the mixture

increased. Another element is the molarity of the alkaline solution; when molarity rises, compressive strength does as well. Additionally, it has been found that the compressive strength decreases when the binder/water ratio increases. Additionally, it has been found that raising the curing temperature improves concrete compressive strength up to a temperature of 75°C, but above that point, there is very little strength development (Lloyd & Rangan, 2010). Apart from these factors, the properties of geopolymer concrete also depend on: (1) CaO content in source materials; (2) molarity of sodium hydroxide solution, greater the molarity, and more compressive strength is observed up to 16 M; (3) compressive strength is decreased when the water/binder ratio increases; (4) excess water can lead to the formation of shrinkage cracks as well as the widening of nanopores formed due to the evaporation of water (Palomo et al., 2014; Wallah & Rangan, 2006; Shah, 2017).

5.2 Experimental program

In order to produce substantially greener concrete, the utilization of wastes like fly ash and GGBS has expanded due to the need for sustainable building materials. High-strength concrete can be made by producing geopolymer concrete with fly ash and GGBS using alkaline activators such as Na_2SiO_3 and NaOH. These materials contain SiO_2 and Al_2O_3 as major components. The Si/Al ratio has a major impact on the strength characteristics of concrete, and research has shown that the ideal range to use is between 1.5 and 3.0.

For this experimental program, black basalt aggregates were used for coarse aggregates and river sand for fine aggregate along with fly ash and GGBS as binders. These binders are activated using alkaline activators like Na_2SiO_3 and NaOH solution.

5.2.1 Materials

5.2.1.1 Coarse and fine aggregates

Aggregates are tested according to IS: 2386-1963 (2016) and specifications are followed according to IS: 383-1970 (2016). Coarse aggregates used for this experiment are of nominal sizes of 10 and 20 mm, and fine sand is used as fine aggregate. The engineering properties of aggregates can be seen in Table 5.1.

The Fineness Modulus (FM) of fine aggregate is found to be 2.76, and from sieve analysis, it was concluded that the fine aggregate is of zone 2 according to IS: 383-2016.

5.2.1.2 Fly ash and GGBS

Fly ash used for this experimental program is procured from Gandhinagar thermal power plant. According to IS: 3812, the proportion of contents was under limitations. According to ASTM C618, fly ash is classified depending on its CaO content in it. Class C fly ash has more than 10% CaO. Class F fly ash has a CaO content of less than

Table 5.1 Engineering properties of aggregates.

Specifications	Values		
	Sand	**20 mm Downsize**	**10 mm Downsize**
Specific gravity	2.20	2.86	2.92
Water absorption (%)	3.70	1.14	2.31
Loose bulk density (kg/m^3)	1535	1581	1413
Compacted bulk density (kg/m^3)	1648	1705	1568
Impact value (%)	–	15.44	15.78
Crushing value (%)	–	18.38	19.51

Table 5.2 Physical and chemical properties of fly ash and GGBS.

Chemical composition	Proportion	
	Fly ash	**GGBS**
LOI	0.39%	0.31%
SiO_2	60.47%	34.37%
Al_2O_3	34.64%	16.98%
CaO	0.80%	34.76%
Fe_2O_3	0.40%	–
MgO	0.28%	8.66%
Na_2O	0.48%	–
SO_3	0.72%	0.22%
Color	Yellowish gray	Light brown
Fineness (m^2/kg)	315	358
Specific gravity	2.20	2.84

10%. Class F fly ash is used for this study and the physical and chemical properties are given in Table 5.2. It is analyzed that the ratio of SiO_2/Al_2O_3 in fly ash is 1.74.

GGBS used for this experimental program is procured from a manufacturing company. It is light brown in color. The physical properties and chemical composition are within the limits given in IS: 12089 and are given in Table 5.2. The test results are supplied by the lab. It is analyzed that the ratio of SiO_2/Al_2O_3 in GGBS is 2.02.

5.2.1.3 Alkaline liquid (Na_2SiO_3)

The alkaline activators used are a combination of NaOH solution and Na_2SiO_3 solution (sodium silicate gel).

Na_2SiO_3, also known as sodium silicate, is a transparent and viscous liquid having adhesive properties and is fire-resistant. It is procured from a local manufacturing company. The chemical composition of the Na_2SiO_3 solution is given in Table 5.3.

Table 5.3 Chemical composition of Na_2SiO_3 solution.

Chemical composition	Proportion
SiO_2	36.44%
Na_2O	16.49%
Water	47.07%
Specific gravity	1660 kg/m^3

Table 5.4 Chemical composition of NaOH flakes.

Chemical composition	Proportion
NaOH (purity)	98.7
Chloride	1
Carbonate (CO_3)	0.01
Silicates (SiO_2)	0.01
Nitrate (NO_3)	0.005
Size	3−6 mm
Color	White

5.2.1.4 Alkaline solid (NaOH)

NaOH flakes:NaOH is the alkaline solid used for the activation of binders in this study. It is available in flakes, granules, pellets, etc. For this work, NaOH flakes are used and procured from a local distributor. The chemical composition of NaOH flakes provided by the distributor is mentioned in Table 5.4.

Sodium hydroxide solution is prepared by dissolving the flakes in a premeasured amount of water. The molar weight of NaOH is 40 g. To prepare 1 molarity (M) solution, 40 g of NaOH flakes must be dissolved in H_2O to make 1 L of solution. For this study, a 12 M solution is used for all the mixes. NaOH flakes are added to water and stirred until all flakes dissolve completely. The solution is prepared 45−60 minutes before use so as to let the solution come to ambient temperature.

5.2.2 Mix design

5.2.2.1 Geopolymer concrete mix design

In this method, the mix design is done based on available literature and lab trials to achieve the trial mix (Palomo et al., 2014; Wallah & Rangan, 2006; Shah, 2017). An approximate guideline for the water-to-solids ratio is provided by Rangan in their study. Also, from other literature studies, it is observed that keeping Si/Al ratio in binders should be kept between 1.5 and 3.0 while Na_2SiO_3/NaOH ratio should be kept between 1.5 and 2.5, and alkaline solution to binder, that is (Na_2SiO_3 + NaOH solution/fly ash + GGBS) should be kept between 0.4 and 0.5.

Table 5.5 Data for design of low-calcium fly ash-based geopolymer concrete.

Water/geopolymer solids ratio in kg	Workability	Design compressive strength (N/mm^2)
0.16	Very stiff	60
0.18	Stiff	50
0.20	Moderate	40
0.22	High	35
0.24	High	30

Source: From Lloyd, N. A., & Rangan, B. V. (2010). Geopolymer concrete with fly ash. In *Second international conference on sustainable construction materials and technologies* (pp. 1493–1504).

By following these criteria mix design can be done. The basic water/geopolymer solids ratio by mass was followed as per Table 5.5.

From Table 5.5, the water/geopolymer solids ratio by mass of 0.18 is used and the corresponding compressive strength is 50 N/mm^2.

Thus from Table 5.6, the mix design for M50 geopolymer concrete is as follows.

Designation fixed for mixture proportions: The following methodology is adopted to give designations to mix proportions for further reference:

%F%GXM which stands for percentage of fly ash(F) + percentage of GGBS (G) + "X" molarity of NaOH solution. For example, 50F50G12M stands for 50% fly ash + 50% GGBS with 12 M concentration of NaOH.

The mix design mentioned in Table 5.7 is observed to be very stiff, hence a need to increase the water-to-solids (W/S) ratio by addition of alkaline solution was done to increase the alkaline solution to binder ratio up to 0.53 to increase the workability of the mix which can be seen in the mix design as shown in Table 5.8.

5.2.2.2 *Chemical composition of geopolymer concrete as per mix design*

This analysis of ratios of various chemical contents shown in Table 5.9, present in binder materials (fly ash and GGBS) and alkaline solution (Na_2SiO_3 + NaOH), helps in identifying the behavior of geopolymer concrete under different proportions of chemical contents present in the binders. This can help in producing GGBS-based mix designs more accurately.

5.2.2.3 *Observations for geopolymer concrete pilot mix revised trial-1*

It was also observed that due to the exothermic reaction of NaOH with water and NaOH solution with sodium silicate, heat was generated which led to a rapid hardening of concrete within 30 minutes. Thus for further trials, the alkaline solution was cooled down before use. The wet concrete was very stiff and cohesive in nature. The density of cubes cast was in the range of 2500–2600 kg/m^3.

Table 5.6 Mix design for M70 grade equivalent geopolymer concrete.

M70 grade concrete	Values	Units
Assuming unit weight of concrete	2400	kg/m^3
Approximate percentage of aggregates in mixture	75%	
Approximate mass of aggregates	1800	kg/m^3
Approximate % aggregates between 20 and 10 mm	40%	
Approximate mass aggregates between 20 and 10 mm	720	kg/m^3
Approximate % aggregates between 10 and 4.75 mm	30%	
Approximate mass of aggregates between 10 and 4.75 mm	540	kg/m^3
Approximate percentage of sand	30%	
Approximate mass of sand	540	kg/m^3
Remaining mass of source material + alkaline liquid	600	kg/m^3
Alkaline liquid/source material	0.4	
Mass of the source material required	428.57	kg/m^3
Mass of the total alkaline solution	171.43	kg/m^3
Ratio of Na_2SiO_3 solution/NaOH solution	2	
Mass of NaOH solution	57.14	kg/m^3
Mass of Na_2SiO_3 solution	114.29	kg/m^3
Percentage of water in Na_2SiO_3 solution	47.07%	
Mass of water in Na_2SiO_3	53.80	kg/m^3
Percentage of solids in Na_2SiO_3 solution	52.93%	
Mass of solids Na_2SiO_3 solution	60.49	
Percentage of water in NaOH 12 M	67.50%	
Mass of water in NaOH	38.57	kg/m^3
Percentage of solids in NaOH 12 M solution	32.5	
Mass of solids in NaOH 12 M solution	18.57	
Total mass of H_2O	92.37	kg/m^3
Total mass of solids	507.63	kg/m^3
Water/solids ratio	0.18	

Table 5.7 Mix proportion for geopolymer concrete.

Material	"50F50G12M" Quantity	Units
Source material (fly ash + GGBS)	428.57	kg/m^3
Coarse aggregates	1260	kg/m^3
Fine aggregates	540	kg/m^3
Alkaline liquid/source material	0.4	
Alkaline liquid (Na_2SiO_3 gel + NaOH solution)	171.43	kg/m^3
Na_2SiO_3 gel/NaOH solution	2	
Na_2SiO_3	114.29	kg/m^3
NaOH solution	57.14	kg/m^3
Extra water added	–	kg/m^3

Table 5.8 Mix designs with varying water-to-solids and alkaline liquid-to-source-material ratio.

Mix design	W/S	Fly ash + GGBS	CA	FA	AL/SM	Na_2SiO_3 sol/NaOH sol	Na_2SiO_3 sol	NaOH sol
50F50G12M	0.18	428.57	1260	540	0.40	2.0	114.29	57.14
50F50G12M[1]	0.23	428.57	1260	540	0.53	2.0	151.11	75.26
50F50G12M[1]	0.25	428.57	1260	540	0.60	2.0	171.43	85.71
70F30G12M	0.23	428.57	1260	540	0.53	2.0	151.11	75.26

[1]Revised mix designed for increased workability.

Table 5.9 Chemical components in fly ash and GGBS-based geopolymer concrete.

Description	50F50G12M (W/S = 0.23)	50F50G12M (W/S = 0.25)	70F30G12M (W/S = 0.25)
Amount of chemical components in binder (655 kg/m^3)			
Na_2O in fly ash	1.03	1.03	1.44
Na_2O in GGBS	–	–	–
Na_2O in Na_2SiO_3	24.92	28.27	24.92
Total Na_2O in binder	25.95	29.30	26.36
SiO_2 in fly ash	129.55	129.55	181.29
SiO_2 in GGBS	73.65	73.65	4.19
SiO_2 in Na_2SiO_3	55.06	62.47	55.06
Total SiO_2 in binder	258.26	265.67	280.54
Al_2O_3 in fly ash	83.57	83.57	103.85
Al_2O_3 in GGBS	36.38	36.38	10.91
Total Al_2O_3 in binder	119.95	119.95	114.76
CaO in fly ash	1.71	1.71	2.40
CaO in GGBS	74.48	74.48	44.69
Total CaO in binder	76.19	76.19	47.09
NaOH flakes required	24.52	27.85	24.52
H_2O in NaOH solution	50.74	57.85	50.74
H_2O in Na_2SiO_3 solution extra H_2O added	71.12–	80.69–	71.12
Total H_2O in binder	121.87	138.54	121.87
H_2O/Na_2O	4.70	4.73	4.62
SiO_2/Na_2O	9.95	9.06	10.64
Al_2O_3/Na_2O	4.62	4.09	4.35
Al_2O_3/CaO	1.57	1.57	2.43
SiO_2/Al_2O_3	2.15	2.21	2.44
SiO_2/CaO	3.39	3.49	5.96
% Na_2O	3.96	4.47	0.40
% SiO_2	39.43	40.56	42.83
%CaO	11.63	11.63	7.19
% H_2O	18.60	21.15	18.60
Percentage of NaOH flakes	3.74	4.25	3.74
% Al_2O_3	18.31	18.31	17.52

5.2.2.4 Mean compressive strength results for all mix trials

As the geopolymer mix design was prepared for M70 grade concrete, it can be observed that the trial mix 50F50G12M (0.53) concrete achieves 49.6 N/mm^2, that is about 71% of its strength within 3 days (Fig. 5.1). At 7 days, it achieves 52.13 N/mm^2, that is only a 5% increase in compressive strength of concrete is observed. But an exponential amount of increase is observed after 14 days as the compressive strength of concrete is 78.33 N/mm^2, that is an increase of about 51% more relative to the strength achieved at 7 days, and after 28 days, concrete achieves 83.09 N/mm^2, that is about 120% of its required strength.

Trial mix 50F50G12M (0.60) concrete achieves about 60% of its strength within 3 days and 68% of its required strength after 7 days. While it achieves only 90% of its required strength after 28 days. Due to an increase in overall water content, decrement in early strength and overall strength is observed.

While for trial mix 70F30G12M (0.53), concrete achieves about 76% of its strength within 3 days and 97% of its required strength after 7 days. While it achieves about 117% of its required strength in 28 days. The compressive strength increment trend is observed to be gradual in this trial, similar to trial mix 50F50G12M (0.60).

From the observations and studies from earlier literature, it can be assumed that the reasons for the early high strength of concrete are high CaO content in GGBS, high molarity of NaOH solution, and high ambient temperatures.

It was also observed that the failure pattern observed in compression test cubes was "explosive" in nature, and thus a satisfactory type of failure is observed in Figs. 5.2 and 5.3.

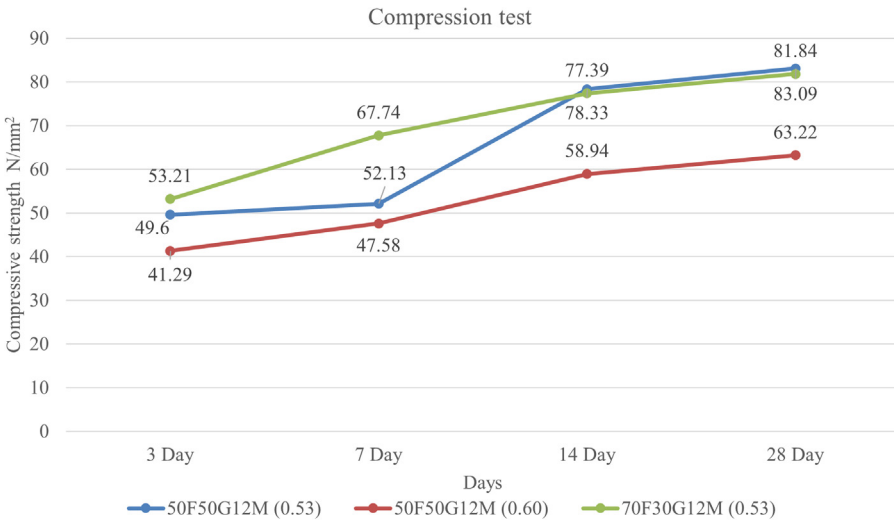

Figure 5.1 Mean compressive strength result comparison for different trial mixes. The figure shows the compressive strength achieved by geopolymer concrete in 28 days for three different mixes having a different alkaline solution to source material ratio.

Figure 5.2 50F50G12M (0.53) failure pattern. The cube tested under compression loading shows an explosive failure pattern.

Figure 5.3 50F50G12M (0.60) failure pattern. The cube tested under compression loading shows an explosive failure pattern.

5.3 Conclusion

With the upcoming need for sustainability in each sector for development in the future, the use of materials that are available in abundance and a greener option compared to materials currently in use, like cement, can be replaced with materials like fly ash and GGBS along with alkali activators like Na_2SiO_3 and NaOH to produce geopolymer concrete. From the results obtained, the geopolymer concrete designed for M70 grade has achieved almost 70% strength within 3 days while at 28 days it achieved about 120% strength in 28 days. From the results, it can also be concluded that with an increase in the water-to-solids ratio and alkaline liquid-to-source material ratio, the workability of fresh concrete increases but the

compressive strength of hardened geopolymer concrete decreases. From the compressive strength increment pattern, it can be concluded that for the mix 70F30G12M (0.53), the polymerization process governs, and an immediate rise in strength is observed. In polymerization-governed processes, there is a gradual strength gain at later stages. This type of behavior is seen in a mixture having higher fly ash content as the source material. While for the mix 50F50G12M (0.53), there is an overlap of polymerization and hydration, initial strength gain is observed, and subsequent strength gain after 28 days is also observed. The ultimate gel results from a mixture of polymerization and hydration and have a complex microstructure.

Abbreviations

AL	alkaline liquid
SM	source materials
GGBS	ground granulated blast furnace slag
CA	coarse aggregate
FA	fine aggregate
Na_2SiO_3	sodium silicate
NaOH	sodium hydroxide
FM	fineness modulus

References

Davidovits, J. (1991). Geopolymers − Inorganic polymeric new materials. *Journal of Thermal Analysis*, *37*(8), 1633−1656. Available from https://doi.org/10.1007/BF01912193.

Davidovits, J. (2016). *Special focus on "Geopolymer Cement Geopolymer Web Workshop"*.

Duxson, P., Fernández-Jiménez, A., Provis, J. L., Lukey, G. C., Palomo, A., & Van Deventer, J. S. J. (2007). Geopolymer technology: The current state of the art. *Journal of Materials Science*, *42*(9), 2917−2933. Available from https://doi.org/10.1007/s10853-006-0637-z.

Hammond, G., Jones, C., Lowrie, F., & Tse, P. (2011). *Building Services Research and Information Association*.

Hardjito, D., Wallah, S. E., Sumajouw, D. M., & Rangan, B. (2004). Factors influencing the compressive strength of fly ash-based geopolymer concrete. *Civil Engineering Dimension*, *6*(2), 88−93.

Kumar, S., Kumar, R., & Mehrotra, S. P. (2010). Influence of granulated blast furnace slag on the reaction, structure and properties of fly ash based geopolymer. *Journal of Materials Science*, *45*(3), 607−615. Available from https://doi.org/10.1007/s10853-009-3934-5.

Lloyd, N.A., & Rangan, B.V. (2010). Geopolymer concrete with fly ash. In *Second international conference on sustainable construction materials and technologies* (pp. 1493−1504). Australia.

Lodiero, G., Fernandez, A., & Palomo, A. (2015). Cement with a low clinker content: Versatile use of raw materials. *Journal of Sustainable Cement-Based Materials*, *4*(2).

Obonyo, E., Kamseu, E., Melo, U. C., & Leonelli, C. (2011). Advancing the use of secondary inputs in geopolymer binders for sustainable cementitious composites: A review.

Sustainability, *3*(2), 410−423. Available from https://doi.org/10.3390/su3020410. Available from, http://www.mdpi.com/2071-1050/3/2/410/pdf.

Palomo, A., Krivenko, P., Garcia-Lodeiro, I., Kavalerova, E., Maltseva, O., & Fernández-Jiménez, A. (2014). A review on alkaline activation: New analytical perspectives. *Materiales de Construcción*, *64*(315), e022. Available from https://doi.org/10.3989/mc.2014.00314.

Sanchez-Herrero, M., Fernandez-Jimenez, J., & Palomo, A. (2015). Alkaline hydration of C2S and C3S. *Journal of American Ceramic Society*, 1−8.

Shah, A. (2017). *Geopolymer concrete with fly-ash and ground granulated blast furnace slag* [Doctoral programme].

Škvára, F., Kopecký, L., Němeček, J., & Bittnar, Z. (2006). Microstructure of geopolymer materials based on fly ash. *Ceramics - Silikaty.*, *50*(4), 208−215. Available from. Available from http://www.ceramics-silikaty.cz/2006/pdf/2006_04_208.pdf.

Wallah, S., & Rangan, B. V. (2006). *Low-calcium fly ash-based geopolymer concrete: Long-term properties*. *Curtin University of Technology*.

Interfacial direct shear behavior of aluminum slag and uniaxial geogrids

6

Bhargav Kumar Karnamprabhakara[1], *Umashankar Balunaini*[1] *and Arul Arulrajah*[2]

[1]Department of Civil Engineering, Indian Institute of Technology Hyderabad, Sangareddy, Telangana, India, [2]Department of Civil and Construction Engineering, Swinburne University of Technology, Hawthorn, Melbourne, Australia

6.1 Introduction

Industrial waste management has become an important task for engineers in the present-day world. Waste reduction or reuse are the preferable solutions for waste management in geotechnical engineering. Increase in land cost and waste disposal charges, and shortage of landfill area for waste disposal push us toward the utilization of waste materials as a civil engineering material.

In the recent past, utilization of industrial wastes such as coal ash, waste foundry sand, slag wastes, rubber wastes, plastic wastes, and construction and demolition wastes has gained attention for use in different geotechnical applications. These applications include as embankment fill material (Bosscher et al., 1997; Disfani et al., 2017; Santos et al., 2011; Yoon et al., 2006, 2009), pavement material (Gill et al., 2013; Havanagi et al., 2007; Karnamprabhakara et al., 2021; Sarkar & Dawson, 2017), soil stabilizer (Cristelo et al., 2012; Higgins, 2005; Saranya et al., 2011; Senol et al., 2006), reinforced fill material (Arulrajah et al., 2014; Karnamprabhakara & Balunaini, 2021; Karnamprabhakara et al., 2021; Kumar & Umashankar, 2018; Kumar et al., 2019; Pant et al., 2019), and so on.

In particular, slag wastes are the wastes generated during the processing of respective metals from their ores; common slag wastes include aluminum slag, steel slag, and copper slag. The waste-to-metal ratio varies based on the metal that is being extracted. For example, the waste-to-product ratios for copper and zinc are 2.2 and 1.6 (Prasad & Ramana, 2016a, 2016b). There are studies available on using slag wastes in different geotechnical applications such as a reinforced fill material (Prasad & Ramana, 2016a, 2016b), soil stabilization (Higgins, 2005; Ismail et al., 2019), and land reclamation (Lim & Chu, 2006), etc. However, there are limited studies available on using aluminum slag as a reinforced backfill material.

The soil−geogrid interface interaction properties are essential in the design of any reinforced soil structure. The soil−geogrid interaction failures in a mechanically stabilized earth wall mainly include (1) sliding mode of failure and (2) pullout

Green Materials in Civil Engineering. DOI: https://doi.org/10.1016/B978-0-443-19106-0.00006-3

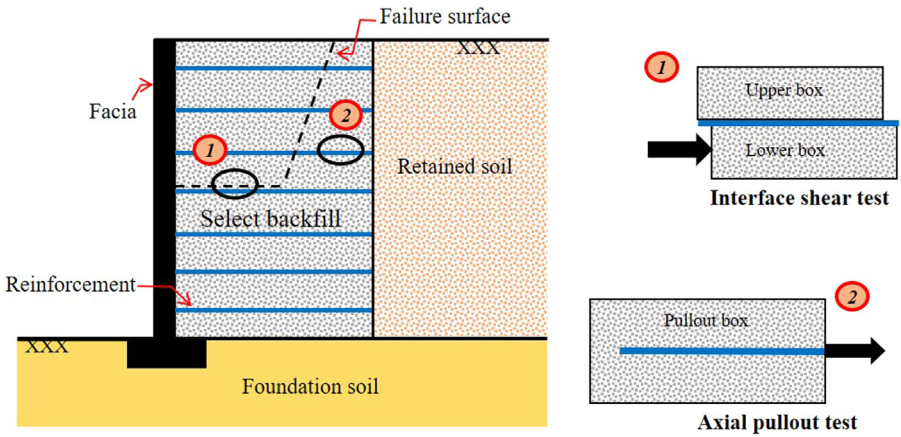

Figure 6.1 Sliding and pullout modes of failures in reinforced retaining walls.

mode of failure, as shown in Fig. 6.1. The pullout mode of failure along the failure plane is in general considered as an axial pullout mode of failure.

In the present study, sliding mode of failure for four different geogrids embedded in aluminum slag particles was studied using large-scale direct shear box. The efficiency of the geogrid (E_{φ}) based on the friction, and the sliding interaction coefficient (R_i) for the four geogrids were proposed.

6.2 Materials used

6.2.1 *Aluminum slag*

Aluminum slag used in the present study was collected from a local supplier based in Melbourne, Australia. Aluminum slag particles are predominantly gravel-size particles in composition and were hard in nature. A few remnants of metal pieces were also observed in the mixture (Fig. 6.2). Hereon, aluminum slag particles in the study were designated as 'AS'.

6.2.2 *Geogrid*

Four different polyester uniaxial geogrids procured from two different manufacturers were used in the present study. The geogrids mainly differ in their tensile strength and geometry. Fig. 6.3 shows the different geogrids used in the present study.

Table 6.1 presents the geometrical and mechanical properties of the four geogrids. More details on the geogrids can be found in the work of Karnam Prabhakara et al. (2021).

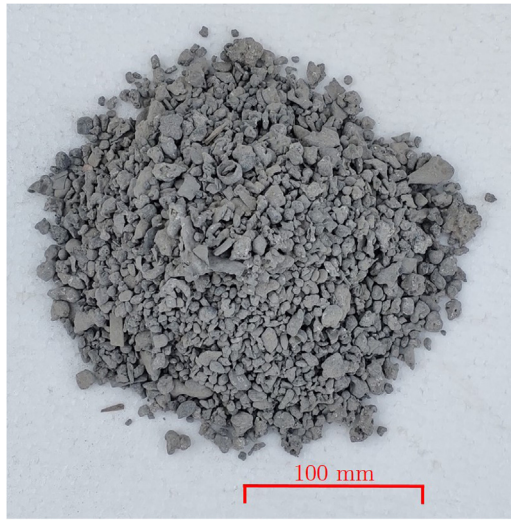

Figure 6.2 Aluminum slag particles used in the study.

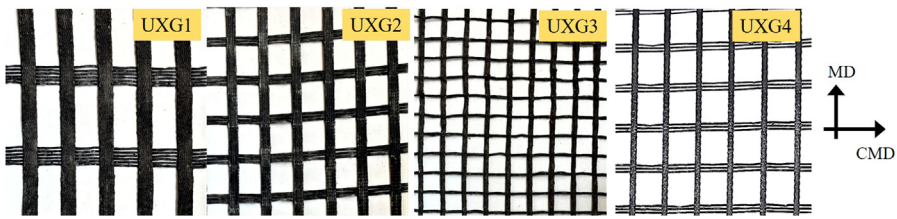

Figure 6.3 Geogrids used in the present study.

Table 6.1 Properties of the geogrids used in the present study.

S. No.	Geogrid	Tensile strength (kN/m)		CRF[b]	IDF[b]	DRF[b]	Aperture size (mm)	
		MD[a]	CMD[a]				MD[a]	CMD[a]
1.	UXG1	200	30	1.47	1.07	1.1	62	24
2.	UXG2	200	30	1.57	1.05−1.15	1.15	30	23
3.	UXG3	60	20	1.47	1.07	1.1	17	19.5
4.	UXG4	60	30	1.57	1.05−1.15	1.15	30	25

[a]MD-Machine direction; CMD-cross machine direction.
[b]CRF-Creep reduction factor; IDF-Installation damage factor; DRF-durability reduction factor.

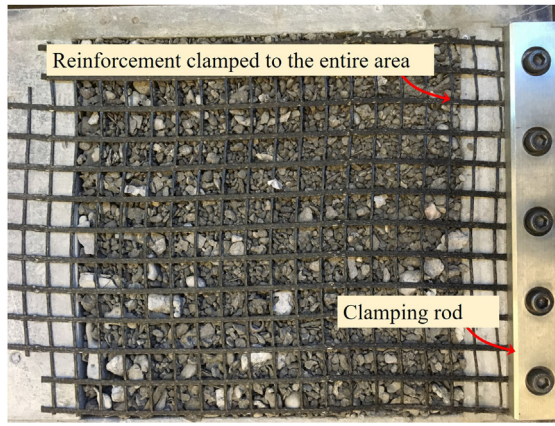

Figure 6.4 Geogrid sample connected at the interface of upper and lower shear boxes.

6.3 Experimental program

Basic characteristics such as particle size distribution, standard Proctor compaction density, pH, and leaching potential were determined for AS particles as per ASTM standards. Further, direct shear tests were performed using a box of dimensions $300 \times 300 \times 200$ mm (length $\times$ width $\times$ depth) on compacted AS particles alone and AS geogrid interfaces. The samples for direct shear strength testing of AS particles were prepared in the shear box in three layers, whereas samples for interface direct shear testing were prepared in four layers with two layers in the lower box, and two layers in the upper box with the geogrid clamped at the interface, as shown in Fig. 6.4. All the AS samples were compacted to 95% relative compaction. More details on the direct shear apparatus can be found in Maghool et al. (2020).

6.4 Results and discussion

The following sections discuss the results from basic characterization of aluminum slag particles, followed by the direct shear and interfacial direct shear testing of aluminum slag and geogrid-reinforced aluminum slag particles.

6.4.1 Basic characteristics of aluminum slag

Aluminum slag particles mainly consisted of gravelly particles. Three samples of 2 kg each were sieved through set of sieves of sizes 25, 19, 9.5, 4.75, 2.36, 1.18, 0.6, and 0.3 mm. Fig. 6.5 presents the average particle size distribution for aluminum slag particles from three trials.

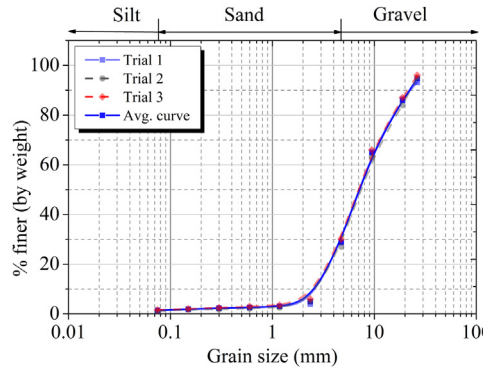

Figure 6.5 Particle size distribution of aluminum slag particles.

The gradation coefficients of the AS particles—uniformity coefficient (C_u) and coefficient of curvature (C_c)—were equal to 3.4 and 0.98, respectively. It is classified as poorly graded gravel type soil as per Unified Soil Classification System classification. The effective (D_{10}) and mean size (D_{50}) aluminum slag particles were equal to 2.7 and 7.2 mm. Based on the visual inspection, the aluminum slag particles were found be highly angular (Fig. 6.2). The effect of addition of water on the compacted density of the aluminum slag particles in standard Proctor compaction test was insignificant due to high gravel content. The maximum dry unit weight and the optimum moisture content were found to be equal to 15.8 kN/m^3 and 4%. However, water content of 2%−3% was added to prepare the sample in order to avoid washing out of fines from the slag particles during preparation. As the material is free draining, a slightly lower water content used for sample preparation is not expected to influence the drained shear strength behavior.

The pH of aluminum slag samples was measured as per ASTM G51, and it was found to be equal to 8.2. Any material with a pH of greater than 3 and less than 9 can be considered as a structural fill material with polyester reinforcement (Elias et al., 2001). Aluminum slag particles are expected to free draining and hence the hydraulic conductivity was not conducted on this material. Permeability of aluminum slag material in fill applications will not be a concern.

6.4.2 Direct shear testing

The direct shear and the interface direct shear tests were conducted at three normal stresses of 10, 20, and 40 kPa. Fig. 6.6 shows the variation of the direct shear stress of aluminum slag particles along the horizontal shearing plane with the displacement of the lower shear box. High shear stresses were observed for aluminum slag particles under all the normal stresses tested. There was a considerable loss of shear strength after attaining the peak shear strength. The percentage loss of shear strength between peak and critical states was equal to 66%, 63%, and 52% under normal stresses equal to 10, 20, and 40 kPa, respectively. The displacements

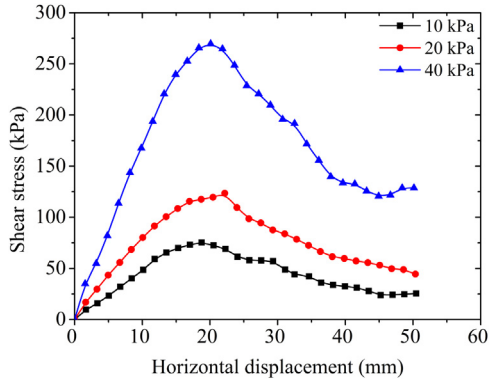

Figure 6.6 Variation of shear stress of aluminum slag particles along the horizontal plane versus the horizontal displacement of lower shear box.

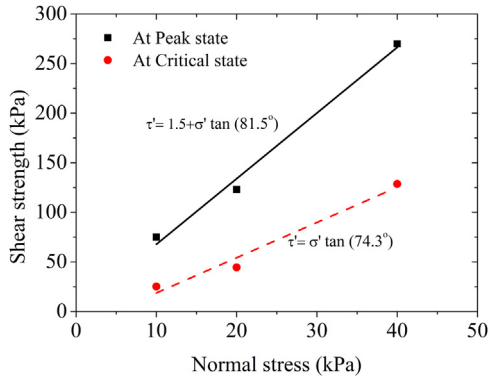

Figure 6.7 Direct shear strength envelopes of aluminum slag particles at peak and critical states.

required to attain the peak shear strength were equal to 18.7, 22.2, and 20.1 mm under normal stresses equal to 10, 20, and 40 kPa, respectively. The larger displacements in attaining the peak shear strength can be attributed to the particle rearrangement along the shearing plane. It could also be observed that within the shearing displacement of 50 mm, the particles did not reach the critical state.

Direct shear parameters for the aluminum slag, apparent cohesion (c), and angle of shearing resistance (φ) were equal to 1.5 kPa and 81.5 degrees, respectively, at the peak state (Fig. 6.7). The aluminum slag particles were highly gravelly with no or negligible fine particles. Higher values of shear strength could be because of highly angular nature of particles contributing to high interparticle friction and dilation. It was observed that the aluminum slag particles exhibited high shear strengths at low normal stresses. For example, under normal stress equal to 20 kPa, aluminum slag showed a shear strength of 123 kPa. High shear strength under low normal stress

could be attributed to pronounced dilatancy. No crushing of particles was observed during shearing of samples for the range of normal stresses considered in the study.

Table 6.2 presents the comparison of direct shear parameters observed for aluminum slag particles and other conventional and nonconventional fill materials from the literature.

The slag wastes and C&D wastes exhibit high to very high shear strengths in comparison with conventional sand sample. The behavior could be mainly attributed to the angularity of the particles of slag wastes in comparison with the conventional and nonconventional fill materials. High apparent cohesion of crushed brick was attributed to the clay particles forming a binding paste in contact with water during compaction.

6.4.3 Interface direct shear testing

Fig. 6.8 shows the shear stress variation along the horizontal displacement of lower shear box for geogrid-reinforced samples. The trends were similar for all the reinforced aluminum samples. Higher shear stresses were observed with the increase in the normal stress for all the samples. The loss of shear strength for the geogrid-reinforced aluminum slag samples between the peak and critical state varies between 8% and 23%, 21% and 33%, and 1% and 44% at normal stresses equal to 10, 20, and 40 kPa, respectively. The observed percentage loss in interfacial shear strength was relatively lower compared to the direct shearing between aluminum slag particles. The displacements corresponding to shear failure for the geogrid-reinforced samples varied between 11.8 and 22.2 mm, relatively lower values than those corresponding to the unreinforced aluminum slag.

Fig. 6.9 shows the comparison of the interfacial shear strength of geogrid-reinforced aluminum samples with the direct shear strength at the peak state. It could be observed that the difference between interfacial shear strength and direct shear strength were lesser at low normal stresses, 10 and 20 kPa, when compared to 40 kPa. This could be because of reduced dilatancy at 40 kPa normal stress in the case of geogrid-reinforced aluminum slag samples. Among the geogrids tested, UXG3 and UXG4 exhibited higher interfacial strength under 40 kPa normal stress. This was because of higher percent open area and the breakage of transverse ribs (Fig. 6.10) during the shearing process leading to more direct contact of aluminum slag particles.

The efficiency of the geogrid on friction for reinforced aluminum slag particles are presented in Table 6.3. Efficiency of geogrid varies between 26% and 53% at the peak state and ranges between 95% and 112% at critical state. It could be observed that efficiency of geogrid shows a relation with the percent open area of the geogrid. Higher the percent open area, higher was the efficiency of the geogrid. High values for efficiency of geogrid at critical state was because of the higher shear strength loss for aluminum slag and lesser loss of interfacial shear strength for reinforced cases. More details on the percent open area can be found in the work of Karnam Prabhakara et al. (2021).

Table 6.2 Comparison of direct shear parameters from the present study with the available literature.

References	Material	Gradation characteristics					Direct shear parameters	
		% Gravel	% Fines	C_u	C_c	Soil classification	Apparent cohesion, c (kPa)	Angle of shearing resistance, φ (degree)
Arulrajah et al. (2014)	Recycled concrete aggregate (RCA)	48%	10%	75.7	3.2	SP	95.0	65.0
Arulrajah et al. (2014)	Crushed brick (CB)	53%	8.7%	40.8	4.1	GP	87.0	57.0
Prasad and Ramana (2016a)	Zinc slag	2%	2%	2.9	0.9	SP	9.7	51.9
Prasad and Ramana (2016b)	Copper slag	0%	1%	2.6	1.0	SP	7.7	48.6
Kumar and Umashankar (2018)	Sand	0%	1%	2.4	0.9	SP	25.0	44.2
This study-Aluminum slag	Aluminum slag	70%	1%	3.0	0.9	GP	1.5	81.5

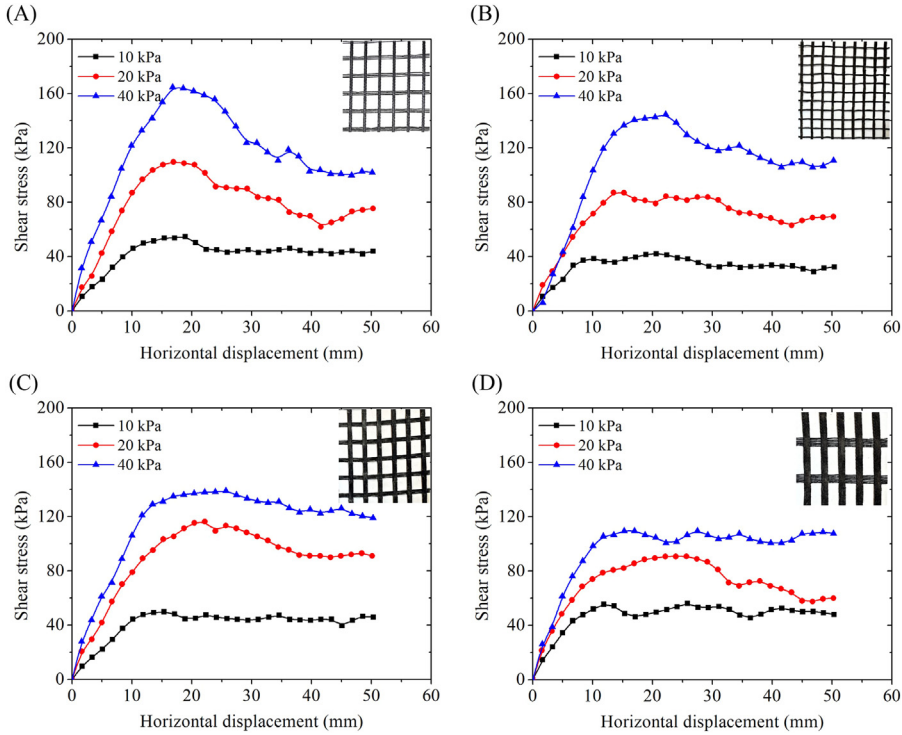

Figure 6.8 Variations of interface shear stress with the horizontal displacement for aluminum slag samples reinforced with (A) UXG1, (B) UXG2, (C) UXG3, and (D) UXG4 (inset: images of different geogrids used).

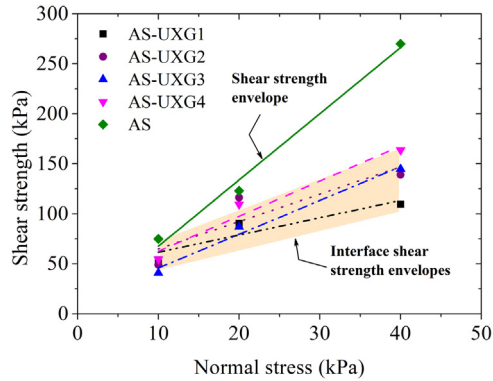

Figure 6.9 Comparison of interfacial shear strength envelopes with direct shear strength envelopes for aluminum slag particles.

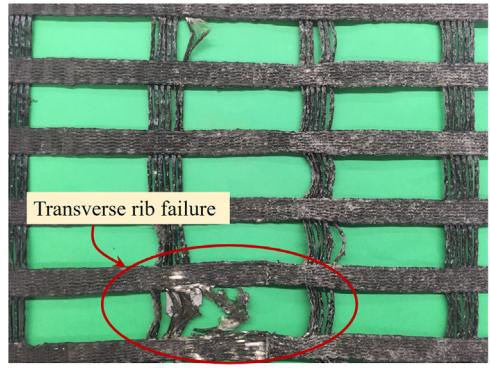

Figure 6.10 Breakage of transverse ribs observed during interface.

Table 6.3 Efficiency of geogrid based on friction embedded in aluminum slag.

Combination	**At peak state**		**At critical state**	$E_{\varphi,\ \text{peak}}$ **(%)**	$E_{\varphi,\ \text{critical}}$ **(%)**
	c/c_a (kPa)	φ_p/δ_p (degree)	φ_c/δ_c (degree)		
AS	1.5	81.5	71.6	–	–
AS-UXG1	44.4	59.9	70.6	26.1	94.8
AS-UXG2	37.8	69.9	73.4	41.2	112.0
AS-UXG3	12.2	73.5	71.2	50.9	97.7
AS-UXG4	27.6	74.1	70.8	52.9	95.8

Table 6.4 Interaction coefficients (R_i) of geogrids embedded in aluminum slag at the peak and critical states.

σ **(kPa)**	**At peak state**				**At critical state**			
	UXG1	UXG2	UXG3	UXG4	UXG1	UXG2	UXG3	UXG4
10	0.72	0.65	0.55	0.73	1.90	1.81	1.28	1.75
20	0.73	0.95	0.71	0.89	1.35	2.04	1.56	1.69
40	0.41	0.51	0.54	0.61	0.83	0.93	0.86	0.79

Interaction coefficient of geogrids defined as the ratio of interfacial shear strength of reinforced sample to the direct shear strength of the unreinforced sample is reported in Table 6.4 for aluminum slag particles. Interaction coefficients varied in the range of 0.41−0.89 at the peak state and 0.86−2.04 at the critical state. Low values of interaction coefficients were observed at higher normal stress of 40 kPa,

whereas high values were observed at lower normal stresses. The behavior could be attributed to reduced dilatancy at high normal stress, compared to low normal stresses, particularly for reinforced cases. High values of interaction coefficients observed at critical state could be because of the minimum loss of shear strength in reinforced case.

6.5 Conclusion

In the present study, aluminum slag particles are assessed for its feasibility to use it as a reinforced backfill material. The basic characteristic tests followed with direct shear and interfacial shear tests were conducted. The primary conclusions are:

1. Aluminum slag particles were of poorly graded gravelly type (GP) with gradation coefficients, uniformity coefficient, C_u and coefficient of curvature, C_c equal to 3.4, and 0.98, respectively.
2. Direct shear parameters, apparent cohesion (c), and angle of shearing resistance (φ) of aluminum slag particles were equal to 1.5 kPa and 81.5 degrees, respectively.
3. Efficiency of geogrid (E_φ) with respect to friction varied between 26% and 53% at the peak state and ranges between 95% and 112% at the critical state for the four geogrids tested in aluminum slag.
4. Interaction coefficients varied in the range of 0.41−0.89 at the peak state and 0.86−2.04 at the critical state for the four geogrids tested in aluminum slag. Geogrids with higher opening area exhibited higher interaction coefficient.

References

Arulrajah, A., Rahman, M. A., Piratheepan, J., Bo, M. W., & Imteaz, M. A. (2014). Evaluation of interface shear strength properties of geogrid-reinforced construction and demolition materials using a modified large-scale direct shear testing apparatus. *Journal of Materials in Civil Engineering*, *26*(5), 974−982. Available from https://doi.org/10.1061/(ASCE)MT.1943-5533.0000897.

Bosscher, P. J., Edil, T. B., & Kuraoka, S. (1997). Design of highway embankments using tire chips. *Journal of Geotechnical Engineering*, *123*(4), 295−304. Available from https://doi.org/10.1061/(ASCE)1090-0241(1997)123:4(295), http://ojps.aip.org/gto/.

Cristelo, N., Glendinning, S., Miranda, T., Oliveira, D., & Silva, R. (2012). Soil stabilisation using alkaline activation of fly ash for self compacting rammed earth construction. *Construction and Building Materials*, *36*, 727−735. Available from https://doi.org/10.1016/j.conbuildmat.2012.06.037.

Disfani, M. M., Tsang, H. H., Arulrajah, A., & Yaghoubi, E. (2017). Shear and compression characteristics of recycled glass-tire mixtures. *Journal of Materials in Civil Engineering*, *29*(6). Available from http://ascelibrary.org/mto/resource/1/jmcee7/.

Elias, V., Christopher, B., & Berg, R. (2001). Mechanically stabilized earth walls and reinforced soil slopes design and construction guidelines. Washington, D.C: U.S. Department of Transportation.

Gill, K. S., Choudhary, A. K., Jha, J. N., & Shukla, S. K. (2013). Large model footing load test on reinforced coal ash slope. *International Journal of Geotechnical Engineering*, *7* (3), 257−265. Available from https://doi.org/10.1179/1938636213Z.00000000040, http://www.maneyonline.com/doi/pdfplus/10.1179/1938636213Z.00000000040.

Havanagi, V. G., Mathur, S., Prasad, P. S., & Kamaraj, C. (2007). Feasibility of copper slag-fly ash-soil mix as a road construction material. *Transportation Research Record*, *2* (1989), 13−20. Available from https://doi.org/10.3141/1989-43.

Higgins, D. (2005). *Soil stabilisation with ground granulated blastfurnace slag*. *Cementitious Slag Makers Association (CSMA)*, 1−15. Available from https://ukcsma.co.uk/wp-content/uploads/2016/08/csma_report_on_soil_stabilisation.pdf.

Ismail, A. I. M., Awad, S. A., & Mwafy, M. A. G. (2019). The utilization of electric arc furance slag in soil improvement. *Geotechnical and Geological Engineering*, *37*(1), 401−411. Available from https://doi.org/10.1007/s10706-018-0619-3, http://www.wkap.nl/journalhome.htm/0960-3182.

Karnam Prabhakara, B. K., Balunaini, U., & Arulrajah, A. (2021). Development of a unique test apparatus to conduct axial and transverse pullout testing on geogrid reinforcements. *Journal of Materials in Civil Engineering*, *33*(1). Available from http://ascelibrary.org/mto/resource/1/jmcee7/.

Karnamprabhakara, B. K., Balunaini, U., Arulrajah, A., & Evans, R. (2021). Axial pullout resistance and interface direct shear properties of geogrids in pond ash. *International Journal of Geosynthetics and Ground Engineering*, *7*(2). Available from https://doi.org/10.1007/s40891-021-00266-x, https://link.springer.com/journal/40891.

Karnamprabhakara, B. K., & Balunaini, U. (2021). Modified axial pullout resistance factors of geogrids embedded in pond ash. *Geotextiles and Geomembranes*, *49*(5), 1245−1255. Available from https://doi.org/10.1016/j.geotexmem.2021.04.003, http://www.elsevier.com/inca/publications/store/4/0/5/8/9/7/index.htt.

Karnamprabhakara, B.K., Guda, P.V., & Balunaini, U. (2021). Deutschland GmbH India resilient modulus of compacted fly ash for pavement applications. *Lecture notes in civil engineering*. Springer Science and Business Media. 134 347-357 23662565 http://www.springer.com/series/15087.

Kumar, K. P. B., Krishna, G., & Umashankar, B. (2019). India evaluation of waste foundry sand and blast furnace steel slag as geomaterials. *Geotechnical Special Publication. American Society of Civil Engineers (ASCE)*, *312*, 304−313. Available from https://doi.org/10.1061/9780784482148.031.

Kumar, K. P. B., & Umashankar, B. (2018). American Society of Civil Engineers (ASCE) India interface studies on geogrid and fly ash. *Geotechnical Special Publication*, *297*, 119−129. Available from https://doi.org/10.1061/9780784481608.012.

Lim, T. T., & Chu, J. (2006). Assessment of the use of spent copper slag for land reclamation. *Waste Management and Research*, *24*(1), 67−73. Available from https://doi.org/10.1177/0734242X06061769.

Maghool, F., Arulrajah, A., Mirzababaei, M., Suksiripattanapong, C., & Horpibulsuk, S. (2020). Interface shear strength properties of geogrid-reinforced steel slags using a large-scale direct shear testing apparatus. *Geotextiles and Geomembranes*, *48*(5), 625−633. Available from https://doi.org/10.1016/j.geotexmem.2020.04.001, http://www.elsevier.com/inca/publications/store/4/0/5/8/9/7/index.htt.

Pant, A., Datta, M., & Ramana, G. V. (2019). Bottom ash as a backfill material in reinforced soil structures. *Geotextiles and Geomembranes*, *47*(4), 514−521. Available from https://doi.org/10.1016/j.geotexmem.2019.01.018, http://www.elsevier.com/inca/publications/store/4/0/5/8/9/7/index.htt.

Prasad, P. S., & Ramana, G. V. (2016a). Feasibility study of copper slag as a structural fill in reinforced soil structures. *Geotextiles and Geomembranes*, *44*(4), 623−640. Available from https://doi.org/10.1016/j.geotexmem.2016.03.007, http://www.elsevier.com/inca/publications/store/4/0/5/8/9/7/index.htt.

Prasad, P. S., & Ramana, G. V. (2016b). Imperial smelting furnace (zinc) slag as a structural fill in reinforced soil structures. *Geotextiles and Geomembranes*, *44*(3), 406−428. Available from https://doi.org/10.1016/j.geotexmem.2016.01.009, http://www.elsevier.com/inca/publications/store/4/0/5/8/9/7/index.htt.

Santos, F., Li, L., Li, Y., & Amini, F. (2011). *Geotechnical properties of fly and bottom ash mixtures for use in highway embankments*. World of Coal Ash (WOCA) Conference - May 9-12, 2011, in Denver, CO, USA.

Saranya, K., Rohini, K., & Naveena, A. (2011). A review on utilization of copper slag and silica fume in geotechnical engineering. *Proceedings of Indian Geotechnical Conference* (pp. 445−448).

Sarkar, R., & Dawson, A. R. (2017). Economic assessment of use of pond ash in pavements. *International Journal of Pavement Engineering*, *18*(7), 578−594. Available from https://doi.org/10.1080/10298436.2015.1095915, http://www.tandfonline.com/loi/gpav20.

Senol, A., Edil, T. B., Bin-Shafique, M. S., Acosta, H. A., & Benson, C. H. (2006). Soft subgrades' stabilization by using various fly ashes. *Resources, Conservation and Recycling*, *46*(4), 365−376. Available from https://doi.org/10.1016/j.resconrec.2005.08.005.

Yoon, S., Balunaini, U., Monica, P., & Rodrigo, S. (2006). Determination of ash mixture properties and construction of test embankment, Part B. *Publication FHWA/IN/JTRP-2006/24-B. Joint Transportation Research Program, Indiana Department of Transportation and Purdue University, West Lafayette, Indiana*. Available from https://doi.org/10.5703/1288284314226.

Yoon, S., Balunaini, U., Yildirim, I. Z., Prezzi, M., & Siddiki, N. Z. (2009). Construction of an embankment with a fly and bottom ash mixture: Field performance study. *Journal of Materials in Civil Engineering*, *21*(6), 271−278. Available from https://doi.org/10.1061/(ASCE)0899-1561(2009)21:6(271).

Fly ash-granulated blast furnace slag: better replacement materials for subbase flexible pavement construction

7

Manjula Devi Balasundar[1] *and Hemant Chore*[2]
[1]Department of Civil Engineering, Datta Meghe College of Engineering, Airoli, Navi Mumbai, Maharashtra, India, [2]Department of Civil Engineering, Dr. B.R. Ambedkar National Institute of Technology, Jalandhar, Punjab, India

7.1 Introduction

India's ever-increasing population needs an extensive system of roads to absorb the high traffic volume. In the coming years, the road pavements are expected to go through a major change with respect to the materials used and procedure of construction. The guidelines on sustainable development are going to be enforced by the government. There is a drive to identify, examine industrial waste material that could be used in place of conventional construction materials. Proper utilization of these materials in the road construction, as it requires large quantities of material, will greatly help in having a better and pleasant environment.

Many researchers conducted different laboratory experiments to identify the potential use of fly ash (FA) for subgrade soil stabilization. Very few were explored it for the subbase and base courses (Jackson et al., 2009; Joshi et al., 1975). The self-cementing characteristic of FA with lime increased the strength and durability of the mix without affecting the environmental quality (Butalia, 2007; Mohanty & Chugh, 2006). Utilizing as much FA as possible in the subgrade and subbase layers for low volume roads has proven to be an economical method of building roads (Mishra & Sudhira, 2011). Different types of FA with various percentages can be used as mineral filler (Katarina et al., 2019). Granulated blast furnace slag (GBFS) can also be used to improve the bearing capacity of soft soil (Yadu & Tripathi, 2013). The resilient modulus and stiffness increases notably at 30% of FA stabilized with reclaimed asphalt pavement materials for the base course construction (Saride et al., 2014). The unique property of geosynthetics (less weight and durability) leads to its use in various civil engineering constructions. Stone dust, FA, and blast furnace slag are three potential industrial wastes that could be used in pavements after being reinforced with high-density plastic waste strips. According to the findings, adding waste plastic strips and industrial wastes increased the subgrade modulus (ks) and California Bearing Ratio (CBR) significantly (Jha et al., 2014). The model pavement tests were conducted on the section consisting

Green Materials in Civil Engineering. DOI: https://doi.org/10.1016/B978-0-443-19106-0.00007-5

of geogrid reinforcement at the interface of the subgrade and subbase. It was concluded that a geogrid-reinforced soil appeared stronger and stiffer, and provided more strength than soil without geogrid reinforcement (Fattah & Aladili, 2016).

The literature survey indicates that our country is far behind as compared to the other countries, especially in the utilization of industrial and Pozzolanic waste (Kumar & Yudhbir, 2003). However, among all other Pozzolanic waste, the work on FA is prominent in stabilization of subgrade soil. The use of GBFS along with FA has been reported to the lesser extent. In the present study, laboratory and small-scale model pavement tests were conducted to evaluate the fly ash-granulated blast furnace slag (FA-GBFS) mixture for road subbase as an alternate material to the conventional cementitious (cement-treated) subbase (CTSB) layer.

7.2 Properties of materials

7.2.1 Fly ash and granulated blast furnace slag

The present work involves the use of Pozzolanic materials like FA and GBFS, in the presence of conventional polymeric reinforcements such as geogrid. Electricity is one of the most vital infrastructural inputs for growth of Indian economy. For the generation of electricity, India has to depend on coal since other sources like hydropower and nuclear resources have not made sizeable contribution. The FA produced by coal-based Thermal Power Plants was approximately 90×10^6 tonnes per year, necessitating the use of an area of 265 km^2 as an ash pond for safe disposal. Currently, less than 5% of this FA is being used profitably (Das & Yudhbir, 2005). FA used in the investigation was procured from Eklahare Thermal Power Plant located in Nashik (Maharashtra) and stored in air tight containers.

Steel plants produce GBFS as a by-product. Most countries use GBFS in road construction to replace natural aggregates in the wearing course, base, and subbase layers, either partially or completely. GBFS has the appearance of a sand particle and can be used in the same way (Valunjkar & Zore, 2010). As a result, GBFS can be utilized as sand in concrete pavements and as a filler in flexible pavements. Because of the benefits of GBFS, MoRTH (2013) approved it for the construction of subbase and base course layers. GBFS, a by-product of steel industries, was collected from JSW Steel Limited, Pen Maharashtra.

The laboratory investigations such as specific gravity (IS: 2720-1980 [Part-3]), standard Proctor test (IS: 2720-1974 [Part-6]), and particle size distribution (IS: 2720-1985 [Part-4]) were carried out for finding out the physical properties of materials. The properties of the FA and GBFS obtained are reported in Table 7.1. The particle distribution curve is shown in Fig. 7.1.

7.2.2 Marine clay

The clayey soil collected from JNPT, Mumbai, is considered for the model pavement studies as a subgrade soil. Various laboratory experiments like specific gravity

Table 7.1 Basic properties of fly ash and granulated blast furnace slag.

Sr. no.	Property	Fly ash	Granulated blast furnace slag
1	Specific gravity (SG)	2.07	2.486
2	Max dry unit weight (MDU) in (kN/m^3)	14.28	14
3	Optimum moisture content (OMC) (%)	19	6.5
4	Sand-sized particles (4.75−0.075 mm) (%)	15	98.55
5	Silt- and clay-sized particles (below 0.075 mm) (%)	85	1.45

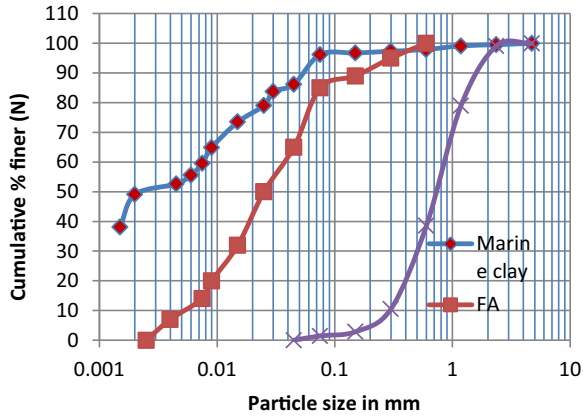

Figure 7.1 Particle size distribution curves.

(SG), Atterberg limits, sieve analysis, standard Proctor, CBR, and free swell index tests were conducted on the soil as per the relevant IS codes. The results are given in Table 7.2.

Various laboratory experiments (tests) were conducted on the materials used in this investigation to understand their basic properties. These tests include: sieve analysis (IS: 2720-1985 [Part-4]), SG (IS: 2720-1980 [Part-3]), standard Proctor test (IS: 2720-1974 [Part-6]), CBR (IS 2720-1979 [Part 16]) and Unconfined Compressive Strength Tests (IS: 4332-1070 [Part-V]). Atterberg limits (IS: 2720-1985 [Part-5]), and free swell index (IS: 2720-1977 [Part-40]) (IS 2720-10, 1991; IS 2720 (Part 40), 1977; IS: 2720 (Part III-1985)., 1995; IS: 2720 (Part IV-1985)., 1995; IS: 2720 (Part V-1985)., 1995; IS: 2720 (Part VIII-1985)., 1997; IS: 2720 (Part XVI-1985)., 1997).

The results are shown in Table 7.2, and the particle size distribution curve is indicated in Fig. 7.1.

Table 7.2 Soil sample properties (Manjula Devi & Chore, 2019).

Sr. no.	Parameters	Value	Sr. no.	Parameters	Value
1	Specific gravity	2.5	8	Unified soil classification	CH
2	Liquid limit (%)	80	9	Soil specification as per AASHTO	A-7−5
3	Plastic limit (%)	35	10	Optimum moisture content (%)	31
4	Plasticity index (%)	45	11	Maximum dry unit weight (kN/m^3)	13.73
5	Shrinkage limit (%)	22.35	12	Unsoaked CBR (%)	4.54
6	Sand (%)	3.9	13	Soaked CBR (%)	1.85
7	Silt + clay (%)	47.1 + 49	14	Free swell index (%)	150

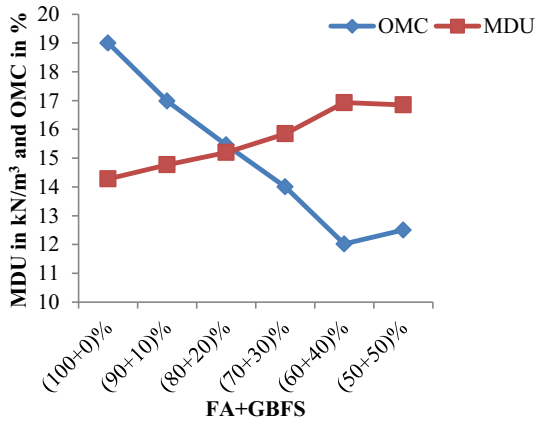

Figure 7.2 Graphical representation of standard Proctor test results.

7.2.3 Reinforcement

In this study, commercially available 1 mm thick biaxial polymeric-coated polyester geogrid with mesh size ± 5 mm (36 mm in machine direction (MD) and 39 mm in transverse direction) was used as a reinforcing element and is shown in Fig. 7.2.

Commercially available nonwoven geotextile was placed at the interface of the subgrade and the subbase course as a separator in all the cases. The properties of the geotextile used in the tests are Grab Strength MD/CD 729/881N and Elongation @ break MD/CD 66.5/72.4%.

7.2.4 Chemical properties of the materials

An X-ray fluorescence spectrometry test was performed on marine clay, FA, and GBFS to better understand the chemical composition of the materials. Table 7.3 summarizes the materials' testing results.

Table 7.3 Chemical composition of the fly ash (FA), granulated blast furnace slag (GBFS), and marine clay.

Constituents	Marine clay (%)	GBFS (%)	FA (%)	Constituents	Marine clay (%)	GBFS (%)	FA (%)
SiO_2	39.10	38.10	60.8	MnO	0.13	0.36	Nil
Al_2O_3	13.30	13.10	25.9	Na_2O	8.60	0.46	Trace
Fe_2O_3	10.80	2.10	4.5	K_2O	1.53	0.47	Trace
CaO	9.62	36.40	1.8	P_2O_5	0.47	0.05	Nil
MgO	3.39	6.32	1.5	SO_3	5.90	1.30	0.10
TiO_2	1.51	0.78	Nil	Cl	4.63	0.07	nil

From Table 7.3, it is observed that the higher percentage of silica and alumina oxides are present in marine clay and FA. According to IS 3812-1981, the FA type is Grade-I as the addition of $SiO_2 + Al_2O_3 + Fe_2O_3$ is more than 70% and produced from bituminous coal. Based on the mineralogical studies, the FA is classified as class-F. Class-F FA, which is often formed from the combustion of bituminous has a CaO content of less than 10% and has Pozzolanic characteristics (ASTM C618). GBFS is a by-product of steel industries. Generally it is composed of silicates and aluminosilicates of lime and other bases (Sridevi & Rao, 2011). A similar result could be seen in the GBFS employed in this investigation.

7.3 Methodology

7.3.1 Laboratory experimentation

As per Indian Road Congress, GSB layer can be divided into two layers: upper subbase and lower subbase. FA-GBFS mixes are considered for the lower subbase to act as a separation layer. As these materials are more cementitious, it is considered as CTSB.

To find out the optimum proportion of FA and GBFS, GBFS was varied from 10% to 50% by dry weight of FA in increments of 10%. Standard Proctor and soaked CBR tests were conducted. The results are shown in Table 7.4 and Figs. 7.2 and 7.3.

GBFS is coarser than FA, such that up to 40%, the mixture of FA and GBFS is compact with less voids, and further addition of GBFS starts to increase the voids in the mix, and subsequently, MDU reduces. The soaked CBR values are found to be higher than unsoaked CBR due to Pozzolanic reaction between SiO_2 in FA and $CaCO_3$ in GBFS, resulting into the formation of calcium silicate gel. The increase in CBR indicates an improvement in the properties of the mix.

The soaking CBR value was increased with the addition of GBFS content till 40% and thereafter, the same is found to be decreased. The increase in CBR is clearly an indication of the improved properties of the mix.

Table 7.4 Standard Proctor and California Bearing Ratio (CBR) tests results.

(FA + GBFS)	(100 + 0)%	(90 + 10)%	(80 + 20)%	(70 + 30)%	(60 + 40)%	(50 + 50)%
OMC (%)	19	16.98	15.46	14	12.02	12.5
MDU (kN/m^3)	14.28	14.77	15.2	15.85	16.93	16.85
CBR (%) (unsoaked)	8.69	11.55	15.65	29.18	31.14	25.745
CBR (%) (soaked)	4.2	12.76	18.54	35.95	43	41.5

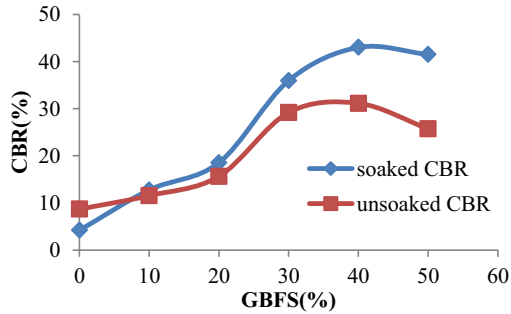

Figure 7.3 California Bearing Ratio test results for various fly ash-granulated blast furnace slag mixes.

7.4 Model pavement

To analyze the load-carrying capacity of the pavement that comprised subgrade and subbase materials, small-scale model pavement was developed, and the experiments were performed for the different subgrade soil conditions. The systematic sketch of the small-scale model pavement used in this study is shown in Fig. 7.4.

The dimensions of the tank are 1 m × 1 m × 1 m and the size of the loading plate is 170 × 170 mm. The vertical load applied at the rate of 1 mm/min through the steel ball of 20 mm diameter was placed over the loading plate by means of a strain-controlled hydraulic system. S-type load cell was used to measure the load and deformations were measured using a data acquisition system (DAQ) as shown in Fig. 7.5.

7.5 Sample preparation of model pavement

7.5.1 Subgrade

The air-dried clayey soil was pulverized and sieved through 4.75 mm sieve as shown in Fig. 7.6. The mass of the soil was calculated based on the predetermined

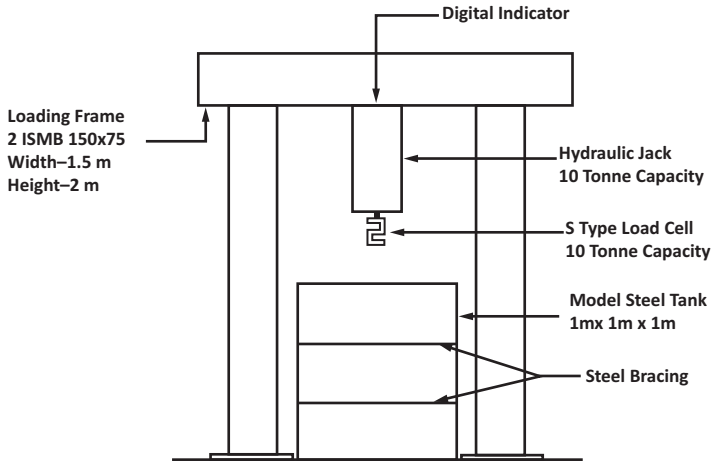

Figure 7.4 The systematic sketch of the small-scale model pavement.

Figure 7.5 Loading arrangements of model test setup.

Figure 7.6 Pulverized clayey soil.

volume of the soil to be filled in the tank. To achieve the homogenous mix, the soil was mixed with predetermined water and covered by the plastic paper for 2 days. The clayey soil was filled in the tank 50 cm high in five layers, each layer being 10 cm high. The compaction force was maintained to achieve uniform density throughout the depth of the subgrade. The properties of clay bed were monitored for each layer.

7.5.2 Subbase layer

The subbase layer thickness considered for this study is 15 cm. Based on the optimum mix and volume required to be filled, the mass of FA and GBFS were calculated and mixed with OMC. To get the uniform mix of FA-GBFS, the mixture was kept in an air-tight plastic cover for 24 h. For a separation, nonwoven geosynthetics were placed above the subgrade as shown in Fig. 7.7. The FA-GBFS mixture was placed and compacted in two layers to achieve the required density and height. In the case of reinforced section, the biaxial geogrid was placed at the mid-depth of FA-GBFS mixture as shown in Fig. 7.8.

7.5.3 Experimental procedure

The test setup arrangements after preparation of the test bed are shown in Fig. 7.5. S-type load cell was used to measure the load, and DAQ system was used to measure the deformation. The load was applied through the hydraulic jack at the rate of 1 mm/min over the prepared test section. Deformation was measured in the interval of 0.5 kN load. Same procedure was observed for reinforced and unreinforced sections.

Figure 7.7 Geosynthetic placed over the subgrade as a separator.

Figure 7.8 Reinforcement in the subbase.

7.6 Results and discussion

From the laboratory investigations, the optimum mix of 60% FA + 40% GBFS was considered as a CTSB layer for the model pavement studies. Detailed test series and parameters considered for the study are shown in Table 7.5.

After preparation of the model pavement, the applied load through the motorized hydraulic jack was measured by using the load cell, and deformation for every increment of 0.5 kN load was measured from the developed DAQ system. The test results are shown in Table 7.6.

Load-deformation curve was plotted for both reinforced and unreinforced sections from the data observed. From Fig. 7.9, less deformation was observed in the case of geogrid-reinforced section. Based on the observation, reinforced FA-GBFS mix can be used as an upper subbase layer because of the more load-carrying capacity. Similar pattern was observed in the evaluation of reinforced subbase layer on expansive subgrade soil (Robayo et al., 2016).

Table 7.5 Detailed tests and parameters considered.

Type of subgrade	Type of subbase	Subgrade influencing parameters
Marine clay	FA-GBFS (unreinforced) FA-GBFS (reinforced)	Subgrade soil stabilized with OMC and corresponding MDD

Table 7.6 Model pavement tests results.

Load in kN	Unreinforced	Geogrid reinforced	Difference in deformation (%)	Load in kN	Unreinforced	Geogrid reinforced	Difference in deformation (%)
	Deformation in mm	Deformation in mm			Deformation in mm	Deformation in mm	
0	0	0	0	7.5	7.92	4.5	76
0.5	0	0	0	8	8.64	5.76	50
1	0.18	0.18	0	8.5	9.72	6.3	54
1.5	0.54	0.36	50	9	10.8	7.74	40
2	0.72	0.36	100	9.5	12.06	8.64	40
2.5	1.22	0.48	154	10	12.96	9.72	33
3	1.8	0.54	233	10.5	14.04	10.98	28
3.5	2.34	0.9	160	11	15.3	11.7	31
4	2.98	1.26	137	11.5	17.28	12.78	35
4.5	3.24	1.98	64	12	19.08	13.68	39
5	4.14	2.34	77	12.5	20.88	14.94	40
5.5	4.86	2.7	80	12.8	22.86	16.2	41
6	5.22	2.88	81	13	24.48	18.72	31
6.5	6.3	3.24	94	14	–	20	
7	7.02	3.6	95				

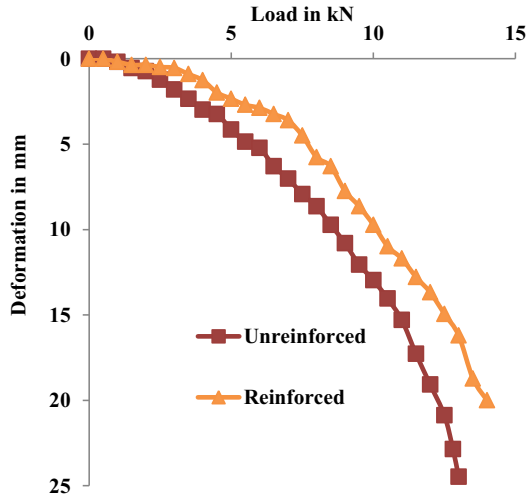

Figure 7.9 Load-deformation curve for reinforced and unreinforced sections.

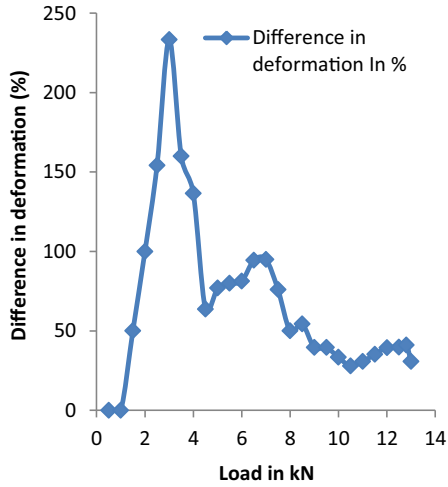

Figure 7.10 Difference in deformation for unreinforced and reinforced cases.

From the Fig. 7.10, it is seen that for the same water content and same void ratio, the reinforced sections show less deformation than that in unreinforced sections due to the reinforcing effects of the geogrid. The difference in percentage deformation is found to increase with increase in load of the pavement section. Higher percentage of the difference in deformation observed for the initial loading clearly indicates the significance of effect of reinforcement in the subbase layer.

7.7 Summary and conclusions

From the detailed laboratory analysis, the optimum mix observed based on the CBR requirements in accordance with IRC and MoRTH specifications is 60% FA + 40% GBFS. From the results obtained in view of various experiments performed on these mixes and the model pavement, the following prominent conclusions are arrived upon:

The mix with FA (60%) + GBFS (40%) is found to perform optimally on the basis of maximum dry unit weight (MDU) and CBR.

As per the IRC: 37-2018 (Kumar & Yudhbir, 2003) and MoRTH (Das & Yudhbir, 2005) specifications, the minimum CBR value for the material should be 30% for use in the subbase course. The 60 FA + 40 GBFS mix satisfies this criteria. Hence, this mix may be recommended for use in the lower subbases as a separation layer in road construction.

The load-carrying capacity of the model test has significantly increased for reinforced FA and GBFS mix laid over poor subgrade.

Higher percentage of the difference in deformation observed for the initial loading clearly indicates the significance of the effect of reinforcement in the subbase layer.

Using FA-GBFS mixture for road subbase reduces the problem of disposing industrial by-product to protect the environment.

References

Butalia, S. T. (2007). *Rehabilitating asphalt highways: Coal fly ash used on Ohio full depth reclamation projects. Case study—18, coal combustion product partnership* (pp. 1—4). United States: Environmental Protection Agency.

Yudhbir, S. K. D. (2005). Geotechnical characterization of some Indian flyashes. *ASCE Journal Materials in Civil Engineering*, *17*(5), 544—552.

Fattah, Y. M., & Aladili, S. A. (2016). Evaluation of reinforced sub-base layer on expansive sub-grade soil. *Engineering and Technology Journal*, *34*(9), Part (A).

IS 2720 (Part 40). (1977). Methods of test for soils: Determination of free swell index of soils. Bureau of Indian standards: New Delhi, India.

IS: 2720 (Part III-1985). (1995). Indian standard methods of test for soils, part-3 determination of specific gravity test of soil. Bureau of Indian standards: New Delhi, India.

IS: 2720 (Part IV-1985). (1995). Indian standard methods of test for soils, part-4 grain size analysis. Bureau of Indian standards: New Delhi, India.

IS: 2720 (Part V-1985). (1995). Indian standard methods of test for soils, part-5 determination of liquid limit and plastic limit. Bureau of Indian standards: New Delhi, India.

IS: 2720 (Part VIII-1985). (1997). Indian standard methods of test for soils, part-9 determination of dry density and moisture content. Bureau of Indian standards: New Delhi, India.

IS: 2720 (Part XVI-1985). (1997). Indian standard methods of laboratory determination of CBR. Bureau of Indian standards: New Delhi, India.

IS 2720-10. (2720). *Methods of test for soils: Laboratory determination of Unconfined compressive strength (UCS)*. New Delhi, India: Bureau of Indian Standards.

Jackson, N. M., Schultz, S., Sander, P., & Schopp, L. (2009). Beneficial use of CFB ash in pavement construction applications. *Journal of Fuel*, 1210−1215.

Jha, J. N., Choudhary, A. K., Gill, K. S., & Shukla, S. K. (2014). Behavior of plastic waste fiber-reinforced industrial wastes in pavement applications. *International Journal of Geotechnical Engineering*, *8*(3), 277−285.

Joshi, R. C., Duncan, D. M., & Master Mc, H. M. (1975). New and conventional engineering uses of fly ash. *Journal of Transportation Engineering*, *101*, 791−806.

Katarina, T., Nikola, T., & Goran, M. (2019). Effect of different types of fly ash on properties of asphalt mixture. *Journal of Advances in Civil Engineering*, 1−11.

Kumar, S., & Yudhbir, D. (2003). Chemistry and mineralogy of some Indian fly ashes. *Indian Concrete Journal*, *77*(12), 1491−1494.

Manjula Devi, B., & Chore, H.S. (2019). Feasibility study on bagasse ash as light weight material for road construction. Materials Today: Proceedings. Elsevier. https://doi.org/10.1016/j.matpr.2020.03.568G.

Mishra, N. K., & Sudhira, R. (2011). Cost effectiveness of clayey soil and moorum, treated with fly ash-lime for construction of low volume roads. *International Journal of Civil and Structural Engineering*, *2*(1), 1−10.

Mohanty, S., & Chugh, Y. P. (2006). Structural performance monitoring of an unsterilized fly ash based road subbase. *Journal of Transportation Engineering*, *132*, 964−969.

MoRTH. (2013). Specifications for road and bridge works. Ministry of Road Transport and Highways, Government of India (morth.nic.in).

Robayo, R. A., Mejia de, R., & Gordillo, M. (2016). Natural pozzolan-and granulated blast furnace slag-based binary geopolymers. *Materiales de Constructión*, *66*(321).

Saride, S., Deepti, A., & Rao, S. (2014). Evaluation of fly-ash-treated reclaimed asphalt pavement for the design of sustainable pavement bases: An Indian perspective Geo-Congress. *Geotechnical Special Publication*.

Sridevi, G., & Rao, A.S. (2011). Utilization of GBS in road sub-base. In *Proceedings of Indian* geotechnical conference, Kochi, India (pp. 283−286).

Valunjkar, S. S., & Zore, T. D. (2010). Utilization of fly ash and steel slag in road construction − A comparative study, Bund. Q *EGJE Journal*.

Yadu, L., & Tripathi, R. K. (2013). Effects of granulated blast furnace slag in the engineering behaviour of stabilized soft soil. *Procedia Engineering*, *51*, 125−131.

High performance concrete using fly ash

8

Sekar Saya Kanappan and Punitha Kumar Akhas
School of Civil Engineering, Vellore Institute of Technology, Vellore, Tamil Nadu, India

8.1 Introduction

High performance concrete (HPC) has been used in the construction industry for achieving more strength and durability than conventional concrete. Mostly, HPC is used for the construction of tall buildings, bridges, tunnels, airport buildings, offshore structures, etc. The ingredients of HPC are supplementary cementitious materials like fly ash, silica fume, ground granulated blast furnace slag, high-quality aggregates, superplasticizers, and water. The mix proportion of HPC is obtained by trial mixture approach. The other process like mixing, placing, consolidation, and curing are also cautiously to be done at the site for achieving HPC.

Manufacturing of cement produces 8%−10% of the world's total CO_2 emissions (Suhendro, 2014). The most efficient way to reduce CO_2 emissions from the construction industry is viable by reducing the Portland clinker content of the cement. The clinker content of the cement can be reduced by utilization of fly ash, ground granulated blast furnace slag, microsilica, ash type of waste, and crushed glass waste (Nielsen & Glavind, 2007). Green concrete is manufactured using a combination of one or more waste material in addition to the other constitution of concrete. The manufacturing process does not create any environmental degradation (Obla, 2009). The green concrete production is achieved by partially replacing cement by fly ash and development of concrete with other waste materials (Suhendro, 2014). Addition of fly ash ensure the standard HPC. The reason for development of HPC is to avoid premature failure of concrete structures (Bharatkumar et al., 2005). HPC usually refers to 28th day compressive strength of the concrete beyond 70−80 MPa; it is made with good quality aggregates and required cement content (Leung, 2001). HPC will typically have a low water-binder ratio of 0.22−0.35 (Neville & Aitcin, 1998). Superplasticizers are commonly used to improve the fluidity and workability. HPC outperforms ordinary concrete in terms of durability and strength (Edward & Nawy, 2000).

This chapter mainly focused on green concrete made by using industrial waste material known as fly ash. The key advantage of fly ash for producing HPC is that it decreases the quantity of calcium hydroxide (lime) that affects the durability. The selection of materials, mix proportions, mixing, placing, consolidation, setting time, curing of concrete, strength, and durability properties of HPC are discussed in this

Green Materials in Civil Engineering. DOI: https://doi.org/10.1016/B978-0-443-19106-0.00008-7

chapter. The construction materials used for manufacturing of high performance green concrete are given in Fig. 8.1.

8.1.1 Applications of high performance concrete

HPC has been used in the following structures:

- Bridges and tunnels
- Hydropower structures
- Pavements
- High-density radiation shielding structures
- Offshore platforms and marine structures
- Vibration dampening areas
- High-rise structures

8.1.2 Advantages of high performance concrete

The various advantages of HPC are listed below:

- High early strength and better durability.
- High elastic property.
- More life in extreme environments and chemical attack.
- Permeability is less.
- Resistance against toughness and impact resistance.
- Ease of transport, placement, and compaction without segregation of aggregate.

8.2 Mix design of high performance concrete

The goal of any mix design is to find a suitable and cost-effective proportion of concrete ingredients that may be utilized for a particular type of concrete. For HPC,

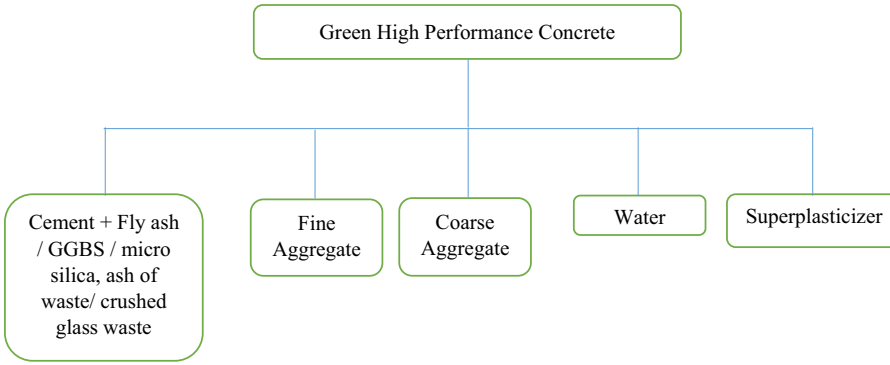

Figure 8.1 The construction materials used for manufacturing of high performance green concrete.

durability, workability, and mechanical properties are very important; many trial mixes are to be prepared to ensure these properties before executing the work. Even though all the ingredients of concrete are interchangeable for developing a mix design procedure that can be utilized globally with any combination of concrete materials. And the selection of admixtures will always be challenging. The mix proportion of HPC is prepared based on durability, mechanical properties, workability, and cost economy (Zhang et al., 2015). Many mix designs are available for HPC currently, one of the mix design method for HPC was developed by Mehta and Aietcin (1990) based on their practical experiences. In 2004 Lim et al. used genetic algorithm for mix proportioning of HPC (Lim et al., 2004). In 1990 the Laboratory Central des Ponts et Chaussees presented a mix design for HPC with specified compressive strength and workability (de Larrard, 1990). Harilal et al. (2019) adopted IS 10262:2009 for green HPC mix design. The HPC mix design parameters are given in Fig. 8.2.

8.3 High performance green concrete

Concrete made up of using industrial waste materials, such as fly ash, slag, recycled aggregate, and crushed glass, without compromising workability, strength, and durability, is called high performance green concrete. The waste material can be added partially or fully to the replacement of aggregate or cement (Reiner et al., 2010). The 828 m tall Burj Khalifa was constructed using green HPC. The cement was partially replaced with fly ash at a level of 13%−20% and silica fume at the level of 5%−10% (Aldred, 2010).

8.3.1 Cement and supplementary cementitious materials

8.3.1.1 Cement

The use of ASTM Type I or II cement is recommended for conventional concrete. If high early strengths are required, Type III cement can be used. To prevent excess heat of hydration, the medium fineness cement may be preferable. For long-term strength, high C_2S content cement is desirable (Bergin et al., 2005). The total cementitious material for HPC will vary from 400 to 550 kg/m^3 (Neville & Aitcin, 1998).

8.3.1.2 Fly ash

Fly ash is an industrial by-product, and it is available in electric power generating plants. In the mid-1900s, fly ash was started to use as a supplementary cementitious material. The purpose of adding fly ash to cement is to improve the workability, pumpability, cohesiveness, ultimate strength, and durability. The approximate 10% of fly ash utilization in concrete will reduce the water content up to 3% (Thomas, 2007). Fly ash is a fine gray powder containing spherical glassy particles. The benefit of adding fly ash into concrete will reduce the mixing water and

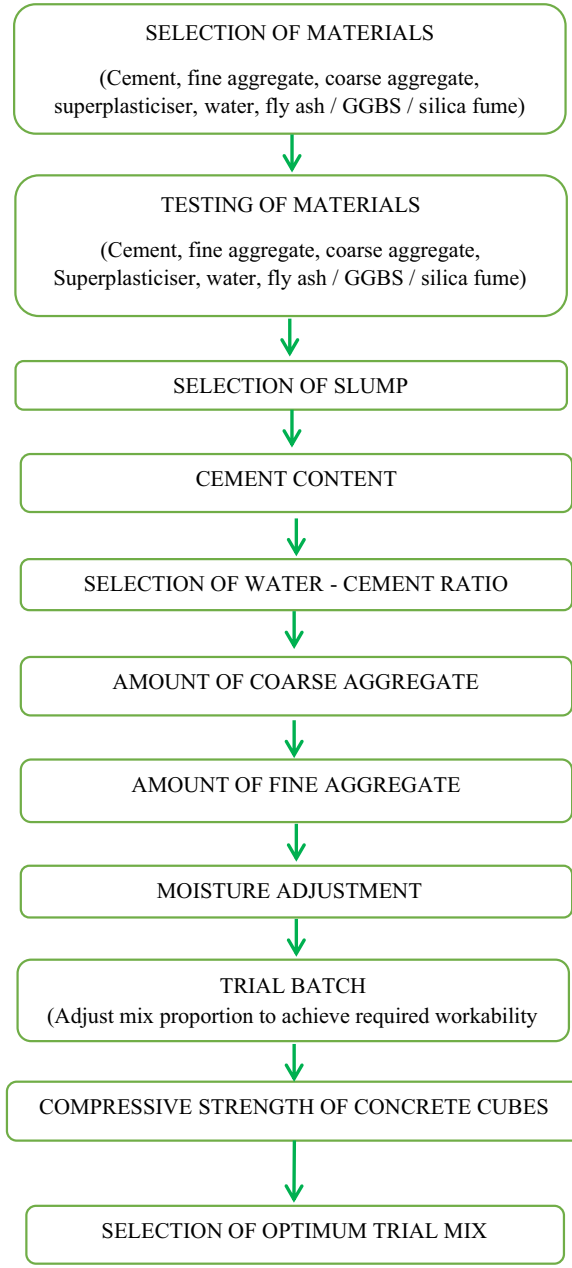

Figure 8.2 Mix proportioning factors for HPC.

improve the workability (Nath & Sarker, 2011). There are two types of fly ash available in power plants, namely, Class C type fly ash and Class F type fly ash. The main difference between Class F and Class C type of fly ash is based on its calcium content. Class F fly ash contains the calcium content less than 10% and Class C fly ash contains the calcium content more than 10% (ASTM C618−03, 2001). The chemical composition of both types of fly ashes is given in Table 8.1 (Wardhono, 2018).

The concrete manufactured using fly ash aggregate will be around 22% lighter, 20% stronger, and drying shrinkage will also be about 33% lesser than the concrete made with natural aggregate. Since the fly ash aggregates have higher durability, it can be used for manufacturing of HPC (Kayali, 2008).

8.3.1.3 Silica fume

Silica fume is also an industrial by-product from the electric arc furnaces (elemental silicon or alloys containing silicon). Silica fume is commonly used as a mineral admixture for the production of HPC due to its pozzolanic reactivity and physical filling effect. The optimum usage of silica fume is 15% in HPC as a cementitious material to increase the strength of concrete (Shannag, 2000).

8.3.1.4 Aggregates

Generally, to maintain the good bond between aggregate and cement paste, good-quality aggregate must be used. The aggregate must be clean, dust or mud should not adhere around the aggregate, and good grading is essential. Flaky and elongated aggregates should be avoided (Bergin et al., 2005; Neville & Aitcin, 1998; Neville, 1995).

8.3.1.5 Fine aggregate

Aggregate size which is less than 4.75 mm is called as fine aggregate. River sand and crushed rock are the most commonly used fine aggregate. In the total volume of concrete, 60%−75% is occupied by fine aggregate. The strength and durability

Table 8.1 The chemical composition of Class F and Class C type fly ash.

Components	Fly ash class F type (%) (Wardhono, 2018)	Fly ash class C type (%) (Wardhono, 2018)
SiO_2	65.43	4.75
Al_2O_3	23.14	17.89
Fe_2O_3	1.46	59.11
CaO	2.09	12.65
MgO	0.00	0.00
K_2O	1.04	0.65
TiO_2	1.35	0.92
Mn_2O_3	0.07	0.55
SO3	0.69	0.86

properties of concrete depend on various parameters like particle size distribution, silt content, fineness modulus, moisture content, and gravity (ACI Committee E-701, 2007). Fineness modulus of fine aggregate is preferably 2.60 and 3.10 for making HPC (Bergin et al., 2005).

8.3.1.6 Coarse aggregate

The size of aggregate larger than 4.75 mm is called as coarse aggregate. To ensure good compatibility, the size of the coarse aggregate must be less than 1 inch (Bergin et al., 2005). The size of coarse aggregate 1 or 3/4 inch was recommended for producing concrete strengths up to 62 MPa, and 1/2 or 3/8 inch size aggregate was recommended for producing concrete strengths above 62 MPa (ACI 211.4R-93, 1993). The 10 mm size of coarse aggregate is recommended for manufacturing high strength concrete (ACI Committee 363, 2010).

8.4 Role of superplasticizer in high performance green concrete

Water−cement ratio is one of the parameters deciding the strength of concrete. If more water is added to concrete than required, the concrete becomes more workable and strength will be reduced. If less water is added to a concrete than required, the concrete becomes difficult to work and strength will be increased. The chemical admixture known as superplasticizer is added to a concrete to obtain more workability with higher strength. Hattori (1979) reported, in 1960s both Japan and Germany used superplasticizer in concrete. Superplasticizer, also known as high range water reducers, is one of the ingredients of concrete and is added to the concrete immediately before or during mixing to produce HPC.

Superplasticizer is added to the concrete to decrease the water content up to the limit of 30%−50% and the optimum percentage is determined by trial and error method. The concrete curing process is also delayed by adding superplasticizers (Bye et al., 2011). In addition to HPC, the superplasticizer is used for manufacturing self-leveling, self-compacting concrete, and high strength concrete. When doing the mix design for HPC, choosing a suitable and efficient superplasticizer is also critical because not all the superplasticizer kinds and brands may respond the same way with cement. Melamine sulfonate, naphthalene sulfonate, lignosulfonate-based, and polyacrylates are the popular superplasticizers used for manufacturing HPC (El Hilal et al., 2018).

8.5 Mix proportion

Bharatkumar et al. studied the mix proportioning of HPC with 53 grade cement, coarse aggregate size less than 12.5 mm, fine aggregate size less than 4.75 mm, fineness modulus of fine aggregate was 2.48, sulfonated naphthalene formaldehyde

type superplasticizer was added, and fly ash type F was used. The cement content of 15% and 25% was replaced with fly ash. The compressive strength was achieved up to 79 MPa (Bharatkumar et al., 2001, 2005).

Sabet et al. utilized type II cement for manufacturing HPC. Fineness and specific gravity of cement values were 290 and 3.14 m^2/kg, respectively. The maximum size of coarse aggregate was 12.5 mm, specific gravity of 2.78, and water absorption of 0.84%. The fineness modulus of fine aggregate used was 2.68 with a specific gravity value of 2.7 and water absorption values of 2.8%. The specific gravity value of the superplasticizer used was (polycarboxylic acid-based) 1.07 and a solid content of 36% (Sabet et al., 2013).

Peter et al. studied the partially replaced cement with class F fly ash to produce HPC. Water to binder ratio was 0.3, fineness modulus and specific gravity of fine aggregate values were between 2.65 and 3.482. The fineness modulus and specific gravity values of coarse aggregate used were 2.71 and 6.91, respectively. The 28th day compressive strength of cement was 63.3 MPa (Peter et al., 1999). To provide durability against chemical attack, freeze and thaw reaction, alternative wetting and drying, and the maximum water to cement ratio for HPC suggested was 0.35. It also produces a discontinuous capillary system (Zia et al., 1991). Aitcin (1998) recommended the water/binder ratio and compressive strength for HPC as shown in Table 8.2. The various mix proportions of HPC are shown in Tables 8.3 and 8.4.

8.6 Strength development

The strength of concrete is influenced by several factors, including the quality/quantity of materials, rate of hydration, rate of loading, testing method, specimen shape, and age of the concrete. The features of the component materials include the fine and coarse aggregate quality, the cement paste, and the bond features which affect the strength. The component materials and curing processes influence the strength growth over time (Bye et al., 2011). Aitcin (1998) has classified HPC into five categories as shown in Table 8.5. The water−cement ratio and corresponding compressive strength are shown in Fig. 8.3, as given in Bharatkumar et al. (2005), Peter et al. (1999), Sabet et al. (2013), and Harilal et al. (2019). It is clearly evident that when the water−cement ratio is low, the strength will be higher.

Table 8.2 Water/binder ratio and compressive strength for high performance concrete (Aitcin, 1998).

Water/binder ratio	Maximum compressive strength range (MPa)
0.4−0.35	50−75
0.35−0.3	75−100
0.3−0.25	100−125
0.25−0.20	< 125

Source: From Aitcin, P. C. (1998). *High-performance concrete*. E & FN SPON.

Table 8.3 Mix proportion of high performance green concrete.

Component	Bharatkumar et al. (2001)							Bharatkumar et al. (2005)	
	C2	**AF15**	**AF25**	**BF15**	**BF25**	**CF15**	**CF25**	**F.0.40**	**F0.36**
Cement (kg/m^3)	454	289	255	345	304	413	365	323	354
Fly ash (kg/m^3)	80	51	85	60	101	73	121	107	118
Fine aggregate (kg/m^3)	1848	800	787	742	726	652	631	754	710
Coarse aggregate (kg/m^3)		1054	1054	1054	1054	1054	1054	1018	1018
Water (kg/m^3)	160	170	170	170	170	170	170	172	172
Superplasticizer (% binder)	2.5	0.6	0.7	0.65	0.85	0.6	0.75	0.75	0.75
28 days compressive strength (MPa)	89.5	35.28	33.53	54.8	53.39	72.06	65.58	54.73	60.17

Table 8.4 Mix proportion of high performance green concrete.

	Peter et al. (1999)				Sabet et al. (2013)		Harilal et al. (2019)
Component	C2	C3	C4	C5	F10	F20	CF
Cement (kg/m^3)	454	428	401	374	450	400	270
Fly ash (kg/m^3)	80	106	135	160	50	100	180
Fine aggregate (kg/m^3)	1848	1848	1848	1848	966	948	744
Coarse aggregate (kg/m^3)					656	656	1017
Water (kg/m^3)	160	160	160	160	160	160	171
Superplasticizer (% binder)	2.5	2.5	2.5	2.5	1.1	0.8	0
28 days compressive strength (MPa)	89.5	87.4	85.2	75.2	67	80.5	48.4

Table 8.5 Classification of high performance concrete (Aitcin, 1998).

High performance class	**I**	**II**	**III**	**IV**	**V**
Compressive strength (MPa)	50–75	75–100	100–125	125–150	Higher than 150

Source: From Aitcin, P. C. (1998). *High-performance concrete*. E & FN SPON.

Strength improvement of any concrete is continuously associated with the release of heat and an amount of the solid volume concentration, and vice versa. Aitcin (1998) schematically explained in the form of the "Bermuda Triangle," as shown in Fig. 8.4.

8.7 Transporting and placing of high performance green concrete

Improper transportation of HPC from batching plant to construction site will affect the performance of concrete. The main difficulty faced during HPC transportation in truck is slump loss and aggregate segregation. If an unexpected delay happened due to traffic congestion or any other issue on the site, a small dosage of a retarder may be added to maintain the slump. HPC has been placed in the formwork using any one of the methods, like pumping, using a crane bucket, ropeway, and conveyor belts. After placing concrete, the entrapped air must be removed by vibration.

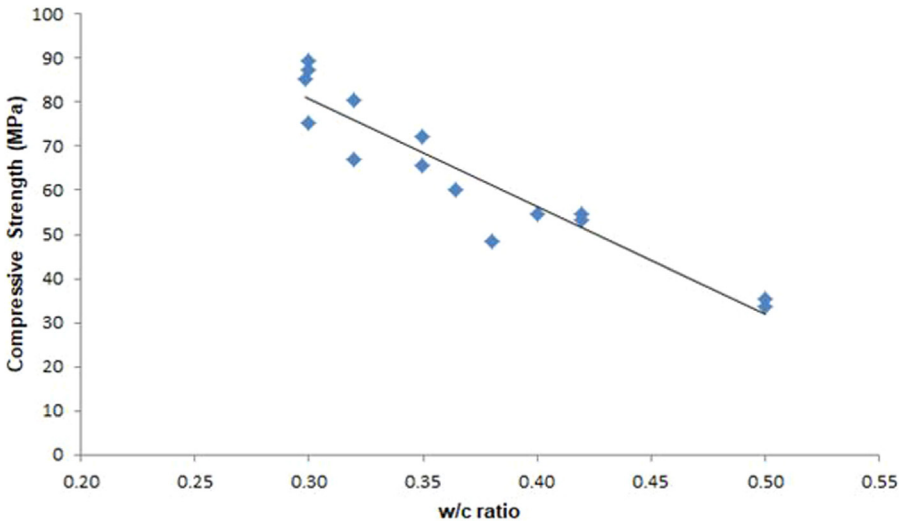

Figure 8.3 Water to cementitious material ratio and strength of high performance concrete (Bharatkumar et al., 2001, 2005; Harilal et al., 2019; Sabet et al., 2013; Peter et al., 1999).

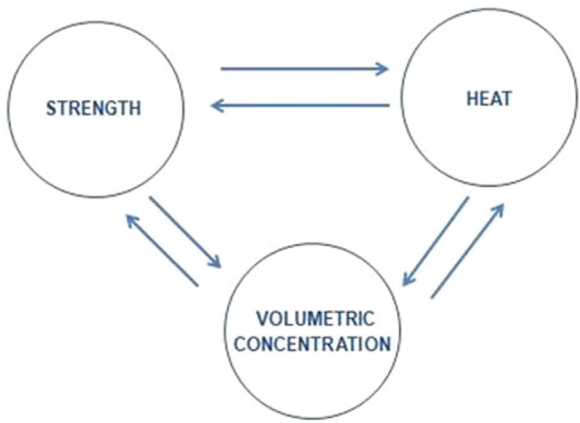

Figure 8.4 The "Bermuda Triangle" of concrete (Aitcin, 1998).

8.8 Curing of high performance green concrete

To complete the hydration process, HPC must be cured properly. The improper curing affects the strength and durability properties. The various methods of curing adopted at the sites are sprinkling of water, membrane curing, ponding, steam curing, and by using concrete curing compounds.

8.9 Conclusion

The utilization of fly ash or any mineral admixtures in HPC leads to reduction of the release of carbon dioxide during the manufacture of cement, cement saving from concrete, and energy saving during manufacturing of cement, and the concrete will become as green concrete. The strength and durability of high performance green concrete depends on the selection of cement, the selection of aggregates, the selection of superplasticizer dosage, mix design, trail mixes, transportation, pumping, compacting, and vibration of concrete. High performance green concrete consists of industrial wastes such as fly ash, silica fumes, slag, recycled aggregates, and ground glass. The quality of fine and coarse aggregates, the cement paste, and the bond between aggregate and cement paste will also affect the strength of HPC.

The ultimate aim of the usage of high performance green concrete is to reduce carbon dioxide in the atmosphere and also to make economical concrete. The current research works reveal that the use of fly ash, silica fume, or any mineral admixtures in cement concrete will enhance the mechanical and durability properties of HPC. This chapter also summarized the various mix proportions of HPC developed by various researchers.

References

Aitcin, P. C. (1998). *High-performance concrete*. E & FN SPON.

Aldred, J. (2010). Burj Khalifa – A new high for high-performance concrete. *Proceedings of the Institution of Civil Engineers - Civil Engineering*, *163*(2), 66–73. Available from https://doi.org/10.1680/cien.2010.163.2.66.

ACI Committee 363. (2010). Report on high-strength concrete (ACI 363R-10). American Concrete Institute.

ACI Committee E-701. (2007). Aggregates for concrete. ACI education bulletin E1–07, materials for concrete construction. American Concrete Institute.

ACI 211.4R-93. (1993). Guide for selecting proportions for high-strength concrete with portland cement and fly ash. American Concrete Institute.

ASTM C618-03. (2001). Standard specification for coal fly ash and raw or calcined natural pozzolan for use in concrete. ASTM International.

Bergin, M., Mullarky, J., & Ozyildirim, C. (2005). High performance concrete (HPC) mix design and proportioning. *High Performance Concrete Structural Designers Guide*, 35–48.

Bharatkumar, B. H., Narayanan, R., Raghuprasad, B. K., & Ramachandramurthy, D. S. (2001). Mix proportioning of high performance concrete. *Cement and Concrete Composites*, *23*(1), 71–80. Available from https://doi.org/10.1016/S0958-9465(00)00071-8.

Bharatkumar, B. H., Raghuprasad, B. K., Ramachandramurthy, D. S., Narayanan, R., & Gopalakrishnan, S. (2005). Effect of fly ash and slag on the fracture characteristics of high performance concrete. *Materials and Structures*, *38*(1), 63–72. Available from https://doi.org/10.1007/bf02480576.

Bye, G., Livesey, P., & Struble, L. (2011). ICE Publishing (pp. 185–195).

de Larrard, F. (1990). Method for proportioning high-strength concrete mixtures. *Cement, Concrete and Aggregates*, *12*(1), 47−52. Available from https://doi.org/10.1520/cca10388j.

Edward, G., & Nawy. (2000). *Fundamentals of high-performance concrete*. Wiley.

El Hilal, B., Khudhair, M. H., & Harfi, A. (2018). Review on different families of polymeric superplasticizers used as adjuvants in the cementitious materials in civil engineering. *Applied Journal Environmental Engineering Science*, *4*, 158−170.

Harilal, M., Rathish, V. R., Anandkumar, B., George, R. P., Mohammed, M. S. H. S., Philip, J., & Amarendra, G. (2019). High performance green concrete (HPGC) with improved strength and chloride ion penetration resistance by synergistic action of fly ash, nanoparticles and corrosion inhibitor. *Construction and Building Materials*, *198*, 299−312. Available from https://doi.org/10.1016/j.conbuildmat.2018.11.266.

Hattori, K. (1979). Experiences with mighty superplasticizer in Japan. American Concrete Institute, ACI Special Publication 01932527 (pp. 37−66). https://www.concrete.org/topicsinconcrete/topicdetail/special%20publicationSP-062.

Kayali, O. (2008). Fly ash lightweight aggregates in high performance concrete. *Construction and Building Materials*, *22*(12), 2393−2399. Available from https://doi.org/10.1016/j.conbuildmat.2007.09.001.

Leung, C. K. Y. (2001). *Concrete as a building material* (pp. 1471−1479). Elsevier BV. Available from http://doi.org/10.1016/b0-08-043152-6/00267-9.

Lim, C. H., Yoon, Y. S., & Kim, J. H. (2004). Genetic algorithm in mix proportioning of high-performance concrete. *Cement and Concrete Research*, *34*(3), 409−420. Available from https://doi.org/10.1016/j.cemconres.2003.08.018.

Mehta, P. K., & Aietcin, P. C. C. (1990). Principles underlying production of high-performance concrete. *Cement, Concrete and Aggregates*, *12*(2), 70−78. Available from https://doi.org/10.1520/CCA10274J.

Nath, P., & Sarker, P. (2011). Effect of fly ash on the durability properties of high strength concrete. *Procedia Engineering*, *14*, 1149−1156. Available from http://doi.org/10.1016/j.proeng.2011.07.144, 18777058.

Neville, A., & Aitcin, P. C. (1998). High performance concrete − An overview. *Materials and Structures*, *31*, 111−117.

Neville, A. M. (1995). *Properties of concrete* (5th ed.). Pearson.

Nielsen, C. V., & Glavind, M. (2007). Danish experiences with a decade of green concrete. *Journal of Advanced Concrete Technology*, *5*(1), 3−12. Available from https://doi.org/10.3151/jact.5.3.

Obla, K. H. (2009). What is green concrete? *Indian Concrete Journal*, *83*(4), 26−28. Available from http://www.icjonline.com/journals/2009_04_POV_KH_Obla.pdf.

Peter, J. A., Neelamegam, M., Dattatreya, J. K., Rajamane, N. P., & Gopalakrishnan, S. (1999). *Utilisation of fly ash as cement replacement material to produce high performance concrete. Fly ash utilisation, NML, Jamshedpur* (pp. 38−49).

Reiner, M., Durham, S. A., & Rens, K. L. (2010). Development and analysis of high-performance green concrete in the urban infrastructure. *International Journal of Sustainable Engineering*, *3*(3), 198−210. Available from https://doi.org/10.1080/19397031003746662.

Sabet, F. A., Libre, N. A., & Shekarchi, M. (2013). Mechanical and durability properties of self consolidating high performance concrete incorporating natural zeolite, silica fume and fly ash. *Construction and Building Materials*, *44*, 175−184. Available from https://doi.org/10.1016/j.conbuildmat.2013.02.069.

Shannag, M. J. (2000). High strength concrete containing natural pozzolan and silica fume. *Cement and Concrete Composites*, *22*(6), 399−406. Available from https://doi.org/10.1016/S0958-9465(00)00037-8.

Suhendro, B. (2014). Toward green concrete for better sustainable environment. *Procedia Engineering*, *95*, 305−320. Available from https://doi.org/10.1016/j.proeng.2014.12.190.

Thomas, M. (2007). Concrete optimizing the use of fly ash in concrete. *Portland Cement Association*, *5420*, 1−24.

Wardhono, A. (2018). Comparison study of class F and class C fly ashes as cement replacement material on strength development of non-cement mortar. *IOP Conference Series: Materials Science and Engineering*, *288*. Available from https://doi.org/10.1088/1757-899X/288/1/012019.

Zhang, H., Zou, K., Ji, X., Zhang, C., Tang, F., & Wu, X. (2015). *Mixture design methods for high performance concrete: A review*. *5th International conference on advanced engineering materials and technology (AEMT 2015)* (pp. 647−653). AEMT. Available from https://www.atlantis-press.com/article/25839291.pdf.

Zia, P.M. L., Shuaib, L., & Ahmad, H. (1991). Strategic highway research program high performance concretes a state-of-the-art report.

Engineering green concrete for sustainable infrastructure

9

Nagesh R. Iyer[1,2]
[1]Indian National Academy of Engineering, New Delhi, India, [2]Department of Civil & Infrastructure Engineering, IIT Dharwad, Dharwad, Karnataka, India

9.1 Introduction

The impact of construction materials on the environment and sustainability is a significant issue that needs to be addressed by the construction industry. The extraction, production, transportation, utilization, and recycling of construction materials can have negative effects on the environment, such as carbon emissions, deforestation, and pollution. The use of reinforced concrete, in particular, has been linked to environmental degradation and an increase in carbon footprint due to the high consumption of cement. One of the major challenges facing the civil engineers of today is to preserve, maintain, and or retrofit these structures (Iyer, 2020).

The degradation of infrastructure, such as reinforced concrete structures, is another issue that affects the environment, sustainability, and security of the built environment. These structures can suffer from degradation due to various factors, including deicing salts, freeze-thaw cycles, and increased live loads or altered function from its original design. Civil engineers face the challenge of preserving, maintaining, and retrofitting these structures to ensure their longevity and safety.

To reduce the negative impact of construction materials on the environment, sustainability, and security of the built environment, it is crucial to adopt sustainable practices in the construction industry. This includes using environmentally friendly materials, reducing carbon emissions, and promoting recycling and reuse of construction materials. By adopting sustainable practices, the construction industry can contribute to economic growth and prosperity while minimizing its impact on the environment.

This chapter presents significance and benefits of the development, use, and deployment of Green Concrete in the construction of physical infrastructure. One of the major contributions of Green Concrete is creation of a sustainable infrastructure while reducing the carbonization in the habitat significantly. Further, the use of Green Concrete in such large-scale infrastructure creation entails substantial reduction in use and thereby enhances savings of natural resources. The materials that are proposed to replace fully or partially the cementitious part in cement concrete are essentially not only eco-friendly but also produced with low amount of energy and have low embodied energy.

Green Materials in Civil Engineering. DOI: https://doi.org/10.1016/B978-0-443-19106-0.00009-9

Since last few decades, there has been considerable concern among the construction industries, users, and the other stakeholders who have been attempting to find reliable and acceptable scientific ways to address the following four key concerns:

1. the emission of CO_2 during the production of cement
2. finding a way to put to productive use of large amount of waste being generated either organic/agricultural or the by-products from the industry
3. uncontrollable use of natural resources for construction purposes and
4. intensive use of energy in producing construction materials

It is certainly a matter of concern that the cement and concrete industry consumes such a large amount of natural aggregates each year. The extraction of these aggregates can have a significant impact on the environment, including soil erosion, habitat destruction, and water pollution.

The use of alternate materials that are durable and sustainable is a promising solution to address this issue. By using waste and recycled materials instead of raw materials, the construction industry can reduce its impact on the environment and move toward a more sustainable future. This shift toward a more circular economy approach can also create new business opportunities and generate economic benefits.

The use of ordinary Portland cement (OPC) is also a significant contributor to the industry's environmental impact, as it is an energy-intensive material associated with large amounts of CO_2 emissions. Stricter regulations and proactive actions by major cement manufacturers are positive steps toward reducing emissions levels, and the experimentation with alternative fuels, such as biomass and waste-derived fuels, can further help reduce the carbon footprint of the industry.

In nutshell, the concrete industry must continue to work toward a more sustainable and environmentally responsible approach to material use, energy consumption, and waste generation. This includes investing in research and development to explore new materials and techniques that can improve the sustainability of the industry, as well as working collaboratively with stakeholders to ensure that sustainability considerations are integrated into all aspects of the construction process.

9.1.1 Concrete and green concrete

The historical development of concrete has indeed undergone several stages. The first stage is the traditional normal strength concrete (NSC), which is made up of cement, water, fine aggregates, and coarse aggregates. NSC has been widely used for various construction purposes, but for large-scale civil engineering projects such as high-rise buildings and long-span bridges, higher compressive strength concrete is necessary.

To achieve higher compressive strength, reducing the water-to-cement ratio is one approach, which can be achieved by adding water-reducing agents or superplasticizers (SP) to the mix. Additionally, admixtures and additives such as silica fume, fly ash, and blast furnace slag are commonly used to improve the properties of high-performance concrete (HPC).

With the growing concern for sustainability and the environment, the use of waste materials in the production of HPC has become increasingly popular. This practice is known as green high-performance concrete (GHPC). GHPC not only reduces the environmental impact of concrete production but also improves its mechanical properties, durability, and long-term performance.

In summary, the development of concrete has progressed from traditional NSC to higher compressive strength concrete and now to GHPC. The use of waste materials in GHPC production represents a more sustainable and environmentally friendly option for the construction industry (Ahmed et al., 2019; Iyer, 2020; Iyer et al., 2013; Munch-Petersen, 2000).

Ultrahigh-strength concrete (UHSC) has great potential in a wide range of engineering applications due to its high compressive strength, which can exceed 100 MPa, and its high tensile strength, which is achieved by embedding short steel fibers in the matrix. The use of steel fibers in UHSC improves its toughness and deformability, making it less brittle and more resistant to cracking.

In recent years, even higher strength UHSC with compressive strength exceeding 140 MPa has been successfully developed. The use of such high strength concrete can offer benefits in a range of applications, including blast shelters, impact-resistant structures, nuclear structures, skyscrapers, corrosion-proof structures, and pavements. However, the production of UHSC is resource-intensive and can have a high environmental impact, and its use should be balanced with sustainability considerations.

Concrete that uses less in energy in its production and produces less carbon dioxide than normal concrete is Green Concrete. In the year 1998, Green Concrete was first developed in Denmark (Munch-Petersen, 2000). Green Concrete is also loosely called/defined as Special Concretes or Engineered Concrete or Ultra High Performance Concrete or RCA Concrete (recycled concrete aggregates) or GCC (geopolymer concrete) offering enhanced engineering properties replacing cement or natural sand or aggregates either fully or partially. Production of such concrete is expected to meet at least one or more of the following criteria in addition to addressing the four concerns expressed in the above:

1. Reduction of CO_2 emissions
2. Reduction in energy and fuel consumption
3. Saving up on nonrenewable energy and material resources

There has been significant research since the late 1970s to address concerns related to the environmental impact of construction materials, particularly with regards to reducing greenhouse gas (GHG) emissions. The Kyoto Protocol, which entered into force in 2005, committed industrialized countries to limit and reduce GHG emissions in accordance with agreed individual targets.

The use of supplementary cementitious materials (SCMs) like fly ash, ground slag, rice husk ash, and metakaolin is a promising way to reduce the carbon footprint of concrete. SCMs can replace a portion of the OPC content in concrete, thereby reducing the overall carbon footprint of the material. Additionally, the use of SCMs can enhance the durability of concrete, which is essential for sustainability.

Blended cements, which incorporate the right type and quality of SCM, can help to further reduce the environmental impact of concrete. Optimizing the use of cement by carefully selecting the mix proportioning and using appropriate construction chemicals to reduce the water-to-cement ratio is also important for producing dense and durable concrete.

In India, there is still a significant use of volume batching for manufacturing "normal" concrete of grades M20 and M25. However, with the proper use of SCMs and other sustainable practices, concrete can be a highly sustainable material that can last for many years if it is manufactured, transported, cast, and cured properly.

9.1.2 Proportioning

Concrete is a heterogeneous composite material that relies heavily on the properties and quantity of its constituent phases. Mix design is an essential tool used in all aspects of concrete technology, with the primary objective being to achieve the desired functional properties at the lowest cost, while considering environmental factors and planned production techniques. Effective mix design methods are thus critical in ensuring sustainable industrial concrete construction practices. A good concrete mix should produce strong and durable concrete, which can be achieved by carefully proportioning and mixing the ingredients. The success of a concrete mix depends on how the voids are filled and packed; otherwise, it can result in rough, honeycombed surfaces and porous concrete products. Concrete is the most widely used building material, thanks to its versatility, ease of access to raw materials, low cost, ease of fabrication, high mechanical strength, impermeability to water, and exceptional durability. As a result, the infrastructure construction industry is the largest consumer of limited natural resources like sand, crushed granite, and water.

Achieving an optimal workability of concrete is crucial for obtaining the desired durability and strength of the hardened mix. A mix with excessive cement paste may be easy to place and create a smooth surface but could lead to greater shrinkage and be cost-ineffective. The quality of the paste, which is the strength of the paste governed by the water-to-cement ratio, is a key factor in achieving this optimal mix. The water-to-cement ratio is determined by dividing the weight of the mixing water by the weight of the cement, and the ideal mix typically consists of 10%−15% cement, 60%−75% aggregate, 15%−20% water, and 5%−8% trapped air. Vibration of the mix is often used to eliminate voids, resulting in high-quality concrete. Each material constituent, including cement, aggregate, and water, has a significant engineering influence on the overall mix. Let us briefly examine each material constituent and its engineering influence on this "magic" mix.

9.1.3 Key ingredients

Concrete is a compound material made up of different components that are held together by cement. "Cement" in general can be defined as any material which has the property to bind together different materials through different reactions. The

binding property of cement is achieved through chemical reactions, which are facilitated by water. A wealth of information is available in textbooks, standards, technical papers, and other sources about cement, the different types of cement, and the various reactions that occur during the process of gaining strength.

9.1.4 Other ingredients

The size and type of aggregate mixture used in concrete depends on the intended application or purpose, as well as the geometry of the structure. It is recommended to use natural water without impurities that is pH neutral or not acidic, as impurities can have negative effects on the setting time and strength of the concrete. Specifications usually set limits on various substances such as chlorides, sulfates, alkalis, and solids in the mixing water, unless tests can be performed to determine their effect on the concrete properties. Small coarse aggregate is suitable for relatively thin building sections, while large dams have used aggregates up to 150 mm (six inches) in diameter. A continuous gradation of particle sizes is preferred for efficient use of the paste, and the aggregates should be clean and free from any matter that might affect the quality of the concrete.

9.1.5 Hydration

The process of hydration, which is the chemical reaction between water and cement, is what causes the concrete to harden and gain strength over time. The mixture is placed into formwork and compacted to remove any air voids, ensuring a dense and durable final product. Technologies, instruments, and tools are used to achieve smooth surface and desirable outcome with precision. Curing is then done to maintain the required moisture content for the ongoing hydration process, which results in the continued gain of strength and stiffness of the concrete. There are various methods of curing, such as normal curing in open bath chamber, thermal curing, alternative cycles of curing, spraying water or covering the surface with plastic sheeting to prevent moisture loss. As the concrete ages, it will continue to gain strength and improve in durability.

9.1.6 Aggregates

Aggregates play a crucial role in determining the strength and mass of concrete. They are generally classified as coarse aggregates and fine aggregates, with fine aggregates typically being less than 4.75 mm in size and coarse aggregates greater than 4.75 mm. Indian standard (IS 383, 1970) outlines specifications for aggregates from natural sources used in making concrete.

Grading of aggregates is important to obtain good concrete. Aggregates can be classified as uniformly graded, well graded, or gap/poorly graded based on particle size distribution. It is recommended to use well-graded aggregates since concrete produced with them will have minimum voids.

When selecting fine aggregates, it is important to choose those with low silt content and free from organic materials to ensure high-quality concrete.

9.1.7 Fine aggregates

The use of natural river sand is widespread in the construction industry as it is currently the most suitable material for fine aggregates. However, the high demand for sand has caused a supply−demand gap, resulting in the excessive exploitation of river beds, depletion of natural resources, and various environmental issues. As a result, there is an urgent need to find alternative materials for river sand in construction.

9.1.8 Coarse aggregates

Coarse aggregates are a crucial component of concrete and make up the majority of its volume. In India, crushed granite is the most commonly used material, but other stones such as limestone, basalt, and igneous rocks can also be suitable. It is essential that the stones used as coarse aggregates are strong and resistant to environmental factors as they provide the majority of the strength in a concrete mix. While broken bricks can be used in some cases, caution should be exercised when using such materials. Stones with high water absorption capacity such as shale and pumice should be avoided as they can lead to excessive cracking in the concrete. The other ingredients of concrete are discussed separately in different chapters.

9.1.9 Reinforcing bars

Concrete is a material that is strong in compression but weak in tension. It is commonly used in applications where the primary stresses are compressive, but this is not always the case. To address this weakness in tension, steel reinforcement is often used. Steel is equally strong in both tension and compression, making it an ideal material for reinforcing concrete. However, steel is more expensive than concrete, so it is not used as the only building material. Instead, it is incorporated into concrete in the form of reinforcing bars, or rebars. The amount of rebars used is determined by the design and is sufficient to withstand any tensile force that the concrete is subjected to before it fails.

9.2 Engineering green concrete strategies for sustainability

Generally, construction of infrastructure and the practices adopted has been driven by economic considerations whereas sustainability considerations demand use of best practices toward long-term affordability, durability, effectiveness, and recyclability driven by life cycle assessment of the final product. Therefore the four key

concerns as stated in Section 9.1 and the brief details provided in the previous sections drive us to explore possibility of alternate sources of construction materials, or those materials that have been produced with lower energy demand levels. These alternate sources can be considered as full or partial replacement of the conventional construction materials. The purpose is to establish using engineering principles: (1) minimizing environmental impact; (2) achieving overall economic savings considering the total life cycle of the infrastructure; and (3) reduce greenhouse effects in construction. This logically extends to setting up of criteria to consider (a) materials replacing (partially or fully) cement, (b) materials replacing aggregate, (c) materials replacing cement and aggregates, and (d) materials forming ternary systems for concrete. We examine each of the criteria and efficacy of the same.

9.2.1 Materials replacing cement

The materials that substitute cement either in part or in full and are used in the production of concrete or other cementitious products qualify to be known as cement replacement materials (CRMs). The basic attribute for this qualification is to possess pozzolanic property. In this context, the industrial and agricultural wastes have been found to be highly effective and shown enhanced engineering performance meeting the sustainability criteria.

One can broadly classify these into two categories, namely: (1) industrial/traditional waste/by-products and (2) agricultural/nontraditional waste. Under traditional or industrial waste materials known to have been used are:

1. [pulverized] Fly ash (FA)
2. Ground granulated blast furnace slag (GGBS)
3. Silica fume (SF)
4. Limestone fines

Whereas some of the well-known agricultural waste materials pursued by researchers are the following:

1. Rice husk ash (RHA)
2. Palm oil fuel ash (POFA)
3. Palm oil clinker aggregate (POCA)
4. Metakaolin (MK)
5. Sipozz
6. Sugarcane bagasse/bagasse ash (BA)

In addition to the above, there are several other potential cementitious materials that can be used as replacements for traditional materials, but they require further testing, validation, and acceptance before widespread use can be established. Some of the most commonly used industrial CRMs, such as pulverized FA, GGBS, and SF, are well-established replacement options. Limestone fines are also added to Portland cement to create composite or combination cement, but there is uncertainty over whether they should be classified as Type I or Type II additions due to their reactivity and particle size.

In contrast, agricultural and nontraditional waste materials, such as POFA, POCA, RHA, and MK, require proven testing and recognition from the construction industry before they can be considered as viable replacements for traditional materials. While these materials can be used to partially replace OPC, their replacement levels are influenced by factors such as particle size, shape, and limiting oxygen index (LOI) which determines flammability. Therefore it is essential to verify the physical properties as well as the chemical composition of these materials.

Heat treatment of POFA in a furnace can reduce the LOI and increase the silica content, resulting in higher strength mortar compared to untreated POFA. Additionally, grinding POCA and BA particles to a higher number of cycles in a grinding machine can increase the fineness of these materials, leading to improved packing ability and increased pozzolanic reaction due to the larger surface area. While other potential cementitious materials exist, discussion and technical details on limestone fines and agricultural waste are not presented in this context due to the scope of the discussion.

9.2.1.1 Fly ash

FA is the most voluminous and well-known form of coal combustion residue, generated from thermal power plants. It is collected using multifield electro-static precipitators (ESPs) installed at the exhaust of power plants, in which the lighter forms of FA are collected from the upper stacks, and the coarser varieties from the lower stacks of ESPs. FA is typically classified as either siliceous pulverized fuel FA or calcareous pulverized fuel FA (which are also known as Class F FA or Class C FA, respectively, as per ASTM Standard C618, based on their chemical composition) (Fig. 9.1). The siliceous FA is produced from burning of anthracite or bituminous coal and typically contains less than 10% CaO, while the calcareous FA is produced by burning of lignite or subbituminous coal and typically contains more than 10% CaO. The major delimiter for this classification is the sum of silica, aluminum, and iron oxide percentages in the FA, being a minimum of 70% for siliceous FA, and a minimum of 50% for calcareous FA. The siliceous FA possesses pozzolanic properties and the calcareous FA possesses both pozzolanic and hydraulic properties.

On combustion, Indian coal yields high amounts of ash, in the order of 30%–45%. The annual generation of FA in India is about 270 million tons (Ministry of Power, Govt. of India, 2022). The chemical composition of Indian fly ashes from different power plants is presented in Table 9.1. It can be noted that the prime variety of FA available in India is siliceous FA. However, the utilization of FA is not significant yet, especially in the top FA-generating countries, that is, India and China. The developed countries, on the other hand, depend mainly on nuclear fuel for generation of electricity, and hence these countries generate lesser amounts of FA. The utilization of FA in those countries is also larger, owing to their stringent pollution control laws and better utilization technologies (Maiti & Prasad, 2016).

The FA has acquired a status of “useful waste” from the position of “hazardous industrial waste” after the launch of Fly Ash Mission in 1994. However, some recent statistics on FA utilization by Central Electricity Authority shows that, for

Figure 9.1 Fly ash.

the year 2021−22, the utilization of FA in India was 95.95%, of its generation which is encouraging. Fig. 9.2 presents various modes of FA utilization in India. However, keeping in view the hazardous effects of airborne FA, containing coarser and finer particulate matters (PM10 and PM2.5) as well as toxic metals, which can contaminate air, water, and soil, eventually causing health hazards such as skin irritations, respiratory issues, lung diseases, or cancer (Lockwood et al., 2015), its utilization in unencapsulated applications such as reclamation of low lying areas, mine filling, ash dyke raising, agriculture cannot be considered as safe. Hence, it is essential to consider employing this material in encapsulated usages such as in cement concrete. FA has acquired an important role in production of Portland Pozzolana Cement (PPC). The permitted quantity of FA as per IS 1489 Part I (IS 1489−1, 1991) in blended cements is 10%−25%. Also, as per the IS 456 (IS 456, 2000) and IRC 112 (IRC, 2020), 20%−35% of FA can be added as admixture to structural concrete made with OPC to improve its performance. However, as noted from Fig. 9.2, its utilization in OPC-based concrete as mineral admixture is only minimal.

The general requirements of siliceous FA for use in concrete as specified by various standards are given in Table 9.2. It is widely known that the reactivity of fly ashes is dependent on their glassy (amorphous) SiO_2 content and other mineral phases present, in addition to their particle size. It was reported that the finer FA (with particle size below 10 μm) displays higher pozzolanicity and is suitable for use in higher amounts in cementitious matrix (Chatterjee, 2011). However, it has been observed that the Indian fly ashes are less amorphous and coarser than those obtained in other countries (Chatterjee, 2011; Fournier et al., 2004). Also, the maximum volume of fly ashes collected in power plants is generally from the lower stacks of ESPs, which are highly coarser and less reactive when used as a mineral admixture in concrete, as compared to those collected from upper stacks of ESPs. Indian fly ashes collected from lower stacks of ESPs are classified as unprocessed (coarser) FA (when 64% of which retained on 10 μm sieve, 49% retained on 20 μm

Table 9.1 Chemical composition of Indian fly ashes (Chandra, 2008).

Power stations	Fly ash compounds (%)									
	SiO_2	Al_2O_3	Fe_2O_3	TiO_2	MnO	MgO	CaO	K_2O	Na_2O_3	LOI
Badarpur, Delhi	57.4	31.8	4.62	1.65	0.21	0.23	0.62	0.59	0.23	2.7
Dadri, Uttar Pradesh	52.7	37.8	3.41	0.90	–	0.24	1.00	0.66	0.14	3.0
Rihand, Uttar Pradesh	59.7	34.1	6.10	0.50	0.4	0.35	0.20	0.45	0.30	0.5
Unchahar, Uttar Pradesh	59.6	30.6	4.20	1.50	0.1	0.40	0.90	0.70	0.20	–
Korba, Chhattisgarh	62.1	31.3	3.33	1.82	–	0.01	0.03	0.04	0.09	1.2
Vindhyanchal, Uttar Pradesh	62.9	27.1	6.12	1.10	–	0.10	0.80	0.27	0.10	1.5
Ramagundam, Telangana	60.8	26.6	4.19	1.13	0.08	0.80	3.03	0.90	0.40	1.8
Vijayawada, Andhra Pradesh	61.6	30.9	3.33	1.72	–	0.05	1.11	0.61	0.13	0.4
Neyveli, Tamil Nadu	38.0	43.4	4.05	1.82	10.12	0.02	7.67	0.05	0.43	3.4
Kahalgoan, Bihar	60.4	30.1	5.62	1.81	–	0.40	0.80	0.56	0.12	0.2
Farakka, West Bengal	60.3	30.9	5.02	1.30	–	0.60	0.90	0.50	0.15	0.3

Source: From Chandra, A. (2009). *Some investigations on fly ash resistivity generated in Indian power plants* (pp. 399–405). Springer Science and Business Media LLC. https://doi.org/10.1007/978-3-540-89251-9_81.

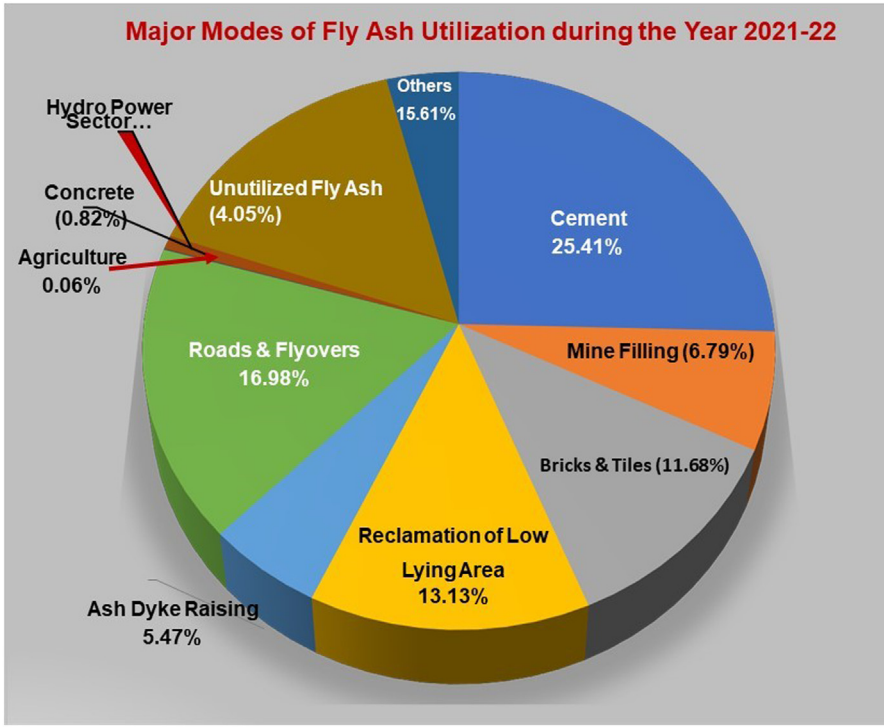

Figure 9.2 Major mode of fly ash utilization in India FY2021−22 (Ministry of Power, Govt. of India, 2022).
Source: From Ministry of Power, Govt. of India. (2022). Report on fly ash generation at coal / lignite based thermal power stations and its utilization in the country for the year 2021 − 22, Central Electricity Authority, Civil Design Division.

sieve, and 24% retained on 45 μm size [by volume of FA]), and such fly ashes are generally not used in higher amounts in concrete. This eventually leads to a need for processing of such fly ashes through mechanical or chemical methods to obtain a finer FA with particle size down to 10 μm, before using the same in concrete.

The FIRST building constructed in India and one of the very few in the world was in 1974. This building was opened on June 2, 1974. The building was constructed at the CSIR-Structural Engineering Research Centre (SERC), Chennai, using FA as partial replacement for cement in the precast channel units and in situ concrete beams, and also in cement mortar for construction of masonry walls (Fig. 9.3).

Durability properties of fly ash concrete

Durability studies of cracked structural members cast using structural grade FACC and the conventional ordinary Portland cement concretes (OPCCs) and having

Table 9.2 Specifications of siliceous fly ash for use in concrete.

Parameters	**ASTM C618 (ASTM C618–19, 2019)**	**EN 450–1 (BS EN 15167–1, 2006)**	**IS 3812 Part II (Ghutke & Bhandari, 2014)**
SiO_2, min (%)	–	–	35
Reactive SiO_2, min (%)	–	25	20
$SiO_2 + Al_2O_3 + Fe_2O_3$, min (%)	70	–	70
Total chloride, max (%)	–	0.1	0.05
Loss on ignition, max (%)	6	5	5
Sulfur trioxide SO_3, max (%)	5	3	3
Residue on 45 μm, max (%)	34	40	34
Blaine's specific surface area, min (m^2/kg)	–	–	320
Soundness, max	0.8%	10 mm	0.8%
Compressive strength at 28 days, corresponding to that of a plain cement mortar cube, min (%)	75 (at 7 or 28 days)	75 (at 28 days) 85 (at 90 days)	80 (at 28 days)

Figure 9.3 A view of first fly ash building built in India at CSIR-SERC, Chennai.

embedded steel reinforcement, subjected to accelerated corrosion under chloride and CO_2 exposures in the laboratory indicated several benefits such as:

- Reduction of carbon footprint.
- FA can be used as partial replacement of cement or as filler material in concrete.

- Use of FA aggregate lead to lightweight concrete.
- Use of FA improves durability of concrete structures due to its pozzolanic property.
- Effective use of waste located at different power stations leading solution of the problem of waste disposal.
- Use of FA bricks and blocks reduces the use of burnt clay bricks leading to sustainable development.
- Lower cost–benefit ratio leads to sizable saving in the construction cost of civil infrastructure development (huge saving for the country).

High volume fly ash concrete

Investigations on high volume fly ash concrete (HVFAC; 50%) also carried out to evaluate the strength and durability characteristics of concrete matrix. Table 9.3 gives the concrete mixture proportions and Table 9.4 gives the mechanical and durability properties of the control and HVFAC. It is seen for Table 9.4 that HVFAC, designed for the same 28-day compressive strength of OPC (control)-based concrete, lags behind OPC-based concrete in compressive strength up to the age of 7 days. The strength values were almost similar at the age of 28 days and it exhibited higher strength at later ages. Also the HVFAC showed very low chloride permeability and reduced water permeability compared to that of OPC-based concrete. These properties improved further for HVFAC with increase in age of the concrete.

The sorptivity values for the concrete mixtures investigated are in the range of 1.90×10^{-6} to 4.74×10^{-6} m/$\sqrt{s}$. It is seen that there is a reduction in the values of sorptivity as w/b ratio decreases. The concrete mixtures with 20% FA also showed a reduction in the value of sorptivity, but the mixtures with 40% FA showed slightly higher values when compared to OPC mixtures. The sorptivity values of those mixtures, which contain higher FA content, may improve with age with increase in the pozzolanic reactivity, which may lead to refinement of pore structure.

It was concluded that by judicious choice of water-to-binder ratio and use of mineral admixtures conforming to standards, it is possible to produce durable

Table 9.3 Concrete mixture proportions.

Materials	Quantity (kg/m^3)	
	OPCC	HVFAC
Cement	300	210
Fly ash	–	210
Sand	806	718
Coarse aggregate 20–12.5 mm	790	712
Coarse aggregate 12.5–4.75 mm	328	305
Water	165	175
Superplasticizer (sulfonated) naphthalene formaldehyde	2.7 L	3.36 L
Water–cement (w/c) ratio	0.55	0.38
Slump	100 mm	150 mm

Table 9.4 Properties of concrete mixtures.

Properties	Age at testing/curing period (day)	OPCC	HVFAC
Compressive strength (MPa)	1	12.11	6.65
	3	26.00	16.64
	7	31.04	25.73
	28	42.65	44.72
	56	45.17	50.07
	90	47.73	54.29
Rapid chloride permeability (Coulombs)	28	2819	341
	56	2489	257
	90	2198	189
Water permeability($\times 10^{11}$ m/s)	28	8.63	7.50
	56	6.08	5.14
	90	3.43	2.34

concretes having the desired rate of strength development. Use of mineral admixture-based concrete, besides ensuring long-term durability of concrete structures would also bring in economy and sustainability in concrete constructions in the country. Further, significant savings on use of cement (OPC), which consumes considerable energy in its production, could be realized by adopting mineral admixtures in concrete mixtures. Some enlightened users have already been adopting mineral admixture-based concrete for various special structures and during the next decade there will certainly be a high rise in the use of mineral admixture-based concrete in India. The outcome of the test results proves that FA concrete if produced properly can be as good as or even better than normal OPC-based concrete.

The use of FA as a partial substitute for cement has several notable features. Firstly, the idea of replacing cement partially with FA was introduced toward sustainable development as early as 1972−73. Secondly, the addition of FA to concrete increases its compressive strength, tensile strength, and flexural strength. It also enhances resistance to alkali aggregate reactions and slows down the ingress of moisture, oxygen, chloride, carbon dioxide, and aggressive chemicals, thereby preventing corrosion.

However, there are some disadvantages to using FA, such as a lower rate of strength gain, increased air entraining, and increased slump loss. Nonetheless, effective utilization of FA, which is a waste material posing huge challenges of disposal by coal-based power generation industries, can lead to a significant reduction in the use of cement. This reduction is important because every ton of cement produced generates an equivalent ton of CO_2, posing significant environmental challenges.

Bond behavior has been studied for "OPC" and OPC with FA (OPF) concretes with different water-to-binder ratios. Pull-out test specimens have been cast as per IS 2770 (Part I) (Roy & Sil, 2012). At initial slips, nearly a linear relationship between load and slip exists from 60% to 70% of the ultimate load for both the specimens of "OPC" and "OPF" concretes. The experimental results showed that for the selective raw materials and mix proportions, the bond strength of the FA

concrete corresponding to 0.025 mm slip is 10%−15% lower to that of OPC concrete. The reduction in bond strength is slightly lower at 0.25 mm slip compared to that at 0.025 mm lip (Table 9.5). This may be due to the fact that, although the friction component is less, the radial pressure component of the bond is greater since FA increases the tensile strength compared to "OPC" concrete and hence the resistance of the cover to splitting improves. This will provide a partial compensation for the reduction in bond strength due to the loss of friction.

9.2.1.2 Ground granulated blast furnace slag

Ground granulated blast-furnace slag, also known as GGBS (Fig. 9.4), is obtained from molten iron slag which is a by-product of iron and steel-making. Blast furnace

Table 9.5 Bond stress—slip values of "OPC" series.

Mix	28 days average cube compressive strength (MPa)	Bond stress (MPa)	
		0.025 mm	0.25 mm
OPC1	25.9	10.60	12.68
OPC2	41.3	13.52	16.32
OPC3	58.8	15.17	21.20
OPF1	24.1	9.20	11.44
OPF2	40.2	12.00	14.70
OPF3	58.0	13.60	19.20

Figure 9.4 Ground granulated blast furnace slag (GGBS).

slags is produced as by-product during iron production. Iron ore, as well as scrap iron, is reduced to a molten state by burning coke fuel with fluxing agents of limestone or dolomite. The molten slag from the furnace is rapidly chilled by quenching in water to form a glassy sand-like material. GGBS is produced by grinding the granulated slag to less than 45 μm size to obtain a fineness of 400−600 m^2/kg (Iyer, 2020). Table 9.6 gives the physical properties of GGBS used in the study. Table 9.7 gives the chemical composition of GGBS used in the study.

It is interesting to note that GGBS concrete has been tested for durability in harsh environments such as exposure to silage effluent solution and magnesium sulfate solution, and has shown promising results. The decrease in permeability, water absorption, capillary suction, mass loss, and compressive strength loss in GGBS concrete when exposed to such conditions is a positive outcome. This indicates that using GGBS as a partial replacement for cement in concrete mixtures can result in a more durable concrete, which could be very beneficial for agricultural applications such as silos. It is exciting to see how sustainable building materials can be tailored to specific applications and environments.

9.2.1.3 Silica fume

In addition to its pozzolanic properties, SF also improves the workability of concrete by acting as a lubricant, reduces bleeding and segregation, and increases the cohesion of the mix. Due to its fine particle size, SF can also help reduce the permeability of concrete, making it more resistant to the ingress of harmful substances such as chlorides and sulfates. This makes it a useful material in the construction of structures exposed to harsh environmental conditions such as marine structures and bridges.

However, the use of SF in concrete also has some drawbacks. The high reactivity of SF can cause rapid setting of concrete, making it challenging for construction work that requires more time to place and finish the concrete. The addition of SF

Table 9.6 Physical properties of ground granulated blast furnace slag (GGBS).

Sl. no.	Descriptions	GGBS
1	Fineness (Sq.m/kg)	400
2	Specific gravity	2.9
3	Glass content (min 67%) (BS EN 15167−1, 2006)	85
4	Loss on ignition (%)	2.1

Table 9.7 Chemical composition of ground granulated blast furnace slag (GGBS).

Specific gravity	Chemical composition						
CaO	SiO_2	Al_2O_3	Na_2O	K_2O	MgO	LOI	
2.91	40.3	43.4	12.5	0.9	0.6	1.5	2.1

can also increase the cost of concrete due to its relatively high price compared to other cementitious materials.

It is interesting to note that the optimum replacement percentage of cement with SF varies between 10% and 15% under Indian conditions, as observed by Ghutke and Bhandari (2014). It is also good to know that SF can improve the performance of concrete in terms of strength, workability, and durability. The study by Roy and Sil (2012) showed that 10% replacement of cement with SF gave the maximum compressive strength and also gave significant increases in tensile and flexural strength. Moreover, adding SF can increase the compressive strength and bond strength of concrete and make it suitable for construction places where chemical attack and frost action are common. Amudhavalli and Mathew (2012) found that the optimum compressive and flexural strength was obtained in the range of 10%–15% replacement of cement by silica, while Pradhan and Dutta (2013) observed that the optimum compressive strength was observed when 20% of cement was replaced by SF. Finally, Shanmugapriya and Uma (2013) concluded that 7.5% SF by weight was inferred to be the optimum dosage for maximum performance of concrete. Compressive strength increased by 15%, tensile strength increased by 20%, and flexural strength increased by 23%.

9.2.2 Materials replacing aggregate

Construction waste materials and industrial waste materials can be utilized in concrete as replacements for coarse and fine aggregates, respectively. For coarse aggregates, materials such as demolished building pieces, bricks, and stone pieces can be used. These materials can perform well when used in concrete, and broken bricks are already being used as a weatherproofing material on terraces.

In the case of fine aggregates, industrial waste materials like quarry dust, glass powder, ceramic dust, and coal dust can be used. The chemical composition of quarry dust is similar to that of granite rock, making it a suitable replacement for fine aggregates in concrete. When used in concrete, the strength and durability of quarry dust are good, resulting in high compressive strength. Similarly, crushed glass particles can be partially used instead of granite rock in concrete, but it may decrease workability and compressive strength, making it more suitable for use in filler areas like deck slabs.

Another material that can be used in concrete is plastic waste. When the plastic material is clean and free from dust or other impurities, it can be mixed with concrete to enhance its workability. Plastic aggregates are mostly used in road construction, where they are mixed with asphalt. Recycling plastic waste into construction materials is an effective way to reduce waste and make use of a material that would otherwise end up in landfills.

Overall, using waste materials in concrete has many benefits, including reducing waste, lowering costs, and enhancing the properties of the resulting concrete.

Advantages of such aggregate replacement materials/constituents are that they are (1) eco-friendly, (2) they reduce waste material dump, (3) reduce usage of natural resources and (4) economical products. However, the demerits are (1) more

material tests are needed, (2) strength of the structure may reduce, and (3) more maintenance work may become necessary to enhance the life of a structure. Generally, the replacement range varies from 20% to 40% depending on the material substitute chosen and its engineering attributes/properties and the overall matrix characteristics.

Notwithstanding the above, FA has been found to be an excellent substitute candidate here too. FA has been very successfully used in the development of aggregates for lightweight structural concretes. Due to depletion of natural resources and restrictions imposed on quarrying operations from ecological considerations, it necessitated a search for alternative synthetic coarse and fine aggregates. Industrial by-products, such as FA, which otherwise pose severe disposal problems, has been gainfully utilized for this purpose. Cement-bonded FA aggregates (4−20 mm size) were developed by palletization (Fig. 9.5A and B) at CSIR-SERC, India and their performance in concrete mixtures was studied in comparison with commercially available sintered FA aggregates and found to be satisfactory (Fig. 9.5C). Typical structural grade concrete mixes M25 to M35 were developed and tested for characteristic mechanical and durability properties. The structural performance of laboratory scale RC beams was also found to be satisfactory. The studies show that FA aggregates could be used for lightweight structural concrete members.

9.2.3 Materials replacing cement and aggregates

One way to reduce the environmental impact of concrete is to partially replace cement with other cementitious materials and/or replace mineral aggregates with renewable ones. Several studies have investigated the effects of such replacements on the density, compressive strength, and split tensile strength of concrete. For example, researchers have looked at the effects of replacing 10%, 20%, and 30% of cement with FA and replacing 20% of mineral aggregates with aggregates made from industrial waste.

Experimental investigations have shown that increasing the amount of FA used for cement replacement results in a decrease in concrete density. However, combining FA with waste aggregates has a positive effect on reducing the concrete density after 28 days of curing. While FA leads to a decrease in concrete compressive strength, it can improve the splitting tensile strength of the concrete when used in volumes of 10% and 20% for cement replacement. Despite registering lower values for mechanical properties, concretes with FA are still appropriate for structural use. Furthermore, their lower density compared to traditional concrete can result in lighter structures, which can have a positive impact on seismic building behavior. Concrete mixtures that incorporate FA and industrial waste are classified as lightweight concretes, making them suitable for nonstructural purposes such as closures, wall finishes, and concrete screeds. Materials such as red mud, pumice, rice husk, manufactured sand or M-sand, slag sand, powdered glass, FA, quarry dust, processed crushed rock fines, mersey silt, sugarcane BA, groundnut shell, cork, tobacco waste can also be considered as substitute aggregate constituents. However, it is cautioned that the mix, proportion of such matrix has to be carefully

(A)

(B)

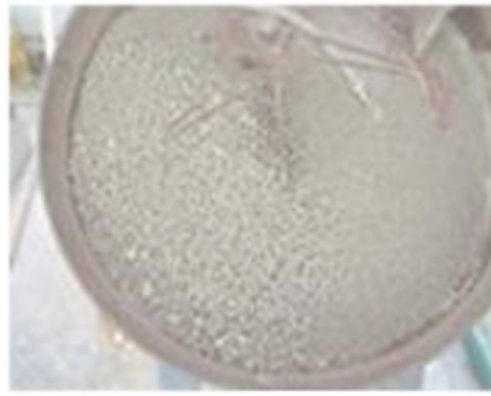

(C)

Figure 9.5 (A) Fly ash palletization. (B) Fly ash aggregate of different sizes. (C) Typical failure through aggregates.

determined through various tests and more particularly reproducibility of results under different conditions when cement is also being partially replaced.

9.2.4 Materials forming ternary systems for concrete

A ternary mixture is one that contains Portland cement and two other materials in the binder, blended either at the cement plant or at the batch plant. Ternary compounds are composed of three or more elements. Ternary compounds are named by stating the cation first, followed by the anion. Positive and negative charges must balance. The materials included may be interground limestone or SCMs such as slag cement, FA, SF, or MK. A ternary solution is a mixture of three components (either two solvents and one solute or one solvent and two solutes). Ternary ionic compounds are sodium nitrate, sodium hypochlorite, sodium chlorite, sodium chlorate, sodium perchlorate, ammonium chloride, iron (III) hydroxide, etc.

Taylor (2014) provides a table that provides useful information on the side effects and interactions of the SCMs. This is presented in Fig. 9.6.

9.3 Engineered concretes

As stated earlier, concrete is a composite product formed out of different material constituents by standardizing the mix matrix to achieve the desirable and required engineering attributes. The very fact that the matrix mix is made up of different constituents, it permits one to experiment either with new materials or replace partially or fully materials that provide desirable engineering attributes and the different tests can be used to assess its suitability as to its durability and sustainability. Some of these have been now developed and established over the years. These are (1) HPC, (2) UHSC, (3) geopolymer concrete (GPC), and (4) recycled concrete aggregates. However, these are suitable for limited or well-defined applications. These concretes are observed to offer enhanced engineering properties while replacing cement or sand or aggregates either fully or partially or has addition of another material constituent. One of the key objectives of development or engineering of such concretes has been to find its application in the development of sustainable infrastructure with (1) enhanced engineering properties, (2) reducing the use of natural resources, (3) uses waste materials including industrial by-products, and (4) reduces the overall cost. Some of these engineered concretes are briefly described.

9.3.1 High-performance concrete

Concrete which meets special performance and uniformity requirements that cannot always be achieved routinely using only conventional materials and normal mixing, placing, and curing practices. Again, here one looks at durability and sustainability aspects while replacing or reducing dependence on the natural resources to the

Properties	Supplementary Cementitious Material					
	Class F Fly Ash	Class C Fly Ash	Slag Cement	Silica Fume	Metakaolin	Limestone
Workability	Significantly improved	Improved	Neutral / Improved	Improved at low dose (<5%), decreased at high dose	Decreased	Slightly improved
Air void system	May be difficult to entrain air with high LOI	Neutral	Neutral	May be difficult to entrain air	May be difficult to entrain air	Neutral
Setting	Delayed	Slightly delayed	Slightly delayed	Accelerated	Neutral	Neutral
Incompatibility	Low risk	Some risk	Low risk	Low risk	Low risk	Low risk
Strength gain	Slower but continues longer	Slightly slower but continues longer	Slightly slower but continues longer	Accelerated initially	Accelerated initially	Neutral
Stiffness	(Related to strength)					
Heat generation	Lower	Slightly lower	Slightly lower	Higher	Slightly higher	Slightly lower
Shrinkage	Neutral	Reduced	Neutral	Increased	Increased	Neutral
Permeability	Improved over time	Improved over time	Improved over time	Improved	Improved	Neutral
ASR	Improved	Improved at sufficient dosage	Improved at high dosages	Slightly improved	Improved	Neutral
Sulfate attack	Improved	Improved at sufficient dosage	Improved at high dosages	Neutral	Neutral	May be worse at high dosages in very cold environments
Corrosion Resistance	Slightly improved	Slightly improved	Improved	Improved	Improved	Neutral

Figure 9.6 Side effects and interactions of the supplementary cementitious materials (SCMs).
Source: From Taylor, P. (2014). The use of ternary mixtures in concrete. *Trans Project Reports*, 74. (Original work published 2014).

extent possible. The requirements may involve enhancement of characteristics such as age, strength, toughness, volume stability, or service life in severe environments. The ingredients that are employed in the development of this concrete are as follows:

1. Conventional ingredients: cement, sand, aggregate, water
2. Mineral admixtures
3. Pozzolanas: SF, FA, high reactivity MK, RHA
4. Cementitious materials: GGBS
5. Inert fines: limestone powder, silica flour
6. Chemical admixtures
7. SP: sulfonated naphthalene formaldehyde
8. Sulfonated melamine formaldehyde

Properties of concrete mixtures made with GGBS as SCM at different CRM levels varying from 20% to 70% were studied and the results are presented below. The chemical composition of GGBS used in the investigation are as shown in Table 9.8, whereas Table 9.9 presents the compressive strengths for different mixes with GGBS.

Table 9.8 Chemical composition of ground granulated blast furnace slag (GGBS).

Compound	Requirement of BS:6699–1992	Properties of slag used in the study
SiO_2	–	32.6
Al_2O_3	–	12.8
Fe_2O_3	–	1.3
CaO	–	41.0
MgO	14	7.2
CaO/SiO_2	Max. 1.4	1.22
(CaO–MgO) SiO_2	Min. 1.0	1.48
Na_2O, K_2O		2.6
SO_3	2.5	0.03
LOI	3.0	0.2
Glass content	67%	85%

Note: fineness: 330 m2/kg.

Table 9.9 Compressive strength of ground granulated blast furnace slag (GGBS)-based concrete mixtures.

Mixture designation	CRM (%)	Compressive strength, σ_c, MPa		
		3 Days	7 Days	28 Days
M-0S	0	63.2	83.5	93.7
M-20S	20	53.9	81.5	93.5
M-30S	30	52.5	77.7	95.0
M-50S	50	46.8	74.3	90.8
M-70S	70	39.2	69.8	87.6

Fig. 9.7 presents the performance of pore size against cumulative intrusion for different mixes. Figs. 9.8 and 9.9 are the mix matrices of different mix compositions as mentioned. Table 9.10 provides the details of micro structures that are arrived at based on Figs. 9.8 and 9.9.

9.3.2 *Ultrahigh-performance concrete (Ambily et al., 2015; Iyer et al., 2013; Prem et al., 2012)*

There is an increasing focus on evaluating the carbon emissions (embodied energy) associated with the production and use of new concrete types. With the development of advanced technologies in construction and the demand for high-performance materials, ultrahigh-performance concrete (UHPC) has emerged as a highly durable and strong material, which can exhibit high ductility when reinforced with steel fibers or tubes. However, current methods of producing UHPC typically require expensive materials and advanced technologies, which can

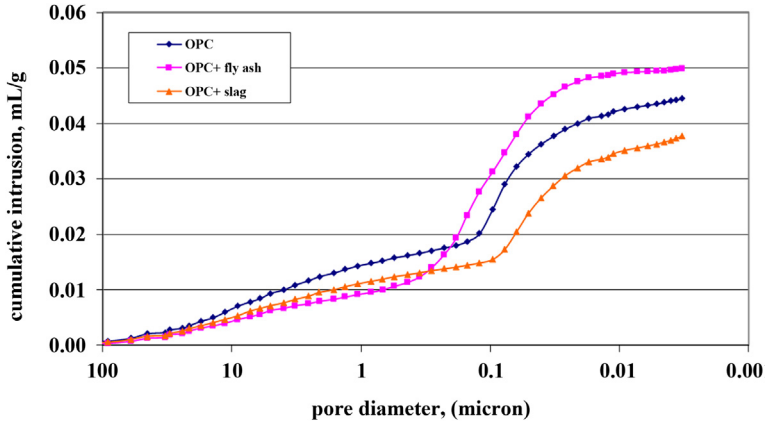

Figure 9.7 Cumulative intrusion versus pore size w/c = 0.36 and 28 days curing.

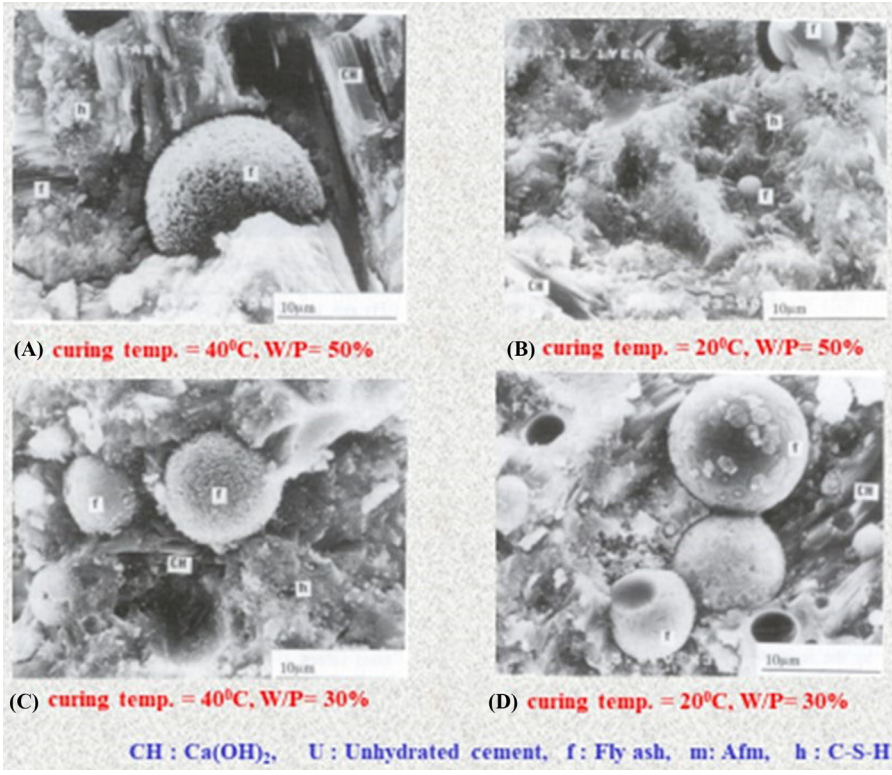

Figure 9.8 XRD of mix.

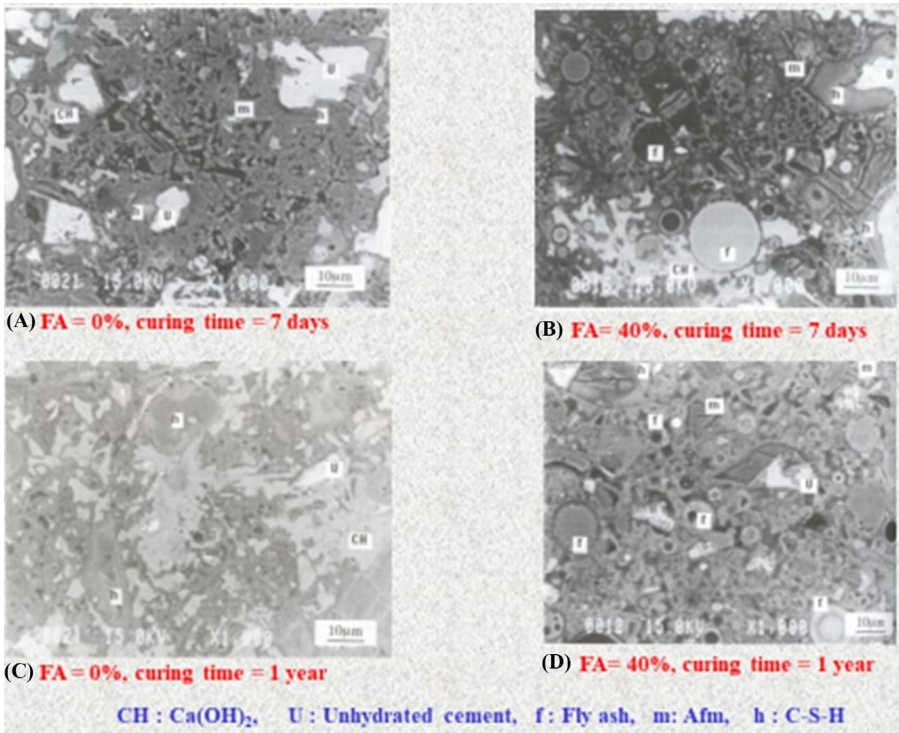

Figure 9.9 XRD of mix matrix with and without fly ash.

Table 9.10 Micro-structure related properties of ground granulated blast furnace slag (GGBS)-based concrete mixtures.

Property	Mixture designation				
	M-0S	M-20S	M-30S	M-50S	M-70S
CRM (%)	0	20	30	50	70
Saturated water absorption, %	3.10	2.38	2.17	1.80	1.85
Porosity, η (%)	7.89	5.92	5.35	4.48	4.55
Coefficient of water absorption $\times 10^{-10}$ m^2/s	1.36	1.13	0.63	0.36	0.32
Modified sorptivity $\times 10^{-10}$ $m/\sqrt{s}$	9.04	8.00	6.58	5.03	4.91
Chloride diffusivity ($\times 10^{-12}$ m^2/s) under 12V DC	0.204	0.128	0.104	0.076	0.084
Chloride permeability (ASTM equivalent) Coulombs	670	416	338	237	273

contribute to a high level of embodied energy. This is not conducive to sustainable development and a green environment. Therefore there is a need to explore more environmentally friendly approaches to producing UHPC. In the following, a specific case study is presented that provides the enhancement in engineering properties of concrete wherein two types of UHPC are considered, one with local sand (standard sand) as aggregate system and the other with complete replacement of standard sand with copper slag as aggregate. The intent of providing the following study is to show that there are many candidates that can qualify as Green Concretes that are engineered for replacement, either partial or full, of aggregate. However, an elaborate study to arrive at acceptable procedure is of paramount importance keeping durability and sustainability aspects in mind. One can look at GGBS and other similar industrial by-products (IBPs) as possible candidates that have been mentioned in the earlier part of this chapter. Other examples being GPCs, steel fiber-reinforced concrete, textile-reinforced concrete, fiber-reinforced polymer composites, recycled concrete aggregates, and so on. One may refer Iyer (2020) for more technical details.

9.3.2.1 Ultrahigh-performance concrete constituents

In this study, the researchers used a variety of materials to create UHPC, which is known for its exceptional strength. The key constituents included Portland cement, SF, quartz powder, fine aggregate, copper slag, steel fibers, SP, and water.

To enhance the strength of the UHPC, the researchers used 53 grade OPC, which meets IS: 12269: 1987 (IS 12269, 1987) and the American Standard ASTM C 150/ Type I. They also used densified SF, which conforms to the American Standard ASTM C 1240−97 (ASTM C, 1998) and has a specific gravity of 2.2.

The researchers used quartz powder with a specific gravity and particle size between 5 and 25 μm to optimize the UHPC's properties. Ennore sand (ES), a standard sand per IS 650−1991 (IS 650, 1991) with a specific gravity of 2.65, was used as the fine aggregate. Since no coarse aggregate was introduced into the mix, the sand contributed the largest particle size in the granular mixture.

Copper slag was also used, which was obtained from Sterlite Industries Ltd., Tuticorin. The steel fibers used in the study were straight brass-coated steel fibers, with a diameter of 0.16 mm and a length of 13 mm, having tensile strength of around 2000 MPa.

For mixing and curing, the researchers used ordinary tap water. Finally, a poly acrylic ester-based high-range wate -reducer (HRWR-Glenium 8045) was used as the SP to optimize the UHPC's workability and reduce water content. Overall, the combination of these materials contributed to the exceptional strength of the UHPC.

9.3.2.2 Physical and chemical properties of copper slag

The copper slag is a black glassy particle and granular in nature and has a similar particle size range like sand. The bulk density of granulated copper slag is varying

from 1.9 to 2.15 g/cc. The free moisture content present in the copper slag was found to be less than 0.5% and the presence of silica is about 26%, which is desirable since it is one of the constituents of the natural fine aggregate used in normal concreting operations. Table 9.11 shows the physical properties of copper slag. The specific gravity and water absorption for copper slag and sand were determined as per IS 2386 Part 3 (IS 2386, 2012). The higher specific gravity of copper slag compared to conventional sand results in production of UHPC with higher density, when used as sand substitution. Due to the low water absorption of copper slag would demand less water than that required by sand in the concrete mix. Therefore it is expected that the free water content in concrete matrix will increase as the copper slag content increases which consequently will lead to increase in the workability of the concrete. Copper slag of different grades was prepared by sieving (similar to standard sand [ES] that grade I: 2−1 mm, grade II: 1−0.5 mm, grade III: 0.5−0.09 mm).

Fig. 9.10 shows the sieve analysis of copper slag done as per IS 383−1970. The fineness modulus was found to be 3.43.

9.3.2.3 Chemical composition of copper slag

Copper slag samples were analyzed for constituent oxides including minor oxides and heavy elements besides mineral phases. The results of chemical analysis are shown in Table 9.12.

9.3.2.4 Optimization of granular materials

Advanced technologies such as UHPC require a specific granulometric composition that reduces the void fraction in the dry mixture, resulting in a harder and less porous concrete. By optimizing the granular material, the number of trial mixes

Table 9.11 Physical properties of copper slag.

Physical properties	Copper slag
Particle shape	Irregular
Appearance	Black and glassy
Type	Air cooled
Specific gravity	3.37
Percentage of voids	43.20%
Bulk density	2.08 g/cc
Fineness modulus	3.43
Water absorption	0.3%−0.4%
Moisture content	0.1%

Source: From Ambily, P. S., Umarani, C., Ravisankar, K., Prem, P. R., Bharatkumar, B. H., & Iyer, N. R. (2015). Studies on ultra high performance concrete incorporating copper slag as fine aggregate. *Construction and Building Materials*, *77*, 233−240. https://doi.org/10.1016/j.conbuildmat.2014.12.092.

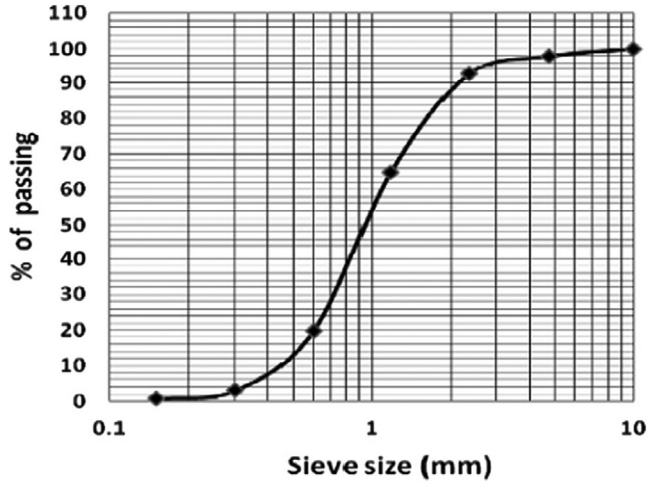

Figure 9.10 Sieve analysis of copper slag.
Source: From Ambily, P. S., Umarani, C., Ravisankar, K., Prem, P. R., Bharatkumar, B. H., & Iyer, N. R. (2015). Studies on ultra high performance concrete incorporating copper slag as fine aggregate. *Construction and Building Materials*, *77*, 233–240. https://doi.org/10.1016/j.conbuildmat.2014.12.092.

Table 9.12 Chemical properties of copper slag.

Sl. no.	Chemical component	% of chemical component
1	SiO_2	25.84
2	Fe_2O_3	68.29
3	Al_2O_3	0.22
4	CaO	0.15
5	Na_2O	0.58
6	K_2O	0.23
7	LoI	6.59
8	Mn_2O_3	0.22
9	TiO_2	0.41
10	SO_3	0.11
11	CuO	1.20
12	Sulfide sulfur	0.25
13	Insoluble residue	14.88
14	Chloride	0.018

Source: From Ambily, P. S., Umarani, C., Ravisankar, K., Prem, P. R., Bharatkumar, B. H., & Iyer, N. R. (2015). Studies on ultra high performance concrete incorporating copper slag as fine aggregate. *Construction and Building Materials*, *77*, 233–240. https://doi.org/10.1016/j.conbuildmat.2014.12.092.

required can be reduced, and the combination of graded materials that provides maximum packing density can be determined. This, in turn, leads to the maximum compressive strength of the mix when combined with the binder.

To obtain an optimal packing density (PD) for copper slag (CS), the material was separated into three grades similar to standard sand size fractions—grade 1 (G1) coarse, grade 2 (G2) medium, and grade 3 (G3) fine. Particle packing was carried out by varying the percentage of CS in three combinations—G1 and G2, G2 and G3, and G3 and G1. For each combination, packing was performed using three methods: loose (shoveling), tamped (rodding), and vibration (using a vibration table), as per ASTM C 29−09 (ASTM C29/C29M-09, 2016).

Ternary combinations were prepared for selected percentages of G1, G2, and G3. The PD of the unitary sand or CS was determined initially, followed by the PD of binary combinations (G1G2, G2G3, and G1G3). Based on the results of unitary and binary packing, the optimal compaction method was selected (vibration-VPD), and ternary combinations were prepared using G1, G2, and G3 in selected percentage combinations (G1G2G3). The details of the optimum packing densities for unitary, binary, and ternary combinations are given in Table 9.13.

From the packing studies, it was found that the maximum PD was achieved with vibration packing. The binary packing densities of standard sand and CS, which gave optimal packing, are shown in Figs. 9.11 and 9.12. CS of grade 1 and grade 3 combinations provided the maximum density. Based on the packing density, binary and ternary combinations that provided maximum packing densities were selected for trial mix preparation.

Five trial mixes were carried out using standard sand and CS for each combination. Two trial mixes were done without fibers, that is, G1 (40%), G3 (60%), and G1 (33%), G2 (30%), G3 (37%). Three other trial mixes were done with fibers, that is, G1 (50%) G3 (50%), G1 (60%) G3 (40%), and G1 (70%) G3 (30%).

9.3.2.5 Mix composition

To achieve the desired mix for UHPC, a total of five different mix proportions were tried using both ES and CS, labeled as 1E-5E and 1C-5C, respectively. CS

Table 9.13 Optimum packing densities of ennore sand (ES) and copper slag (CS).

Packing	Material	% Combination	VPD
Unitary	G1 (ES)	100	0.612
Unitary	G2 (CS)	100	0.641
Binary	G1G2 (ES)	70−30	0.639
Binary	G1G2 (CS)	30−70	0.649
Binary	G2G3 (ES)	20−80	0.637
Binary	G2G3 (CS)	30−70	0.671
Binary	G1G3 (ES)	60−40	0.672
Binary	G1G3 (CS)	70−30	0.683
Ternary	G1G2G3 (ES)	33−30−37	0.670
Ternary	G1G2G3 (CS)	33−30−37	0.680

Source: From Ambily, P. S., Umarani, C., Ravisankar, K., Prem, P. R., Bharatkumar, B. H., & Iyer, N. R. (2015). Studies on ultra high performance concrete incorporating copper slag as fine aggregate. *Construction and Building Materials*, *77*, 233−240. https://doi.org/10.1016/j.conbuildmat.2014.12.092.

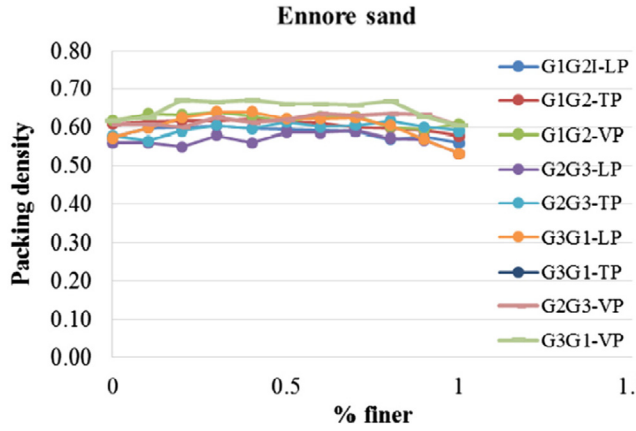

Figure 9.11 Binary packing densities of ennore sand (ES).
Source: From Ambily, P. S., Umarani, C., Ravisankar, K., Prem, P. R., Bharatkumar, B. H., & Iyer, N. R. (2015). Studies on ultra high performance concrete incorporating copper slag as fine aggregate. *Construction and Building Materials*, *77*, 233−240. https://doi.org/10.1016/j.conbuildmat.2014.12.092.

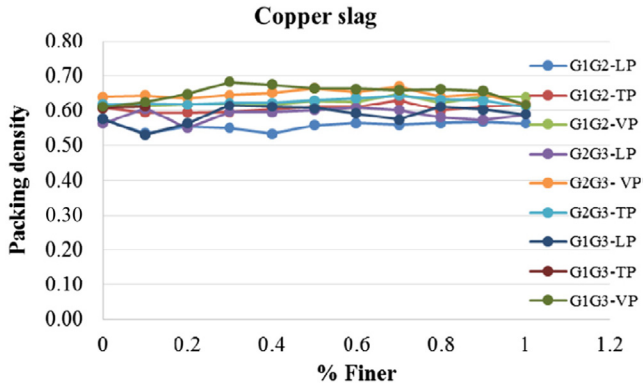

Figure 9.12 Binary packing densities of copper slag (CS).
Source: From Ambily, P. S., Umarani, C., Ravisankar, K., Prem, P. R., Bharatkumar, B. H., & Iyer, N. R. (2015). Studies on ultra high performance concrete incorporating copper slag as fine aggregate. *Construction and Building Materials*, *77*, 233−240. https://doi.org/10.1016/j.conbuildmat.2014.12.092.

was used as a complete replacement for fine aggregate, comprising 100% of the mixture. In order to enhance the PD and pozzolanic properties of the cementitious system, 25% and 40% by weight of cement dosage of SF and quartz powder were used, respectively. A water-to-cement (w/c) ratio of 0.22 was chosen. The mix also included micro steel fibers coated with brass, with a 2% volume dosage in the concrete. To improve workability at lower w/b ratios, a high range water reducer

(HRWR) was also incorporated into the mix. The mix proportions chosen for UHPC are outlined in detail in Table 9.14.

9.3.2.6 Optimized mix

Based on the trials, mix 5E/5C grade I (70%) and grade III (30%) of CS/ES was used for developing the final UHPC. Two mixes with the same proportion of cement, SF, quartz powder, and ES/CS was prepared with and without fibers, that is, CS without fibers (C1), CS with fibers (CF), ES without fibers (E1) and ES with fibers (EF) were prepared. The details of the mixes are tabulated in Table 9.15.

9.3.3 Mixing of ultrahigh-performance concrete

9.3.3.1 Preparation of trial mixes

To create the UHPC trial mixes, a Planetary mixer machine with a capacity of 10 kg was utilized. The machine's speed could be adjusted to four different levels: stir (slow), speed (low), speed 2 (medium), and speed 3 (high), with corresponding agitator RPMs of 59, 107, 198, and 365. Initially, the dry binder powder was added to the mixing bowl, and dry mixing was conducted for 6–8 minutes at slow speed. Around 70% of the required water was then added, and the mixing speed was increased to medium for another 6–8 minutes. When the ingredients were thoroughly blended, the SP and the remaining water were added and mixed at high speed for 2–3 minutes to achieve a flowable mix. The mixing speed was then lowered to slow, and the fibers were randomly distributed for approximately 3 minutes. Finally, the ingredients were fully mixed at high speed for 1 minute to ensure even

Table 9.14 Ultrahigh-performance concrete (UHPC) mix proportions of trial mixes.

Materials	Mix 1E/1C	Mix 2E/2C	Mix 3E/3C	Mix 4E/4C	Mix 5E/5C
Cement	1	1	1	1	1
Silica fume	0.25	0.25	0.25	0.25	0.25
Quartz powder	0.40	0.40	0.40	0.40	0.40
ES/copper slag	1.1	1.1	1.1	1.1	1.1
Grade I	40%	33%	50%	60%	70%
Grade II	–	30%	–	–	–
Grade III	60%	37%	50%	40%	30%
Steel fibers	–	–	2%	2%	2%
Superplasticizer	2%	2%	2%	2%	2%
Water-to-cement ratio	0.21	0.21	0.22	0.22	0.22
Water-to-binder[a] ratio	0.13	0.13	0.13	0.13	0.13

[a]Binder = cement + silica fume + quartz powder.
Source: From Ambily, P. S., Umarani, C., Ravisankar, K., Prem, P. R., Bharatkumar, B. H., & Iyer, N. R. (2015). Studies on ultra high performance concrete incorporating copper slag as fine aggregate. *Construction and Building Materials*, *77*, 233–240. https://doi.org/10.1016/j.conbuildmat.2014.12.092.

Table 9.15 Ultrahigh-performance concrete (UHPC) mix proportions for optimized mixes (kg/m^3).

Materials	C1	CF	E1	EF
Cement	847.5	788.6	847.5	788.6
Silica fume	235	197.2	235	197.2
Quartz powder	339	315.4	339	315.4
Copper slag	932	868	–	–
ES	–	–	932	868
Grade I	652	608	652	608
Grade III	280	260	280	260
Steel fibers	–	157.7	–	157.7
Superplasticizer	21.7	19.7	21.7	19.7
Water	186.4	173.5	186.4	173.5

Source: From Ambily, P. S., Umarani, C., Ravisankar, K., Prem, P. R., Bharatkumar, B. H., & Iyer, N. R. (2015). Studies on ultra high performance concrete incorporating copper slag as fine aggregate. *Construction and Building Materials*, *77*, 233–240. https://doi.org/10.1016/j.conbuildmat.2014.12.092.

distribution. A Planetary mixer machine with a capacity of 300 kg was used to prepare the final mix. The workability of the ES and CS mixes ranged from 200 to 210 mm and 230 to 240 mm, respectively. The workability was determined using a flow table test according to ASTM C230/C230M (ASTM C230/C230M-20, 2021). The mixing process is illustrated in the flowchart in Fig. 9.13.

9.3.3.2 Casting of ultrahigh-performance concrete specimens

Trial mix

To test the compressive strength of the UHPC mixes, 30 cubes measuring $70.6 \times 70.6 \times 70.6$ mm were cast from each of the five trial mixes shown in Table 9.15. The trial mixes were carried out using different proportions of ES and CS. The first two trial mixes were done without fibers, with a mix of grade I (40%) and grade III (60%) and a mix of grade I (33%), grade II (30%), and grade III (37%). The next three trial mixes were done with fibers, with a mix of grade I (50%) and grade III (50%), a mix of grade I (60%) and grade III (40%), and a mix of grade I (70%) and grade III (30%). In total, 10 trial mixes were done, and the specimens were cured under heat and water for 7, 14, and 28 days.

Optimized mix

Each UHPC mix was used to cast 16 cubes of $100 \times 100 \times 100$ mm, 16 cubes of $70.6 \times 70.6 \times 70.6$ mm, and 6 beams of $70 \times 70 \times 350$ mm size. The mix proportion used was the optimized one, consisting of grade I (70%) and grade III (30%) of CS and ES, with and without steel fibers. The specimens were then cured for 3, 7, 14, and 28 days.

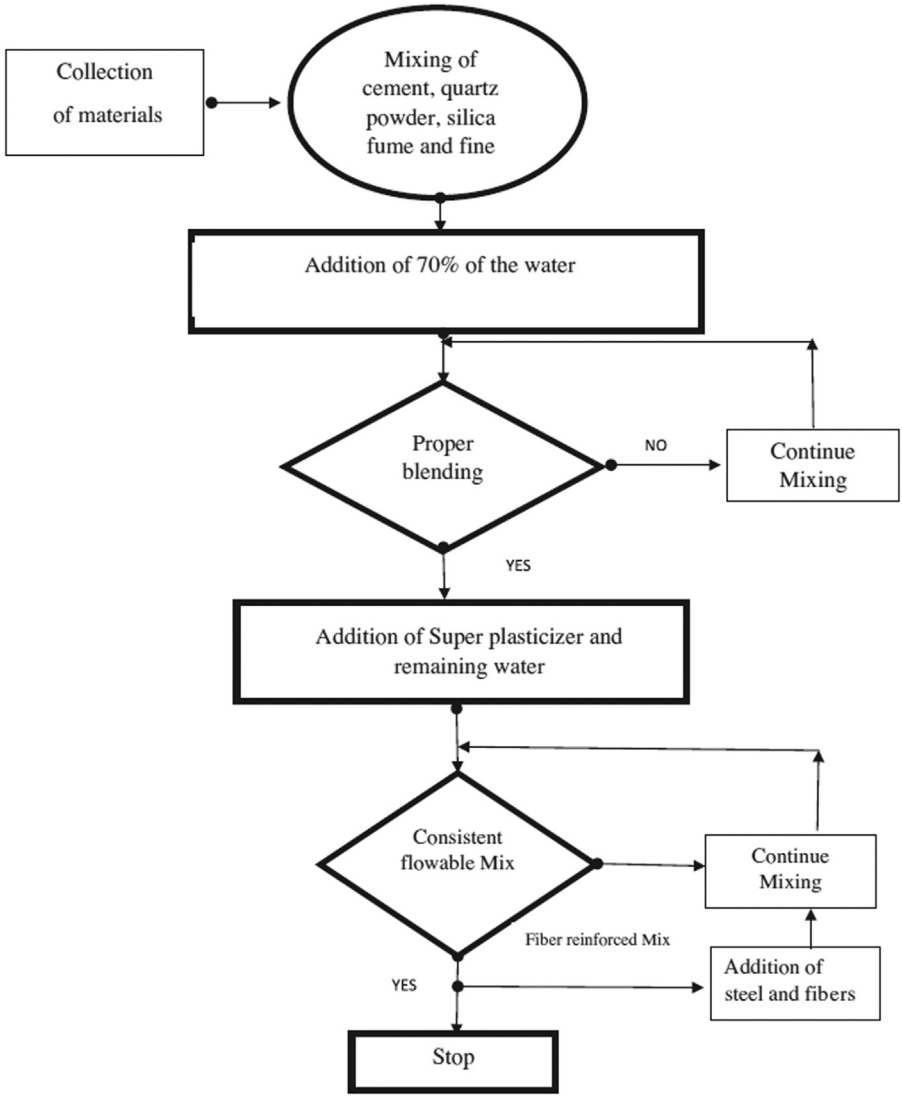

Figure 9.13 Mixing of UHPC.
Source: From Ambily, P. S., Umarani, C., Ravisankar, K., Prem, P. R., Bharatkumar, B. H., & Iyer, N. R. (2015). Studies on ultra high performance concrete incorporating copper slag as fine aggregate. *Construction and Building Materials*, *77*, 233−240. https://doi.org/10.1016/j.conbuildmat.2014.12.092.

9.3.3.3 Specimen preparation

After the UHPC mixes were prepared, they were transferred into steel molds in three layers and compacted using a vibrating table for 20−30 s. The vibrating

table had dimensions of 2×1 m, with a load capacity of 1500 kg, frequency of 66 Hz, and amplitude of 0.8 mm. Fig. 9.14 presents the specimens after casting. The specimens were demolded after 1 day and subjected to two different curing regimes.

9.3.3.4 Curing regime

In order to heat cure the UHPC specimens, a thermal cyclic chamber was utilized, which is capable of reaching temperatures up to $300 \pm 1°C$. The temperature rise and drop rate was set at 2°C/minute. The curing regime used in this study was chosen after conducting several trials. Two curing regimes were employed for comparison purposes (see Fig. 9.15). The first regime involved demolding the specimens after 24 hours and submerging them in water until the time of testing. The second regime involved demolding the specimens after 24 hours and subjecting them to a temperature of 150°C for 48 hours, followed by leaving them undisturbed until the temperature returned to ambient conditions. The specimens were then cured under water until the respective ages of testing. For the optimized mixes, three specimens from each mix were tested for 3-day compressive strength after heat curing, but before being submerged in water.

9.3.3.5 Tests on ultrahigh-performance concrete

Compressive strength test

The compressive strength of UHPC was tested on standard cube specimens of size $100 \times 100 \times 100$ mm and $70.6 \times 70.6 \times 70.6$ mm according to ASTM C109. The

Figure 9.14 Preparation of ultrahigh-performance concrete (UHPC) specimens.
Source: From Ambily, P. S., Umarani, C., Ravisankar, K., Prem, P. R., Bharatkumar, B. H., & Iyer, N. R. (2015). Studies on ultra high performance concrete incorporating copper slag as fine aggregate. *Construction and Building Materials*, *77*, 233–240. https://doi.org/10.1016/j.conbuildmat.2014.12.092.

(A)

(B)

Figure 9.15 Curing regimes: (A) water curing, (B) oven curing.

tests were carried out at the ages of 3, 7, 14, and 28 days for each mix. For trial mixes, the average of five cubes was taken for each age, while for optimized mixes, the average of three cubes was taken. A compression testing machine with a capacity of 3000 kN was used to apply the compressive load.

Flexural strength test

The flexural performance of UHPC is evaluated following the test method outlined in the ASTM C 1609 standard for fiber-reinforced concrete. This involves testing a

simply supported beam under third-point loading using a closed-loop, servo-controlled testing system to obtain the flexural strength.

Fracture energy test

The fracture energy (GF) was determined by testing the simply supported notched beam specimens under center point loading. The beam specimens had a size of $70 \times 70 \times 350$ mm and a notch-to-depth ratio of 0.3. The span of the beam specimen was 300 mm. The tests were carried out using a closed-loop servo-controlled CTM with a capacity of 3000 kN, with a rate of opening of 0.0005 mm/s. A clip gauge attached with knife edges was epoxied to the bottom flange on either side of the starter notch to measure the crack mouth opening displacement (CMOD). The LVDT was rigidly fastened to the reference frame with the moving tips lying on a plate fastened to one of the two halves of the specimen. The deflection was observed from the beam and the clip gauge was recorded using a data logger. The critical stress intensity factor (Kic), and fracture energy (GF) were calculated as per RILEM recommendations.

9.3.3.6 Test results

Trial mix results

Tables 9.16 and 9.17 display the average compressive strength of UHPC samples at 7, 14, and 28 days for various trials. Table 9.16 presents the compressive strength development of UHPC using ES with and without heat treatment, while Table 9.17 displays the compressive strength development of UHPC using CS with and without heat treatment. Mix 5E, with and without fibers, had the highest compressive strength using ES, with values of 182 and 202 MPa, respectively, at 28 days. Conversely, mixes 1E and 2E had the lowest compressive strength at 28 days without fibers. After 28 days, the specimens subjected to heat curing had a significantly higher compressive strength compared to the specimens that underwent water curing.

Table 9.16 Results for compressive strength of ultrahigh-performance concrete (UHPC) with ennore sand (ES).

Mix	Compressive strength (N/mm^2) Without heat treatment			Compressive strength (N/mm^2) With heat treatment		
	7 Days	14 Days	28 Days	7 Days	14 Days	28 Days
1E	85.8	91.2	102.6	91.6	94.8	108.1
2E	81.2	82.6	85.1	80.4	81.9	82.3
3E	110.9	133.6	152.3	134.9	152.3	164.8
4E	109.4	147.3	167.9	146.4	164.1	181.0
5E	132.0	146.2	182.4	154.0	183.5	202.0

Source: From Ambily, P. S., Umarani, C., Ravisankar, K., Prem, P. R., Bharatkumar, B. H., & Iyer, N. R. (2015). Studies on ultra high performance concrete incorporating copper slag as fine aggregate. *Construction and Building Materials*, 77, 233–240. https://doi.org/10.1016/j.conbuildmat.2014.12.092.

Table 9.17 Results for compressive strength of ultrahigh-performance concrete (UHPC) with copper slag.

Mix	Compressive strength (N/mm^2) Without heat treatment			Compressive strength (N/mm^2) With heat treatment		
	7 Days	14 Days	28 Days	7 Days	14 Days	28 Days
1C	86.7	86.8	87.9	84.2	92.3	100.5
2C	82.3	87.8	89.7	88.4	89.7	92.9
3C	109.0	110.0	128.3	90.0	92.0	134.8
4C	92.0	122.0	137.4	102.0	110.0	141.2
5C	107.0	131.0	143.8	112.0	134.0	152.0

Source: From Ambily, P. S., Umarani, C., Ravisankar, K., Prem, P. R., Bharatkumar, B. H., & Iyer, N. R. (2015). Studies on ultra high performance concrete incorporating copper slag as fine aggregate. *Construction and Building Materials*, *77*, 233–240. https://doi.org/10.1016/j.conbuildmat.2014.12.092.

Replacing sand with CS, specifically grade I and grade III, in UHPC had a positive impact on compressive strength development. Mix 5C, which contained 70% grade I and 30% grade III CS replacement with fibers, achieved the highest compressive strength of about 143 and 152 MPa at the age of 28 days. However, mixes 1C and 2C, which contained 40% grade I and 60% grade III and 33% grade I, 30% grade II, and 37% grade III CS replacement without fibers, respectively, had the lowest compressive strength of 88 and 101 MPa at the age of 28 days. The highest compressive strength achieved using CS and ES was 152 and 202 MPa at the age of 28 days. Various researchers have reported a reduction in compressive strength of mixes with CS due to its lower water absorption characteristics, which can lead to the formation of internal voids and capillary channels in concrete.

Optimized mix results

Based on the results of trial mix, 5C and 5E with heat treatment are selected as optimized mix and further study on the mixes are reported here after.

Cube compressive strength

In order to investigate the influence of specimen size on compressive strength, both 100 and 70 mm cubes were utilized. As depicted in Fig. 9.16, the optimized mixes were tested for their compressive strength. The results of 70 mm cubes using ES and CS indicate that UHPC mixes with fibers exhibited 81%–95% higher compressive strength compared to the UHPC mix without fibers. The mixes with ES achieved the highest compressive strength of 191 MPa, while those with CS reached 162 MPa.

Similarly, the results of 100 mm cubes using ES and CS demonstrated that UHPC mixes with fibers showed 79%–86% higher compressive strength compared to the UHPC mix without fibers. The highest compressive strength of 172 MPa for mixes with ES and 158 MPa for CS was recorded.

This study has investigated how the size of the specimen affects the compressive strength of UHPC mixes. The study presented the ratio of compressive strength of

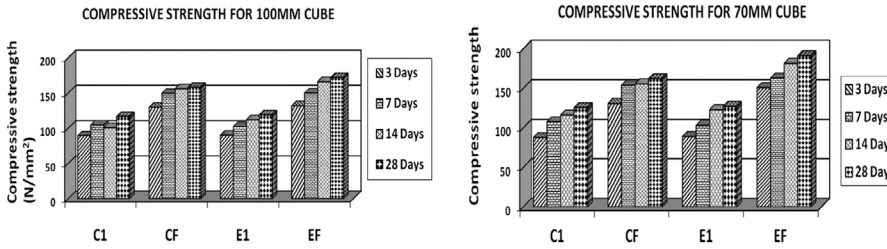

Figure 9.16 Compressive strength of 100 and 70 mm cubes.
Source: From Ambily, P. S., Umarani, C., Ravisankar, K., Prem, P. R., Bharatkumar, B. H., & Iyer, N. R. (2015). Studies on ultra high performance concrete incorporating copper slag as fine aggregate. *Construction and Building Materials*, *77*, 233–240. https://doi.org/10.1016/j.conbuildmat.2014.12.092.

Table 9.18 Ratio of the compressive strength of 7 cm cubes to 10 cm cubes at various ages.

Mix ID	Compressive strength (N/mm^2)			
	3 Days	7 Days	14 Days	28 Days
C1	0.980984	1.026769	1.151936	1.074893
CF	1.006163	1.028056	0.996795	1.02402
E1	0.986696	1.006843	1.098214	1.073171
EF	1	0.9375	1.422764	1.110465

Source: From Ambily, P. S., Umarani, C., Ravisankar, K., Prem, P. R., Bharatkumar, B. H., & Iyer, N. R. (2015). Studies on ultra high performance concrete incorporating copper slag as fine aggregate. *Construction and Building Materials*, *77*, 233–240. https://doi.org/10.1016/j.conbuildmat.2014.12.092.

UHPC cubes at different ages and for different mixes in Table 9.18. The results showed that the compressive strength of 70 mm cubes was higher than that of 100 mm cubes at the age of 28 days, indicating that specimen size can affect the results obtained from compression testing of UHPC mixes.

Additionally, the statement mentions Fig. 9.17 A–C, which depicts the compression testing and failure pattern of UHPC with CS. Although it is unclear what specific insights can be gleaned from this figure without viewing it, understanding the failure pattern of concrete under compression can provide valuable information about its performance and behavior.

Flexural strength of ultrahigh-performance concrete

The study examined the flexural strength of UHPC using a four-point bending test with beams that were $70 \times 70 \times 350$ mm in size. The study included 12 prisms that were cast with both ES and CS, with and without fibers. The plain concrete failed abruptly at the end of linearity. However, the fiber-reinforced UHPC showed an approximately twofold increase in flexural strength compared to UHPC without

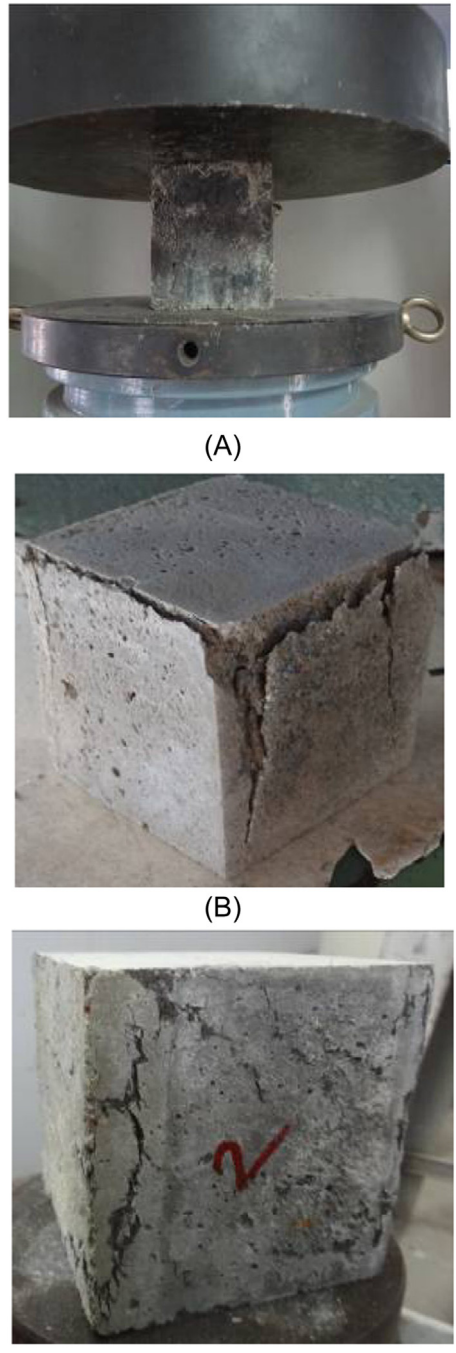

Figure 9.17 Compression testing of mixes with copper slag and failure pattern of C1, CF. (A) Compression testing, (B) C1 specimen, (C) CF specimen.

fibers, as shown in Fig. 9.18. Additionally, the postcrack behavior of UHPC with fiber showed a ductile material behavior, with a main crack expanding along the high direction of the beam observed after cracking.

The study describes the behavior of fiber-reinforced UHPC beams during loading and the effect of fiber addition on flexural strength. During loading, the fiber-reinforced UHPC beam remained intact until the last step, with steel fibers still connected and fractures planes and plane of fracture being regular. The study found that the mean flexural stress of specimens with CS that underwent heat treatment was 12.34 MPa without fibers, which increased to 32.43 MPa with fibers. For specimens with ES, the mean flexural strength was 12.4 MPa without fibers and 32.58 MPa with fibers.

Overall, the study concluded that the addition of fibers significantly increased the flexural strength of UHPC and resulted in a more ductile material behavior, which is desirable for applications where energy absorption and crack control are important. The results suggest that fiber reinforcement can enhance the performance and durability of UHPC, making it a more viable option for various construction applications.

Fracture energy of ultrahigh-performance concrete prisms

To determine the basic behaviors of individual cracks in UHPC prisms, tests were performed on notched prisms with and without fibers using CS and ES. Three prisms were tested for each scenario. The fracture energy was calculated using a linear elastic fracture mechanics approach, and the area under the load-deflection plot (shown in Fig. 9.19) was used to indirectly measure the fracture energy. The crack mouth opening displacement was also determined using a clip gauge and plotted in Fig. 9.20.

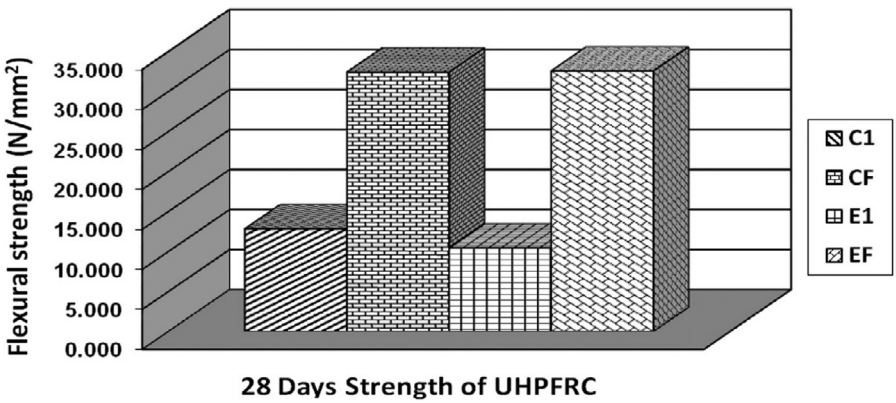

Figure 9.18 Flexural strength of ultrahigh-performance concrete (UHPC).
Source: From Ambily, P. S., Umarani, C., Ravisankar, K., Prem, P. R., Bharatkumar, B. H., & Iyer, N. R. (2015). Studies on ultra high performance concrete incorporating copper slag as fine aggregate. *Construction and Building Materials*, *77*, 233–240. https://doi.org/10.1016/j.conbuildmat.2014.12.092.

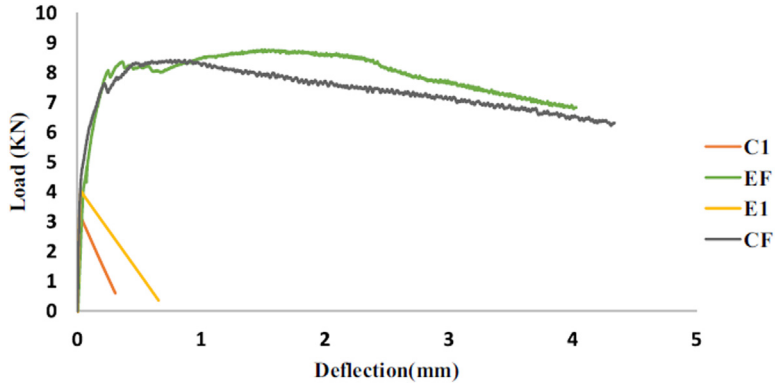

Figure 9.19 Load versus deflection of notched ultrahigh-performance concrete (UHPC) specimens.
Source: From Ambily, P. S., Umarani, C., Ravisankar, K., Prem, P. R., Bharatkumar, B. H., & Iyer, N. R. (2015). Studies on ultra high performance concrete incorporating copper slag as fine aggregate. *Construction and Building Materials*, *77*, 233−240. https://doi.org/10.1016/j.conbuildmat.2014.12.092.

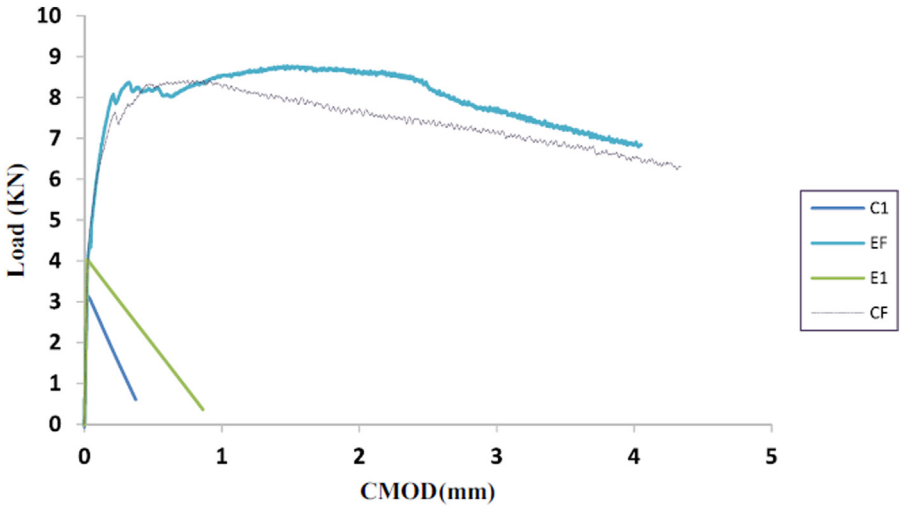

Figure 9.20 Load versus crack mouth opening displacement (CMOD) of notched ultrahigh-performance concrete (UHPC) specimens.
Source: From Ambily, P. S., Umarani, C., Ravisankar, K., Prem, P. R., Bharatkumar, B. H., & Iyer, N. R. (2015). Studies on ultra high performance concrete incorporating copper slag as fine aggregate. *Construction and Building Materials*, *77*, 233−240. https://doi.org/10.1016/j.conbuildmat.2014.12.092.

Higher energy (Gf) indicates higher concrete ductility, and the results clearly show an increase in Gf and Kic due to the presence of fibers. Fracture parameters indicate the behavior of concrete ductility and energy absorbing capacity. The results indicate a significant increase in Gf and Kic due to the presence of fibers. The fracture energy of the specimens was found to be in the order C1 < E1 < CF < EF, as seen in Table 9.19. Overall, the study suggests that the addition of fibers improves the ductility and energy absorbing capacity of UHPC, making it a more viable option for construction applications where crack control and energy absorption are important factors.

One can observe the following from the case study presented here:

- Studies on particle packing reveals that vibration packing will give the optimum packing density for granular materials for unitary, binary, and ternary combinations.
- The optimum PD for CS obtained in the binary combination of G1 (70%) and G3 (30%).
- CS, a locally available waste material, makes it possible to produce UHPC with a mean compressive strength of greater 150 MPa at 28 days.
- The mean compressive strength of UHPC using the CS and ES was 162 and 191 MPa, respectively, at the age of 28 days.
- UHPC with fibers (UHPFRC) generally exhibit high fracture toughness (five to seven times) compared to UHPC without fiber.
- Complete replacement of standard sand by CS resulted in a maximum reduction of compressive strength of around 15%−25%. This may be due to the high free water presence in the case of CS-based mixes for the same proportion compared to ES mixes. The reduction in mechanical properties when 100% standard sand is replaced by CS can be taken into account by suitable modification in the mix.
- Results obtained with the CS shows a very promising future for the manufacture of the UHPFRC. As this waste material is produced industrially, its availability and its low price would favor for its development.

Table 9.19 Flexural strength of ultrahigh-performance concrete (UHPC) mixes.

	C1	**CS**	**E1**	**ES**
Length (L)	350	350	350	350
Span (S)	300	300	300	300
Depth (D)	70	70	70	70
Breadth (B)	70	70	70	70
Notch/depth	0.3	0.3	0.3	0.3
Peak load	3162	8427	4034	8776
Kic	7.85	20.92	10.01	21.79
Wf (n-mm)	578	3779	881	4040
Gf (J/m^2)	168.65	1101.89	256.99	1177.98

Source: From Ambily, P. S., Umarani, C., Ravisankar, K., Prem, P. R., Bharatkumar, B. H., & Iyer, N. R. (2015). Studies on ultra high performance concrete incorporating copper slag as fine aggregate. *Construction and Building Materials*, *77*, 233−240. https://doi.org/10.1016/j.conbuildmat.2014.12.092.

References

Ahmed, A.-M., Chow, C. L., Feo, L., Penna, R., & Lau, D. (2019). Green concrete: By-products utilization and advanced approaches. *Sustainability*, *11*, 5145. Available from https://doi.org/10.3390/su11195145.

Ambily, P. S., Umarani, C., Ravisankar, K., Prem, P. R., Bharatkumar, B. H., & Iyer, N. R. (2015). Studies on ultra high performance concrete incorporating copper slag as fine aggregate. *Construction and Building Materials*, *77*, 233–240.

Amudhavalli, N. K., & Mathew, J. (2012). Effect of silica fume on strength and durability parameters of concrete. *International Journal of Engineering Sciences & Emerging Technologies*, *3*(1).

ASTM C 1240–97. (1998). *Standard specification for silica fume for use as mineral admixture in hydraulic cement, mortar, concrete & grout*.

ASTM C230/C230M-20. (2021). *Standard specification for flow table for use in tests of hydraulic cement*.

ASTM C29/C29M-09. (2016). *Standard test method for bulk density ("unit weight") and voids in aggregate*.

ASTM C618-19. (2019). *Standard specification for coal fly ash and raw or calcined natural pozzolan for use in concrete* (2012). West Conshohocken: ASTM International.

BS EN 15167-1. (2006). *Ground granulated blastfurnace slag for use in concrete, mortar and grout - definitions, specifications and conformity criteria (includes corrigendum 16763)*.

Chandra, A. (2008). Some investigations on fly ash resistivity generated in Indian power plants. Proceedings of 11th international conference on electrostatic precipitation, pp. 399–406.

Chatterjee, A. K. (2011). Indian fly ashes: Their characteristics, and potential for mechano-chemical activation for enhanced usability. *Journal of Materials in Civil Engineering*, *23*(6), 783–788.

Fournier, B., Lu, D., Charland, J. P., & Li, J. (2004). Evaluation of Indian fly ashes for use in HVFA concrete, part 1: Characterization. *The Indian Concrete Journal*, 22–30.

Ghutke, V.S., & Bhandari, P.S. (2014). *Influence of silica fume on concrete. International conference on advances in engineering & technology (ICAET 2014)*, 45–47.

IRC 112. (2020). Code of practice for concrete road bridges, *Indian Roads Congress*.

IS 12269. (1987). *53 grade ordinary Portland cement [CED 2: cement and concrete]*.

IS 1489-1. (1991). *Specification for Portland pozzolana cement, part 1: Flyash based [CED 2: cement and concrete]*.

IS 2386 - Part 3-1963 - Reaffirmed. (2021). *Methods of test for aggregates for concrete, part 3: Specific gravity, density, voids, absorption and bulking [CED 2: cement and concrete]*.

IS 456. (2000). *Plain and reinforced concrete - code of practice [CED 2: cement and concrete]*.

IS 650. (1991). *Specification for standard sand for testing of cement [CED 2: cement and concrete]*.

IS 383. (1970). *Specification for coarse and fine aggregates from natural sources for concrete*.

Iyer, N. R. (2020). An overview of cementitious construction materials – I. In P. Samui, D. Kim, N. Iyer, & S. Chaudhary (Eds.), *New materials in civil engineering* (1st ed.). The Netherlands: Elsevier Science.

Iyer, N. R., Ravisankar, K., Ramachandra Murthy, A., Gopinath, S., Rameshkumar, V., Bharathkumar, B. H., et al. (2013). New building materials and technologies - innovations in concrete, IBC:20:2013 *Indian Building Congress*.

Lockwood, C. L., Stewart, D. I., Mortimer, R. J. G., et al. (2015). Leaching of copper and nickel in soil-water systems contaminated by bauxite residue (red mud) from Ajka, Hungary: The importance of soil organic matter. *Environmental Science and Pollution Research*, *22*, 10800−10810.

Maiti, D., & Prasad, B. (2016). Revegetation of fly ash − a review with emphasis on grass-legume plantation and bioaccumulation of metals. *Applied Ecology and Environmental Research*, *14*(2), 185−212. Available from https://doi.org/10.15666/aeer/1402_185212.

Munch-Petersen, M. G. C. (2000). 'Green' concrete in Denmark. *Structural Concrete*, *1*(1), 19−25. Available from https://doi.org/10.1680/stco.2000.1.1.19.

Ministry of Power, Govt. of India. (2022). *Report on fly ash generation at coal/lignite based thermal power stations and its utilization in the country for the year 2021−22*, Central Electricity Authority, Civil Design Division.

Pradhan, D., & Dutta, D. (2013). Influence of silica fume on normal concrete. *International Journal of Engineering Research and Applications*, *3*(5), 79−82.

Prem, P. R., Bharatkumar, B. H., & Iyer, N. R. (2012). Mechanical properties of ultra high performance concrete. *World Academy of Science, Engineering and Technology*, *68*, 1969−1978.

Roy, K., & Amit, S. (2012). Effect of partial replacement of cement by silica fume on hardened concrete. *International Journal of Emerging Technology and Advanced Engineering*, *2*(8), 472.

Shanmugapriya, T., & Uma, R. N. (2013). Experimental investigation on silica fume aspartial replacement of cement in high performance concrete. *The International Journal of Engineering and Science*, *2*(5), 40−45.

Taylor, P. (2014). The use of ternary mixtures in concrete, in *Trans Project Reports*. 74, http://lib.dr.iastate.edu/intrans_reports/74.

Behavior assessment of poor subgrade soil using natural coir geotextile under static and repeated load condition

10

D. Harinder[1] *and S. Shankar*[2]
[1]Civil Engineering, Vallurupalli Nageswara Rao Vignana Jyothi Institute of Engineering and Technology, Hyderabad, Telangana, India, [2]National Institute of Technology, Civil Engineering Department, Warangal, Telangana, India

10.1 Introduction

The construction of low-volume roads (LVRs) over weak subgrade soil causes failure in the pavement in terms of large deformation and high settlement due to its low bearing capacity and high swelling and shrinkage properties. The LVRs laid over weak subgrade (BC soil) soil have poor performance and high maintenance costs. The periodic maintenance of these roads is limited due to the low maintenance cost. To reduce the cost of construction and maintenance consideration, many of the conventional techniques were adopted in the flexible paved/unpaved roads. But these techniques are not eco-friendly or economical; in addition to this problem, this is time-consuming and requires skilled labor in the field. In view of the consideration, geosynthetics are used as an alternate material to improve the performance of the weak subgrade.

The construction and maintenance of LVRs over poor soil subgrade consist of several problems, large deformation, and settlement in the pavement structure. It was obtained due to the swelling and shrinkage of black cotton (BC) soil, and its volume change behavior with respective seasonal changes. It causes several failures in pavement structures and poses poor performance. The periodic maintenance of this road is limited due to the low maintenance cost. The quality of the pavement requires stiffness and strength of pavement layers. It is consuming a large amount of natural resources. In another case, the large network and huge construction of road infrastructure lead to the scantiness of natural materials. In order to reduce these problems, it is essential to utilize industrial waste in road constructions, like fly ash, bentonite, silica fume lime, cement, gypsum, and other conventional stabilization techniques were used (Giroud & Han, 2004; Ozdemir, 2016; Sharma & Sivapullaiah, 2016; Yadu & Tripathi, 2013). But these methods are not eco-friendly and do not fully fill the requirements of pavement structure like reinforcement, separation, and drainage. These methods require skilled labor, large equipment, and are time-consuming. In order to overcome this problem, an alternate new material is used to improve the performance of the pavement with the replacement of natural resources (Zornberg, 2011). Since the 1980s, geosynthetics and geotextiles have

Green Materials in Civil Engineering. DOI: https://doi.org/10.1016/B978-0-443-19106-0.00010-5

gained attention toward incorporating the reinforcement, drainage, filtration, and separation functions in pavement layers. The study demonstrated the uses of geosynthetics to address the above functions. Especially, it has been used as separation material between the two layers (Giroud, 2009). The study demonstrated the use of geosynthetics in the pavement to reinforce the weak soil subgrade, which indicates the three-dimensional geogrid and geotextile are strengthening the bases of the pavement (Zornberg, 2011). The provision of a three-dimensional geocell acts as a semirigid and gives better reinforcement to the soil while distributing the load over a wider area (Zornberg, 2011). In another study, it was noticed that the provision of geogrid gives reinforcement to the pavement structure, the geogrid shows proper interlock and stabilized layers, which leads to a load distribution mechanism in pavement layers (Adams et al., 2016). The reinforcement mechanism was described using different soil with respective optimum moisture content; the reinforcement of geotextile and geogrid depends on the placement position and types of materials (Giroud & Noiray, 1981).

The study explains the geogrid and geotextile reinforcing method that was implemented as a result of the bearing capacity, increased lateral restraint, and tensioned elements (Bueno et al., 2005; Giroud et al., 1984; Holtz et al., 1998; Perkins & Ismeik, 1997a, 1997b). From the umbrella of geosynthetics, geotextiles are also utilized as reinforcement in pavement structures (Benjamim et al., 2007; Miura et al., 1990). The field study reported the construction of the control section and the uncontrol section with geogrid; it is indicated the control section has more rutting than the reinforced section of a 50 mm thinner base course (Al-Qadi et al., 1994). The experiments are carried out in the laboratory using the large-scale pavement model under cyclic plate load with and without reinforcement section (Cancelli et al., 1996; Haas et al., 1988; Hsieh & Mao, 2005; Perkins, 1999). This prototype model pavement was constructed with reinforcement of geosynthetics placed in between the subgrade and the base course. It is imposed with the repeated load on the surface and generates a maximum of 550 kPa pressure, and the data were collected with Linear Variable Differential Transformer (LVDT) and load cell. The cyclic load test was carried out with geotextile and geogrid, describing the traffic benefit ratio and base course reduction using the cyclic load test (Rao & Balan, 2000). Several studies describe that the addition of coir fiber enhances the engineering properties of poor soil (Babu & Choksey, 2010; Dasaka & Sumesh, 2011; Prasad et al., 1983; Sridhar & Prathap Kumar, 2018). It is obtained due to the impurities of coir fiber like pectin, lignin, and hemicellulose (Rao & Dutta, 2006). Various researchers reported the benefits and application of coir geotextile in unpaved roads (Som & Sahu, 1999; Subaida et al., 2009).

In view of the above extensive literature review, it was noticed that, extensive studies are available with geogrid and geotextile in various aspects of civil engineering. Several studies are found the difficulties in compaction, placing poor soil and anchoring the geotextile over the prepared subgrade. This study addresses the uses of coir mats and their benefits over the coir fiber under repetitive load. This study brought out the application of fiber in the pavement over the California Bearing Ratio (CBR) test using the geotextile mats. Further, the study was carried

out with various coir mats and addressed the application of coir geotextile mats under realistic behavior of material, using the wheel tracking test (WTT) apparatus.

10.2 Materials used for the study

Subgrade soil: The experimental investigation was carried out using BC soil borrowed from the lake near NIT, Warangal. The engineering properties of the selected subgrade were evaluated and summarized in Table 10.1. It was observed that the CBR values of BC soil are very low (less than 5%), hence it is poor in strength and not suitable for the action of pavement subgrade.

Subbase: The subbase layer is adopted with sandy gravel soil. It consists of the higher sandy particle; due to these particles, it shows poor cohesive strength. The engineering properties of sandy gravel soil are shear strength parameter C and ω (0, 310), OMC (8%), Maximum Dry Density (MDD) (1.87%), and soaked CBR value is 21 as per the MoRTH classification. Coir geotextile fiber and mats: Coir geotextile fibers are obtained from the husk of coconuts, and later, these fibers are manufactured as coir geotextile mats. Among the other natural geotextiles, coir geotextile consists of high durability. It also has better rigidity due to the presence of lignin in fiber. The physical properties of coir fiber are evaluated and presented in Table 10.2.

In the present study, three types of coir geotextile mats are used, as shown in Fig. 10.1. Namely, CC is coir composite, WCM is woven coir mat, and NWCM is nonwoven coir mat.

10.3 Experimental setup

To evaluate the rutting potential of the pavement model layer, an attempt has been made in the laboratory with the varying contact pressure. The CBR test was performed in the laboratory as per the standard as well as the moving load condition of the WTT used. The sample was tested for a 40 mm rut depth limit, a maximum limit available with this instrument in the laboratory. The fabricated angles control the loading onto the pavement model section. The maximum load applied over the two-layer pavement structure was 55 kg (0.055 ton) through the moving wheel of diameter 200 mm, the width of 50 mm made of solid rubber. The experimental setup used in the study is shown in Fig. 10.2.

Table 10.1 Engineering properties of subgrade black cotton soil.

Properties	LL %	PL %	PI %	Classification	Specific gravity	OMC %	MDD (g/cc)	FSI %	Soaked CBR (%)
Values	58	27	34	CH	2.63	17	1.7	77	2

Table 10.2 Physical properties of coir fiber.

Coir properties	Length (mm)	Diameter (mm)	Specific gravity	Density (g/cc)	Breaking elongation (%)	Rigidity modulus (dynes/cm)	Specific heat	Swelling in water (%)	Young's modulus (GN/m^2)
Values	1.15−1.4	0.1−1.5	1.15	1.15−1.4	30	1.8924	0.27	5	4.5

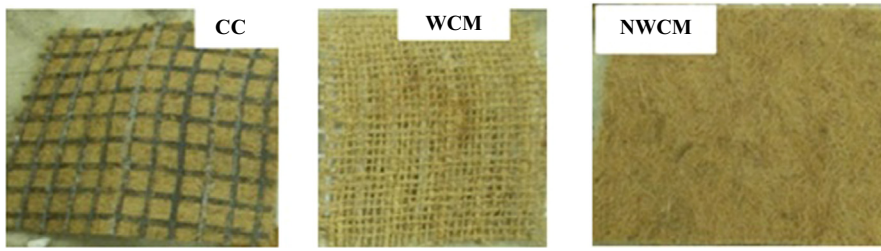

Figure 10.1 Materials used in the current study.

Figure 10.2 Experimental setup with fabricated mold.

10.4 Results and discussion

10.4.1 California Bearing Ratio test results

In the laboratory, the CBR test was performed in order to determine the potential benefits to improve the CBR values. The benefits of coir fiber are measured in soaked and unsoaked conditions. The CBR is being improved by the percentage of coir geotextile fibre added. The soaked and unsoaked CBR values along with coir fiber are given in Table 10.3.

In unsoaked conditions, the soil has a CBR value of 5.5%; this value increases to 8.1% when coir geotextile is added at a rate of 1%. The percentage increase in CBR value is 47%.

The CBR test was carried out with BC soil as subgrade soil with adding of water at OMC and compacted at MDD. The test results are noticed at the soaked and unsoaked conditions, with and without the reinforcement of coir fiber. The load

Table 10.3 California Bearing Ratio test results with and without coir reinforcement of unsoaked and soaked conditions.

Fiber content (%)	Unsoaked CBR value (%)	Soaked CBR value (%)
0.00	5.51	0.51
0.25	5.58	0.76
0.50	6.28	1.07
0.75	7.20	1.53
1.00	8.12	1.80
1.25	7.5	1.7

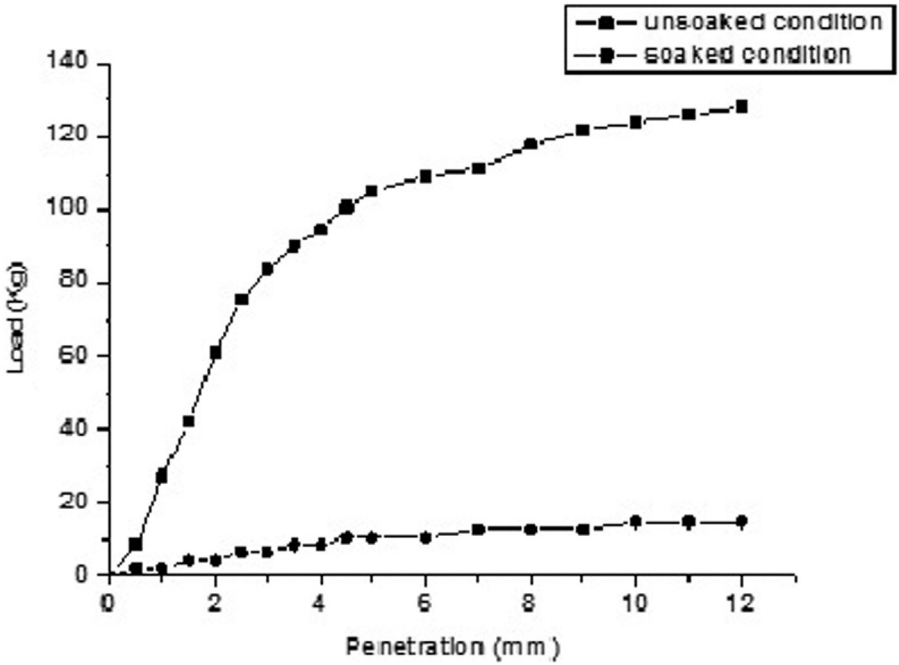

Figure 10.3 Unsoaked and soaked California Bearing Ratio values of black cotton soil.

versus penetration curve of BC soil in soaked and unsoaked conditions is shown in Fig. 10.3. The unsoaked CBR value of the soil is 5.51%, and soaked CBR value is 0.5%. Because of the influence of montmorillonite in the BC soil and the water content in the soaked condition, the soaked CBR value is quite low.

The coir fiber is incorporated into the BC soil in order to increase the percentage, such as 0.25, 0.50, 0.75, 1, and 1.25 by dry weight of the BC soil to conduct the CBR test. The CBR test was conducted in soaked and unsoaked conditions, and soaked CBR values are raised due to the presence of the coir fiber. The coir fiber helped to improve the load-deformation behavior of the BC soil and became the

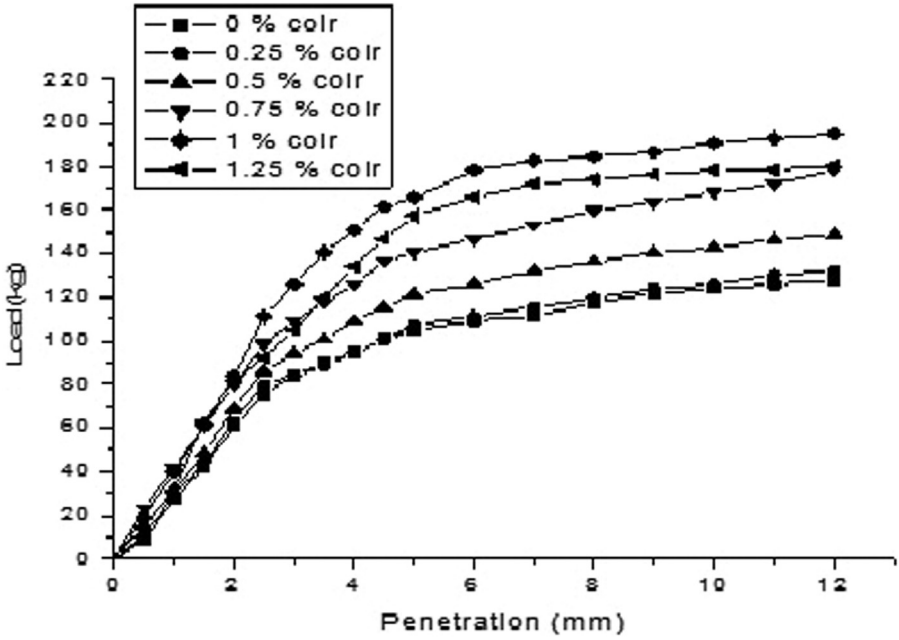

Figure 10.4 Unsoaked California Bearing Ratio values at various percentages of coir fiber.

stiffer material. The coir fiber is added in increasing percentages such as 0.25, 0.5, 0.75, 1, and 1.25; it is revealed that added coir fiber improved the CBR values in both conditions. The maximum CBR value is noticed at 1% of the coir fiber. When coir fibre is added in excess of 1% (1.25), lumps of BC soil and coir fibre form, which lowers the CBR value. The unsoaked CBR values at various percentages of coir fiber are shown in Fig. 10.4.

In a similar vein, CBR values are measured in wet conditions, with 1.8% and 1% of the coir fibre exhibiting the highest CBR values. The increasing percentage of coir fiber (0.25, 0.5, 0.75, and 1) improved CBR values in soaked conditions are 0.76%, 1.07%, 1.53%, and 1.8%, respectively. The randomly distributed coir fiber helps in forming the confinement to the BC soil, which improved the CBR values due to the homogeneity of the materials. Fig. 10.5 shows the soaked condition CBR values with coir fiber. The randomly distributed coir fiber improves its load-deformation behavior by interacting with the soil particles.

10.4.2 Wheel tracking test results

The experimental study was conducted in the laboratory using three types of coir geotextile mats (CC, WCM, and NWCM) under the WTT. This study evaluated the deformation characteristics of coir in terms of rutting. The two-layer pavement model layers were prepared as subgrade and subbase, such as BC and sandy gravel

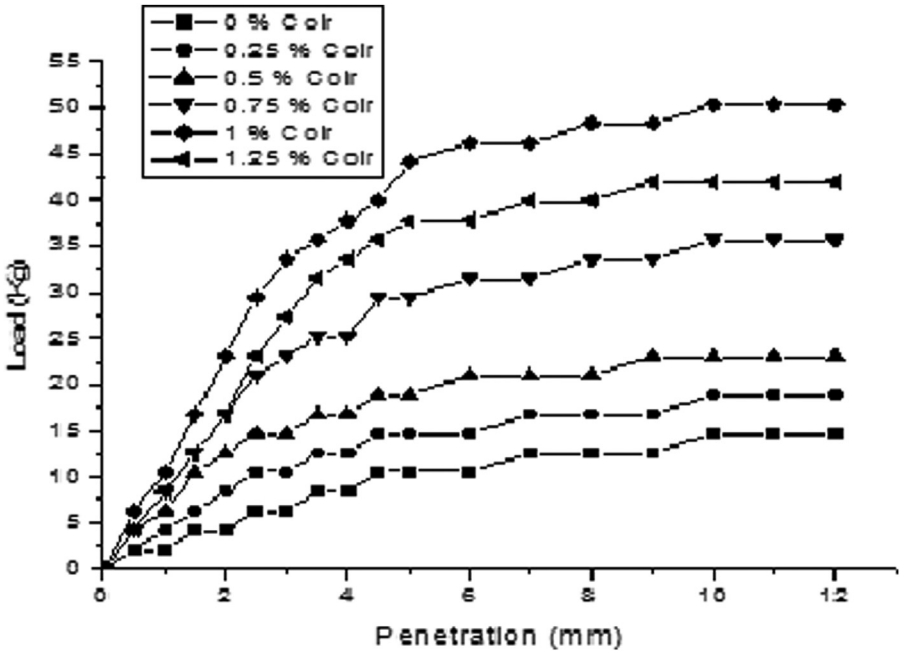

Figure 10.5 Soaked California Bearing Ratio values at various percentages of coir fiber.

soil, respectively. The coir geotextile mats are provided in fabricated mold at positions of H/2, H/3, and H/4 from the bottom.

The functions of coir geotextile ensure the multifunction in pavement applications such as reinforcement and separation, especially in the case of coir composite materials. The woven coir mats possess the reinforcement to the pavement but fail in separation function as compared to the NWCM. The nonwoven coir geotextile mats provided with geogrid give better reinforcement. The placement position of three types of coir mats at the H/2 position shows a similar performance compared with the H/3 position. The failure occurs in the pavement model layer due to the uplift pressure of coir mats and also the lower shear strength of grade sandy gravel soil. But in the case of the H/3 position, the provision of coir mats will show better performance than the H/2 and H/4 position. The placement position of coir mats at the H/2 position is presented in Fig. 10.6.

The incorporation of coir mats at the H/3 position shows a similar rut depth compared with the H/2 position. The provision of WCM raise suddenly, later settle slowly, and reduce the deformation of the pavement. The uniform deformation was found at the H/3 place with unreinforcement and reinforcement of WCM. The provision of coir mats at the H/3 position is shown in Fig. 10.7. The condition of coir composite (CC) mats keeping at the H/3 position has led to the variance in rut depth when compared with the H/2 position. A higher improvement was observed at the

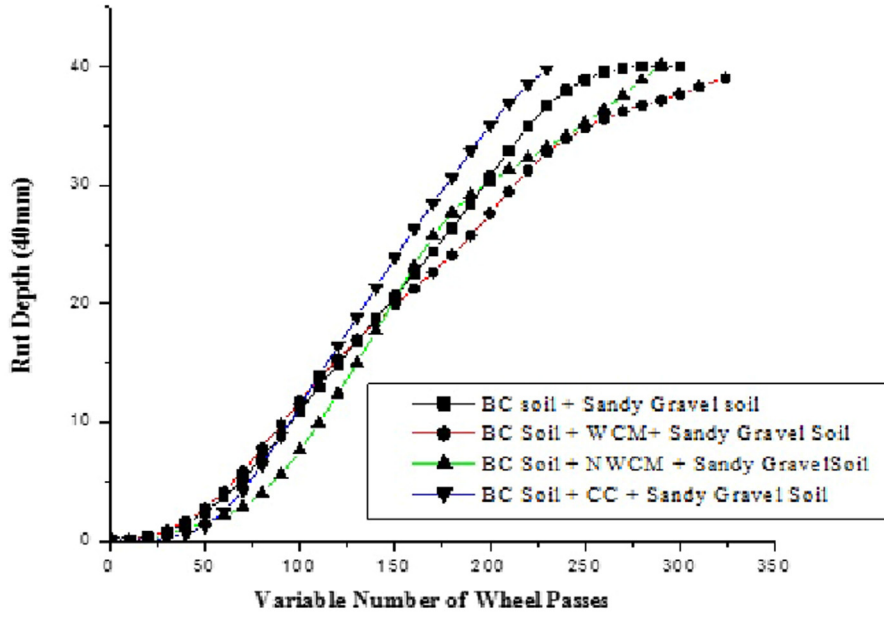

Figure 10.6 Wheel passes with respective rut depth at H/2 position of coir geotextiles.

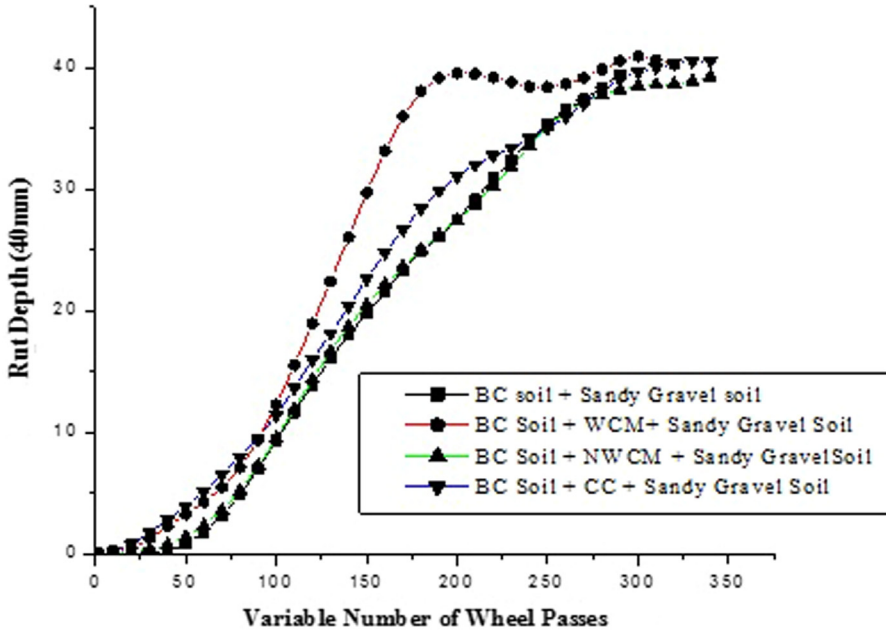

Figure 10.7 Wheel passes with respective rut depth at H/3 position of coir geotextiles.

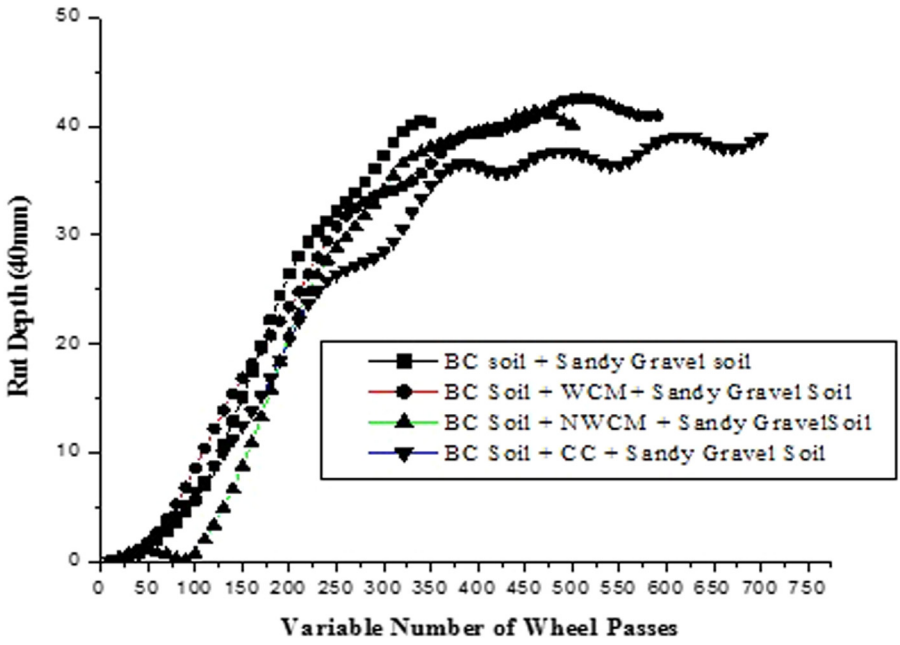

Figure 10.8 Wheel passes with respective rut depth at H/4 position of coir geotextiles.

H/3 position with CC materials than the WCM and NWCM in terms of the wheel passes at the H/3 position with sandy gravel soil with different types of coir mats.

In the case of the H/4 position, the provision of coir geotextile mats gives more wheel passes with similar rut depth. Because the subbase soil is weak, failure occurs there; nevertheless, the coir mats will support the weight and elevate the wheel passes. The position of coir mats at the H/4 location is more effective while reducing the thickness of the subbase layer. The provision of geotextile coir geotextile mats at the H/4 position more greatly reduces the deformation of the weak subgrade soil pavements than the provision of the mats at H/2 and H/3. The incorporation of coir mats at the H/4 position is shown in Fig. 10.8. The WCM mats are effective in reinforcement, but at the same time, it is ineffective in posing the separation function due to their opening size. The CC mats are more significant to pose the multifunction to the pavement, such as reinforcement and separation and improve the durability of the LVRs.

10.5 Conclusion

The current study derives the strength characteristics of subgrade BC soil with and without the inclusion of coir fiber in terms of CBR, and effective reinforcement of coir geotextiles is evaluated through the WTT under rutting parameters. The study

revealed that adopted coir geotextile materials improve the strength of BC soil subgrade. The following are the findings are obtained by the current investigation.

The CBR value of the soil increases with the inclusion of the coir fiber for both soaked and unsoaked conditions. One percent of the coir fiber is more significant than the other percentages to improve the stiffness of the pavement.

The soaked and unsoaked CBR value with the addition of optimum coir fiber of 1 percentage improves the strength of BC soil subgrade from 0.51% to 1.8% and 5.5% to 8.1%, respectively.

The rutting distress of the pavement can be studied effectively with WTT apparatus and simulated with the filed conditions.

The provision of coir mats at the H/4 position is more significant to increase the repetitions (750), here CC mats are placed near the wheel load so that it is very effective in the reduction of deformation.

The study concluded that WCM gives a better separation function; it effectively reduces the settlement characteristics of the weak subgrade. It reduces the deformation of the pavement. The study revealed that the added coir geotextile provided reinforcement to the BC soil and enhanced its performance.

References

Adams, C. A., Tuffour, Y. A., & Kwofie, S. (2016). Effects of soil properties and geogrid placement on CBR enhancement of lateritic soil for road pavement layers. *American Journal of Civil Engineering and Architecture*, *4*(2), 62−66.

Al-Qadi, I. L., Brandon, T. L., Valentine, R. J., Lacina, B. A., & Smith, T. E. (1994). Laboratory evaluation of geosynthetic-reinforced pavement sections. *Transportation Research Record*, *1439*, 25−31.

Babu, G. L. S., & Choksey, S. K. (2010). Model for analysis of fibre-reinforced clayey soil. *Geomechanics and Geoengineering: An International Journal*, *5*(4), 277−285.

Benjamim, C. V. D. S., Bueno, B. D. S., & Zornberg, J. G. (2007). Field monitoring evaluation of geotextile-reinforced soil-retaining walls. *Geosynthetics International*, *14*(2), 100−118.

Bueno, B.S., Benjamim, C.V., & Zornberg, J.G. (2005). Field performance of a full-scale retaining wall reinforced with non-woven geotextiles. *Slopes and retaining structures under seismic and static conditions*, ASCE GSP No. 140, Austin, Texas (CD-ROM).

Cancelli, A., Montanelli, F., Rimoldi, P., & Zhao, A. (1996). Full scale laboratory testing on geosynthetic-reinforced paved roads. Earth reinforcement, In: *Proceedings of the international symposium on earth reinforcement*, Fukuoka, Kyushu, Japan, November 1996 (pp. 573−578).

Dasaka, S. M., & Sumesh, K. S. (2011). Effect of coir fibre on the stress−strain behavior of a reconstituted fine grained soil. *Journal of Natural Fibers*, *8*(3), 189−204.

Giroud, J.P. (2009). An assessment of the use of geogrids in unpaved roads and unpaved areas, In: *Proceedings of the jubilee symposium on polymer geogrid reinforcement*, Institution of Civil Engineers, London, UK (pp. 23−36).

Giroud, J.P., Ah-Line, C., & Bonaparte, R. (1984). Design of unpaved roads and trafficked areas with geogrids. Polymer grid reinforcement. A conference sponsored by SERC and Netlon, Ltd., Thomas Telford, London, England (pp. 116−127).

Giroud, J. P., & Han, J. (2004). Design method for geogrid-reinforced unpaved roads. I. Development of design method. *Journal of Geotechnical and Geoenvironmental Engineering*, *130*(8), 775−786.

Giroud, J. P., & Noiray, L. (1981). Geotextile-reinforced unpaved roads. *Journal of Geotechnical Engineering Division, American Society of Civil Engineers*, *107*, 1233−1254, No GT9.

Haas R., Walls, J., & Carroll, R.G. (1988). Geogrid reinforcement of granular bases in flexible pavements. *Transportation research record* 1188, Washington DC (pp. 19−27).

Holtz, R.D., Christopher, B.R., & Berg, R.R. (1998). Geosynthetic design and construction guidelines. *Federal highway administration*, Washington, DC, FHWA-HI-98-038 (p. 460).

Hsieh, C., & Mao, L. (2005). A bench-scale performance test for evaluation of the geosynthetic reinforcement effects on granular base courses. *GRI-18 geosynthetics research and development in progress*, Geofrontiers, Austin, TX.

Miura, N., Sakai, A., Taesiri, Y., Yamanouchi, T., & Yasuhara, K. (1990). Polymer grid reinforced pavement on soft clay grounds. *Geotextiles and Geomembranes*, *9*(1), 99−123.

Ozdemir, M. A. (2016). Improvement in bearing capacity of a soft soil by addition of fly ash. *Procedia Engineering*, *143*, 498−505.

Perkins, S. W. (1999). Mechanical response of geosynthetic-reinforced flexible pavements. *Geosynthetics International*, *6*(5), 347−382.

Perkins, S. W., & Ismeik, M. (1997a). A synthesis and evaluation of geosynthetic-reinforced base course layers in flexible pavements: Part I experimental work. *Geosynthetics International*, *4*(6), 549−604.

Perkins, S.W. & Ismeik, M. (1997b). A synthesis and evaluation of geosynthetic-reinforced base course layers in flexible pavements: Part II analytical work. Geosynthetics international, 4(6), pp. 605−621.

Prasad, S. V., Paviandthran, C., & Rohatgi, P. K. (1983). Alkali treatment for coir fibres for coir-polyester composites. *Journal of Material Science*, *18*(5), 1443−1454.

Rao, G.V., & K. Balan (2000). *Coir geotextiles: Emerging trends*. Kerala State Coir Corporation Limited, Kerala, India.

Rao, G. V., & Dutta, R. K. (2006). Coir geotextiles in rural roads. *Highway Research Bulletin*, *74*, 9−15.

Sharma, A. K., & Sivapullaiah, P. V. (2016). Ground granulated blast furnace slag amended fly ash as an expansive soil stabilizer. *Soils and Foundations*, *56*(2), 205−212.

Som, N., & Sahu, R. B. (1999). Bearing capacity of a geotextile-reinforced unpaved road as a function of deformation − A model study. *Geosynthetics International*, *6*(1), 1−17.

Sridhar, R., & Prathap Kumar, M. T. (2018). Cyclic response of coir fibre-reinforced sand. *Innovative Infrastructure Solutions*, *3*(1), 13.

Subaida, E. A., Chandrakaran, S., & Sankar, N. (2009). Laboratory performance of unpaved roads reinforced with woven coir geotextiles. *Geotextiles and Geomembranes*, *27*(3), 204−210.

Yadu, L., & Tripathi, R. K. (2013). Effects of granulated blast furnace slag in the engineering behaviour of stabilized soft soil. *Procedia Engineering*, *51*, 125−131.

Zornberg, J.G. (2011). Advances in the use of geosynthetics in pavement design. In: Second national conference on geosynthetics, pp. 3−21.

Utilization of higher percentage of reclaimed asphalt pavement material in bituminous mixtures

11

Sridhar Raju and Bhanuprasad Katla
Department of Civil Engineering, Birla Institute of Technology and Science, Pilani Hyderabad Campus, Hyderabad, Telangana, India

11.1 Introduction

One of the main impediments to using reclaimed asphalt pavement (RAP) material higher than 30% is the variation in RAP gradation and diffusion time between the virgin bitumen and RAP binder (Ding et al., 2016; Katla et al., 2022). Due to higher temperatures and weathering, the binder in RAP material oxidizes further, making it stiffer and harder (Al-Qadi et al., 2007). Use of a softer grade binder or a rejuvenator or reduced RAP usage is a few of the strategies recommended by the researchers to mitigate the effects of a stiffer RAP binder (Bennert et al., 2014; Zhang et al., 2017). The use of SBS-modified binder and rejuvenators significantly influences the rutting and fatigue cracking resistance of the RAP-added mixtures (Katla et al., 2021; Zhou et al., 2019).

The literature has reported that increasing the RAP material in a bituminous mixture can enhance the stiffness by 25%−60% (Bonicelli et al., 2017; Rashid et al., 2019). Mogawer et al. (2016) showed that bituminous mixtures with 40% RAP had nearly 50% higher stiffness when compared to mixtures without RAP material. Chen et al. (2021) observed that adding 30%−50% RAP material to bituminous mixtures increased the brittleness and low-temperature cracking susceptibility. Therefore rejuvenators have been found to be the most successful additive for high RAP content bituminous mixtures and at the same time for improving the resistance to cracking. According to Mogawer et al. (2013), rejuvenators can reduce the stiffness of aged binders and improve the workability and fatigue resistance of RAP-added mixtures. Zaumanis et al. (2013) and Yu et al. (2014) have tried using 100% RAP material in the design of bituminous mixtures and concluded that only an appropriate rejuvenator improves the workability.

Ghabchi et al. (2015) conducted laboratory studies with 15%, 25%, and 40% RAP material to evaluate rutting, fatigue, and rheological performances using a PMB40 binder (Ghabchi et al., 2016). They carried out the multiple-stress creep recovery test on RAP-blended PMB40 and observed a decreased rutting resistance. The rejuvenator and PMB40 resulted in better performance with high RAP bituminous mixtures (Bhanuprasad et al., 2019). Though polymer modified bitumen (PMB) has the potential to improve rutting and fatigue resistance, pavement performance depends mainly on the compatibility of PMB with RAP bitumen (Huang & Turner, 2014).

Green Materials in Civil Engineering. DOI: https://doi.org/10.1016/B978-0-443-19106-0.00011-7

According to the literature, few researchers have highlighted the effect of rejuvenators and PMB binders on the characterization of the RAP mixtures. Furthermore, this researcher was limited to a lower amount of polymer content and one or two rejuvenators. Therefore this study highlights the use of a higher percentage of polymer in the modified binder and its effect on different rejuvenators.

11.2 Material

11.2.1 Reclaimed asphalt pavement

The RAP material was obtained after milling from national highway (NH-16) near Nellore, India. The milled material was obtained from 10-year-old severely distressed bituminous pavements. The binder was extracted from the RAP material using the Soxhlet extractor in accordance with ASTM D2712. The RAP binder content was calculated from 10 average extraction trials, and the binder content was found to be 3.5% by weight.

11.2.2 Virgin and reclaimed asphalt pavement aggregate properties

Virgin and RAP aggregates were tested for physical properties and the values obtained are tabulated in Table 11.1. The obtained values were compared with the book of specifications from the Ministry of Road Transport and Highways (MoRT&H-2013) published by the Indian Roads Congress.

11.2.3 Virgin and extracted reclaimed asphalt pavement binder

The virgin bitumen was obtained from Tiki Tar and Shell India Pvt. Ltd, Mumbai, India. The base binder was modified using Styrene-Butadiene-Styrene (SBS) block copolymers. The bitumen was modified in the laboratory using a high shear blender for 90 minutes, and after cross-linking, it was blended using a low shear blender for

Table 11.1 Properties of reclaimed asphalt pavement and virgin aggregates.

Properties	Virgin aggregates	Reclaimed asphalt pavement	Permissible limit	Test procedure
Impact value (%)	24.2	19.8	≤ 27.0	ASTM C535
Specific gravity	2.670	2.580	2.500−3.000	ASTM C127
Water absorption (%)	0.2	1.4	<2.0	ASTM C127
Abrasion value (%)	28.9	26.8	≤ 35.0	ASTM C535
Combined flakiness and elongation indices (%)	15.0	10.0	≤ 35.0	ASTM D4791

Table 11.2 Binder properties of 7% PMB and reclaimed asphalt pavement extracted binder.

Test	Reclaimed asphalt pavement binder	7% PMB	Standard
Penetration at 25°C, 5 s, 100 g	16.8	45.0	IS: 1203
Softening point, °C	68.6	98.0	IS: 1205
Specific gravity	1.040	1.030	IS: 1202
Temperature (°C) at G*/sin δ = 1 kPa	92.1	89.6	IS: 15462-2019
PG grade (G*/sin δ)	PG 88-10	PG 88-10	IS: 15462-2019
MSCR grade at 64°C	PG 64E-10	PG 64E-10	IS: 15462-2019

90 minutes. The RAP material was extracted using the Soxhlet extraction apparatus to find the binder content and to get the aged binder for further testing. The properties of RAP and modified binders are given in Table 11.2.

11.2.4 Rejuvenating agent and the process for arriving at the optimum dosage

Three rejuvenators were used to assess their impact on the performance of RAP-added mixtures. The bio-based rejuvenator used in this study is commercially available. The waste vegetable oil (WVO) was collected from the restaurant, while the waste engine oil (WEO) was obtained from the nearby automobile service center. Fig. 11.1 shows the three different rejuvenators used in this study. After collecting, WVO and WEO were sieved through #200 sieve to remove any debris if present. The viscosity and specific gravity of WVO and WEO are given in Table 11.3.

The optimum dosage of the rejuvenator was selected based on the change in the performance grade (PG) of the RAP binder when tested in accordance with AASHTO M320. The PG of RAP and VG30 binders were PG88-XX and PG64-XX, respectively. The rejuvenators used in this study were tested for different dosages, with 2% increment from the initially adopted 10% dosage. The minimum dosage of rejuvenators was chosen based on the research carried out earlier (Jia et al., 2014; Turner et al., 2015; Zaumanis et al., 2014). The results showed that the optimal rejuvenator dosages for bio-based rejuvenator, WVO, and WEO were 14%, 16%, and 20% by weight of RAP binder, respectively.

11.2.5 Aggregate gradation

BC-I grading was adopted with 0% and 50% RAP contents. A three-level fractionation process was adopted by obtaining RAP material passing 9.5, 4.75, and 1.18 mm sieves for maintaining homogeneity in the gradation (Katla et al., 2021). Fig. 11.2 shows the combined grading of virgin aggregate with 0% and 50% RAP contents.

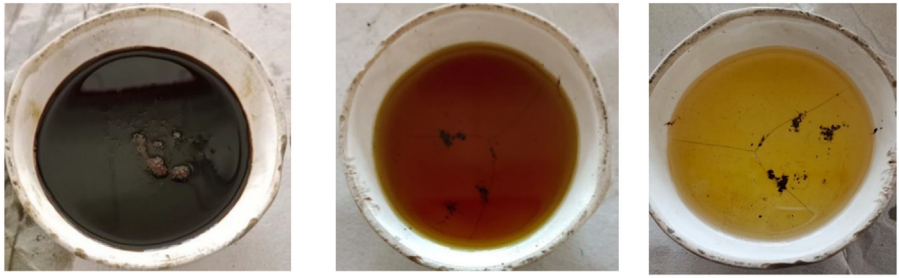

(A) (B) (C)

Figure 11.1 Three types of rejuvenators: (A) waste engine oil, (B) waste vegetable oil, (C) biobased.

Table 11.3 Viscosity and specific gravity of the rejuvenators.

Property	WEO	WVO	Biobased
Viscosity (cP) Specific gravity	172 0.96	162 0.93	153 0.95

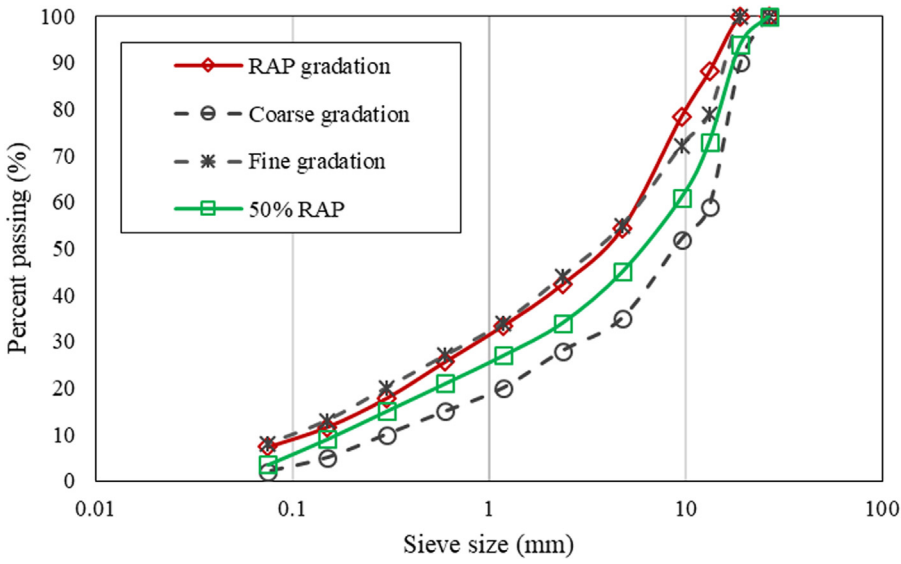

Figure 11.2 Combined gradation for reclaimed asphalt pavement and virgin aggregates experimental plan.

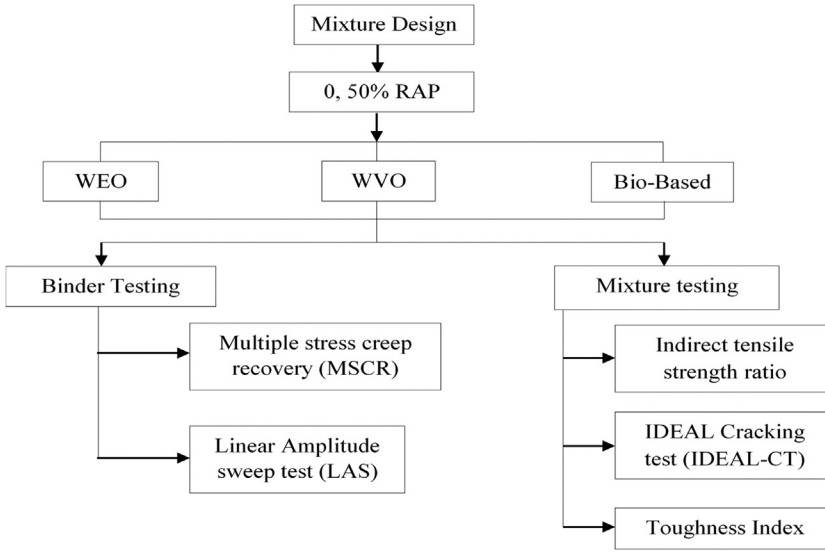

Figure 11.3 Flow chart.

The experimental plan of the study using 0% and 50% RAP contents by weight of the mixture, virgin binder with 7% polymer, bio-based rejuvenator, WVO and WEO is shown in Fig. 11.3.

11.3 Marshall mixture design

Marshall method of mixture design was followed as per the Asphalt Institute's Manual Series 2 (MS-2) for BC-I mixture design with and without RAP. Marshall specimens having 100 mm diameter and 63.5 ± 2.5 mm height were prepared at the rate of three specimens per binder content and at five different binder contents for arriving at the optimum binder content (OBC). The optimum quantity of rejuvenator was directly added to the heated RAP material (140°C) and mixed thoroughly for 30 seconds. The rejuvenated RAP material was added to the heated virgin aggregates (180°C) and thoroughly mixed for 30 seconds. To the above-blended aggregate mix, a hot virgin bitumen was added and mixed for another 120 seconds (Taherkhani & Noorian 2020; Veeraragavan et al., 2017). The mixture was subjected to the short-term aging by keeping in oven at 140°C for 2 hours and then compacted in a cylindrical Marshall mold by giving 75 blows on each face. The RAP added BC-I mixtures were denoted as RX-P, where X denotes the percentage of RAP in each mixture (say 0 and 50), and P denotes the rejuvenator type (say WEO or WVO). The volumetric properties and the strength parameters of BC-I mixtures are summarized in Table 11.4.

Table 11.4 Marshall parameters at optimum binder content for specimens with and without reclaimed asphalt pavement.

Parameter	0% RAP	50% RAP	MoRT&H Specification
Bulk density (kg/m^3)	2.382	2.385	–
Air voids (%)	4.0	4.0	3–6
VMA (%)	14.01	13.96	Min. 11
VFB (%)	71.4	71.3	65–75
Marshall stability, kN	11.8	13.8	Min. 9
Flow (mm)	3.2	2.5	2–4
Marshall quotient (kg/mm)	368	552	250–500
OBC (%)	5.3	5.6	–

11.4 Test method

11.4.1 Multiple stress creep recovery

The multiple stress creep recovery (MSCR) test was conducted in accordance with AASHTO M 332 using a DSR (Anton Paar MCR 302) at 64°C, considering the expected maximum pavement temperature. Bituminous binder samples were subjected to 10 repeated loading and unloading cycles at two different stress levels of 0.1 and 3.2 kPa. Each loading consists of 1 second creep load followed by a 9 second recovery time at two stress levels of 0.1 and 3.2 kPa. The nonrecoverable creep compliance (J_{nr}) and percent recovery (%R) are used to assess the rutting resistance of bitumen binders at high temperatures.

11.4.2 Linear amplitude sweep test

Linear amplitude sweep (LAS) test is used to evaluate the fatigue properties of bitumen according to AASHTO TP 101-12. An intermediate temperature of 25°C is generally adopted for the LAS test. As per ASHTO TP 101-12, the bitumen was tested in two stages, and the first stage was the frequency sweep test, followed by the amplitude sweep test. In the frequency sweep test, the frequency is varied from 0.2 to 30 Hz at a constant shear strain level of 0.1% in a linear viscoelastic range. It is conducted to obtain the undamaged material property. In the amplitude sweep test, the amplitude is varied between 0.1% and 30% at a constant frequency of 10 Hz. After carrying out the test, the fatigue life (N_f) is determined using Eq. (11.1).

$$N_f = A(\gamma_{max})^B \tag{11.1}$$

where

N_f is fatigue life;

A and B are the viscoelastic continuum damage model coefficients; and

γ_{max} is the percentage of maximum expected binder strain.

11.4.3 Indirect tensile strength test

Indirect tensile strength (ITS) test was conducted as per AASHTO T283 to find the moisture resistance of the RAP-added bituminous mixtures. Two sets of three specimens each were prepared at OBC with 7% air voids. One set of conditioned samples (ITS_{wet}) was kept in a water bath maintained at 60°C for 24 hours followed by 2 hour conditioning in a water bath maintained at 25°C. The other set of unconditioned samples (ITS_{dry}) were tested after keeping them in the air at 25°C for 4 hours. The ITS and the tensile strength ratio (TSR) were calculated using Eqs. (11.2) and (11.3), respectively.

$$ITS = \frac{2P}{\pi Dt} \tag{11.2}$$

where

1. P is the maximum load in N;
2. D is the diameter of the sample in mm; and
3. t is the thickness of the sample in mm.

$$\text{TSR} = \frac{ITS_{wet}}{ITS_{dry}} \times 100 \tag{11.3}$$

where

1. ITS_{wet} is the conditioned specimen; and
2. ITS_{dry} is the unconditioned specimen.

11.4.4 IDEAL cracking test

The ideal cracking test (IDEAL-CT) test developed by Zhou et al. (2017) has gained popularity as it is a simple test to perform and a quick indicator of the cracking resistance of the bituminous mixtures. A sample with a diameter of 150 mm and a thickness of 62 mm was prepared using a modified Marshall hammer. The IDEAL-CT test was performed at a constant loading rate of 50.8 m/min using a Zwick-Roell Z100 UTM with a 100 kN capacity, in accordance with ASTM D 8255-19. The cracking tolerance index (CT_{index}) was computed using Eq. (11.4), the fracture energy G_f was calculated using Eq. (11.5), and the 75% postpeak slope was calculated using Eq. (11.6). The test setup and the load versus displacement curve for one sample are shown in Fig. 11.4.

$$CT_{\text{index}} = \frac{t}{62} \times \frac{l_{75}}{D} \times \frac{G_f}{|m_{75}|} \times 10^6 \tag{11.4}$$

$$G_f = \frac{W_f}{t * D} \tag{11.5}$$

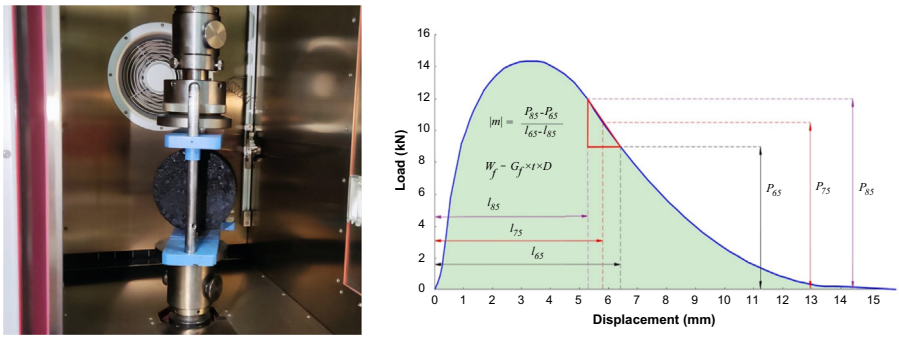

(A) Testing sample (B) Data analysis

Figure 11.4 Test setup and the load versus displacement curve for calculating the (A) testing sample and (B) IDEAL-CT.

$$|m_{75}| = \left|\frac{P_{85} - P_{65}}{l_{85} - l_{65}}\right| \tag{11.6}$$

where

1. G_f is fracture energy (J/m^2);
2. W_f is work done (Joules);
3. $|m_{75}|$ is postpeak slope (75% of peak load);
4. l_{75} is displacement corresponding to 75% of peak load;
5. t is sample thickness (mm);
6. D is sample diameter (mm);
7. P_{85} and P_{65} are loads at the postpeak stage (85% and 65% of peak load); and
8. l_{85} and l_{65} are displacements at the postpeak stage (85% and 65% of peak load).

11.4.5 Toughness index

The ITS test was carried out using Zwick/Roell Z100 universal testing machine at a loading rate of 50 mm/min, while maintaining the testing and the sample temperatures at 25°C as per AASHTO T 245. The load and vertical deformation is continuously recorded to calculate the normalized ITS value. The plot of normalized ITS versus strain is plotted to calculate the toughness index (TI) using Eq. (11.7) (see Fig. 11.5).

$$TI = \frac{A_\varepsilon - A_P}{(\varepsilon - \varepsilon_P) \times \sigma_{\text{peak}}} \tag{11.7}$$

where

A_ε is area under the normalized ITS-strain (%) curve up to the terminal strain;
ε is terminal strain;
A_P is area under normalized ITS-strain (%) curve up to strain ε_P;
ε_P is strain corresponding to peak stress; and
σ_{peak} is peak stress.

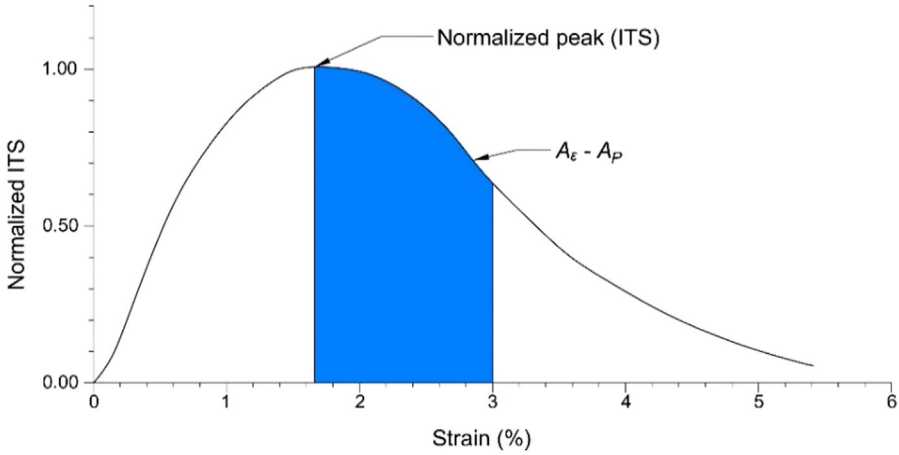

Figure 11.5 Normalized indirect tensile strength versus strain (%).

11.5 Result and discussion

11.5.1 Multiple stress creep recovery

Fig. 11.6 shows the nonrecoverable creep compliance (J_{nr}) at 3.2 kPa stress level. The rutting resistance of the binder is expected to be higher, with a lower J_{nr} value at 3.2 kPa. From the figure, it can be observed that 50% RAP-blended binder has a lesser J_{nr} value compared to the 7% SBS-modified binder without RAP. This is due to the addition of the stiffer RAP binder deteriorating the properties of PMB. On the other hand, the addition of the rejuvenator resulted in increased J_{nr} value. The bio-based rejuvenator resulted in a higher J_{nr} value compared to the other rejuvenators. The addition of rejuvenators helped in reducing the stiffness caused due to RAP-aged binders. The mixtures with 50% RAP, a bio-based rejuvenator, and a PMB with 7% SBS showed higher rutting and higher J_{nr} value at 3.2 kPa stress level, indicating the influence of bio-based rejuvenator in reducing the stiffness of RAP-aged binder. Fig. 11.7 shows the stress sensitivity ($J_{nr\ diff}$) of the binder. The stress sensitivity of the RAP-blended binder without a rejuvenator is higher than the rejuvenated binder. This could be due to the higher stiffness with the addition of the RAP binder. The addition of the rejuvenator resulted in decreased J_{nr_diff} value.

11.5.2 Linear amplitude sweep test

The LAS test was developed to determine the binders' fatigue tolerance at intermediate temperatures. The frequency sweep test was performed first, followed by the amplitude sweep test, in accordance with AASHTO TP 101-14, to characterize the binders fatigue resistance using the LAS test. The shear stress versus shear strain plot obtained from the amplitude sweep test and carried out for the 50%

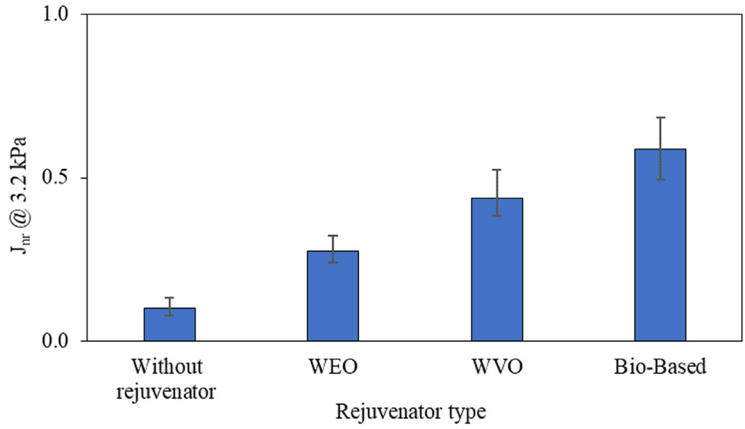

Figure 11.6 J_{nr} value for reclaimed asphalt pavement-blended PMB with different rejuvenators.

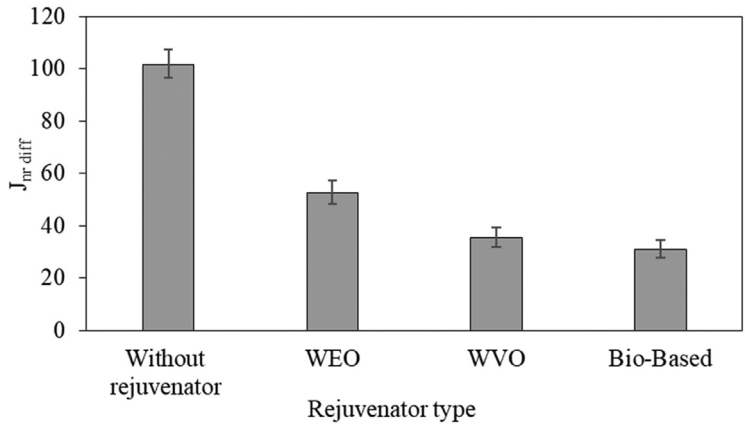

Figure 11.7 J_{nr_diff} value for reclaimed asphalt pavement-blended PMB with different rejuvenators.

RAP-blended binders with and without rejuvenators is shown in Fig. 11.8. A slow variation in shear stress with strain level was observed in the PMB with 7% SBS because the elastic network generated by polymer is less strain-dependent and has a stronger elastic response to loading. Fig. 11.8 shows that the inclusion of the RAP binder with 7% SBS-modified binder showed a sharp reduction in shear stress after reaching the peak load. This was due to the increased stiffness of RAP-blended binders, which indicated a higher strain dependency of the material. The strain dependency of the material was marginal for RAP-blended binders with rejuvenators, resulting in a lower binder stiffness.

Fig. 11.9 shows the fatigue life versus strain rate of the binders. The N_f value of the RAP-blended 7% SBS-modified binder was reduced by 44% when compared to

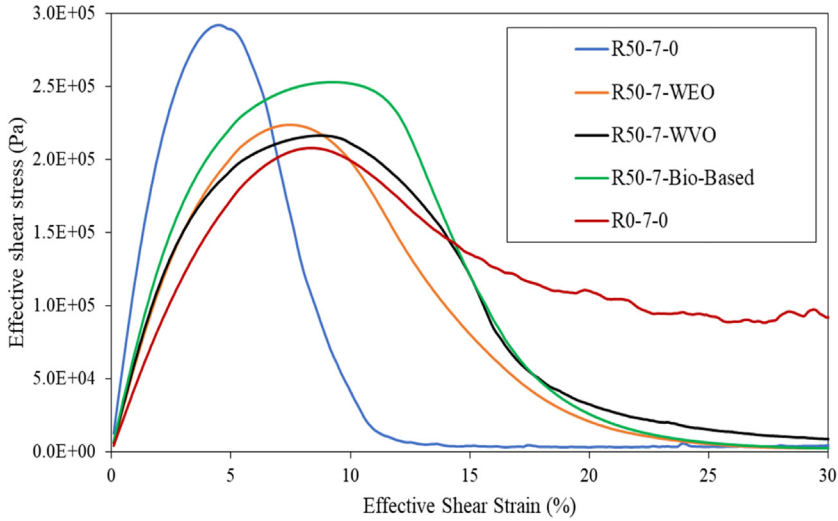

Figure 11.8 Shear stress versus shear strain of all combinations of binder.

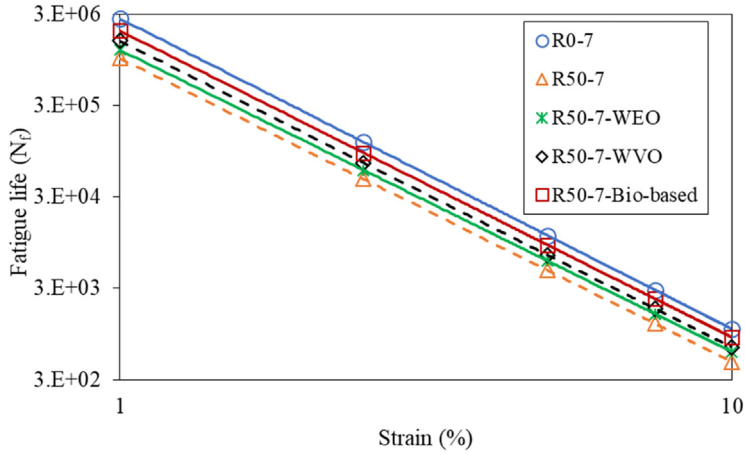

Figure 11.9 Fatigue-life curves.

the modified binder without RAP. However, with the inclusion of a bio-based rejuvenator, the N_f value increased by 1.9 times, while it increased by 1.6 times and 1.2 times with WVO and WEO, respectively.

11.5.3 Indirect tensile strength test

The ITS for conditioned (wet) and unconditioned (dry) specimens is shown in Fig. 11.10. The indirect tensile strength ratio (ITSR) in accordance with AASHTO

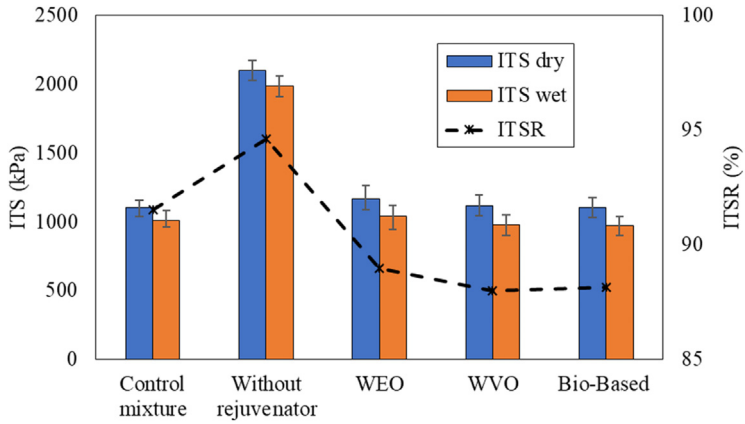

Figure 11.10 Tensile strength ratio values of the mixtures with and without reclaimed asphalt pavement.

T283 for all the specimens is shown in Fig. 11.10. The ITS values of 50% RAP-added bituminous mixtures prepared with the 7% SBS-modified binder increased by 67% compared to the bituminous mixture without RAP. The higher ITS values are due to the stiffer binder in RAP. On the other hand, the ITS value was reduced with the inclusion of the rejuvenator. ITS values were reduced by 34%, 37%, and 38% for 50% RAP with WEO, WVO, and bio-based rejuvenated mixtures with 7% SBS-modified binder, respectively. From the findings, it can be inferred that a bio-based rejuvenator is preferred over WVO and WEO for mixtures with a higher percentage of RAP to reduce the stiffness in RAP-aged binders. However, the addition of the renovator resulted in the reduction of the ITSR value, and higher reduction is for the bio-based rejuvenator, followed by the WVO and WEO.

11.5.4 IDEAL cracking test

The CT_{index} values are shown in Fig. 11.11. From the figure, it is observed that the CT_{index} was decreased by 48% for RAP-added bituminous mixtures with 7% SBS-modified binders compared to similar SBS content mixtures without RAP material. On the other hand, the addition of a rejuvenator to RAP mixtures increased the CT_{index}. RAP-aged binder can attribute this improvement to the absorption of oily fractions from the rejuvenator, thereby balancing the binder components and reducing the stiffness in an aged binder at intermediate temperatures. The RAP-added bituminous mixtures with a bio-based rejuvenator had a significantly higher CT_{index} value compared to WVO and WEO. The improvement in the CT_{index} is less in the WEO rejuvenator compared to the WVO and bio-based rejuvenator because the WEO softens the aged binder, not improving the physical properties of the binder.

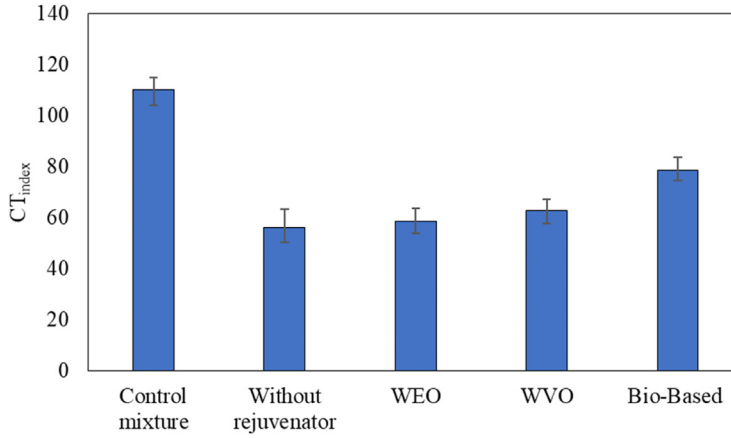

Figure 11.11 Cracking tolerance index results of all combinations of the mixtures.

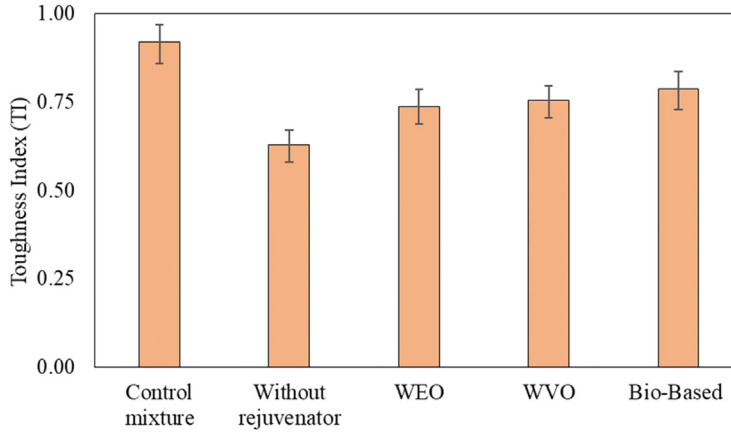

Figure 11.12 Toughness index of for all combinations of bituminous mixtures.

11.5.5 Toughness index

TI is a measure of a bituminous mixture's postfailure load-carrying capacity. The TI values of all the bituminous mixtures are shown in Fig. 11.12. With the addition of the RAP material, TI values decreased, indicating the brittleness of the samples. The TI values increased by 17%, 20%, and 25% with the addition of WEO, WVO, and bio-based rejuvenator, respectively, indicating an improvement in cracking resistance. Similar results were observed in the binder fatigue test.

11.6 Conclusions

1. The MSCR studies showed that the RAP binder blended with a 7% SBS-modified binder had the lowest J_{nr} value at 3.2 kPa stress level, indicating that the bitumen can perform better under extreme environmental and traffic conditions. The bio-based rejuvenator has the higher J_{nr} value, followed by WVO and WEO.
2. The RAP binder (50%) + bio-based rejuvenator with 7% SBS-modified binder showed significantly increased fatigue life compared to WVO and WEO.
3. The moisture resistance of the bituminous mixture with 50% RAP was higher than the control mixture. However, adding the rejuvenator resulted in a reduced ITSR value; a higher reduction was observed with the bio-based rejuvenator, followed by WVO and WEO.
4. The CT_{index} was decreased by 48% compared to similar SBS content mixtures without RAP material. The addition of a rejuvenator to RAP mixtures increased the $CT_{index.}$ The WEO had the lowest CT_{index} compared to the other two rejuvenators, indicating that it only softens the RAP binder and does not improve the chemical properties.
5. The TI value increased with the addition of rejuvenators but was not equal to a control mixture.

References

Al-Qadi, I. L., Elseifi, M., & Carpenter, S. H. (2007). *Reclaimed asphalt pavement—a literature review*. The National Academies Press.

Bennert, Thomas, Daniel, Jo. Sias, & Mogawer, Walaa (2014). Strategies for incorporating higher recycled asphalt pavement percentages. *Transportation Research Record: Journal of the Transportation Research Board*, *2445*(1), 83−93. Available from https://doi.org/10.3141/2445-10.

Bhanuprasad, K., Raju, S., Sarkar, A.K., Singh, S.K., & Ravindranath, S. (2019). Performance of reclaimed asphalt pavement (RAP) material in asphalt mixtures AAPA International flexible pavements conference.

Bonicelli, A., Calvi, P., Martinez-Arguelles, G., Fuentes, L., & Giustozzi, F. (2017). Experimental study on the use of rejuvenators and plastomeric polymers for improving durability of high RAP content asphalt mixtures. *Construction and Building Materials*, *155*, 37−44. Available from https://doi.org/10.1016/j.conbuildmat.2017.080.013.

Chen, Y., Chen, Z., Xiang, Q., Qin, W., & Yi, J. (2021). Research on the influence of RAP and aged asphalt on the performance of plant-mixed hot recycled asphalt mixture and blended asphalt. *Case Studies in Construction Materials*, *15*, e00722. Available from https://doi.org/10.1016/j.cscm.2021.e00722.

Ding, Y., Huang, B., & Shu, X. (2016). Characterizing blending efficiency of plant produced asphalt paving mixtures containing high RAP. *Construction and Building Materials*, *126*, 172−178. Available from https://doi.org/10.1016/j.conbuildmat.2016. 090.025.

Ghabchi, R., Singh, D., & Zaman, M. (2015). Laboratory evaluation of stiffness, low-temperature cracking, rutting, moisture damage, and fatigue performance of WMA mixes. *Road Materials and Pavement Design*, *16*(2), 334−357.

Ghabchi, R., Singh, D., Zaman, M., & Hossain, Z. (2016). Laboratory characterisation of asphalt mixes containing RAP and RAS. *International Journal of Pavement Engineering*,

17(9), 829–846. Available from https://doi.org/10.1080/10298436.2015.1022778, http://www.tandfonline.com/loi/gpav20.

Huang, S. C., & Turner, T. F. (2014). Aging characteristics of RAP blend binders: Rheological properties. *Journal of Materials in Civil Engineering*, *26*(5), 966–973. Available from https://doi.org/10.1061/(ASCE)MT.1943-5533.0000898.

Jia, X., Huang, B., Bowers, B. F., & Zhao, S. (2014). Infrared spectra and rheological properties of asphalt cement containing waste engine oil residues. *Construction and Building Materials*, *50*, 683–691.

Katla, B., Ravindra, W. A., Kota, S. K., & Raju, S. (2021). RAP-added SMA mixtures: How do they fare? *Journal of Materials in Civil Engineering*, *33*(8), 04021199.

Katla, B., Raju, S., Waim, A. R., & Danam, V. A. (2022). Utilization of higher percentages of RAP for improved mixture performance by adopting the process of fractionation. *International Journal of Pavement Research and Technology*, *15*(2), 349–366. Available from https://doi.org/10.1007/s42947-021-00026-0, https://link.springer.com/journal/42947.

Mogawer, W. S., Booshehrian, A., Vahidi, S., & Austerman, A. J. (2013). Evaluating the effect of rejuvenators on the degree of blending and performance of high RAP, RAS, and RAP/RAS mixtures. *Road Materials and Pavement Design*, *14*, 193–213. Available from https://doi.org/10.1080/14680629.2013.812836.

Mogawer, W. S., Fini, E. H., Austerman, A. J., Booshehrian, A., & Zada, B. (2016). Performance characteristics of high reclaimed asphalt pavement containing bio-modifier. *Road Materials and Pavement Design*, *17*(3), 753–767. Available from https://doi.org/10.1080/14680629.2015.1096820, http://www.tandf.co.uk/journals/TRMP.

Rashid, F., Hossain, Z., & Bhasin, A. (2019). Nanomechanistic properties of reclaimed asphalt pavement modified asphalt binders using an atomic force microscope. *International Journal of Pavement Engineering*, *20*(3), 357–365. Available from https://doi.org/10.1080/10298436.2017.1293268, http://www.tandfonline.com/loi/gpav20.

Taherkhani, H., & Noorian, F. (2020). Comparing the effects of waste engine and cooking oil on the properties of asphalt concrete containing reclaimed asphalt pavement (RAP). *Road Materials and Pavement Design*, *21*(5), 1238–1257.

Turner, P., Taylor, A., & Tran, P. N. (2015). Laboratory evaluation of SYLVAROADTM RP 1000 rejuvenator. *National Center for Asphalt Technology*, Auburn, AL.

Veeraragavan, R. K., Mallick, R. B., Tao, M., Zaumanis, M., Frank, R., & Bradbury, R. L. (2017). Laboratory comparison of rejuvenated 50% reclaimed asphalt pavement hot-mix asphalt with conventional 20% RAP mix. *Transportation Research Record*, *2633*(1), 69–79.

Yu, X., Zaumanis, M., Dos Santos, S., & Poulikakos, L. D. (2014). Rheological, microscopic, and chemical characterization of the rejuvenating effect on asphalt binders. *Fuel*, *135*, 162–171. Available from https://doi.org/10.1016/j.fuel.2014.060.038, http://www.journals.elsevier.com/fuel/.

Zaumanis, M., Mallick, R., & Frank, R. (2013). Evaluation of rejuvenator's effectiveness with conventional mix testing for 100% reclaimed Asphalt pavement mixtures. *Transportation Research Record*, *2370*, 17–25. Available from https://doi.org/10.3141/2370-03.

Zaumanis, M., Mallick, R. B., & Frank, R. (2014). 100% recycled hot mix asphalt: A review and analysis. *Resources, Conservation and Recycling*, *92*, 230–245.

Zhang, J., Simate, G. S., Hu, X., Souliman, M., & Walubita, L. F. (2017). Impact of recycled asphalt materials on asphalt binder properties and rutting and cracking performance of plant-produced mixtures. *Construction and Building Materials*, *155*, 654−663. Available from https://doi.org/10.1016/j.conbuildmat.2017.080.084.

Zhou, Z., Gu, X., Dong, Q., Ni, F., & Jiang, Y. (2019). Rutting and fatigue cracking performance of SBS-RAP blended binders with a rejuvenator. *Construction and Building Materials*, *203*, 294−303. Available from https://doi.org/10.1016/j.conbuildmat.2019.010.119.

Zhou, F., Im, S., Sun, L., & Scullion, T. (2017). Development of an IDEAL cracking test for asphalt mix design and QC/QA. *Road Materials and Pavement Design*, *18*(sup4), 405−427.

Mineral wastes

12

O. Kehinde, D. Hughes and E.H. Amalu
Department of Engineering, School of Computing, Engineering and Digital Technologies, Teesside University, Middlesbrough, United Kingdom

12.1 Introduction

Mineral extraction and mining are foundation industries which underpin the construction sector (Natural Resource Governance Institute, 2015). Current rates of extraction are unsustainable and have wide ranging environmental and socioeconomic repercussions (Aznar-Sánchez et al., 2018; Popovic et al., 2015). During mineral extraction, a range of wastes are generated; the global waste generation as it stands is anticipated to be over 1.2 billion tonnes annually, with rise expectation of 2.2 billion tonnes by 2025 (Yap et al., 2021). Mineral waste is produced worldwide at a rate of 2.54 million tonnes per year and is one of the largest global solid wastes (Al-Fakih et al., 2019; Kaza et al., 2018; Vijayan & Parthiban, 2020; Yliniemi et al., 2016). The standard end-of-life for mineral wastes is landfill (Kehinde et al., 2020). Therefore a better solution and utilization of these wastes is necessary.

Fig. 12.1 shows all waste generated in the United Kingdom by waste materials in 2018 alone.

Current in-organic materials within the construction sector like cement, concretes, and screeds are resource-intensive and contribute heavily to global CO_2 emissions (Brander, 2012; Vivien & Bedrosyan, 2014). CO_2 is produced in cement manufacturing by a mixture of process-related emissions from limestone decarbonation, along with the energy-related emissions from combustion processes (Barcelo et al., 2013). Though cement is a high-energy product, concrete on the other hand is one of the world's top CO_2-efficient and durable building materials (Portland Cement Association, n.d.). Alternative green cements or cement additives need to build on the durability and scale of traditional cements while addressing the inherent resource and production challenges.

12.2 Mineral waste

Mineral wastes are the by-products of the extraction and beneficiation of ores and minerals. They are generated in a range of forms, including waste rock, mill tailings, coal refuse, wash slimes, and wasted oil shale (Palmer et al., 2010). Mineral waste

Green Materials in Civil Engineering. DOI: https://doi.org/10.1016/B978-0-443-19106-0.00012-9

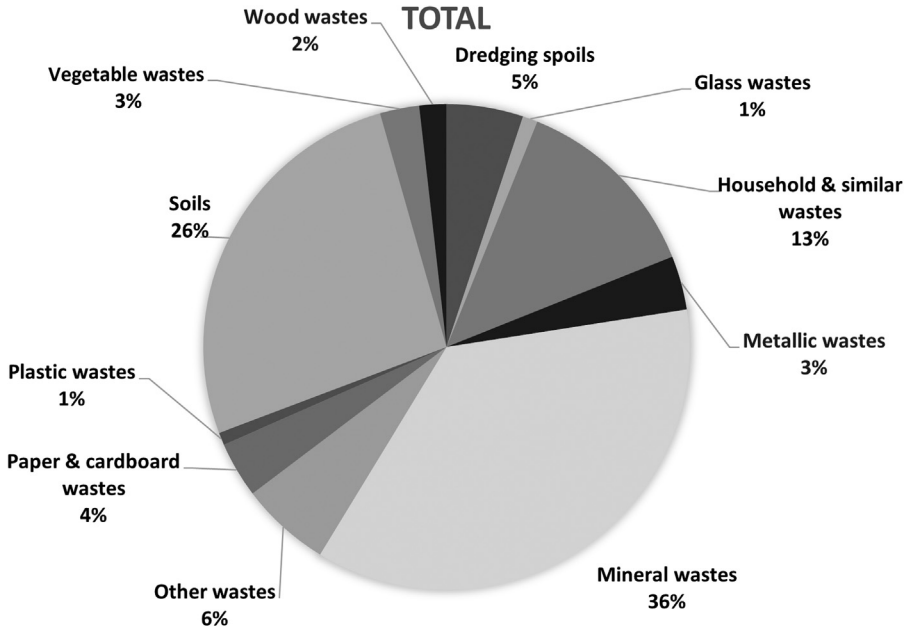

Figure 12.1 The United Kingdom and territory recycling rates for household waste, 2015−2020 (DEFRA, 2016).

from the extraction and processing of these minerals, ores, and rocks are commonly stored in waste piles, lagoons, or tailing heaps (Harrison et al., 2002). One of the main challenges of mineral wastes is storage (Agboola et al., 2020; Aznar-Sánchez et al., 2018) as, depending on their chemistry, they can be harmful to the environment and possess health-related risks to both humans and animals (Wei & Huang, 2001).

To mitigate these risks, mineral wastes are generally kept in tailing ponds, dams, or tips to avoid negative environmental impacts. As a consequence, mineral wastes can be in either a liquid or solid form. Detailed waste management and control treatment laws apply for extraction locations, as well as valorization routes where technically practicable (Bagur et al., 2009; Hudson-Edwards & Dold, 2015).

A deposition of mineral waste on site is presented in Fig. 12.2.

Depending on the metals, oil and gas, or minerals being extracted and their geological location, there are numerous types of mineral wastes generated (Ferguson, 2016). The main forms of mineral waste are discussed in the subsequent section.

Waste rock: The bulk of primary rock and soil that is extracted from the ground to reach a targeted mineral deposit is referred to as waste rock. Waste rock is made up of coarse, pulverized, or blocky material of various shapes and sizes, ranging between big boulders or blocks to micro grain-size particles and powder. To extract 1 tonne of mineral ore, around 5 tonnes of waste rock are typically displaced. Surface mining operations like open-pit copper, phosphate, uranium, iron, and taconite mines generate large quantities of waste rock, while underground mining

Figure 12.2 Mineral waste tailing heap (background) with a close-up of the material in the foreground.

produces lower quantities (Barton, 2008; Olivier, 2016). Tailings and waste rock are the two most prevalent mine wastes that requires short- and long-term management (Gorakhki & Bareither, 2017).

Fines: Quarry fines are a residual by-product of rock or aggregate processing that has high material value for several civil engineering applications (Zhang et al., 2019). Quarry fines are produced unavoidably as a result of quarrying and the related processing procedures. The quantity produced is determined by the geology, the type of rock quarry, the effectiveness of the extraction, processing, and the regional market for quarried goods (Mitchell, 2009). Fines particle size again depends on geology but can be defined as less than 6 mm or less than 100 microns (Wei & Huang, 2001).

Mill tailings: Mill tailings are a sludgy material that arise from mineral processing. They are often poisonous and may include significant amounts of manufacturing chemicals; therefore they should not be released into the environment but rather are pumped into tailing ponds using slurry pumps. Mill tailing waste is stored and held in these ponds (Gorakhki & Bareither, 2017; Australian Centre for Geomechanics, 2013). The majority of mill tailings are extremely tiny particles discarded during raw material grinding, screening, or processing. They are usually hard, angular siliceous particles with a substantial proportion of fines and are often homogeneous in character and size. Mill tailings generally range in particle size from sand to silt-clay, depending on the severity of processing necessary to restore the ore (ELAW, 2010).

Coal refuse: Coal mining mineral wastes are particularly hazardous, including heap instability, residual coal self-heating, acid mine drainage owing to sulfide oxidation, water pollution, air pollution, and a variety of other issues (Nádudvari & Fabiańska, 2016; Pinetown et al., 2007; Pudasainee et al., 2017; Querol et al., 2011; Zhao et al., 2007). The discarded material created during the processing and washing of coal is known as coal refuse. The reject material commonly consists of different proportions of slate, shale, sandstone, siltstone, and clay minerals that occur within or close to the coal seam, as well as some coal that is not separated during processing (Vriens et al., 2020).

Slimes: 11%−19% of the raw material generated during mineral extraction and processing are wasted in slime ponds/tailing dams as slimes (Chintala et al., 2016). These wastes are produced by processes that employ high volumes of water, forming slurries with low solids concentration and fines in suspension, and even after long periods of drying, they usually contain high levels of water. Large holding ponds are used to store these rejected materials. There are no practically recognized uses for washing slimes due to the difficulty in drying.

Oil shale: The use of fossil fuels is a major source of pollution in the environment (Leben et al., 2019). Oil shale is extracted for its recoverable oil. Spent oil shale is a waste by-product that remains after oil extraction. It is a dark residue formed whenever oil shale is retorted (vaporized and distilled) to form kerogen, an organic oil-bearing material. Oil shale is also a sedimentary rock rich in hydrogen-rich organic materials known as kerogen. The genesis, composition, calorific value, and oil output of distinct oil shales vary depending on the deposit (Easac, 2007).

12.3 Utilization of mineral wastes

Green concrete technology has accelerated rapidly in recent years. Specific focus has been on traditional pozzolanic materials like ground granulated blast furnace slag (GGBS) and fly ash. Clearly there is significant opportunity in using mineral wastes. These opportunities are summarized as: (1) mineral stabilization in an inert matrix, (2) use as a pozzolanic filler, (3) uses in alkali-activated and geopolymer cements, and (4) applications for mineral carbon sequestration (MCS) within construction products.

12.3.1 Utilization of mineral wastes in cement and concrete as in-active fillers

Aggregates, fines, and fillers are substances used in traditional cementitious materials and concrete whose primary functions depend on shape and size. They can work with cement in a variety of ways, such as to increase particle packing, provide new qualities to freshly laid concrete, and lower cement content without sacrificing strength (Murtazaev et al., 2015). Currently, the vast majority of mineral wastes are valorized by employing them as fillers for construction. Utilizing mineral waste

materials to build dikes, impoundments, haul roads, and mine rehabilitation projects such as cemented mine backfill is considered a common practice in the mining sector (Collins & Miller, n.d.). The process of utilizing mineral wastes within concrete has been shown to be environmentally beneficial (Gou et al., 2019). The use of quarry fines for soil stabilization or as a replacement for sand in concrete are also well established (Amadi, 2014; Gurbuz, 2015; Jones et al., 2015; Karakuş, 2011; Karaşahin & Terzi, 2007; Medina et al., 2018; Oncu & Bilsel, 2016; Rai et al., 2014; Sivrikaya et al., 2014; Vijayalakshmi et al., 2013). Quarry fines have also been valorized for agricultural applications such as aglimmer, fertilizer filler, and animal feeds, environmental applications such as liming ponds and watersheds, preventing landfill leachate, as well as other uses like industrial fillers and paint-related industries (Kumar & Hudson, 1992).

Even though a filler is inactive, it may also increase the strength of the concrete by adding more fine particles to the paste rather than through a chemical reaction (Moosberg et al., 2003). Abbass et al. (2019) have demonstrated how ultrafine mineral additions up to around 8% contribute to compressive strength by 8% while higher percentages lead to significant reductions in strength as void spaces are saturated.

Molybdenum mine tailings have been demonstrated for creating masonry mortar with characteristics that are comparable to those of traditional mortar and in enhancing the strength of mortar by reducing the cement content (Cui et al., 2022).

Mineral fillers are crucial for making asphalt mixtures more stable and workable (Awoyera et al., 2019; Fan et al., 2019). Use of coal mine waste rocks have been demonstrated in local road construction as a novel way of recycling by solidification (Amrani et al., 2020). Similarly, oil shale has been demonstrated for highway engineering construction in particular circumstances and regions, depending on aggregates calorific value, freezing and thawing resistance, and fragmentation resistance (Tohver, 2010; United States Congress: Oil Shale Advisory Committee, 1980).

12.3.2 Mineral wastes for use as supplementary cementitious materials

Supplementary cementitious materials (SCMs) are cement alternative materials which exhibit pozzolanic and/or cementitious properties (Panesar, 2019). The use of SCMs have been shown as an efficient way to reduce embodied CO_2 within cement (Rakhimov et al., 2017). SCMs are solubilized siliceous, aluminosiliceous, or calcareous aluminosiliceous particles that can be used to substitute clinker in cements or Portland cement in concrete mixtures (Juenger et al., 2019). SCMs such as fly ash, GGBS, silica fume, calcined clays, and natural pozzolans are widely blended with clinker to form Portland cement or used as a partial substitute for Portland cement in concrete (Juenger & Siddique, 2015). Incorporating various SCMs modifies the characteristics of concrete to some extent in both the fresh and hardened phases (Johari et al., 2011).

The addition of SCMs into cements has been shown to improve concrete durability, strength, and workability as well as positively impact economic and environmental factors (Ghrici et al., 2007; Pacewska & Wilińska, 2020; Snellings et al., 2012).

Because SCMs encompasses so many distinct materials, it is difficult to categorize precisely; however, pozzolanic materials maybe classified into two types: natural pozzolans and artificial pozzolans. Fig. 12.3 shows the classification of pozzolans and their various examples with a focus on mineral sources.

Hamidi et al. (2013) used andesitic material, which is a mineral waste found mostly in Algeria blended with cement; the result was a decrease in the energy used to make a tonne of binder. This study showed that activating mineral waste for use as a pozzolanic filler reduced the embodied CO_2 in producing cement, as the filler helped facilitate reaction using less heat. Similar results have been seen observed in basalt and sodium bentonite (El-Didamony et al., 2015).

The most widely used SCMs are GGBS, a waste of the iron industry, fly ash, and waste from coal combustion in power plants. The use of fly ash and blast furnace slag instead of cement has been widely implemented as a way to lessen the cement industry's environmental impact (Ma et al., 2016).

Studies into novel sources of SCMs and their impacts on cementitious materials have accelerated in recent years, and this trend will continue as demands for these materials develop (Juenger et al., 2019).

12.3.3 Geopolymer and alkali-activated cements

Given the volume of mineral wastes generated and the environmental impacts of their disposal, research has focused on the activation of mineral wastes in geopolymers and alkali-activated cements (AAC). Research has shown great improvements in the utilization of these wastes, by mixing with alkali activators (Davidovits, 2011) in mostly reducing environmental impacts and improving mechanical properties. In addition to reducing the environmental problems caused by the mining sector, alkali-activation or geopolymerization technology is a viable method for the management of mining wastes (Allahverdi et al., 2013). It has the potential to significantly reduce the consumption of raw materials used in construction applications (Gökçe et al., 2021; Mabroum et al., 2020). Geopolymers and AAC have the potential to be a significant and cost-effective (Rafeet et al., 2017) part of the future toolset of sustainable building materials when made from locally accessible raw materials, with well-formulated mix, and production under acceptable levels of quality control (Provis, 2018). A typical example is the fly ash-based geopolymer (FAGP) and alkali-activated slag (AAS). Adam (2009) showed the impact of activating and dosing FAGP and AAS with Na_2O. In AAS concrete, the research indicated that a Na_2O dosage of 5% and an activator modulus of Ms = 1, at a water-to-binder ratio (W/b) of 0.45 were the ideal mix; while the appropriate mix for FA-based geopolymer concrete was Ms = 1.25 at W/b = 0.29. However, a greater Na_2O dosage may be employed if higher strength is necessary or required as the performance of the FA-based geopolymer concrete produced by the 7.5% Na_2O dosage was comparable to that of a concrete made from Ordinary Portland Cement (OPC).

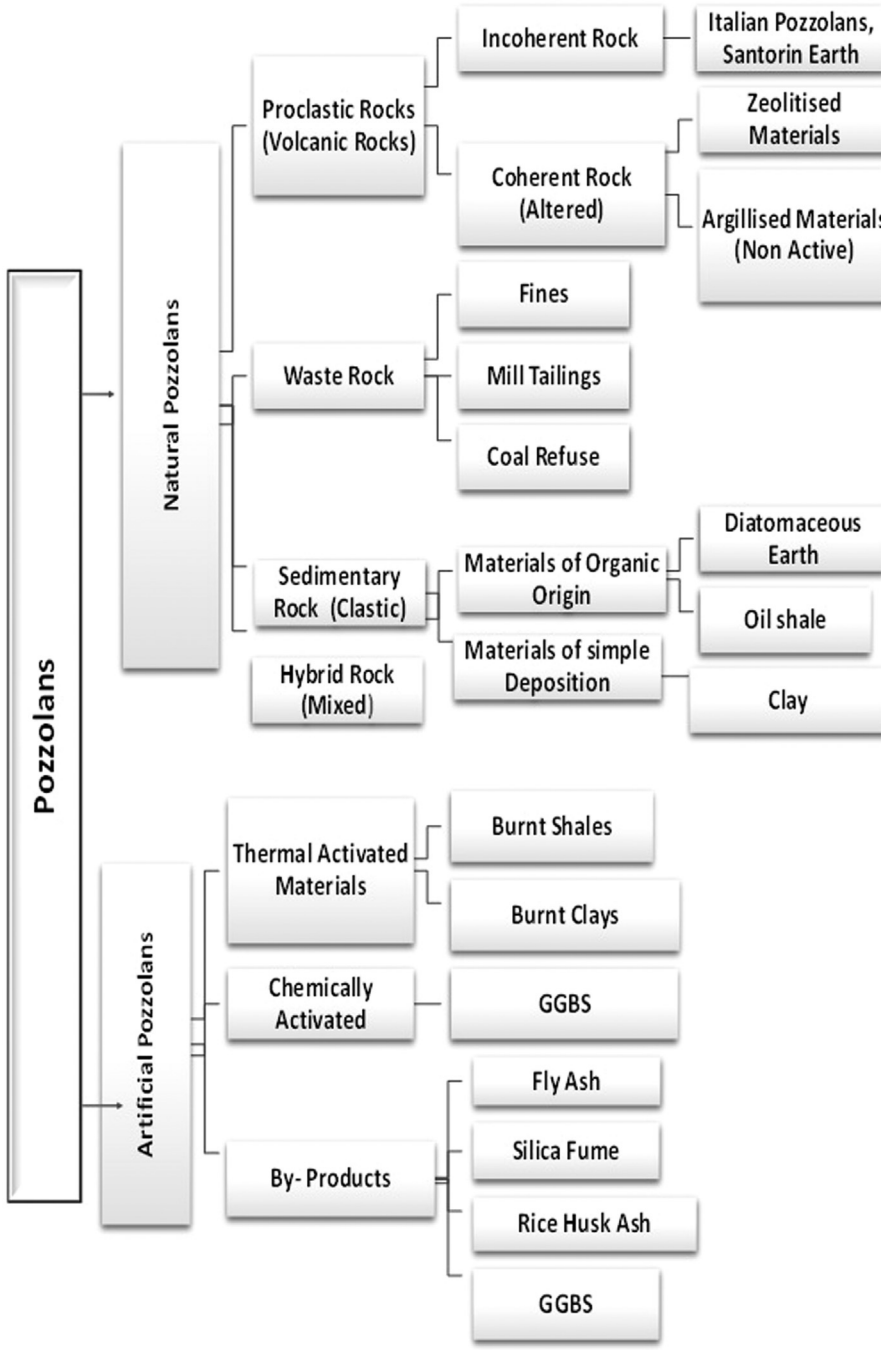

Figure 12.3 Classification of pozzolans (National Geographic Society, n.d.; Nemet et al., 2018; Scrivener & Capmas, 2004).

For the successful manufacturing of AACs with compressive strength of 35−70 MPa, GGBS can be combined with steel, electric arc and ladle furnace, ferroalloy, copper, and silico-manganese slags (Rakhimova, 2020; Turner & Collins, 2013; Zhang et al., 2020). Materials made of AA copper slag can offer good early strength, Lithium slag can be used after preheating to 700°C. Furthermore, it has been discovered that ferrochrome slag concrete has good fire resistance (Farhan et al., 2019; Rakhimova, 2020). Red mud could also be used with fly ash and GGBS as well as other materials (silica fume, metakaolin, waste mudstone, and rice husk ash) in producing concrete that is comparable with OPC (Kumar et al., 2021). Fig. 12.4 illustrates the comparative compressive strength performance of a range of mineral-derived geopolymers and AACs compared to traditional OPC.

Alsalman et al. (2021) compared AAC to OPC; the findings showed that AAC has the potential to be a more environmentally friendly alternative to OPC for similar performance. AAC has also been employed as an alternate binder to OPC in fiber-reinforced concretes, proving to be more cost-effective and environmentally friendly (Kim et al., 2015).

Mine tailings can be used in cementitious binders not only as fillers but also as an alkali-activated material precursor, a supplemental cementitious material, a direct cement substitute, or as a raw material for clinker. For these uses, mine tailings may undergo chemical and physical alteration by thermal treatment, alkali activation, and grinding to acquire desired qualities (Maruthupandian et al., 2021; Mporas et al., 2020).

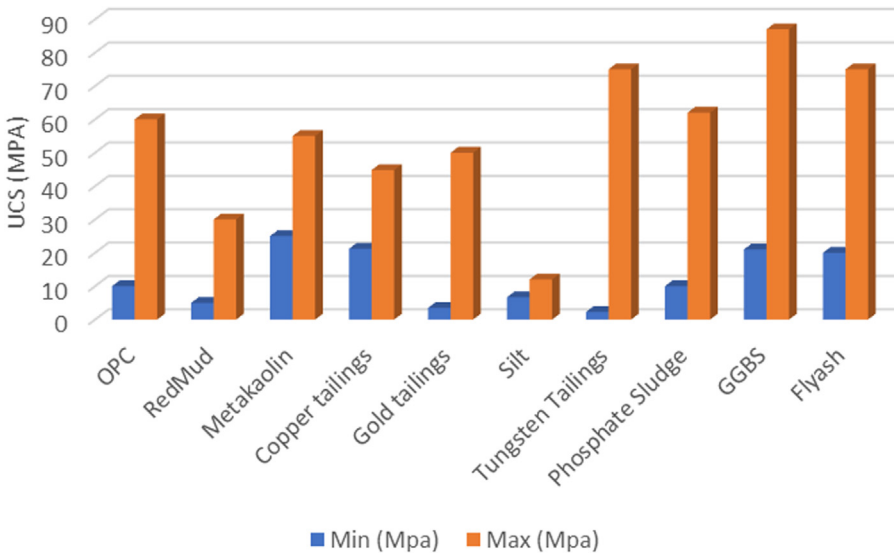

Figure 12.4 Comparison of reported compressive strengths for mineral-derived geopolymers and alkali-activated cements compared to Ordinary Portland Cement (Duxson et al., 2005; Mabroum et al., 2020; Ozer & Soyer-Uzun, 2015; Solouki et al., 2020; Ukritnukun et al., 2021; Ye et al., 2016; Zhang et al., 2017).

12.3.4 Application for mineral carbon sequestration within construction products or during manufacture

There is no doubt that the global climate system is warming; since the late 19th century, average global temperatures have increased by around 0.8°C temperature, and over the decades, they have increased at a rate of about 0.2°C temperature each year (Jenkins et al., 2009). Owing to this rise in carbon dioxide emissions that are detrimental to the environment and human health, climate change and global warming are becoming serious issues on a worldwide scale (Yang et al., 2008). The recent warming has probably been significantly influenced by human activity (Jenkins et al., 2009; Prigiobbe et al., 2009). It is undeniable that the use of carbon fuels in the construction, industrial, and transport sectors has been a critical contributor in the exponential growth of carbon emissions since the start of the industrial revolution. However, as a result, in order to reduce emissions, experts are identifying alternative energy sources to replace fossil fuels (Minx et al., 2021). A single solution would not be enough to reduce the carbon footprint due to the high level of energy consumption; this is where carbon capture and storage (CCS) and MCS come into play.

CCS is by far the most extensively utilized method of decreasing CO_2 emissions. This technology captures CO_2 from an emitter, such as a cement plant, refineries, or thermal power plant and often injects it into underground storage or uses it for other purposes, such as food processing and enhanced oil recovery in the petrochemical sector (Markewitz et al., 2012). While MCS or mineral carbonation (MC) is a method of carbon capture and sequestration which involves reacting carbon dioxide with alkali substrates to create solid carbonate minerals (Woodall et al., 2019). Using the former techniques is expensive and consumes a lot of energy (Huijgen et al., 2007; Nemet et al., 2018; Pera-Titus, 2014; Sipilä et al., 2008). Therefore MC methods are being investigated due to their low cost, sustainability, reliability, and availability. MC is also a promising option, owing to its secure and a stable CO_2 storage (Ghacham et al., 2016).

Huntzinger et al. (2009) looked at the viability of carbon sequestration in cement kiln dust (CKD) under different conditions; the results were at normal pressures and temperatures, CKD quickly absorbs CO_2. Kusin et al. (2020) aimed to assess the functionality of MC of sedimentary mine tailings and their possible reuse as SCM; waste materials from gold and limestone quarries were salvaged for use as SCM during construction purposes and to test the feasibility for carbon sequestration. The results where limestone tailings were expedited at a pH level of 10 and a reduced particle size of about 38 μm demonstrated a greater compressive strength and a lower water absorption than gold tailings (Kusin et al., 2020). Although gold tailings demonstrated pozzolanic characteristics, resulting in lower carbonation potential, those of limestone are more advisable. Higher temperature and pressure combined with finely powdered silicate ash can speed up carbon sequestration during manufacturing; however, the costs are high and restrict industrial application due to the fact that a significant portion of the estimated costs ($>60\%$) of the total costs is related to grinding the silicate minerals (Salek et al., 2013). Along with

great stability and availability, clay minerals have also shown potential behavior for catalysis and adsorption in CO_2 capture processes (Chouikhi et al., 2019). If all waste products are converted to CCS, mineral waste resources that are suitable for mineralization have the theoretical capacity to absorb 14 Mt of CO_2 annually (Sanna et al., 2012).

The most promising mineral wastes for use in MS are strong alkalis; these are usually calcium or magnesium-containing or from alternative sources like ashes from waste incineration, demolition waste and slags (Huijgen et al., 2005). Carbonation of these wastes can also reduce the presence of environmentally harmful components.

12.4 Optimal utilization of mineral wastes

Having reviewed both the available mineral waste feedstocks and the currently available methods of utilization, it is important to evaluate the suitability of these methods for different material types. Fig. 12.5 shows a decision tree for optimal mineral waste feedstocks utilization.

The decision tree demonstrates recommended outcomes based on mineral chemistry of mineral waste feedstocks. It begins with the waste feedstock, oxides like MgO and CaO may eventually generate expansion reactions that reduce the compressive strength of concrete. Such oxides may ultimately lead to the deterioration of concrete or alternative cementitious materials or alternative cementitious materials if they were present in significant concentrations (Borhan, 2017). Thus feedstocks rich in these minerals are well suited to CO_2 mineral (Rajamathi et al., 2021; Yan et al., 2019; Yang et al., 2013). Once carbonated, the minerals commonly become inert and may be used as inert

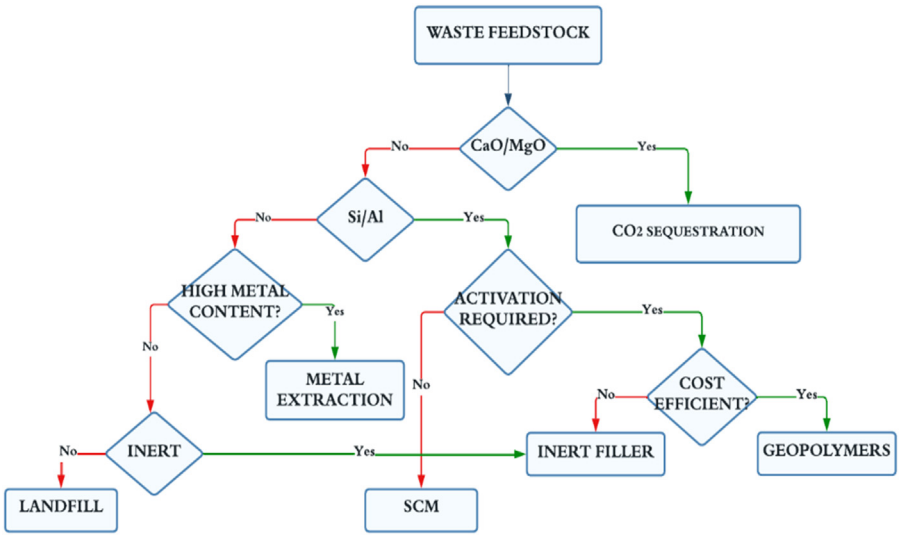

Figure 12.5 Decision tree for optimal mineral waste feedstocks utilization.

fillers. The second decision juncture separates minerals low in CaO/MgO and Si/Al from those which are Si/Al rich. For those with low Si/Al content, there is little scope for active use within traditional cementitious materials. Where there is a high metal content, metal recovery can be considered. The remaining materials which are low in CaO/MgO and Si/Al can be used as inert filler if chemically stable within the binder structure, if they contain reactive compounds; however, there remain limited opportunities for valorization at the present time. For materials which are rich in Si/Al, the opportunities as active binder constituents exist. This can be in the form of SCMs or geopolymer cements as discussed in the previous sections. The third key decision juncture is if the waste feedstock requires activation to be used as a cementitious material. SCMs exhibit pozzolanic and/or cementitious properties in the form of solubilized siliceous, aluminosiliceous, or calcareous aluminosiliceous particles. They require no or little activation before use. These can be directly implemented as a substitute to clinker in cements or Portland cement in concrete mixtures. They are usually in the form of industrial by-products like GGBS or fly ash. While activation can be used to generate SCMs, it is increasingly considered environmentally favorable to use activation for the generation of low carbon cements like geopolymers and AAC. Activation can be in the form of thermal, mechanical, chemical, or hybrid methods. Activation efficiency is a function of the percentage of Si/Al and other bindable components within the minerals and also the ability for mineral conversion to a reactive amorphous phase. Where this is not cost- or energy-efficient, minerals can still be used as inert fillers. The decision tree will support mineral waste planning and handling to drive the development of green materials.

12.5 Conclusions

This chapter has presented a discussion on mineral waste in the construction and process industry. It defines key terminologies associated with mineral wastes while discussing its main forms, which include waste rock, mill tailings, coal refuse, wash slimes, and oil shale.

The work supports identification of alternative mineral wastes as a route to achieving sustainable development in the building and construction industry. This follows presentation on the need to find replacements for OPC owing to continued environmental concern arising from its usage. Thus it examined implementation and utilization of mineral waste in four key areas which include use: (1) as inactive fillers, (2) as SCM, (3) as geopolymer and AACs, and (4) for use in MCS.

Examples of previous utilization of mineral wastes within cementitious materials have been successful with increased environmental benefit. In addition, it shares that use of mineral wastes as SCMs significantly lowers the environmental negative impact caused by the cement industry. Furthermore, mineral alkali-activation or geopolymerization technology is shown to offer future environmental and financial advantages. It is discussed how the role of alkali mineral wastes have applications in MCS, involving ashes and slags waste rich in calcium or magnesium.

Mineral waste-based cementitious materials are compared to OPC based on maximum and minimum compressive strengths, demonstrating the mechanical potential of mineral waste-derived green cements.

Finally, a decision tree is developed based on utilization opportunities to inform mineral waste planning and handling and to drive the development of green materials within the construction sector.

References

Abbass, W., Khan, M. I., & Mourad, S. (2019). Experimentation and predictive models for properties of concrete added with active and inactive SiO_2 fillers. *Materials*, *12*(2). Available from https://doi.org/10.3390/ma12020299.

Adam, A. (2009). *Strength and durability properties of alkali activated slag and fly ash-based geopolymer concrete*. Doctoral dissertation, RMIT University.

Agboola, O., Babatunde, D. E., Isaac Fayomi, O. S., Sadiku, E. R., Popoola, P., Moropeng, L., Yahaya, A., & Mamudu, O. A. (2020). A review on the impact of mining operation: Monitoring, assessment and management. *Results in Engineering*, *8*, 100181. Available from https://doi.org/10.1016/j.rineng.2020.100181, October.

Al-Fakih, A., Mohammed, B. S., Liew, M. S., & Nikbakht, E. (2019). Incorporation of waste materials in the manufacture of masonry bricks: An update review. *Journal of Building Engineering*, *21*, 37−54. Available from https://doi.org/10.1016/j.jobe.2018.09.023, September 2018.

Allahverdi, A., & Kani, E. N. (2013). *Use of construction and demolition waste (CDW) for alkali-activated or geopolymer cements*. *Woodhead publishing series in civil and structural engineering* (pp. 439−475). Woodhead Publishing In F. Pacheco-Torgal, V.W.Y. Tam, J.A. Labrincha, Y. Ding, & J.B.T.-H. of R.C. and D.W. de Brito (Eds.). Available from https://doi.org/10.1533/9780857096906.3.439.

Alsalman, A., Assi, L. N., Kareem, R. S., Carter, K., & Ziehl, P. (2021). Energy and CO2 emission assessments of alkali-activated concrete and Ordinary Portland Cement concrete: A comparative analysis of different grades of concrete. *Cleaner Environmental Systems*, *3*, 100047. Available from https://doi.org/10.1016/j.cesys.2021.100047, April.

Amadi, A. A. (2014). Enhancing durability of quarry fines modified black cotton soil subgrade with cement kiln dust stabilization. *Transportation Geotechnics*, *1*(1), 55−61. Available from https://doi.org/10.1016/j.trgeo.2014.02.002.

Amrani, M., Taha, Y., Haloui, Y. E., Benzaazoua, M., & Hakkou, R. (2020). Sustainable reuse of coal mine waste: Experimental and economic assessments for embankments and pavement layer applications in morocco. *Minerals*, *10*(10), 1−17. Available from https://doi.org/10.3390/min10100851.

Australian Centre for Geomechanics. (2013). Chapter 10 Tailings and waste rock management. Twin Bonanza 1 Gold Mine, ABM RESOURCES NL, DRAFT Environmental Impact Statement. https://shorturl.at/pFIW5.

Awoyera, P. O., Adesina, A., & Gobinath, R. (2019). Role of recycling fine materials as filler for improving performance of concrete − A review. *Australian Journal of Civil Engineering*, *17*(2), 85−95. Available from https://doi.org/10.1080/14488353.2019.1626692.

Aznar-Sánchez, J. A., García-Gómez, J. J., Velasco-Muñoz, J. F., & Carretero-Gómez, A. (2018). Mining waste and its sustainable management: Advances in worldwide research. *Minerals*, *8*(7). Available from https://doi.org/10.3390/min8070284.

Bagur, M. G., Morales, S., & López-Chicano, M. (2009). Evaluation of the environmental contamination at an abandoned mining site using multivariate statistical techniques-The Rodalquilar (Southern Spain) mining district. *Talanta*, *80*(1), 377−384. Available from https://doi.org/10.1016/j.talanta.2009.06.075.

Barcelo, L., Kline, J., Walenta, G., & Gartner, E. (2013). *Cement and carbon emissions* (2008, pp. 1−15). Available from https://www.researchgate.net/profile/Ellis_Gartner/publication/257895979_Cement_and_carbon_emissions/links/56cad3fb08aee3cee54075ff.pdf%0Ahttps://www.researchgate.net/profile/Ellis_Gartner/publication/257895979_Cement_and_carbon_emissions/links/56cad3fb08.

Barton, N. (2008). Shear strength of rockfill, interfaces and rock joints, and their points of contact in rock dump design. In: *Rock dumps 2008: Proceedings of the First International Seminar on the Management of Rock Dumps, Stockpiles and Heap Leach Pads* (pp. 3−17).

Borhan, T. M. (2017). Combined effect of MgO and So3 contents in cement on compressive strength of concrete. *Journal For Engineering Sciences*, *9*(4), 492−502.

Brander, M. (2012, August 2−4). GHGs-CO2-CO2e-and-Carbon-What-Do-These-Mean-v2.1. *Ecometrica*.

Chintala, R., Rath, R. K., & Kumar, A. (2016). Recovery of iron values from iron ore slimes using reagents. *Journal of Materials & Metallurgical Engineering*, *6*(3), 32−43. Available from https://doi.org/10.1007/s12666-015-0809-0.

Chouikhi, N., Cecilia, J. A., Vilarrasa-García, E., Besghaier, S., Chlendi, M., Duro, F. I. F., Castellon, E. R., & Bagane, M. (2019). CO_2 adsorption of materials synthesized from clay minerals: A review. *Minerals*, *9*(9), 1−22. Available from https://doi.org/10.3390/min9090514.

Collins, R. J., & Miller, R. H. (n.d.). Availability of mining wastes and their potential for use as highway material. In: *Federal Highway Administration, Report No. FHWA-RD-76-106*. Washington, DC. Available from https://www.fhwa.dot.gov/publications/research/infrastructure/structures/97148/mwst1.cfm#:~:text=.

Cui, L., Chen, P., Wang, L., Xu, Y., & Wang, H. (2022). Reutilizing waste iron tailing powders as filler in mortar to realize cement reduction and strength enhancement. *Materials*, *15*(2). Available from https://doi.org/10.3390/ma15020541.

Davidovits, J. (2011). Application of Ca-based geopolymer with blast furnace slag, a review. In: *Proceeding of the Second International Slag Valorisation Symposium* (pp. 33−49).

DEFRA. (2016). *UK statistics on waste*. Governmental Statistical Service. Available from https://www.gov.uk/government/collections/waste-and-recycling-statistics.

Duxson, P., Provis, J. L., Lukey, G. C., Mallicoat, S. W., Kriven, W. M., & van Deventer, J. S. J. (2005). Understanding the relationship between geopolymer composition, microstructure and mechanical properties. *Colloids and Surfaces A: Physicochemical and Engineering Aspects*, *269*(1−3), 47−58. Available from https://doi.org/10.1016/j.colsurfa.2005.06.060.

Easac. (2007). A study on the EU oil shale industry − Viewed in the light of the Estonian experience. *Energy*, 1−65.

ELAW. (2010). Chapter 1: Overview of mining and its impact. In: *Guide for evaluating mining projects EIAs* (p. 122).

El-Didamony, H., Helmy, I. M., Osman, R. M., & Habboud, A. M. (2015). Basalt as Pozzolana and filler in ordinary Portland cement. *American Journal of Engineering and Applied Sciences*, *8*(2), 263−274. Available from https://doi.org/10.3844/ajeassp.2015.263.274.

Fan, Z., Wang, X., Zhang, Z., & Zhang, Y. (2019). Effects of cement-mineral filler on asphalt mixture performance under different aging procedures. *Applied Sciences*, *9*(18). Available from https://doi.org/10.3390/app9183785.

Farhan, N. A., Sheikh, M. N., & Hadi, M. N. S. (2019). Investigation of engineering properties of normal and high strength fly ash based geopolymer and alkali-activated slag concrete compared to ordinary Portland cement concrete. *Construction and Building Materials*, *196*, 26–42. Available from https://doi.org/10.1016/j.conbuildmat.2018.11.083.

Ferguson, P. (2016). *Physical and geochemical characteristics of waste rock and contaminated materials*. RUM JUNGLE DR Jones Environmental Excellence.

Ghacham, A. B., Pasquier, L. C., Cecchi, E., Blais, J. F., & Mercier, G. (2016). CO_2 sequestration by mineral carbonation of steel slags under ambient temperature: Parameters influence, and optimization. *Environmental Science and Pollution Research*, *23*(17), 17635–17646. Available from https://doi.org/10.1007/s11356-016-6926-4.

Ghrici, M., Kenai, S., & Said-Mansour, M. (2007). Mechanical properties and durability of mortar and concrete containing natural pozzolana and limestone blended cements. *Cement and Concrete Composites*, *29*(7), 542–549. Available from https://doi.org/10.1016/j.cemconcomp.2007.04.009.

Gökçe, H. S., Tuyan, M., & Nehdi, M. L. (2021). Alkali-activated and geopolymer materials developed using innovative manufacturing techniques: A critical review. *Construction and Building Materials*, *303*. Available from https://doi.org/10.1016/j.conbuildmat.2021.124483, August.

Gorakhki, M. H., & Bareither, C. A. (2017). Sustainable reuse of mine tailings and waste rock as water-balance covers. *Minerals*, *7*(7). Available from https://doi.org/10.3390/min7070128.

Gou, M., Zhou, L., & Then, N. W. Y. (2019). Utilization of tailings in cement and concrete: A review. *Science and Engineering of Composite Materials*, *26*(1), 449–464. Available from https://doi.org/10.1515/secm-2019-0029.

Gurbuz, A. (2015). Marble powder to stabilise clayey soils in sub-bases for road construction. *Road Materials and Pavement Design*, *16*(2), 481–492. Available from https://doi.org/10.1080/14680629.2015.1020845.

Hamidi, M., Kacimi, L., Cyr, M., & Clastres, P. (2013). Evaluation and improvement of pozzolanic activity of andesite for its use in eco-efficient cement. *Construction and Building Materials*, *47*, 1268–1277. Available from https://doi.org/10.1016/j.conbuildmat.2013.06.013.

Harrison, D. J., Bloodworth, A. J., Eyre, J., Macfarlane, M., Mitchell, C. J., Scott, P., & Steadman, E. J. (2002). Utilisation of mineral waste: Case studies. In: *Economic Minerals and Geochemical Baseline Programme Commissioned Research report CR/02/227N* (p. 92).

Hudson-Edwards, K. A., & Dold, B. (2015). Mine waste characterization, management and remediation. *Minerals*, *5*(1), 82–85. Available from https://doi.org/10.3390/min5010082.

Huijgen, W. J. J., Comans, R. N. J., & Witkamp, G. J. (2007). Cost evaluation of CO_2 sequestration by aqueous mineral carbonation. *Energy Conversion and Management*, *48*(7), 1923–1935. Available from https://doi.org/10.1016/j.enconman.2007.01.035.

Huijgen, W., Witkamp, G. J., & Comans, R. (2005). Mineral CO_2 sequestration in alkaline solid residues. *Greenhouse Gas Control Technologies*, 2415–2418. Available from https://doi.org/10.1016/B978-008044704-9/50344-X.

Huntzinger, D. N., Gierke, J. S., Sutter, L. L., Kawatra, S. K., & Eisele, T. C. (2009). Mineral carbonation for carbon sequestration in cement kiln dust from waste piles. *Journal of Hazardous Materials*, *168*(1), 31–37. Available from https://doi.org/10.1016/j.jhazmat.2009.01.122.

Jenkins, G. J., Perry, M. C., & Prior, M. J. (2009). *The climate of the UK and recent trends*. Met Office Hadley Center. Available from http://ukclimateprojections.defra.gov.uk/images/stories/trends_pdfs/Trends.pdf.

Johari, M. A. M., Brooks, J. J., Kabir, S., & Rivard, P. (2011). Influence of supplementary cementitious materials on engineering properties of high strength concrete. *Construction and Building Materials*, *25*(5), 2639–2648. Available from https://doi.org/10.1016/j.conbuildmat.2010.12.013.

Jones, M. R., Halliday, J. E., Csetenyi, L. J., Zheng, L., & Strompinis, N. (2015). Feasibility of utilising quarry fines and waste silts to manufacture synthetic lightweight sand. *Magazine of Concrete Research*, *67*(12), 656–664. Available from https://doi.org/10.1680/macr.15.00021.

Juenger, M. C. G., & Siddique, R. (2015). Recent advances in understanding the role of supplementary cementitious materials in concrete. *Cement and Concrete Research*, *78*, 71–80. Available from https://doi.org/10.1016/j.cemconres.2015.03.018.

Juenger, M. C. G., Snellings, R., & Bernal, S. A. (2019). Supplementary cementitious materials: New sources, characterization, and performance insights. *Cement and Concrete Research*, *122*, 257–273. Available from https://doi.org/10.1016/j.cemconres.2019.05.008, May.

Karakuş, A. (2011). Investigating on possible use of Diyarbakir basalt waste in Stone Mastic Asphalt. *Construction and Building Materials*, *25*(8), 3502–3507. Available from https://doi.org/10.1016/j.conbuildmat.2011.03.043.

Karaşahin, M., & Terzi, S. (2007). Evaluation of marble waste dust in the mixture of asphaltic concrete. *Construction and Building Materials*, *21*(3), 616–620. Available from https://doi.org/10.1016/j.conbuildmat.2005.12.001.

Kaza, S., Yao, L., Bhada-Tata, P., & Van Woerden, F. (2018). *What a waste 2.0: a global snapshot of solid waste management to 2050.*

Kehinde, O., Ramonu, O. J., Babaremu, K. O., Justin, L. D., Fahim Huseien, G., Mirza, J., Ismail, M., Ghoshal, S. K., Abdulameer Hussein, A., & Council, A. C. (2020). Plastic wastes: Environmental hazard and instrument for wealth creation in Nigeria. *Heliyon*, *80*(10). Available from https://doi.org/10.1016/j.heliyon.2020.e05131.

Kim, S. W., Jang, S. J., Kang, D. H., Ahn, K. L., & Yun, H. D. (2015). Mechanical properties and eco-efficiency of steel fiber reinforced alkali-activated slag concrete. *Materials*, *8*(11), 7309–7321. Available from https://doi.org/10.3390/ma8115383.

Kumar, A., Saravanan, T. J., Bisht, K., & Kabeer, K. I. S. A. (2021). A review on the utilization of red mud for the production of geopolymer and alkali activated concrete. *Construction and Building Materials*, *302*, 124170. Available from https://doi.org/10.1016/j.conbuildmat.2021.124170, April.

Kumar, D. S., & Hudson, W. R. (1992). *Use of quarry fines for engineering and environmental applications. Special report*. Nat. Stone Association, Centre for Transportation Research University of Texas, Austin, TX.

Kusin, F. M., Hasan, S. N. M. S., Hassim, M. A., & Molahid, V. L. M. (2020). Mineral carbonation of sedimentary mine waste for carbon sequestration and potential reutilization as cementitious material. *Environmental Science and Pollution Research*, *27*(11), 12767–12780. Available from https://doi.org/10.1007/s11356-020-07877-3.

Leben, K., Mõtlep, R., Paaver, P., Konist, A., Pihu, T., Paiste, P., Heinmaa, I., Nurk, G., Anthony, E. J., & Kirsimäe, K. (2019). Long-term mineral transformation of Ca-rich oil shale ash waste. *Science of the Total Environment*, *658*, 1404–1415. Available from https://doi.org/10.1016/j.scitotenv.2018.12.326, March.

Ma, F., Sha, A., Yang, P., & Huang, Y. (2016). The greenhouse gas emission from portland cement concrete pavement construction in China. *International Journal of Environmental Research and Public Health*, *13*(7). Available from https://doi.org/10.3390/ijerph13070632.

Mabroum, S., Moukannaa, S., El Machi, A., Taha, Y., Benzaazoua, M., & Hakkou, R. (2020). Mine wastes based geopolymers: A critical review. *Cleaner Engineering and Technology*, *1*, 100014. Available from https://doi.org/10.1016/j.clet.2020.100014, June.

Markewitz, P., Kuckshinrichs, W., Leitner, W., Linssen, J., Zapp, P., Bongartz, R., Schreiber, A., & Müller, T. E. (2012). Worldwide innovations in the development of carbon capture technologies and the utilization of CO_2. *Energy and Environmental Science*, *5*(6), 7281−7305. Available from https://doi.org/10.1039/c2ee03403d.

Maruthupandian, S., Chaliasou, N. A., & Kanellopoulos, A. (2021). In I. Mporas, P. Kourtessis, A. Al-Habaibeh, A. Asthana, V. Vukovic, & J. Senior (Eds.), *Recycling mine tailings for a sustainable future built environment BT − Energy and sustainable futures* (pp. 163−169). Springer International Publishing.

Medina, G., Sáez del Bosque, I. F., Frías, M., Sánchez de Rojas, M. I., & Medina, C. (2018). Durability of new recycled granite quarry dust-bearing cements. *Construction and Building Materials*, *187*, 414−425. Available from https://doi.org/10.1016/j.conbuildmat.2018.07.134.

Minx, J. C., Lamb, W. F., Andrew, R. M., Canadell, J. G., Crippa, M., Döbbeling, N., Forster, P. M., Guizzardi, D., Olivier, J., Peters, G. P., Pongratz, J., Reisinger, A., Rigby, M., Saunois, M., Smith, S. J., Solazzo, E., & Tian, H. (2021). A comprehensive and synthetic dataset for global, regional, and national greenhouse gas emissions by sector 1970−2018 with an extension to 2019. *Earth System Science Data*, *13*(11), 5213−5252. Available from https://doi.org/10.5194/essd-13-5213-2021.

Mitchell, C. (2009). In Quarries, & Mines (Eds.), *Quarry fines and waste* (pp. 63−67). Ten Alps, World Bank Publications.

Moosberg, H., Lagerblad, B., & Forssberg, E. (2003). The use of by-products from metallurgical and mineral industries as filler in cement-based materials. *Waste Management and Research*, *21*(1), 29−37. Available from https://doi.org/10.1177/0734242X0302100104.

Mporas, I., Kourtessis, P., Al-habaibeh, A., Asthana, A., Vukovic, V., & Senior, J. (2020). Energy and sustainable futures. In: *Proceedings of 2nd ICESF 2020*. Available from http://www.springer.com/series/13370.

Murtazaev, S. A. Y., Mintsaev, M. S., Saydumov, M. S., & Aliev, S. A. (2015). Strength and strain properties of concrete, comprising filler, produced by screening of waste crushed concrete. *Modern Applied Science*, *9*(4), 32−44. Available from https://doi.org/10.5539/mas.v9n4p32.

Nádudvari, Á., & Fabiańska, M. J. (2016). The impact of water-washing, biodegradation and self-heating processes on coal waste dumps in the Rybnik Industrial Region (Poland). *International Journal of Coal Geology*, *154−155*, 286−299. Available from https://doi.org/10.1016/j.coal.2016.01.009.

National Geographic Society. (n.d.). *Oil shale* (pp. 1−9).

Natural Resource Governance Institute. (2015). *The mining industry overview and trends*. Natural Resource Governance Institute.

Nemet, G. F., Callaghan, M. W., Creutzig, F., Fuss, S., Hartmann, J., Hilaire, J., Lamb, W. F., Minx, J. C., Rogers, S., & Smith, P. (2018). Negative emissions − Part 3: Innovation and upscaling. *Environmental Research Letters*, *13*(6). Available from https://doi.org/10.1088/1748-9326/aabff4.

Olivier, D. (2016). *Waste rock dump management and stability evaluation* (pp. 1−20). SRK Consult.

Oncu, S., & Bilsel, H. (2016). Ageing effect on swell, shrinkage and flexural strength of sand and waste marble powder stabilized expansive soil. *E3S Web of Conferences*, *9*. Available from https://doi.org/10.1051/e3sconf/20160913003.

Ozer, I., & Soyer-Uzun, S. (2015). Relations between the structural characteristics and compressive strength in metakaolin based geopolymers with different molar Si/Al ratios. *Ceramics International*, *41*(8), 10192−10198. Available from https://doi.org/10.1016/j.ceramint.2015.04.125.

Pacewska, B., & Wilińska, I. (2020). Usage of supplementary cementitious materials: Advantages and limitations. *Journal of Thermal Analysis and Calorimetry*, *142*(1), 371−393. Available from https://doi.org/10.1007/s10973-020-09907-1.

Palmer, M. A., Bernhardt, E. S., Schlesinger, W. H., Eshleman, K. N., Foufoula-Georgiou, E., Hendryx, M. S., Lemly, A. D., Likens, G. E., Loucks, O. L., Power, M. E., White, P. S., & Wilcock, P. R. (2010). Mountaintop mineral consequences. *American Association for the Advancement of Science*, *327*(5962), 148−149.

Panesar, D. K. (2019). 3 - Supplementary cementing materials. In: *Woodhead Publishing Series in Civil and Structural Engineering, Developments in the Formulation and Reinforcement of Concrete. S. Mindess (Ed.)* (2nd, pp. 55−85). Woodhead Publishing. Available from https://doi.org/10.1016/B978-0-08-102616-8.00003-4.

Pera-Titus, M. (2014). Intrinsic flexibility of the zeolitic imidazolate framework ZIF-7 unveiled by CO_2 adsorption and Hg intrusion. *ChemPhysChem: A European Journal of Chemical Physics and Physical Chemistry*, *15*(8), 1581−1586. Available from https://doi.org/10.1002/cphc.201400084.

Pinetown, K. L., Ward, C. R., & van der Westhuizen, W. A. (2007). Quantitative evaluation of minerals in coal deposits in the Witbank and Highveld Coalfields, and the potential impact on acid mine drainage. *International Journal of Coal Geology*, *70*(1−3 SPEC. ISS.), 166−183. Available from https://doi.org/10.1016/j.coal.2006.02.013.

Popovic, V., Miljkovic, J. Ž., Subic, J., Jean-Vasile, A., Adrian, N., & Nicolaescu, E. (2015). Sustainable land management in mining areas in Serbia and Romania. *Sustainability (Switzerland)*, *7*(9), 11857−11877. Available from https://doi.org/10.3390/su70911857.

Portland Cement Association. (n.d.). *Carbon footprint: What is it?* (pp. 8−9). Portland Cement Association. 0020-11-105. Available from https://www.cement.org/docs/default-source/th-paving-pdfs/sustainability/carbon-foot-print.pdf.

Prigiobbe, V., Hänchen, M., Werner, M., Baciocchi, R., & Mazzotti, M. (2009). Mineral carbonation process for CO_2 sequestration. *Energy Procedia*, *1*(1), 4885−4890. Available from https://doi.org/10.1016/j.egypro.2009.02.318.

Provis, J. L. (2018). Alkali-activated materials. *Cement and Concrete Research*, *114*, 40−48. Available from https://doi.org/10.1016/j.cemconres.2017.02.009.

Pudasainee, D., Seo, Y. C., Sung, J. H., Jang, H. N., & Gupta, R. (2017). Mercury co-beneficial capture in air pollution control devices of coal-fired power plants. *International Journal of Coal Geology*, *170*, 48−53. Available from https://doi.org/10.1016/j.coal.2016.08.013.

Querol, X., Zhuang, X., Font, O., Izquierdo, M., Alastuey, A., Castro, I., van Drooge, B. L., Moreno, T., Grimalt, J. O., Elvira, J., Cabañas, M., Bartroli, R., Hower, J. C., Ayora, C., Plana, F., & López-Soler, A. (2011). Influence of soil cover on reducing the environmental impact of spontaneous coal combustion in coal waste gobs: A review and new experimental data. *International Journal of Coal Geology*, *85*(1), 2−22. Available from https://doi.org/10.1016/j.coal.2010.09.002.

Rafeet, A., Vinai, R., Soutsos, M., & Sha, W. (2017). Guidelines for mix proportioning of fly ash/GGBS based alkali activated concretes. *Construction and Building Materials*, *147*, 130−142. Available from https://doi.org/10.1016/j.conbuildmat.2017.04.036.

Rai, B., Kumar, S., & Satish, K. (2014). Effect of fly ash on mortar mixes with quarry dust as fine aggregate. *Advances in Materials Science and Engineering*, *2014*. Available from https://doi.org/10.1155/2014/626425.

Rajamathi, R., Bhojaraj., & Nethravathi, C. (2021). Porous CaO−MgO nanostructures for CO_2 capture. *ACS Applied Nano Materials*, *4*(10), 10969−10975. Available from https://doi.org/10.1021/acsanm.1c02428.

Rakhimov, R. Z., Rakhimova, N. R., Gaifullin, A. R., & Morozov, V. P. (2017). Properties of Portland cement pastes enriched with addition of calcined marl. *Journal of Building Engineering*, *11*, 30−36. Available from https://doi.org/10.1016/j.jobe.2017.03.007, February.

Rakhimova, N. R. (2020). Recent advances in blended alkali-activated cements: A review. *European Journal of Environmental and Civil Engineering*, *0*(0), 1−23. Available from https://doi.org/10.1080/19648189.2020.1858170.

Salek, S. S., Kleerebezem, R., Jonkers, H. M., Witkamp, G. J., & van Loosdrecht, M. C. M. (2013). Mineral CO_2 sequestration by environmental biotechnological processes. *Trends in Biotechnology*, *31*(3), 139−146. Available from https://doi.org/10.1016/j.tibtech.2013.01.005.

Sanna, A., Dri, M., Hall, M. R., & Maroto-Valer, M. (2012). Waste materials for carbon capture and storage by mineralisation (CCSM) − A UK perspective. *Applied Energy*, *99*, 545−554. Available from https://doi.org/10.1016/j.apenergy.2012.06.049.

Scrivener, K. L., & Capmas, A. (2004). Lea's chemistry of cement and concrete: Chapter 13. *Science*, *58*(10), 1066. Available from http://www.dbpia.co.kr/view/ar_view.asp?arid = 1536305.

Sipilä, J., Teir, S., & Zevenhoven, R. (2008). Carbon dioxide sequestration by mineral carbonation literature review update 2005−2007. *Report VT*, *52*. Available from http://users.abo.fi/rzevenho/MineralCarbonationLiteratureReview05-07.pdf.

Sivrikaya, O., Kıyıldı, K. R., & Karaca, Z. (2014). Recycling waste from natural stone processing plants to stabilise clayey soil. *Environmental Earth Sciences*, *71*(10), 4397−4407. Available from https://doi.org/10.1007/s12665-013-2833-x.

Snellings, R., Mertens, G., & Elsen, J. (2012). *Supplementary Cementitious Materials*, *74*, 211−278. Available from https://doi.org/10.2138/rmg.2012.74.6, Blezard 2001.

Solouki, A., Viscomi, G., Lamperti, R., & Tataranni, P. (2020). Quarry waste as precursors in geopolymers for civil engineering applications: A decade in review. *Materials*, *13*(14), 1−29. Available from https://doi.org/10.3390/ma13143146.

Tohver, T. (2010). Utilization of waste rock from oil shale mining. *Oil Shale*, *27*(4), 321−330. Available from https://doi.org/10.3176/oil.2010.4.05.

Turner, L. K., & Collins, F. G. (2013). Carbon dioxide equivalent (CO_2-e) emissions: A comparison between geopolymer and OPC cement concrete. *Construction and Building Materials*, *43*, 125−130. Available from https://doi.org/10.1016/j.conbuildmat.2013.01.023.

Ukritnukun, S., Koshy, P., Feng, C., Rawal, A., Castel, A., & Sorrell, C. C. (2021). Development of low-alkali, fly ash/slag geopolymers: predictive strength modelling and analyses of impact of curing temperatures. *Minerals*, *11*(1), 60.

United States Congress: Oil Shale Advisory Committee. (1980). *An assessment of oil shale technologies*. Available from http://www.princeton.edu/∼ota/disk3/1980/8004_n.html.

Vijayalakshmi, M., Sekar, A. S. S., & Ganesh Prabhu, G. (2013). Strength and durability properties of concrete made with granite industry waste. *Construction and Building Materials*, *46*, 1−7. Available from https://doi.org/10.1016/j.conbuildmat.2013.04.018.

Vijayan, D. S., & Parthiban, D. (2020). Effect of solid waste based stabilizing material for strengthening of expansive soil − A review. *Environmental Technology and Innovation*, *20*, 101108. Available from https://doi.org/10.1016/j.eti.2020.101108.

Vivien, F., & Bedrosyan, D. (2014). Understanding CO_2 emissions from the global energy sector. *The World Bank*, *3*, 1–12.

Vriens, B., Plante, B., Seigneur, N., & Jamieson, H. (2020). Mine waste rock: Insights for sustainable hydrogeochemical management. *Minerals*, *10*(9), 1–38. Available from https://doi.org/10.3390/min10090728.

Wei, M. S., & Huang, K. H. (2001). Recycling and reuse of industrial wastes in Taiwan. *Waste Management*, *21*(1), 93–97. Available from https://doi.org/10.1016/S0956-053X(00)00073-8.

Woodall, C. M., McQueen, N., Pilorgé, H., & Wilcox, J. (2019). Utilization of mineral carbonation products: Current state and potential. *Greenhouse Gases: Science and Technology*, *9*(6), 1096–1113. Available from https://doi.org/10.1002/ghg.1940.

Yan, X., Li, Y., Ma, X., Zhao, J., Wang, Z., & Liu, H. (2019). CO_2 capture by a novel CaO/MgO sorbent fabricated from industrial waste and dolomite under calcium looping conditions. *New Journal of Chemistry*, *43*(13), 5116–5125. Available from https://doi.org/10.1039/c8nj06257a.

Yang, M. H., Chen, T. H., Wang, S. E., Tsai, Y. F., Su, C. H., Wu, C. W., Lui, W. Y., & Shyr, Y. M. (2008). Biochemical predictors for absence of common bile duct stones in patients undergoing laparoscopic cholecystectomy. *Surgical Endoscopy and Other Interventional Techniques*, *22*(7), 1620–1624. Available from https://doi.org/10.1007/s00464-007-9665-2.

Yang, X., Zhao, L., Yang, S., & Xiao, Y. (2013). Investigation of natural CaO–MgO sorbent for CO_2 capture. *Asia-Pacific Journal of Chemical Engineering*, *8*(6), 906–915. Available from https://doi.org/10.1002/apj.1735.

Yap, Z. S., Khalid, N. H. A., Haron, Z., Mohamed, A., Tahir, M. M. Hasyim, S., & Saggaff, A. (2021). Waste mineral wool and its opportunities—a review. *Materials*, *14* (19), 5777.

Ye, N., Yang, J., Liang, S., Hu, Y., Hu, J., Xiao, B., & Huang, Q. (2016). Synthesis and strength optimization of one-part geopolymer based on red mud. *Construction and Building Materials*, *111*, 317–325. Available from https://doi.org/10.1016/j.conbuildmat.2016.02.099.

Yliniemi, J., Kinnunen, P., Karinkanta, P., & Illikainen, M. (2016). Utilization of mineral wools as alkali-activated material precursor. *Materials*, *9*(5). Available from https://doi.org/10.3390/ma9050312.

Zhang, P., Han, S., Ng, S., & Wang, X. H. (2017). Advanced cementitious building materials with applications in civil engineering. *Advances in Civil Engineering*, *2017*. Available from https://doi.org/10.1155/2017/9654910.

Zhang, T., Zhi, S., Li, T., Zhou, Z., Li, M., Han, J., Li, W., Zhang, D., Guo, L., & Wu, Z. (2020). Alkali activation of copper and nickel slag composite cementitious materials. *Materials*, *13*(5), 1–15. Available from https://doi.org/10.3390/ma13051155.

Zhang, Y., Korkiala-Tanttu, L. K., & Borén, M. (2019). Assessment for sustainable use of quarry fines as pavement construction materials: Part II-stabilization and characterization of quarry fine materials. *Materials*, *12*(15). Available from https://doi.org/10.3390/ma12152450.

Zhao, F., Cong, Z., Sun, H., & Ren, D. (2007). The geochemistry of rare earth elements (REE) in acid mine drainage from the Sitai coal mine, Shanxi Province, North China. *International Journal of Coal Geology*, *70*(1–3 SPEC. ISS.), 184–192. Available from https://doi.org/10.1016/j.coal.2006.01.009.

Morphology and strength of concrete incorporating natural rubber latex and plastic fibers

13

Paul O. Awoyera[1], *Folashayo Oluyemi*[1], *Naraindas Bheel*[2], *Oluwatobi Aluko*[3], *Afonso R.G. de Azevedo*[4] *and Oladimeji B. Olalusi*[5]
[1]Department of Civil Engineering, Covenant University, Ogun State, Nigeria, [2]Department of Civil Engineering, Universiti Teknologi Petronas, Bandar Seri Iskandar, Tronoh, Perak, Malaysia, [3]Civil Engineering Department, School of Civil Engineering, Universiti Teknologi Malaysia, Skudai, Johor, Malaysia, [4]Civil Engineering Laboratory – LECIV, State University of the Northern Rio de Janeiro—UENF, Alberto Lamego, Campos dos Goytacazes, Rio De Janeiro, Brazil, [5]Department of Civil Engineering, Structural Engineering & Computational Mechanics Group (SECM), University of KwaZulu-Natal, Durban, South Africa

13.1 Introduction

There is currently a surge in construction demand across all sectors (industrial, residential, and commercial) of developing countries. Thus there is a continuing demand for long-lasting and dependable building materials and methods. Moreover, for environments having critical geographical features, high-strength materials that can withstand severe and changing climatic conditions are required for buildings. Rapid infrastructural development indicates economic growth and can further stimulate economic growth through the construction industry and other related sectors (CEBR, 2016). Concrete is used extensively in constructing these permanent and long-lasting structures. However, such concrete should have a longer service life, resist environmental corrosion, and be more durable (Blikharskyy et al., 2021; Shcherban et al., 2022).

On the other hand, Portland cement concrete has some disadvantages, such as low chemical resistance (acids, sulfate, or chloride), low thermal strength, phase defeat, bleeding, and other properties including flexural strength, brittleness, and low failure strain (Ismail et al., 2009; Muhammad & Ismail, 2012). The space between the aggregate and the cement paste generates a gap that contributes to porosity and natural differences between aggregates and cement paste on different occasions. However, supplementary cementitious materials, fibers, and other additives serving as the filler in the development of high-strength concrete have been considered beneficial in overcoming the limitations of Portland cement concrete (Al-Yousuf et al., 2021).

Green Materials in Civil Engineering. DOI: https://doi.org/10.1016/B978-0-443-19106-0.00013-0

The filling of cement composites that use additions is a factor of great concern in several studies, the type, geometry, and configuration of the incorporations and/or additions can cause considerable problems in the microstructure of the materials (Zanelato et al., 2019). Fibers, for example, have a greater capacity to reinforce cementitious matrices, and depending on the surface configuration, they can improve the anchoring and adhesion effect with the matrix, by increasing the contact area (de Azevedo et al., 2020). Meanwhile, the incorporation of particulate waste can promote better internal packing of the matrix, which can also be beneficial (Carvalho et al., 2014).

Moreover, plasticizers are used in concrete to combat the limitations of concrete. It is utilized to achieve a certain level of workability, lower concrete water demand and the w/c (water/cement) value in general, regulate the hydration process, and slow the setting process. Adding supplemental components and admixtures to fresh concrete alters the interfacial zone and improves the rheology to create impermeable and low-porous concrete (Skibsted & Snellings, 2019). The environmental impact of cement and the huge cost consequences of construction are two of the most pressing challenges in these contemporary construction activities. According to studies, excessive cement consumption is environmentally harmful. This is due to the emission of greenhouse gases and other environmentally hazardous substances during cement and concrete manufacturing (Scrivener et al., 2018). Also, brittle failure and low failure strain present a significant challenge to concrete structures. The presence of brittle failure or strain failure could considerably facilitate water, chloride, and chemical penetration, triggering corrosion and consequently leading to structural failure.

However, research has shown that polymer application in concrete during production could significantly eliminate the aforementioned concrete limitations. A variety of polymers, such as natural rubber latex (NRL) (Muhammad & Ismail, 2012), altered natural rubber (Wuri Andayani et al., 2016), synthetic rubber, styrene-butadiene rubber (Pacheco-Torgal & Jalali, 2009), epoxy polyvinyl, and others (Elalaoui et al., 2012; Nagaraj et al., 1988) have been studied in numerous countries. One of the research pioneers in NRL-modified concrete reported that 2% dry NRL content could optimally enhance the compressive, splitting tensile, and ductility of concrete. Adding a polymer like NRL to a concrete mix could increase its strength and durability. From research, concrete deteriorates when exposed to high temperatures, which affects its design life, safety, and service behavior. The addition of polymeric fiber in concrete bare to high temperatures was one of the research breakthroughs. Polypropylene is capable of reducing the vapor pressure build-up and consequently mitigating explosive spalling and crackings in heated high-strength concrete (Arunachalam & Jayakumar, 2015). Besides, NRL can prevent cracking and maintain stiffness and ductility at low temperatures (Yun & Choi, 2014), while simultaneously boosting shear resistance at high temperatures (Azahar et al., 2016).

Moreover, Shobha (2014) reported a study on the mechanical properties of a latex-modified high-strength concrete, in a proportion of 0.5%, 1%, and 1.5%. The compressive strength improved with a 1% optimum dosage of NRL. Also, reported

a study on the capability of NRL in enhancing concrete mechanical properties. NRL was used to replace the water with latex-to-water ratios of 4%, 5%, and 6%. It was observed from the results that NRL improved compressive strength because of the polymerization of latex monomer in concrete. Tensile and flexural strength was enhanced because of the incorporation of polymer in the modified phase making it more ductile (Salazar et al., 2020). However, the workability is reduced with an increase in polymer because it creates a passive layer around calcium silicate hydrate and calcium aluminate, increasing the viscosity (Liyanage & Gamage, 2021). Therefore adding natural latex to concrete composite offers more sustainable, renewable, and durable materials for construction.

The use of macro plastic fibers to reinforce concrete has attracted the interest of both scientists and the building industry due to the multiple sustainability benefits they bring compared to steel fibers and steel reinforcing mesh (Yin et al., 2015). Plastic use has expanded dramatically worldwide, resulting in massive amounts of plastic-based garbage. Plastic garbage presents a considerable challenge in treatment and management because it is a toxic, nonbiodegradable material (TamilThendral et al., 2018). Environmentally beneficial techniques to dispose of plastic waste is becoming a major concern in recent years. As an alternative to disposal, waste can be used as a construction material in the construction industry (De Jesus et al., 2018). Concrete with plastics as fibers, resins, and aggregates has been studied since the last decade of the 20th century. In preparing lightweight concrete for specific uses, raw plastic in granules was employed. Plastic aggregates from diverse sources, including the shredding of discarded plastic bottles, were used in this type of concrete (Basha et al., 2020).

Atul (2012) reported study on the incorporation of plastic in concrete with specimens containing 0.2%−1% by weight of plastic bits. The result indicated that a 0.8% volume fraction improves the tensile strength of the concrete, indicating that plastic may be utilized to boost the tensile strength of concrete. However, the compressive strength of concrete decreased as plastic content increased. Similarly, Ghernouti et al. (2009) studied the use of recycled plastic bag trash as sand in a concrete mix and substituted sand in the concrete mix at 10%, 20%, 30%, and 40%. The experiments revealed that the workability, density, and compressive strength were enhanced even at a higher replacement fraction. And also reported the use of plastic waste in lightweight concrete production. Five concrete mixtures were made with different proportions of polyethylene terephthalate (PET), 1%, 3%, 5%, 7%, and 10% by weight. The result showed improved compressive strength at 1% PET content, but a loss as the waste-added content increased. Splitting tensile and flexural strength also improved, with the highest flexural strength from the specimen at 7%. However, Jaivignesh and Sofi (2017) studied the applicability of nonbiodegradable plastic aggregate in concrete by replacing sand with plastic fine aggregates by weight in 10%, 15%, and 20% in the matrix, while coarse aggregate was replaced by weight in 15%, 20%, and 25% of the matrix. Even with 0.3% steel fiber addition, the test results showed that plastic fine aggregate and plastic coarse aggregate to concrete diminished its compressive, splitting tensile, and flexural strength (Awoyera, Olalusi, & Ekpe, 2021; Awoyera, Olalusi, & Iweriebo, 2021).

Past reports indicate that the durability characteristics of NRL-modified cementitious composites have been explored largely, with some promising results. However, there is still a scarcity of valid studies on improving the microstructures and strength of NRL-modified concrete. Also, many previous researchers focused on using natural latex alone in a composite. However, one way of improving composite properties is to harness the properties of each material in the composite synergistically. Thus Natural Reubber Latex (NRL) and Waste Plastic Fibre (WPF) could provide combined advantages in improving the microstructure and strength of the composite. Therefore this study presents the influence of natural latex and plastic fiber on the behavior of both fresh and hardened Portland cement concrete. This study shows the possible advantage of incorporating natural latex and plastic fibers in ordinary Portland cement (OPC). In addition, it offers a potential solution to the problem of recycling. This research is also in line with Sustainable Development Goals (SDG) goal 6 (clean water and sanitation), goal 9 (industry, innovation, and infrastructure), and goal 11 (sustainable cities and communities) of the United Nations.

13.2 Materials and method

13.2.1 Materials

The materials used in this study include OPC, water, granite, river sand, NRL, and plastic fibers. Tests were carried out on both coarse and fine aggregates to ascertain the strength and durability of the aggregate. Some of the tests carried out include the sieve analysis test, water absorption test, and specific gravity test. A grade 42.5 OPC following ASTM (2002) was used as a binding agent when preparing the concrete samples, with the manufacturer's detailed chemical composition shown in Table 13.1. NRL was purchased from Liquid Latex Direct, the United Kingdom, in liquid form in a 25 kg, stackable jerrycan. The plastic fibers used in creating the

Table 13.1 Ordinary Portland cement (OPC) chemical composition.

Constituent	Weight (%)
Lime (CaO)	64.64
Silica (SiO_2)	21.28
Alumina (Al_2O_3)	5.60
Iron oxide (Fe_22O_3)	3.36
Magnesia (MgO)	2.06
Sulfur trioxide (SO_3)	2.14
Total alkalis	0.05
Insoluble residue	0.22
Loss of ignition	0.92
Lime saturated factor	0.92
Silica modulus	2.38

recycled waste concrete samples came from Covenant University's collection of shredded waste PET bottles. The NRL and plastic fibers are shown in Fig. 13.1A and B, respectively.

13.2.2 Testing methods

13.2.2.1 Specific gravity and water absorption test

This test was carried out to measure the degree of toughness of the aggregates and their overall quality following (C, 2001) ASTM. The water absorption test measures the aggregate's capacity to retain water. These tests were employed to evaluate the aggregate's quality, strength, and water retention sufficiency.

The parameters were determined using the following expressions:

$$\text{Specific gravity} = \frac{D}{C-(A-B)} \times 100\% \tag{13.1}$$

$$\text{Water absorption} = (\%\ \text{of dry weight}) = \frac{C-D}{D} \times 100\% \tag{13.2}$$

where

A = mass of saturated aggregate in water ($A_1 - A_2$) (g).
B = mass of the saturated surface dry aggregate in air (g).
C = mass of oven-dried aggregate in air (g).

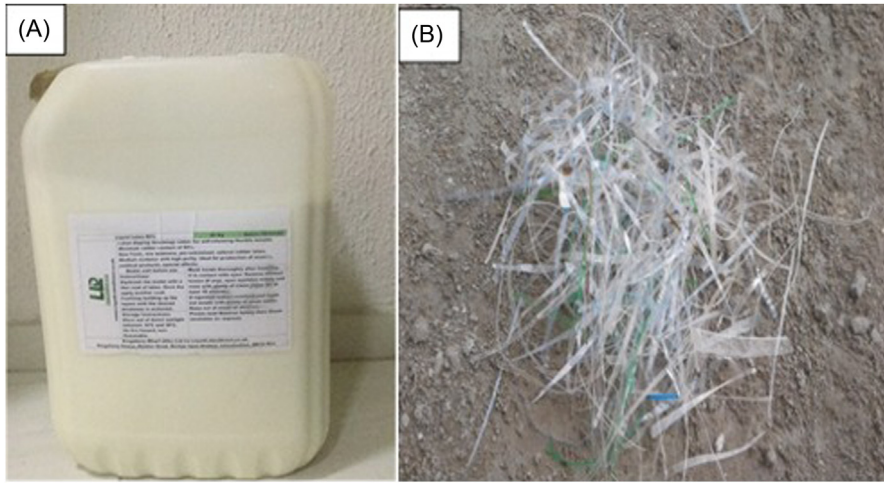

Figure 13.1 Materials used: (A) natural rubber latex, (B) plastic fiber.

13.2.2.2 Sieve analysis

This test was used to determine the size distribution of particles defined using the mass of the sample passing and retained on each sieve and was done according to ASTM (2006). The sample used was graded with stacked sieves shaking, with the largest sieve opening at the top and the smallest sieve size at the bottom. The particle size distribution for sand is shown in Fig. 13.2. The aggregate impact value was calculated using the expression:

$$\text{Aggregate impact value (\%)} = \left(\frac{W1 - W2}{W1}\right) \times 100\% \tag{13.3}$$

where

Total weight of dry sample W_1 (g).

Weight of portion passing 2.36 mm sieve W_2 (g).

$$\text{Coefficien to fcurvature (sand)} = \frac{D30^2}{D60 \times D10}; \frac{0.6^2}{0.875 \times 0.3} = 1.37 \tag{13.4}$$

$$\text{Coefficient of uniformity (sand)} = \frac{D60}{D10} = 2.92 \tag{13.5}$$

The specific gravity and water absorption sands were 2.9% and 1.13%, respectively.

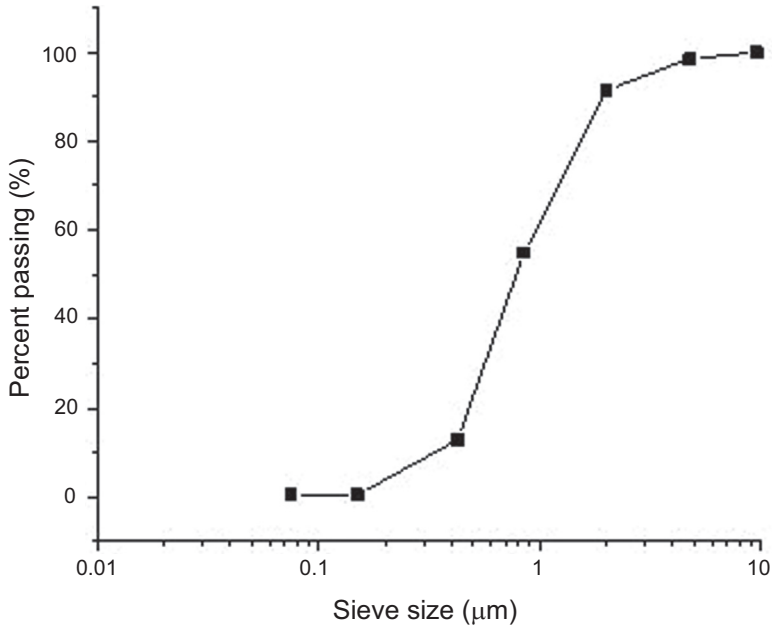

Figure 13.2 Particle size distribution for sand.

13.2.2.3 Mix design and concrete specimens preparations

A design mix ratio of 1:1.5:3 (cement:sand:granite) and a water-to-cement ratio of 0.50 are adopted in this study. This mix ratio was also utilized to calculate the various percentages of cement, natural latex, and plastic fiber in concrete production. The mix proportions of samples are presented in Table 13.2.

The right quantities of aggregates, cement, plastic fibers, and NRL were measured based on the mix proportion shown in Table 13.2. The materials were thoroughly mixed in the electrically controlled mixer before the slump tests. The fresh property of concrete was determined using the slump apparatus. With this test, the workability of the fresh mix was ascertained. Then the fresh concrete was placed in lubricated molds and compacted on a vibrating table to ensure adequate compaction. The specimens were de-molded after 24 hours and placed in a curing tank for wet curing until the 3rd, 7th, and 28th respective days of testing.

13.2.2.4 Compressive strength test

The concrete compressive strength was assessed after 3, 7, and 28 days curing by subjecting the 150 mm concrete cube to loading in a compressive strength testing machine. The test was carried out following ASTM C39/C39M (2012) (Standard Test Method for Compressive Strength of Cylindrical Concrete Specimens, n.d.). Three sets of specimens for each mix were tested after the curing days. The specimens to be tested were duly prepared and positioned properly between the upper and the lower metal bearing plates of the compression testing machine as specified by the relevant standard. A constant loading rate (50 N/s) was then selected and applied to the specimen until failure of the specimen occurred. The compressive strength of the specimens was calculated using the following expression:

$$f = \frac{P}{\mathrm{A}} \tag{13.6}$$

Table 13.2 Mix proportions of tested samples.

Designation	Cement (%)	Latex (%)	Plastic fiber (%)	Sand (%)	Granite (%)
Control	18	0.0	0.0	27	55
LPMC 0.5%/0.2%	18	0.9	3.6	27	55
LPMC 1.0%/0.4%	18	1.8	7.2	27	55
LPMC 1.5%/0.6%	18	2.7	10.8	27	55
LPMC 2.5%/0.8%	18	4.5	14.4	27	55

CC signifies control concrete. LPMC-0.5 signifies latex plastic concrete (0.5% natural latex and 0.2% plastic fiber). LPMC-1.0 signifies latex plastic-modified concrete (1.0% natural latex and 0.4% plastic fiber). LPMC-1.5 signifies latex plastic-modified concrete (1.5% natural latex and 0.6% plastic fiber). LPMC-2.5 signifies latex plastic-modified concrete (2.0% natural latex and 0.8% plastic fiber).

where f = compressive strength of cube in MPa, P = failure load in N, and A = cross-sectional area of the cube in mm^2. The compression test setup is shown in Fig. 13.3.

13.2.2.5 Microstructural and mineralogy tests

The crushed concrete rubbles taken from selected mixtures were examined using a scanning electron microscope and an X-ray diffractometer to explore the specimen's microstructure and mineralogy. The equipment scanned the concrete sample with an electron beam provides a magnified image for analysis. Scanning Electron Microscopy (SEM) analysis, often known as SEM microscopy, is a technique that has been effectively utilized for both microanalysis and failure analysis of solid inorganic materials. This test is performed at high magnification, resulting in high-resolution photographs and precise measurements of very small features and objects. SEM refers to a high-performance method employed in investigating the structure of the materials. However, diffraction is used in X-ray Diffraction (XRD) analysis. It is a physical phenomenon that happens when electromagnetic waves escape objects whose size is comparable to the wavelength.

Figure 13.3 Concrete samples subjected to loading.

13.2.3 Results and discussion

The results of multiple tests conducted on materials used, fresh and hardened concrete specimens, including the general performance of the manufactured concrete specimens, are presented as follows.

13.2.4 Slump test

The test was performed to determine the workability of concrete, as indicated in the preceding section. This is done by placing the slump cone next to the obtained slump and measuring the slump cone's height and the slump. The slump values are shown in Fig. 13.4. It is obvious from the chart that the slumps of mixes decrease with an increase in latex and plastic content and LPMC 2.5% has the lowest, like 33%, 37% of the control, and LPMC 0.5%, LPMC 1%, respectively.

13.2.5 Hardened concrete properties

Compressive strength tests and microstructural analyses were performed on the test specimens in this study.

Fig. 13.5 shows the compressive strength development at curing ages 3, 7, and 28.

It was observed that the poorest mix at 3, 7, and 28 days is the LPMC 2.5% with values 6.33, 6.56, and 11.56 MPa, respectively, which attained 49.8%, 43.73%, and 48.39% of the control concrete strength, respectively. It was also observed that the

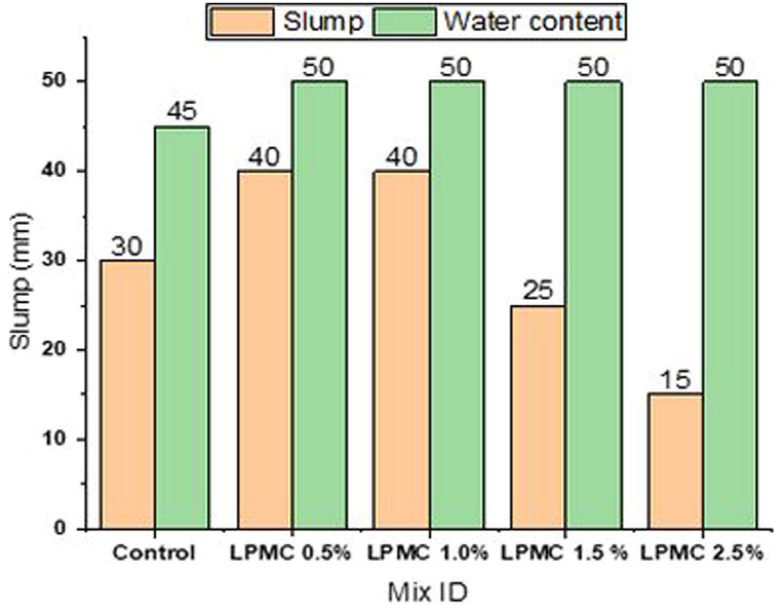

Figure 13.4 Slump result of concrete mixes.

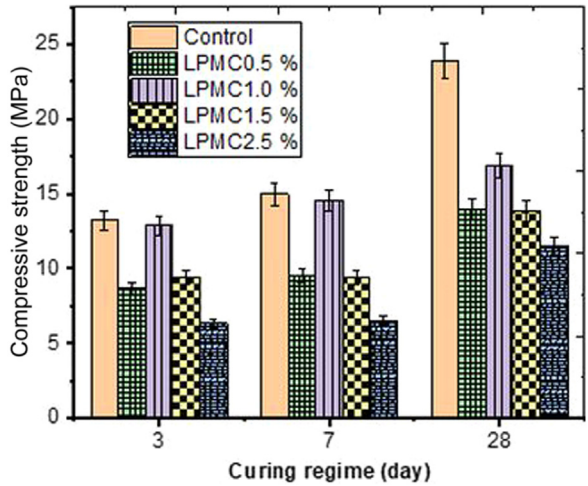

Figure 13.5 Compressive strengths of concrete.

best three mixes at 28 days in ascending order are: LPMC 1.5%, LPMC 0.5%, and LPMC 1.0% which attained 58.14%, 58.60%, and 70.70% of the control concrete strength, respectively. The LPMC 1.0% mix had the maximum compressive strength of all the mixes for all 3 days, with values of 12.89 MPa, 14.56 N/mm^2, and 16.89 MPa. Although the compressive strength was not up to the value of the control mixes, it can be deduced that the maximum compressive strength would be attained between LPMC 0.5% and LPMC 1.0%.

Also, as the compressive strengths hit their peak, which was at LPMC 1.0%/0.4%, they proceeded to decline, leaving mix LPMC 2.5%/0.8% as the lowest compressive strength for all 3 days.

13.2.5.1 Microstructural analysis

For microstructural analysis, the analyzed result of the four mixes used for this research work, including the control sample at 28 days, is presented below. The microstructures of LPMC 0.5%/0.2%, LPMC 1.0%/0.4%, LPMC 1.5%/0.6%, and LPMC 2.5%/0.8% are examined and compared with the control sample.

The SEM image in Fig. 13.6 represents the microstructure of mix 1 (LPMC 0.5%/0.2%). It shows more void spaces with little C-S-H formation within the specimen. The reduction that occurs in the formation of C-S-H increases the pore spaces in the specimen, thereby reducing the concrete's strength.

However, the SEM micrograph in Fig. 13.7 represents the microstructure of mix 2 (LPMC 1.0%/0.4%). There is an excellent development of C-S-H gel evident in the image, which is distributed. This results in the reduction of voids in the specimen, causing an increase in the strength of the specimen. Also, there will be a reduction in the water permeability, making the specimen more durable.

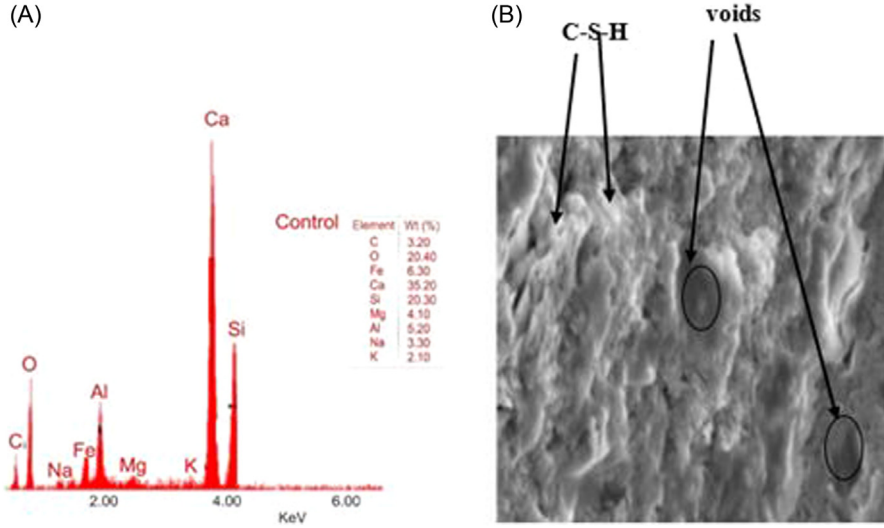

Figure 13.6 (A) EDX analysis for control mix. (B) SEM.

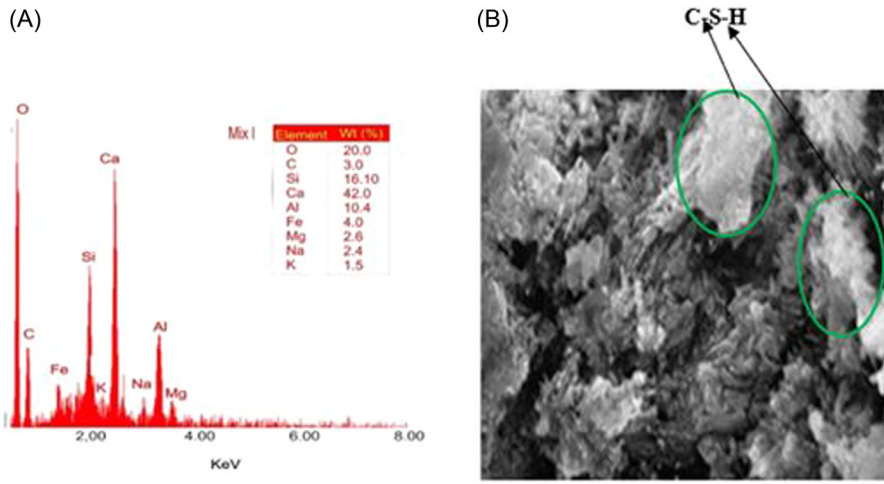

Figure 13.7 (A) EDX analysis for mix 1. (B) SEM.

The SEM micrograph of mix 3 (LPMC 1.5%/0.6%) is shown in Fig. 13.8. Few pore spaces and an insignificant formation of C-S-H gel were found, thereby influencing the strength properties of the concrete specimen.

From Fig. 13.9, the SEM micrograph of mix 4 (LPMC 2.5%/0.8%) can be analyzed. The microstructure of this mix presents the presence of many pore spaces due to the reduction in C-S-H gel formation, leading to an increase in water absorption, making the specimen.

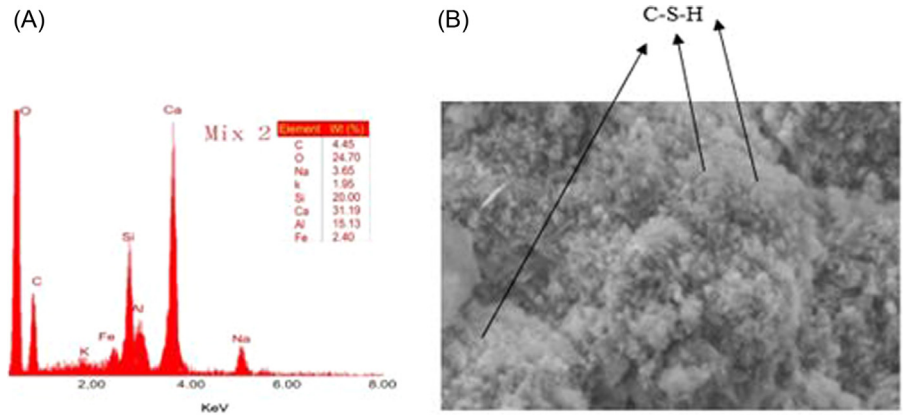

Figure 13.8 (A) EDX analysis for mix 2. (B) SEM.

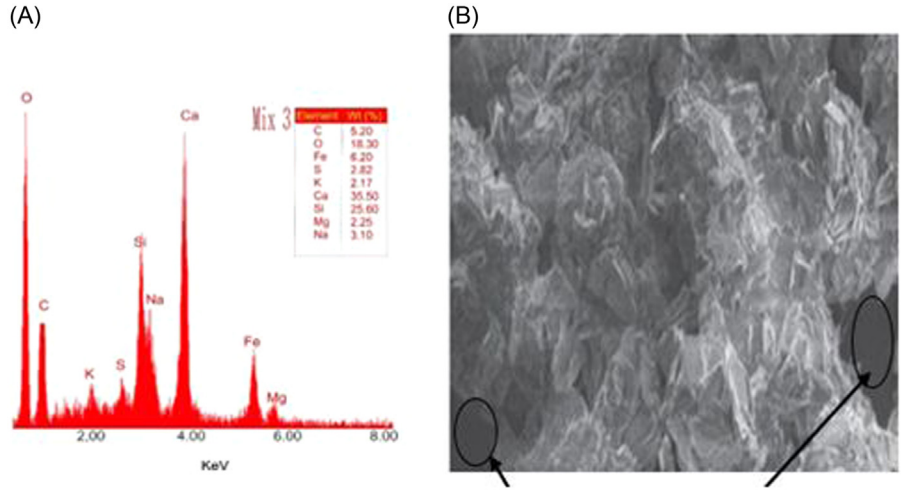

Figure 13.9 (A) EDX analysis for mix 3. (B) SEM.

The Energy Dispersive X-Ray (EDX) analysis shows that control contains 35.20% calcium, 20.40% oxygen, 20.30% silicon, 3.20% carbon, 6.30% iron, 4.10% magnesium, 5.20% aluminum, 3.30% sodium, and 2.10% potassium.

The EDX analysis shows that mix 2 (LPMC 1.0%/0.4%) contains 31.19% calcium, 24.70% oxygen, 20.00% silicon, 4.45% carbon, 2.40% iron, 4.10% magnesium, 15.13% aluminum, 3.65% sodium, and 1.95% potassium.

The EDX analysis shows that mix 3 (LPMC 1.5%/0.6%) contains 35.50% calcium, 18.30% oxygen, 25.60% silicon, 5.20% carbon, 6.20% iron, 2.25% magnesium, 5.20% aluminum, 3.10% sodium, 2.82% sulfur, and 2.17% potassium.

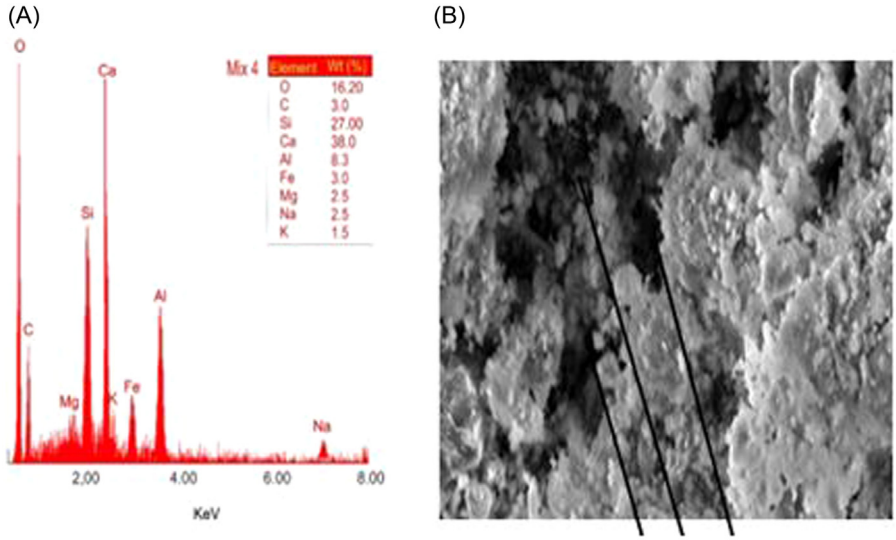

Figure 13.10 (A) EDX analysis for mix 4. (B) SEM.

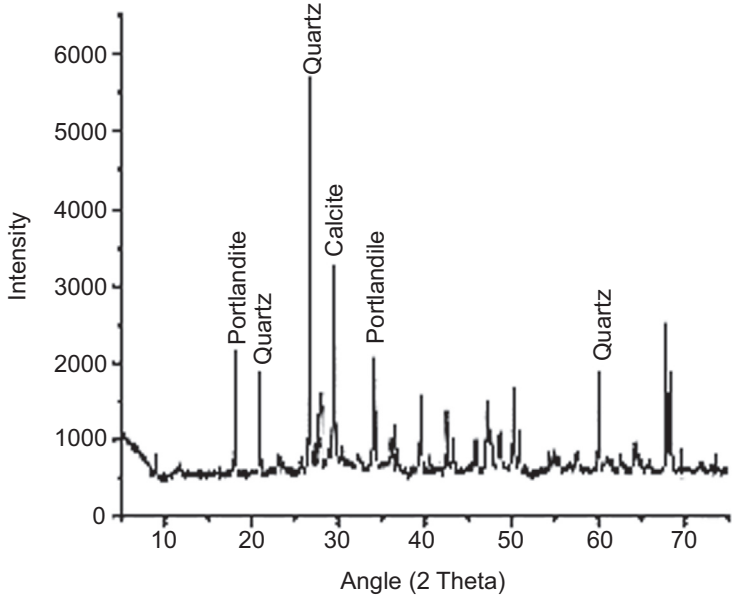

Figure 13.11 X-ray diffraction analysis for control mix.

The EDX analysis shows that mix 4 (Fig. 13.10) (LPMC 2.5%/0.8%) contains 38.0% calcium, 16.20% oxygen, 27.00% silicon, 3.00% carbon, 3.0% iron, 2.5% magnesium, 8.3% aluminum, 2.50% sodium, and 1.5% potassium.

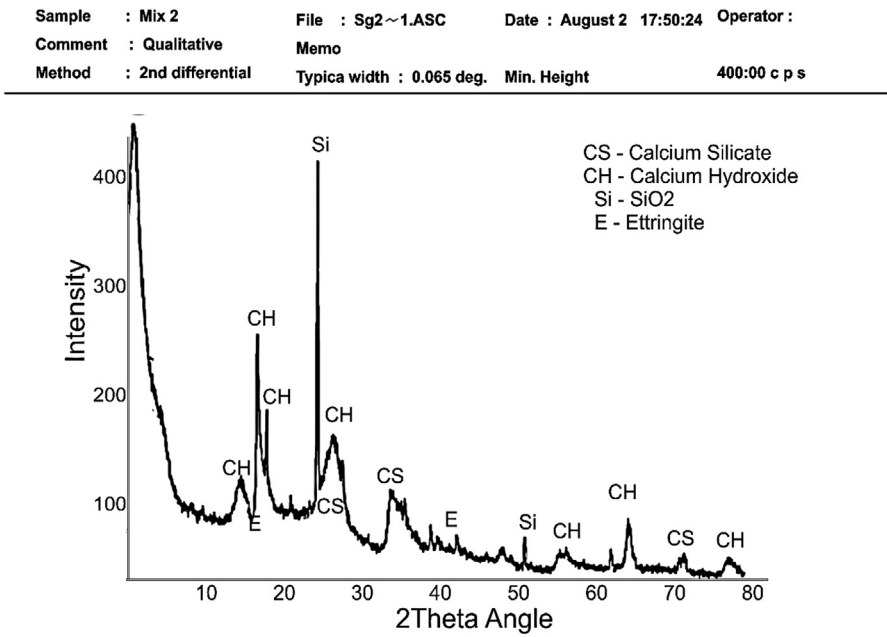

Figure 13.12 X-ray diffraction analysis for LPMC 1.0%/0.4% mix.

Selected samples were evaluated using the X-ray diffraction apparatus. The machine operates by passing a ray of light through the samples, which helps detect the mineral development in the material. For this test, the control mix and the mix 2 sample (LPMC 1.0%/0.4%) were used. Figs. 13.11 and 13.12 show the minerals formed in the samples.

It can be seen that the control mix had Portlandite, Quartz, and calcite as dominant minerals; while the selected mix (LPMC 1.0%/0.4%) has calcium silicate, calcium hydroxide, and ettringite as dominant minerals. The addition of natural latex changes the chemical composition of the concrete.

13.3 Conclusion

The influence of natural latex and plastic fibers on the behavior of fresh and hardened Portland cement concrete was experimentally investigated in this research work. The compressive strength and slump value were influenced by the natural latex and the plastic fibers.

The experiment results indicate that natural latex and plastic fiber can be effectively used in cement concrete. The workability of the concrete mixes 1 and 2 increased but at mixes 3 and 4, there was a noticeable decrease. The development in strength for mixtures containing the natural latex and plastic fiber are lower than that of the control mix. The various percentages of natural latex and plastic fiber

added to the control mix give the optimum percentage, among all other mixes, as LPMC 1.0%/0.4%. The difference between the compressive strength at 3 days and 7 days between the control mix and the LPMC 1.0%/0.4% was not so significant; however, the percentage at 28 days was about 29% compared to the control mix. For mixes after the optimum percentage (LPMC 1.0%/0.4%), there was a considerable reduction in the compressive strength, particulaly for mix 3 and mix 4. It could be assumed that a higher compressive strength could be obtained between 0.5% and 1.0% natural latex replacement. The microstructural analysis shows that mix 2 (LPMC 1.0%/0.4%) was tightly packed with fewer voids in the specimen compared to mix 4 (2.5%/0.8%) specimen.

Funding

The authors declare that no funds, grants, or other support were received during the preparation of this manuscript.

Data availability

Research data will be made available by the authors upon request.

Competing interests

The authors have no relevant financial or nonfinancial interests to disclose.

References

Al-Yousuf, A., Pokharel, T., Lee, J., Gad, E., Abdouka, K., & Sanjayan, J. (2021). Effect of fly ash and slag on properties of normal and high strength concrete including fracture energy by wedge splitting test: Experimental and numerical investigations. *Construction and Building Materials*, *271*, 121553. Available from https://doi.org/10.1016/j.conbuildmat.2020.121553.

ASTM. (2002). ASTM C39/C39M-18 standard test method for compressive strength of cylindrical concrete specimensA ASTM - ASTM International, West Conshohocken, PA. ASTM, 1-7.

Arunachalam, A., & Jayakumar, K. (2015). Influence of polypropylene fibres on the mechanical and durability properties of high performance concrete. In: Proceedings of the International Conference FIBRE CONCRETE 9788001056837 (pp. 42−51). Czech Technical University in Prague India. Available from http://concrete.fsv.cvut.cz/fcproceedings/index.php.

ASTM. (2006). *ASTM C 136-06: Standard test method for sieve analysis of fine and coarse aggregates* (pp. 5–9).

Atul, M. (2012). Use of plastic in a concrete to improve its properties. *International Journal of Advanced Engineering Research*.

Awoyera, P. O., Olalusi, O. B., & Ekpe, C. O. (2021). Plastic fiber-strengthened interlocking bricks for load bearing applications. *Innovative Infrastructure Solutions*, *6*(2). Available from https://doi.org/10.1007/s41062-021-00495-z, https://www.springer.com/journal/41062.

Awoyera, P. O., Olalusi, O. B., & Iweriebo, N. (2021). Physical, strength, and microscale properties of plastic fiber-reinforced concrete containing fine ceramics particles. *Materialia*, *15*, 100970. Available from https://doi.org/10.1016/j.mtla.2020.100970.

Azahar, N. B. M., Hassan, N. B. A., Jaya, R. P., Kadir, M. A. B., Ab, N. Z. B. M., Yunus, M. Z. H., & Mahmud. (2016). An overview on natural rubber application for asphalt modification. *International Journal of Agriculture*, *2*, 212–218.

de Azevedo, A. R. G., Klyuev, S., Marvila, M. T., Vatin, N., Alfimova, N., de Lima, T. E. S., Fediuk, R., & Olisov, A. (2020). Investigation of the potential use of Curauá fiber for reinforcing mortars. *Fibers*, *8*(11), 69. Available from https://doi.org/10.3390/fib8110069.

Basha, S. I., Ali, M. R., Al-Dulaijan, S. U., & Maslehuddin, M. (2020). Mechanical and thermal properties of lightweight recycled plastic aggregate concrete. *Journal of Building Engineering*, *32*, 101710. Available from https://doi.org/10.1016/j.jobe.2020.101710.

Blikharskyy, Y., Selejdak, J., Kopiika, N., & Vashkevych, R. (2021). Study of concrete under combined action of aggressive environment and long-term loading. *Materials*, *14*(21). Available from https://doi.org/10.3390/ma14216612, https://www.mdpi.com/1996-1944/14/21/6612/pdf.

Carvalho, A., de Castro Xavier, G., Alexandre, J., Pedroti, L. G., de Azevedo, A. R. G., Vieira, C. M. F., & Monteiro, S. N. (2014). Environmental durability of soil-cement block incorporated with ornamental stone waste. *Materials Science Forum*, *798–799*, 548–553. Available from http://www.ttp.net/0255-5476.html, https://doi.org/10.4028/scientific.net/MSF.798-799.548.

CEBR. (2016). Engineering and economic growth: a global view. *Royal Academy of Engineering*.

Elalaoui, O., Ghorbel, E., Mignot, V., & Ben Ouezdou, M. (2012). Mechanical and physical properties of epoxy polymer concrete after exposure to temperatures up to 250°C. *Construction and Building Materials*, *27*(1), 415–424. Available from https://doi.org/10.1016/j.conbuildmat.2011.07.027.

Ghernouti, Y., Rabehi, B., Safi, B., & Chaid, R. (2009). Use of recycled plastic bag waste in the concrete. *Journal of International Scientific Publications: Materials, Methods and Technologies*, *8*, 480–487.

Ismail, M., Muhammad, B., & Mohamad, A. (2009). Durability performance of natural rubber latex. *Malaysian Journal of Civil Engineering*, *21*(2), 195–203.

Jaivignesh, B., & Sofi, A. (2017). Study on mechanical properties of concrete using plastic waste as an aggregate. *IOP Conference Series: Earth and Environmental Science*. Available from http://www.iop.org/EJ/volume/1755-1315.

De Jesus, R. M., Pelaez, E. B., & Caneca, M. C. (2018). Experimental study on mechanical behaviour of concrete beams with shredded plastics. *International Journal of Geomate*, *14*(42), 71–75. Available from https://doi.org/10.21660/2018.42.7172, http://www.geomatejournal.com/sites/default/files/articles/71-75-7172-DeJesus-Feb-2018-c1.pdf.

Liyanage, J. B., & Gamage, R. P. (2021). The hydration and volume expansion mechanisms of modified expansive cements for sustainable in-situ rock fragmentation: A review. *Energies*, *14*(18). Available from https://doi.org/10.3390/en14185965, https://www.mdpi.com/1996-1073/14/18/5965/pdf.

Muhammad, B., & Ismail, M. (2012). Performance of natural rubber latex modified concrete in acidic and sulfated environments. *Construction and Building Materials*, *31*, 129−134. Available from https://doi.org/10.1016/j.conbuildmat.2011.12.099.

Nagaraj, T. S., Sundara Raja Iyengar, K. T., & Kameswara Rao, B. (1988). Super-plasticized natural rubber latex modified concretes. *Cement and Concrete Research*, *18*(1), 138−144. Available from https://doi.org/10.1016/0008-8846(88)90131-7.

Pacheco-Torgal, F., & Jalali, S. (2009). Sulphuric acid resistance of plain, polymer modified, and fly ash cement concretes. *Construction and Building Materials*, *23*(12), 3485−3491. Available from https://doi.org/10.1016/j.conbuildmat.2009.08.001.

Salazar, B., Aghdasi, P., Williams, I. D., Ostertag, C. P., & Taylor, H. K. (2020). Polymer lattice-reinforcement for enhancing ductility of concrete. *Materials and Design*, *196*. Available from https://doi.org/10.1016/j.matdes.2020.109184, https://www.journals.elsevier.com/materials-and-design.

Scrivener, K. L., John, V. M., & Gartner, E. M. (2018). Eco-efficient cements: Potential economically viable solutions for a low-CO_2 cement-based materials industry. *Cement and Concrete Research*, *114*, 2−26. Available from https://doi.org/10.1016/j.cemconres.2018.03.015, http://www.sciencedirect.com/science/journal/00088846.

Shcherban, E. M., Stel'makh, S. A., Beskopylny, A., Mailyan, L. R., & Meskhi, B. (2022). Increasing the corrosion resistance and durability of geopolymer concrete structures of agricultural buildings operating in specific conditions of aggressive environments of livestock buildings. *Applied Sciences*, *12*(3), 1655. Available from https://doi.org/10.3390/app12031655.

Shobha, M. S. (2014). Mechanical properties of latex modified high performance concrete. *IOSR Journal of Mechanical and Civil Engineering*, *11*(1), 13−19. Available from https://doi.org/10.9790/1684-11131319.

Skibsted, J., & Snellings, R. (2019). Reactivity of supplementary cementitious materials (SCMs) in cement blends. *Cement and Concrete Research*, *124*, 105799. Available from https://doi.org/10.1016/j.cemconres.2019.105799.

Standard test method for compressive strength of cylindrical concrete specimens ASTM C39/C39M-12.

TamilThendral, V., Anand, K. S., Shandra Banu, K., & Thirumoorthy, B. (2018). Experimental investigation on tannery waste with partial replacement of coarse aggregate in concrete. *International Research Journal of Engineering and Technology*, *5*(9), 7039−7041.

Wuri Andayani, S., Suratmana, R., Imrana, I., Mardiyatia, Y., & Basukib, A. (2016). Preliminary research on strength of polymer modified concrete with copolymer natural rubber as concrete additives. *Journal of Chemical Engineering and Materials Science*, *7*(2), 18−27. Available from https://doi.org/10.5897/JCEMS2016.0252.

Yin, S., Tuladhar, R., Shi, F., Combe, M., Collister, T., & Sivakugan, N. (2015). Use of macro plastic fibres in concrete: A review. *Construction and Building Materials*, *93*, 180−188. Available from https://doi.org/10.1016/j.conbuildmat.2015.05.105.

Yun, K. K., & Choi, P. (2014). Causes and controls of cracking at bridge deck overlay with very-early strength latex-modified concrete. *Construction and Building Materials*, *56*, 53−62. Available from https://doi.org/10.1016/j.conbuildmat.2014.01.055.

Zanelato, E. B., Alexandre, J., Rangel Garcez de Azevedo, A., & Marvila, M. T. (2019). Evaluation of roughcast on the adhesion mechanisms of mortars on ceramic substrates. *Materials and Structures*, *52*(3). Available from https://doi.org/10.1617/s11527-019-1353-x.

Fiber-reinforced polymer nanocomposites for structural retrofitting applications

14

Bhuvaneshwari Balasubramaniam[1] *and Nagesh R. Iyer*[2]
[1]Department of Chemistry, Indian Institute of Technology (BHU), Varanasi, Uttar Pradesh, India, [2]Department of Mechanical Engineering, Indian Institute of Technology, Dharwad, Karnataka, India

14.1 Introduction

The ideal ways for climate-resilient construction are constructing concrete buildings and structures with versatile and long-lasting characteristics. However, due to concrete's colossal carbon footprint, it accounts for at least 8% of global emissions as the main ingredient is cement which is responsible for the carbon dioxide (CO_2) emission (Ellis et al., 2020). Hence, it is highly necessary to decarbonize this cement industry sector (Ellis et al., 2020; Monteiro et al., 2017). According to the data, 30 billion tonnes of concrete/year is used worldwide. And its demand is growing steeply every year than that of for steel or wood (Fig. 14.1; Monteiro et al., 2017). The specialty of structures constructed using concrete have shown its potential in the form of survival during wars and natural disasters, outlasting the civilizations that built them. It is necessary to protect the concrete/steel structures from the adverse environmental effects. The amount of time and effort invested for the construction of any structures that are very simple or gigantic is enormous, hence it is important to protect them in a vivid manner through technological advancements.

In general, the reinforced concrete (RC) structures consist of steel as reinforcement bar to support the tensile load and concrete as casing to support the compressive loads. In comparison, the elastic modulus of concrete is lesser than steel, hence RC structures are built with steel reinforcement. Nowadays, sustainable design and management is the "center of focus" while designing RC structures in context of life-cycle assessment of structures. Due to different deterioration scenarios, the durability and long-term performance of the RC structures would be severely affected, which results in reduced life cycle of RC structures. According to the 2017 American Society of Civil Engineers (ASCE) infrastructure report card, it is estimated that $123 billion was spent to rehabilitate 56,007 structurally damaged bridges (Guo et al., 2020). The main issue with the RC structures is the erosion media-induced corrosion, which caused the cost of $20.6 billion for corrosion-related repair and rehabilitation work as stated in the US Government Accountability Office report

Green Materials in Civil Engineering. DOI: https://doi.org/10.1016/B978-0-443-19106-0.00014-2

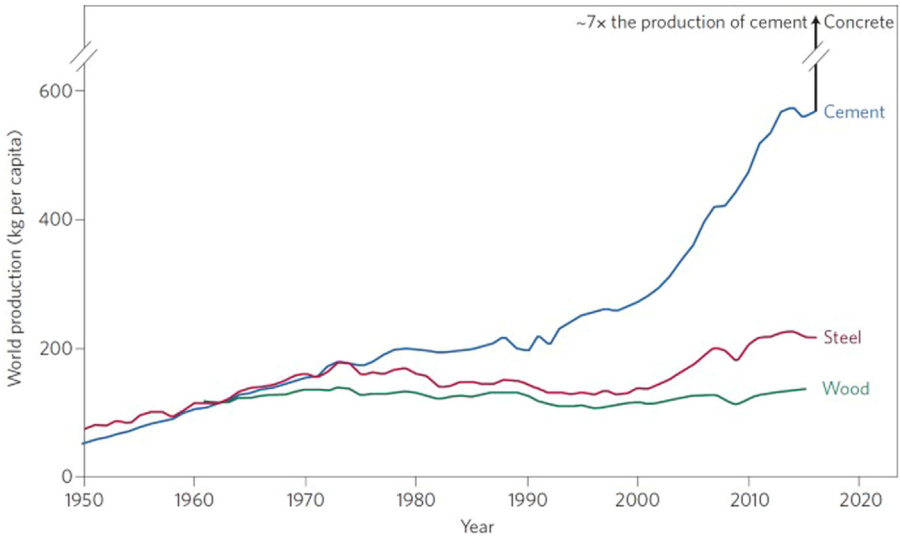

Figure 14.1 The demand of infrastructure material and its worldwide production.
Source: From Monteiro, P. J. M., Miller, S. A., & Horvath, A. (2017). Towards sustainable concrete. *Nature Materials*, *16*(7), 698−699. https://doi.org/10.1038/nmat4930.

(Guo et al., 2020). China also reported the corrosion-related issues which accounts for 3.3% GDP in 2014 (Guo et al., 2020). At worldwide, the expected cost of corrosion would be ∼2.5 trillion US dollars per year with respect to the global economy (Balasubramaniam et al., 2018; Bhuvaneshwari, Selvaraj, et al., 2020). Therefore special attention needs to be paid to safeguard the RC structures and its durability thereby life-cycle increment can be achievable (Bhuvaneshwari, Vivekananthan, et al., 2020).

One strategy being used for structural protection is repair or retrofit that can be achieved using the modern fiber-reinforced polymer (FRP) technology. Now a days, FRP is considered as modern construction material especially in structural strengthening applications in steel/concrete structures due to its excellent mechanical and durability performances (Al-Saoudi et al., 2021; Hu et al., 2020; Lu et al., 2014; Nye et al., 2018; Rashid & Bahrami, 2023; Sbahieh et al., 2022; Teng et al., 2008). There are two main types of FRPs: carbon fiber-reinforced polymer (CFRP) and glass fiber-reinforced polymer (GFRP) composites (Yoo et al., 2019). Their usage in field applications is drastically increasing every year in the field of civil/structural engineering (Fig. 14.2; details extracted from Seica & Packer, 2007). The history of composites in construction is explained in Seica and Packer (2007). In 1972 onwards, the FRP composite applications started gradually increasing in multiple fields and in the year 1990 onwards, it stepped into almost all the fields such as bridges, transmission line towers, tubular structures, footbridges, offshore. Further, the introduction and advantages of FRP and FRP nanocomposites in civil/structural engineering field was summarized by the authors in 2019 (Balasubramaniam, 2019). The history, development,

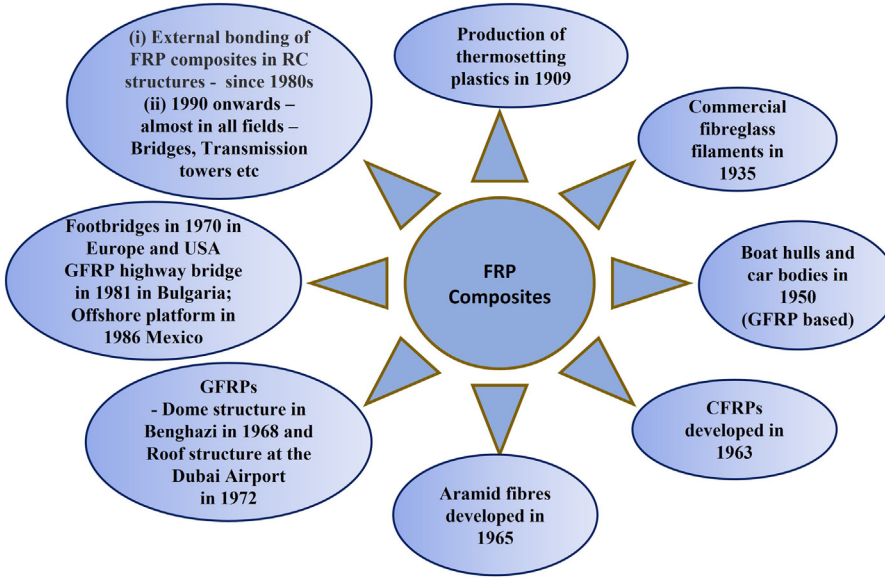

Figure 14.2 The history, development, and applications of fiber-reinforced polymer (FRP) in construction.

and applications of FRP in construction-related details are extracted from Seica and Packer (2007).

14.2 Characteristics of fiber-reinforced polymers

The two major types of FRPs in construction sector are CFRP and GFRP. In comparison, CFRP possess more tensile strength than GFRP. With the development of composite technology, its potential in aircraft applications witnessed in the year 1950. Next big success with this technology is manufacturing FRP-based boat hulls and car bodies based on glass fiber reinforcement. The major advantage of GFRP is its nonconductive nature, expected to show insulator behavior thereby prevention of galvanic corrosion of metals. However, the drawback of GFRP is its sensitiveness to alkaline environments and moisture attack, which harms the fiber's integrity. Further, the creep affect is also high in GFRPs.

As far as CFRP is concerned, the major advantage of them is their high stiffness to strength ratio. CFRPs are developed in the year 1963 for some specialized applications. Carbon fiber is an electrical conductor and due to this nature, galvanic corrosion may take place if it is placed under direct contact with metal. The excellent creep behavior of carbon fibers against deformation and relaxation is one of the highly commendable functions of CFRP. The orientation of fibers in CFRP is shown in Fig. 14.3.

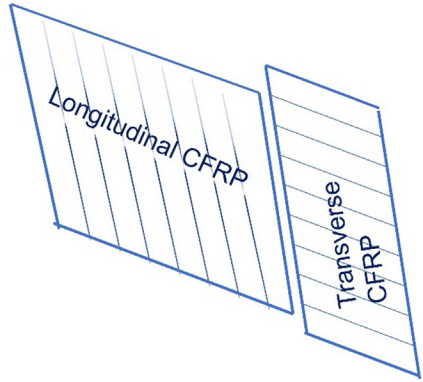

Figure 14.3 The orientation of fibers in carbon fiber-reinforced polymer (CFRP).

14.3 Fiber-reinforced polymer nanocomposites

The nanomaterials incorporation in polymer matrices toward generating heterogeneous materials with improved properties and excellent performance has garnered great attention in the polymer nanocomposites research fraternity over the last two decades. This type of new materials is classified as nanocomposites, that are been designed, synthesized, and functionally graded for optimal properties in a wide range of applications, mainly for coatings, energy harvesting and storage, sensing, magnetism, and packaging to name a few. Nanocomposites properties mainly rely on the choice of polymer matrix, the nano-reinforcements geometrical and chemical features, and the functional interaction between both matrix and nano inclusions, that are collectively called as components (Nasser et al., 2020).

As described previously, the fiber-reinforced nanocomposites are gaining an increased attention in the civil/structural fields due to their unique applications in the area of repair and retrofitting of both concrete and steel structure. It includes service life enhancement, improving the structural and durability parameters, control on moisture absorption characteristics of concrete, controlled delamination characteristics under cyclic as well dynamic loadings, interface strengthening through improved adhesive and bonding strengths. Through this continuous effort, the buildings or structures that are already built before 50−70 years and has the potential for surviving next 20 years with little or few requirements on repair and rehabilitation-based servicing would pay a great deal of attention in improving the service life of those structures in the society. By doing so, two major advantages such as the dependency of new structures can be dealt accordingly, which also helps to control the CO_2 emission as the cement which will be used in any construction is going to be part of greenhouse gas emission index. Secondly, the investment on new constructions can be avoided for quite sometimes until the urgent need arises.

The binder used for structural strengthening of steel or concrete structures during repair and retrofitting is usually based on epoxy resin along with amine-based curing agent. The major part on achieving a desired strength after FRP wrapping

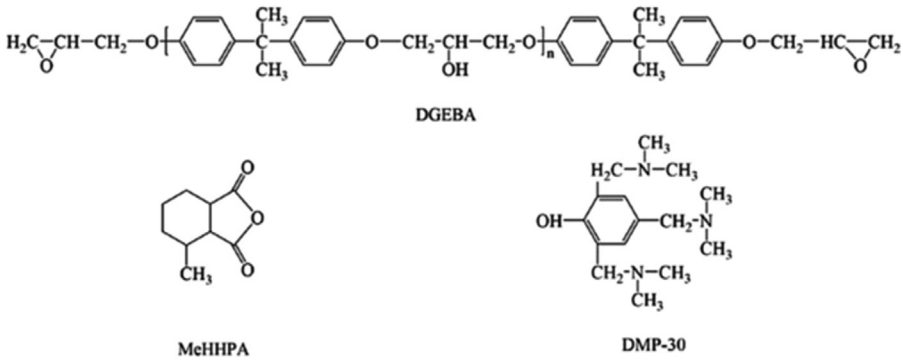

Figure 14.4 Chemical structures of the epoxy system (epoxy polymer based on bisphenol-A (DGEBA) and an anhydride curing agent (MeHHPA)); Tris (dimethylaminomethyl) phenol (DMP-30, accelerator).

totally depends on the nature and the binding capacity of epoxy polymer. The factors such as resin to curing agent ratio, mixing phenomena, curing characteristics, and the interface binding capacity decide the overall strength of the composites which include concrete or steel matrix-binder-FRP layers. The chemical structure of epoxy resin polymer and amine-based curing agents used for composite application are shown in Fig. 14.4 (Lu et al., 2015).

The FRP laying procedure follows certain ways like uniaxial wrapping, poly axial wrapping, single layer or multiple layers wrapping. It is completely based on the application needs. However, due to the various factors namely temperature, salt intrusion with combined environmental impacts, the moisture diffusion in epoxy resin is uncontrollable. It results in debonding of FRPs from the matrix and delamination of layers from the structures, hence the structure failure occurs. To tackle this issue, nanotechnology-based applications are considered as "holy grail approach" for strengthening the interface between concrete or steel matrix and FRPs using the resin developed based on epoxy polymer nanocomposites. Although the field is yet to reach its maxima in many field applications, its footprint in construction field brings enormous scope in repair and retrofit of structures toward life cycle enhancement. The importance of nanocomposites in epoxy binder formulations are already presented in Balasubramaniam (2019). The inclusion of nanomaterials such as nanosilica, nanoalumina, nanoclay, Carbon Nanotubes (CNTs), nano $CaCO_3$ into the epoxy binder helps in achieving improved mechanical properties, interface strengthening, moisture diffusion controlling, thermostability, thermomechanical stability, chemical resistance, pore engineering, durability enhancement through pore modulations, chloride ingress control, etc. (Balasubramaniam, 2019; Ilyas et al., 2022/2022; Li et al., 2017; Ogrodowska & Urbański, 2023). The very purpose of nanocompositing epoxy resin is to upgrade its strength bearing capacity as well as interface strengthening through eliminating the weak zone regions in the interface.

As far as steel structures are concerned, due to the high tensile nature of FRPs, it promotes the strength and stiffness related enhancement in the structures, particularly in fatigue strength. CFRP wrapping has proved to be a superior alternative for

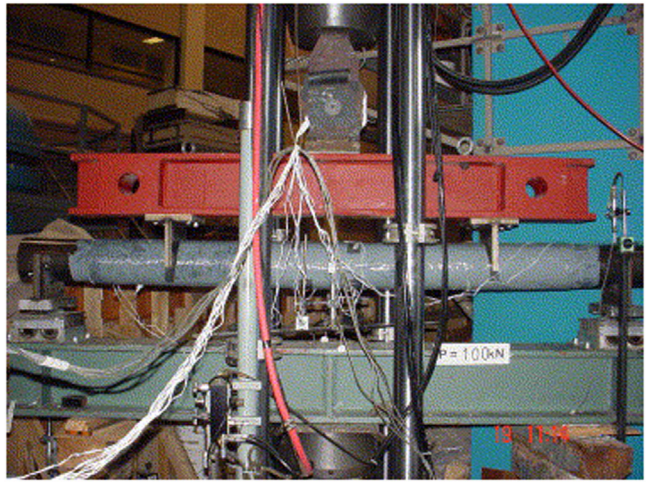

Figure 14.5 Carbon fiber-reinforced polymer (CFRP)-wrapped beam under test.
Source: From Seica, M. V., & Packer, J. A. (2007). FRP materials for the rehabilitation of tubular steel structures, for underwater applications. *Composite Structures*, *80*(3), 440–450. https://doi.org/10.1016/j.compstruct.2006.05.029

seismic strengthening and rehabilitation. For seismic strengthening and rehabilitation of steel structures, CFRP wrapping has shown promising potential as it delays the local buckling, and improves the impact resistance and energy absorption in addition to enhancing the fatigue performance of joints. However, the FRP applications in underwater steel tubular or concrete structures are still at early stage of development, hence the recent studies are mainly focusing on that field (Guo, 2022; Seica & Packer, 2007). The FRP-wrapped beam under test condition is showed in Fig. 14.5 (Seica & Packer, 2007).

There are few computational-based models such as micromechanical models, atomic models created for understanding the epoxy binder characteristics, macro simulations, machine learning approaches developed for understanding the load carrying characteristics of FRP-wrapped concrete/steel structures (Bai et al., 2023; Büyüköztürk et al., 2011; Chen et al., 2021; Li et al., 2023; Wang, 2023; Xing & Tang, 2022; Yoo et al., 2019).

14.4 Standard practices and codes involved in fiber-reinforced polymer-structural retrofit

Few important standard practices based on the national and international codes used for FRP-structural retrofit are briefly presented below:

1. ISO—ISO 18319–2:2022—FRP reinforcement for concrete structures—part 2: specifications of CFRP strips.

2. ACI CODE-440.11−22: Building code requirements for structural concrete reinforced with GFRP bars.
3. ACI 440.2R: Guide for the design and construction of externally bonded FRP systems for strengthening concrete structures.
4. CAN/CSA S806: The Canadian design and construction of building composites with FRPs.
5. CAN/CSA S6−06: The Canadian highway bridge design code.
6. fib-TG9.3: European fib bulletin 14: Design and use of externally bonded fiber polymer reinforcements (FRP EBR) for reinforced concrete structures and design guidelines on strengthening concrete structures using fiber composite materials.
7. JSCE: Japan Society of Civil Engineering recommendations for upgrading of concrete structures with use of continuous fiber sheets.
8. ISIS based on Canadian Codes (CAN/CSA S6−06 and CAN/CSA S806−02): The manual for strengthening reinforced concrete structures with externally bonded FRPs.
9. NCHRP report 678: Design of FRP systems for strengthening concrete girders in shear.

14.5 Summary and conclusion

This book chapter mainly discusses about the origin of polymer composites and its application in concrete industry. The functionality of FRP composites for structural strengthening of concrete/steel structures is discussed. The major goal of repair and retrofit strategy using FRP and its nanocomposites for life cycle improvement of structures are briefly explained in a simplistic manner. Further the standards and codes followed for the repair and retrofitting of structures with FRP are summarized.

Acknowledgments

Authors acknowledge and appreciate the support and encouragement provided by the IIT (BHU) Varanasi, IIT Kanpur, and IIT Dharwad.

References

Al-Saoudi, A., Kalfat, R., Al-Mahaidi, R., Cervenka, J., & Pryl, D. (2021). Numerical and experimental investigation into the fatigue life of FRP bonded to concrete and anchored with bidirectional fabric patches. *Engineering Structures*, *239*. Available from https://doi.org/10.1016/j.engstruct.2021.112335.

Bai, Y. L., Zhang, Y. F., Sun, P. X., Dai, J. G., & Ozbakkaloglu, T. (2023). Experimental and numerical study on seismic performance of PEN FRP-jacketed circular RC columns. *Journal of Composites for Construction*, *27*(2). Available from https://doi.org/10.1061/JCCOF2.CCENG-3983, https://ascelibrary.org/journal/jccof2.

Balasubramaniam, B. (2019). Fiber reinforced polymer nanocomposites for structural engineering applications materials science and technology. 1−20.

Balasubramaniam, B., Selvaraj, A., Iyer, N. R., Ravikumar, L., Rai, P. K., Mondal, K., & Gupta, R. K. (2018). Electrochemical and microstructural analysis of azomethine

polyamides as inhibitor for rebar corrosion under chloride contaminated pore solution. *Frontier Research Today*, *1*. Available from https://doi.org/10.31716/frt.201801004.

Bhuvaneshwari, B., Selvaraj, A., & Iyer, N. R. (2020). *Corrosion inhibitors for increasing the service life of structures*. *New materials in civil engineering* (pp. 657−676). India: Elsevier. Available from https://www.elsevier.com/books/new-materials-in-civil-engineering/samui/978-0-12-818961-0, http://doi.org/10.1016/B978-0-12-818961-0.00020-X.

Bhuvaneshwari, B., Vivekananthan, S., Sathiyan, G., Palani, G. S., Iyer, N. R., Rai, P. K., Mondal, K., & Gupta, R. K. (2020). Doping engineering of V-TiO_2 for its use as corrosion inhibitor. *Journal of Alloys and Compounds*, *816*. Available from https://doi.org/10.1016/j.jallcom.2019.152545.

Büyüköztürk, O., Buehler, M. J., Lau, D., & Tuakta, C. (2011). Structural solution using molecular dynamics: Fundamentals and a case study of epoxy-silica interface. *International Journal of Solids and Structures*, *48*(14−15), 2131−2140. Available from https://doi.org/10.1016/j.ijsolstr.2011.030.018.

Chen, J., Wan, L., Ismail, Y., Hou, P., Ye, J., & Yang, D. (2021). Micromechanical analysis of UD CFRP composite lamina under multiaxial loading with different loading paths. *Composite Structures*, *269*. Available from https://doi.org/10.1016/j.compstruct.2021.114024.

Ellis, L. D., Badel, A. F., Chiang, M. L., Park, R. J.-Y., & Chiang, Y. M. (2020). Toward electrochemical synthesis of cement—An electrolyzer-based process for decarbonating $CaCO_3$ while producing useful gas streams. *Proceedings of the National Academy of Sciences*, *117*(23), 12584−12591. Available from https://doi.org/10.1073/pnas.1821673116.

Guo, F. (2022). Durability of fibre reinforced polymers in exposure to dual environment of seawater sea sand concrete and seawater. Materials. (14).

Guo, H., Dong, Y., & Gu, X. (2020). Durability assessment of reinforced concrete structures considering global warming: A performance-based engineering and experimental approach. *Construction and Building Materials*, *233*.

Hu, W., Li, Y., & Yuan, H. (2020). Review of experimental studies on application of FRP for strengthening of bridge structures. *Advances in Materials Science and Engineering*, *2020*. Available from https://doi.org/10.1155/2020/8682163, http://www.hindawi.com/journals/amse/.

Ilyas, R. A., Nurazzi, N. M., & Norrrahim, M. N. F. (2022). Fiber-reinforced polymer nanocomposites. *Nanomaterials*, *12*.

Li, Y., Liu, X., & Li, J. (2017). Experimental study of retrofitted cracked concrete with FRP and nanomodified epoxy resin. *Journal of Materials in Civil Engineering*, *29*(5). Available from https://doi.org/10.1061/(ASCE)MT.1943-5533.0001810, http://ascelibrary.org/mto/resource/1/jmcee7/.

Li, P. D., Zhang, T., & Zeng, J. J. (2023). Unified ultimate axial strain model for large rupture strain FRP-confined concrete based on energy approach. *Journal of Composites for Construction*, *27*(2). Available from https://doi.org/10.1061/JCCOF2.CCENG-3944, https://ascelibrary.org/journal/jccof2.

Lu, Y., Li, N., & Li, S. (2014). Behavior of FRP-confined concrete-filled steel tube columns. *Polymers*, *6*(5), 1333−1349. Available from https://doi.org/10.3390/polym6051333, http://www.mdpi.com/2073-4360/6/5/1333/pdf.

Lu, Z., Xian, G., & Li, H. (2015). Effects of exposure to elevated temperatures and subsequent immersion in water or alkaline solution on the mechanical properties of pultruded BFRP plates. *Composites Part B: Engineering*, *77*, 421−430. Available from https://doi.org/10.1016/j.compositesb.2015.030.066, https://www.journals.elsevier.com/composites-part-b-engineering.

Monteiro, P. J. M., Miller, S. A., & Horvath, A. (2017). Towards sustainable concrete. *Nature Materials*, *16*(7), 698−699. Available from https://doi.org/10.1038/nmat4930, http://www.nature.com/nmat/.

Nasser, J., Zhang, L., Lin, J., & Sodano, H. (2020). Aramid nanofiber reinforced polymer nanocomposites via amide−amide hydrogen bonding. *ACS Applied Polymer Materials*, *2*(7), 2934−2945. Available from https://doi.org/10.1021/acsapm.0c00430.

Nye, T. K., Pantelides, C. P., & Burningham, C. A. (2018). Unidirectional GFRP composite connections between precast concrete wall panels under simulated seismic loads. *Composite Structures*, *203*, 624−635. Available from https://doi.org/10.1016/j.compstruct.2018.070.042, http://www.elsevier.com/inca/publications/store/4/0/5/9/2/8.

Ogrodowska, K., & Urbański, M. (2023). Nanosilica modification of epoxy matrix in hybrid basalt-carbon FRP bars—Impact on microstructure and mechanical properties. *Materials*, *16*(5).

Rashid, S. M. P., & Bahrami, A. (2023). Structural performance of infilled steel−concrete composite thin-walled columns combined with FRP and CFRP: A comprehensive review. *Materials*, *16*(4). Available from https://doi.org/10.3390/ma16041564, http://www.mdpi.com/journal/materials.

Sbahieh, S., Tahir, F., & Al-Ghamdi, S. G. (2022). Environmental and mechanical performance of different fiber reinforced polymers in beams. *Materials Today: Proceedings*, *62*, 3548−3552. Available from https://doi.org/10.1016/j.matpr.2022.040.398, https://www.sciencedirect.com/journal/materials-today-proceedings.

Seica, M. V., & Packer, J. A. (2007). FRP materials for the rehabilitation of tubular steel structures, for underwater applications. *Composite Structures*, *80*(3), 440−450. Available from https://doi.org/10.1016/j.compstruct.2006.050.029.

Teng, J. G., Smith, S. T., & Chen, J. F. (2008). *Flexural strengthening of reinforced concrete (RC) beams with fibre-reinforced polymer (FRP) composites*. *Strengthening and rehabilitation of civil infrastructures using fibre-reinforced polymer (FRP) composites* (pp. 112−140). Hong Kong: Elsevier Ltd. Available from http://www.sciencedirect.com/science/book/9781845694487, 10.1533/97818456948900.112.

Wang, S. B. (2023). Machine learning approach for analysing and predicting the modulus response of the structural epoxy adhesive at elevated temperatures. Journal of Adhesion.

Yoo, D. Y., Banthia, N., Gupta, R., Kim, Y. H., & Bhutta, A. (2019). Polymer-based construction materials for civil engineering. *International Journal of Polymer Science*, *2019*. Available from https://doi.org/10.1155/2019/8914073, http://www.hindawi.com/journals/ijps/.

Xing, W., & Tang, Y. (2022). *Modeling and simulation of failure in fiber-reinforced polymer composites* (pp. 1059−1092). Springer Science and Business Media LLC. Available from 10.1007/978-981-19-3603-6_42.

Biological materials for geotechnical engineering

15

Toshiro Hata
Geotechnical Laboratory, Department of Civil and Environmental Engineering, Graduate School of Advanced Science and Engineering, Hiroshima University, Hiroshima, Japan

15.1 Introduction

This section describes a technique that utilizes the metabolic function of soil microorganisms as a new eco- and environmentally friendly geo material with "self-mediation" and "self-healing" properties. As a method of utilizing the metabolic function of microorganisms, they can improve soil properties, soil quality, etc. The improvement of soil characteristics such as strength and decreased permeability by precipitating inorganic minerals such as calcium carbonate (Hata et al., 2011), biopolymer based (Chang et al., 2018), silica based (Balouchkhaneh et al., 2023), calcium-magnesium based (Balouchkhaneh et al., 2023), and other systems such as improvement of durability (Hata et al., 2020) are explained. Some of them are being evaluated for improving the bio-based ground improvement, including under low-crystal volume conditions and self-healing ground improvement. The low-crystal volume ground improvement technique combines enzyme-based calcite precipitation with milk protein, skim milk, and pure casein (Almajed et al., 2019; Miyake et al., 2022). The other application is self-healing (self-mediated) cement-based ground improvement. This application can revise the durability of cement-based ground improvement under the seawater exposure condition (Ikoma et al., n.d.). These technologies for crystal precipitation using microbial functions are collectively referred to as "microbial produced enzyme-based crystal precipitation technologies." In this microbial crystal precipitation technology, the reaction substrate is retained in the target material or injection with soluble substances combined with microbial cultivation medium. It enhances the crystal precipitation or maintenance of the water permeability caused by the cracks clogging and other gaps that occur when the material is damaged or has initial voids, and the microorganisms that naturally inhabit the material, or are artificially added to it, grow to increase the mineralization capacity.

Green Materials in Civil Engineering. DOI: https://doi.org/10.1016/B978-0-443-19106-0.00015-4

15.2 Overview of mechanisms of crystal precipitation by microbial functions and their engineering applications

There are various types of crystallization technologies based on microbial functions. Here, we present examples of crystal deposition technologies using typical microbial functions and show typical applications.

15.2.1 Biopolymers

Biopolymers is a general term for macromolecular substances (e.g., proteins) that constitute living organisms and are composed of polysaccharides, proteins, etc. Biopolymers are generally safer than industrially synthesized polymers and are easily degraded by biological actions. Compared to industrially synthesized polymers, biopolymers are generally safer and more easily degraded by biological action. As examples of attempts to apply biopolymers to geotechnical engineering (especially soil improvement), Chang and Cho et al. reported that mixing purified β1,3-glucan with soil increased uniaxial compressive strength (1); and Goto et al. and Takahata et al. reported that nonwater-soluble biopolymers are produced outside of bacteria. Goto et al. and Takahata et al. found that the use of a microorganism (*Enterobacter* sp. strain CJF-002), which produces a nonwater-soluble biopolymer outside the bacteria, can be expected to reduce soil permeability and increase liquefaction strength (2, 3); and Kaga et al. found that using PVA, a biodegradable polymer, can increase strength above 100 kPa (4). The mechanism of the reduction of soil permeability and increase of compressive strength by biopolymers is thought to be that the polymers generated in the interstitial spaces between soil particles play a cross-linking role and that the free movement of soil pore water is inhibited by the generated polymers.

15.2.2 Silicate

Silica-based soil improvement technology is used to increase strength and decrease permeability by injecting a silica compound into the ground to form silica gel. The formation of silica gel means that sodium silicate in the silica compound is neutralized by an acid added as a pH adjuster, which removes the sodium and condenses the silanol groups to form siloxane bonds, resulting in the formation of a high molecular weight silica gel. The mechanism of silica mineral formation by microbial function is shown in Eq. (15.1).

$$\mathbf{nSi}\ \mathbf{(OH)}_4 \rightarrow (SiO_2) + 2nH_2O \tag{15.1}$$

By utilizing the metabolic function of microorganisms widely found in soil as a pH adjuster, it is expected to be effective in obtaining high strength with less

unreacted silica by ensuring a longer gelatinization time compared to conventional technologies.

15.2.3 Sulfate

Focusing on anaerobic biostimulation, which is already at the level of practical application, this technology focuses on the function of sulfate-reducing bacteria, which are believed to be widely found in soil. By keeping the ground in a reducing state, the sulfate-reducing bacteria precipitate sulfides and fill the pore spaces, thereby reducing the permeability of the ground. The sulfate-reducing bacteria responsible for the reaction have been reported to exist widely in nature, such as in fields, lakes, river sediments, and submarine soils, so the application is not restricted, and it has been shown to have a water sealing effect.

15.2.4 Calcium-magnesium

The most frequently studied technology for microbial solidification is the one that utilizes the metabolic function of microorganisms to promote the precipitation of calcium-magnesium minerals. The metabolic function of microorganisms is used to accelerate the aerobic and anaerobic decomposition of organic matter and hydrolysis reaction of urea to obtain carbonate ions, and to promote the precipitation of crystal minerals by preparing calcium and magnesium ions in the pore water and alkaline conditions suitable for precipitation. The calcium and magnesium ions in the pore water and the alkaline conditions suitable for precipitation promote the precipitation of crystal minerals. The calcium and magnesium ions are supplied to the pore water at a certain ratio. A technique to precipitate dolomite, which is considered to have relatively higher corrosion resistance than calcium carbonate, by supplying calcium and magnesium ions in pore water at a certain ratio is also under investigation. Eqs. (15.2)–(15.4) show the mechanism of obtaining calcium carbonate minerals by the metabolic function of microorganisms when glucose is used as an organic nutrient source, and Eqs. (15.5)–(15.7) show the mechanism of obtaining calcium carbonate minerals by the hydrolysis reaction by enzymes (urease) derived from microorganisms.

Aerobic and anaerobic metabolism of organic matter:

$$\mathbf{C}_6\mathrm{H}_{12}\mathrm{O}_6 + 6\mathrm{O}_2 \rightarrow 6\mathrm{CO}_2 + 6\mathrm{H}_2\mathrm{O} \tag{15.2}$$

$$\mathbf{C}_6\mathrm{H}_{12}\mathrm{O}_6 \rightarrow 2\mathrm{CO}_2 + 2\mathrm{C}_2\mathrm{H}_5\mathrm{OH} \tag{15.3}$$

$$\mathbf{Ca}_2^+ + \mathrm{CO}_2 + \mathrm{H}_2\mathrm{O} \rightarrow \mathrm{CaCO}_3 + 2\ \mathrm{H}^+ \tag{15.4}$$

Hydrolysis reaction of urea:

$$\mathbf{CO(NH}_2)_2 + 2\mathrm{H}_2\mathrm{O} \rightarrow 2\mathrm{NH}_3^+\mathrm{CO}_2 \tag{15.5}$$

$$\mathbf{CO_2} + H_2O \rightarrow CO_3^{2-} + 2H^+ \tag{15.6}$$

$$Ca^{2+} + CO^{32-} \rightarrow CaCO^3 \tag{15.7}$$

In the reactions shown in Eqs. (15.2)−(15.4), a wide range of microorganisms with the ability to metabolize organic substances can be used, but the addition of pH adjusters should be considered because of concerns about a decrease in pH due to the formation of organic acids. On the other hand, the reactions shown in Eqs. (15.5)−(15.7) require microorganisms capable of producing urease, an enzyme that hydrolyzes urea, but the ammonia produced maintains an alkaline environment, which is expected to result in efficient calcium carbonate precipitation. In addition, dolomite precipitation is expected under conditions where calcium and magnesium ions coexist. It has been reported that this dolomite has better dissolution resistance and binder properties than calcite.

15.2.5 Selection of microbial functions with potential for engineering applications

As mentioned earlier, it is clear that various "self-healing" functions can be expected from the microbial functions inhabiting the soil. Table 15.1 summarizes the characteristics of each of them.

The following functions of crystal deposition that can be used for engineering purposes are expected: (1) filling of cracks, (2) stability of crystals in the general environment, and (3) reduction of hazardous by-products. In this case, it is important that the microbial function itself supports the formation of inorganic minerals. For this purpose, sulfate-reducing and calcium-magnesium systems are expected to be candidates. In addition, the fact that crystalline minerals can be expected to be deposited in both aerobic and anaerobic conditions, and that dolomite, which is expected to be produced by supplying magnesium ions, has superior corrosion resistance compared to calcium carbonate, are taken into consideration. The present status of the development of new ground improvement technology that improves the long-term stability of cement-improved soil and suppresses the generation of harmful by-products will be reported.

Table 15.1 Comparison of bio-based self-healing geomaterials.

	Microbial universality	**Inorganic mineralization**	**Durability**	**Applicability**
Biopolymers	○	×	△	△
Silicate	○	△	○	○
Sulfate	○(Aerobic)	○	○	○
Calcium-magnesium	◎(Aerobic/Anaerobic)	○	◎	◎

15.3 Development of preservation materials with self-healing and environmental preservation functions based on the microbial functions

This section focuses on calcium-magnesium systems, which are expected to have self-healing and environmental preservation functions through microbial functions. It describes the current status of technological development and prospects of the long-term stability technology by adding self-healing functions to cement-improved soil, which has been reported to deteriorate under marine environments, and functional granulated materials developed to preserve the bottom sediment environment at the World Natural Heritage site. Moreover, the low environmental biomediated soil improvement combined with EICP plus food waste will explain. This section describes the current status and prospects of technological development.

15.3.1 Development of the biomediated self-healing ground improvement technology which applied to the marine environment

In many cases, cement is used as a soil improvement technology to develop social infrastructure in port and harbor areas. It has been reported that when this cement-improved soil is exposed to seawater for an extended period, magnesium present in the seawater reacts with the calcium in the cement-improved soil to form magnesium hydroxide ($Mg(OH)_2$), which changes into a highly soluble form and leaches into the seawater, causing the cementation material to collapse, thus accelerating mechanical deterioration. This is reported to accelerate mechanical degradation by causing the cementation material to disintegrate. In order to control the degradation of cementation-improved soil under seawater exposure conditions, a technology focusing on the enhancement of calcium carbonate precipitation by microorganisms is being studied. In this technology, *Sporosarcina aquimarina*, which is from the sea and has urease activity and is expected to precipitate calcium carbonate, and a terrestrial microorganism, which is from the land area named *Sporosarcina pasteurii* were used as comparison targets because coastal areas were assumed to be the target. The characteristics of the two microorganisms are shown in Table 15.2.

Table 15.2 The characteristics of microbes.

	Sporosarcina pasteurii	*Sporosarcina aquimarina*
Source of microbes	Land area	Marine area
Salt tolerance (NaCl %)	10	13
Rational growth temperature (°C)	30	25
Rational growth pH	9	6.5−7.0
Anaerobic growth	+	+
Access no.	ATCC11859	JCM10887

Cement (blast-furnace cement type B), commercial clay, silica sand, and self-healing components (urea and culture medium) were mixed using a soil mixer, packed in a $\varphi = 35$ (mm), $H = 80$ (mm) column, and allowed to cure in the air at 20°C for 28 days before an 84-day exposure test using artificial seawater was started. The exposure conditions were as follows: Two types of exposure conditions were tested: 20°C, which is normally used for air-curing of cement-amended soil, and 30°C, which is the optimum incubation temperature for *S. pasteurii* and close to the optimum incubation temperature for *S. aquimarina*. Artificial seawater used for exposure was sampled every 14 days, and the seawater was changed and sampled every 28 days. The calcium and magnesium ion concentrations in the artificial seawater before and after replacement were measured using an atomic absorption spectrophotometer after filtration through a 0.2-μm membrane filter. In addition, needle penetration tests were conducted every 28 days to estimate the degree of mechanical degradation in the vertical direction due to seawater. Needle penetration tests were conducted on the exposed and sealed surfaces until a load of 5 N (10% of the load cell capacity) was applied, and the depth at which the difference in penetration between the exposed and sealed surfaces was observed was evaluated as the amount of accelerated deterioration.

Fig. 15.1 (Mihara et al., 2016) shows the amount of magnesium adsorbed and calcium eluted from the concentration of calcium and magnesium ions in the artificial sea during the exposure test period. This figure shows that the amount of calcium eluted/magnesium absorbed decreased at 20°C/30°C. In the test cases where

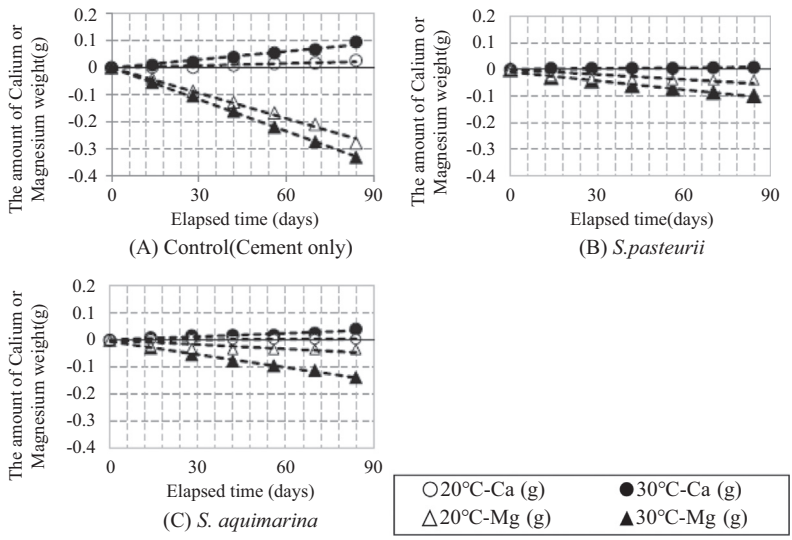

Figure 15.1 The trend of calcium elution weight and magnesium adsorption weight. (A) Control (cement treated clay). (B) Cement treated clay with *S.pasteurii*. (C) Cement treated clay with *S. aquimarina*.
Source: From Mihara et al. (2016).

calcite was expected to be recrystallized by the microorganisms in the terrestrial (*S. pasteurii*) (Fig. 15.1B) and marine (*S. aquimarina*) (Fig. 15.1B) environments compared with conventional method (Fig. 15.1A). This may be due to the recrystallization of calcium carbonate in the degraded areas of the specimens by the microbial function.

Fig. 15.2 shows the results of cone penetration tests conducted to evaluate this phenomenon. The test results show that the amount of accelerated degradation was suppressed under both 20°C and 30°C temperature conditions. In particular, in the case of *S. pasteurii* (Fig. 15.2B), the amount of accelerated degradation was suppressed to almost the same level at 20°C and 30°C. Although *S. aquimarina* (Fig. 15.2C) did not suppress degradation as much as *S. pasteurii* (Fig. 15.2B), it is clear that it can be expected to suppress degradation compared to cement alone (Fig. 15.2A). *S. aquimarina* was not as effective as *S. pasteurii* in inhibiting deterioration. It is assumed that the microbial function promoted the precipitation of calcium carbonate in the area where deterioration occurred due to exposure to seawater and increased the density of the deteriorated area, thereby reducing the amount of accelerated deterioration. The results indicate that the microbial function can be used to control the degradation of cement-improved soil.

15.3.2 Overview of functional granules for sediment conservation at the World Natural Heritage site

This section introduces the method of using microorganisms already living in situ as much as possible, instead of bringing in microorganisms from outside

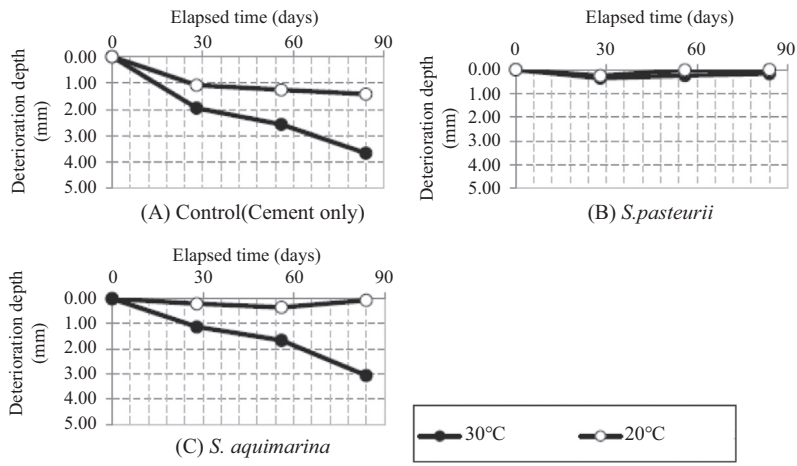

Figure 15.2 The trend of deterioration depth from the top of specimens. (A) Control (cement treated clay). (B) Cement treated clay with *S.pasteurii*. (C) Cement treated clay with *S .aquimarina*.
Source: From Mihara et al. (2016).

(Hata et al., 2019). The effectiveness of the functional granules (hereinafter referred to as "functional granules"), which are made by mixing dredged bottom sediment with a minimum amount of cement and a solidification accelerator such as urea for self-healing function, as an environmentally friendly construction material is described. The target area was Lake Ichkeul, a World Natural Heritage site in Tunisia, where microorganisms capable of producing urease, an enzyme that hydrolyzes urea, have already been confirmed as inhabitants based on the results of a preliminary survey. This paper presents the results of a study on the applicability of the microorganisms to environmental restoration. Fig. 15.3 shows the procedure for creating functional granules with a self-healing function. In this case, considering that the subject is a World Natural Heritage site, the amount of cement added was kept to the minimum necessary, and the solidification component eluted from the granulated material was used to generate a thin film of calcite in the surface layer to suppress resuspension of the surface sediments, and the nitrogen component eluted from the solidification component was used to promote growth of aquatic plants. The results of our study on the effectiveness of conservation techniques that promote the growth of aquatic plants by leaching nitrogen from the solidified component are explained.

Nitrification and denitrification reactions by in situ microorganisms derived from ammonia generated by the hydrolysis of urea are shown in Eq. (15.5) and in Eqs. (15.8)–(15.11).

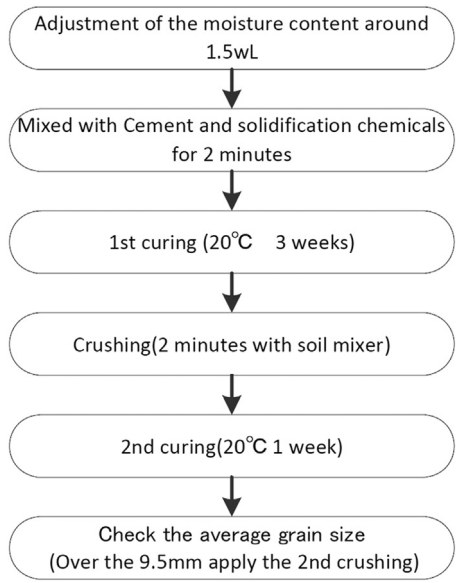

Figure 15.3 Procedure for granular material preparation.
Source: From Hata et al. (2019).

Nitrification and denitrification:

$$NH_4^+ + 1.5O_2 \rightarrow NO_2^- + H_2O + 2H^+ \quad (15.8)$$

$$\mathbf{NO_2^-} + 0.5O_2 \rightarrow NO_3^- \quad (15.9)$$

$$\mathbf{NO_3^-} + 2H_2 \rightarrow NO_2^- + H_2O \quad (15.10)$$

$$2\mathbf{NO_2^-} + 3H_2 \rightarrow N2 + 2H_2O + 2OH^- \quad (15.11)$$

The added urea-derived ammonia is expected to be partially absorbed and utilized by the plant body during the nitrification and denitrification reactions and, finally to be wholly decomposed as nitrogen gas.

Fig. 15.4 shows a panoramic view of the exposure test column installed in Lake Ichkeul, a World Natural Heritage site in Tunisia, before and after the test for 6 months. The growth of aquatic plants was observed on the surface of the nonwoven fabric wrapped around the column surface, confirming the possibility that plant growth is promoted by nutrients supplied from the granulated material or the surrounding environmental water.

The results of calcium and total nitrogen measurements in the granules before and after the test showed that calcium and nitrogen leached from the functional granules created by the proposed method after 6 months of exposure (see Fig. 15.5), suggesting that the granules created by the proposed method are superior in both increasing strength and restoring vegetation. The granules created by the proposed method are considered to be superior in terms of both strength enhancement and vegetation restoration.

(A) Column at installation (showing geomembrane).

(B) Salvaged column (geomembrane covered with aquatic plants).

Figure 15.4 Images of the exposure column at the start (A) and end (B) of the experiment. *Source*: From Hata et al. (2019).

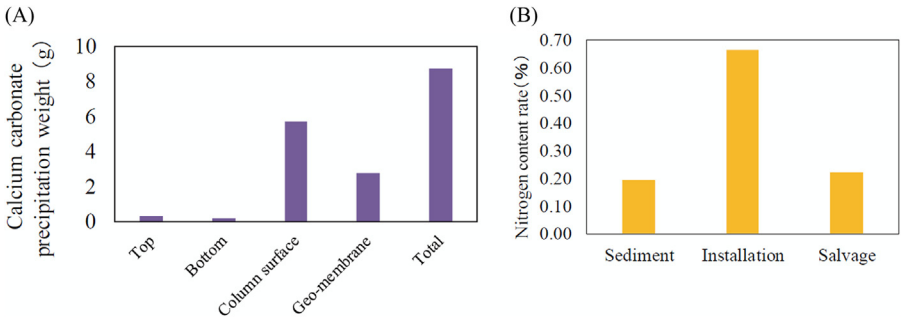

Figure 15.5 (A) The weights of precipitated calcium carbonate in the various samples. (B) The nitrogen content of each sample.
Source: From Hata et al. (2019).

15.4 Summary

In this chapter, we have described the outline of the technology focusing on microbial functions as a composite material with self-healing properties. Although various microbial functions that can contribute to self-healing (crystal deposition) have been reported, this chapter focuses on urease, an enzyme that hydrolyzes urea, and introduces an outline of a technology that contributes to suppressing the deterioration of cement-improved soil, improving the strength of bottom sediment surface layers, and supporting the growth of aquatic plants. Microorganisms capable of producing urease are widely distributed in the environment and have the advantage of being readily available, for example, as a source of nitrogen for agricultural land. On the other hand, the treatment of ammonia, which is a replicating organism, has been an issue, but it may be possible to apply this technology to a wider range of environments by appropriately controlling the concentration of added microorganisms and combining nitrification and denitrification reactions by soil microorganisms as well.

References

Almajed, A., Tirkolaei, H. K., Kavazanjian, E., & Hamdan, N. (2019). Enzyme induced biocementated sand with high strength at low carbonate content. *Scientific Reports*, *9*(1). Available from https://doi.org/10.1038/s41598-018-38361-1, http://www.nature.com/srep/index.html.

Balouchkhaneh, S. A., Shahnavaz, B., Moghaddam, A. M., & Karrabi, M. (2023). Mitigating alkali-silica reaction in cement mortars through smicrobial carbonate precipitation technique. *Construction and Building Materials*, *367*, 130155. Available from https://doi.org/10.1016/j.conbuildmat.2022.130155, https://www.sciencedirect.com/science/article/pii/S0950061822038119.

Chang, I., Im, J., Chung, M.-K., & Cho, G.-C. (2018). Bovine casein as a new soil strengthening binder from diary wastes. *Construction and Building Materials*, *160*, 1−9. Available from https://doi.org/10.1016/j.conbuildmat.2017.11.009, https://www.sciencedirect.com/science/article/pii/S0950061817322183.

Hata, T., Suetsugu, D., & Kasama, K. (2020). A biomediated deterioration mitigation method for cement-treated soil. *Environmental Geotechnics*, *7*(6), 435−444. Available from https://doi.org/10.1680/jenge.18.00011, http://www.icevirtuallibrary.com/toc/jenge/current.

Hata, T., Suetsugu, D., Kawachi, A., & Irie, M. (2019). Development of an eco-friendly bio-based granular geomaterial for the environmental restoration of Ichkeul Lake, Tunisia. *Euro-Mediterranean Journal for Environmental Integration*, *4*(1), 21. Available from https://doi.org/10.1007/s41207-019-0111-3, https://doi.org/10.1007/s41207-019-0111-3.

Hata, T., Tsukamoto, M., Inagaki, Y., Mori, H., Kuwano, R., & Gourc, J. P. (2011). Evaluation of multiple soil improvement techniques based on microbial functions. *Geo-Frontiers 2011: Advances in Geotechnical Engineering*.

Ikoma, S., Hata, T., Yagi, M, & Senjyu. (2023). Mitigating deterioration of cement-treated clay by microbe.

Mihara, K., Daisuke, S., Kasama, K., & Hata, T. (2016). A study of reducing for cement treated soil's deterioration by microbial function. *Journal of Japan Society of Civil Engineers, Ser. B3 (Ocean Engineering).*, *72*(2), I_414−I_419. Available from https://doi.org/10.2208/jscejoe.72.I_414.

Miyake, M., Kim, D., & Hata, T. (2022). Casein-assisted enhancement of the compressive strength of biocemented sand. *Scientific Reports*, *12*(1). Available from https://doi.org/10.1038/s41598-022-16879-9, http://www.nature.com/srep/index.html.

A review on microstructural characteristics of bacterial concrete

16

Sk Rahaman[1], *Arkamitra Kar*[1], *Jayati Ray Dutta*[2] *and Mohna Bandyopadhyay*[3]

[1]Department of Civil Engineering, Birla Institute of Technology and Science-Pilani, Hyderabad Campus, Hyderabad, Telangana, India, [2]Biological Sciences Department, Birla Institute of Technology and Science-Pilani, Hyderabad Campus, Hyderabad, Telangana, India, [3]Sharp Edge Labs, Pittsburgh, PA, United States

16.1 Introduction

The raw materials used in structural concrete include portland cement (PC), and aggregates are procured from natural resources. Concrete, the most widely used material all over the globe for infrastructural development, is leading to the depletion of natural limestone, thereby deteriorating environmental balance. Simultaneously, the rapidly increasing usage and production of PC concrete result in equivalent carbon dioxide emission, a major contributor to global warming (Garside, 2021). PC production alone contributes 2.8 G tons per year of CO_2, which is nearly 8% of the emissions globally (Ellis et al., 2020). Additionally, the propensity of crack development in PC concrete subjected to tensile loading is well established, irrespective of the mix proportions (Luhar et al., 2022). The appearance of these cracks results from numerous circumstances such as improper mix design, unexpected loading, various types of shrinkage, and natural disasters. These cracks initiate the effortless ingress of moisture, water, acid substances, harmful chemicals, and different kinds of salts into concrete. Furthermore, these cracks can damage the embedded reinforcement through corrosion and decrease the life of structural concrete (Fan et al., 2020). Hence, a sustainable solution to mitigate or repair the cracks is essential to overcome these problems. The existing maintenance and rehabilitation techniques for concrete need continuous monitoring and skilled labor, apart from being non-eco-friendly and expensive (Mondal & Ghosh, 2018; Souradeep & Kua, 2016). A possible solution to the aforementioned problems is the use of bacterial inclusions in concrete to heal the cracks. This chapter investigates the effects of incorporating bacteria on the microstructural characteristics of hardened cementitious systems and, subsequently, the characteristics of concrete at the specimen level.

Bacterial concrete can autonomously heal cracks by producing microbiologically induced calcite precipitation (MICP) (Achal et al., 2013; Vijay et al., 2017). It is

Green Materials in Civil Engineering. DOI: https://doi.org/10.1016/B978-0-443-19106-0.00016-6

reported that bacterial concrete is a sustainable, cost-effective, and almost maintenance-free method of crack healing (Rao et al., 2013; Tziviloglou et al., 2016). Also, the healing of cracks through bacterial inclusions prevents the need for regular maintenance and repairs during the service life of a concrete structure. Hence, autonomous self-healing of concrete using bacterial incorporation is a topic of importance for both research and industrial applications. Existing studies recommend the usage of bacterial strains that can survive in the form of spores in a harsh concrete medium with a pH of ~ 13 and temperature of $\sim 48^{\circ}C$. Some commonly reported bacterial strains are *Bacillus subtilis*, *Bacillus cereus*, and *Bacillus licheniformis* (Rahaman et al., 2020). Incorporating bacteria along with calcium-rich nutrient sources such as calcium lactate facilitates MICP through the metabolism of the bacteria under aerobic conditions. The MICP gradually heals newly formed microcracks in concrete as the cracks provide access to moisture and aerobic conditions for the bacterial spores to rejuvenate. The metabolic activity of bacterial cultures in the presence of nutrients and a favorable moist aerobic environment to precipitate calcite are shown in Eqs. (16.1) and (16.2). Table 16.1 presents a list of microorganisms that can form spores and use ureolysis to precipitate calcite as a by-product.

$$Ca^{2+} + \text{Cell} \rightarrow \text{Cell} - Ca^{2+} \tag{16.1}$$

$$\text{Cell} - Ca^{2+} + CO_3^{2-} \rightarrow \text{Cell} - CaCO_3 \tag{16.2}$$

It is reported that incorporating bacterial strains in concrete enhances the durability by the healing of cracks and also improves its mechanical performance (Wiktor & Jonkers, 2011). The enhancement in mechanical and durability performance is due to microstructural changes in the internal chemistry of concrete. Several existing studies focus on the mechanical and durability performance of bacterial concrete (Buller et al.,

Table 16.1 List of microorganisms that can form spores and use ureolysis to precipitate calcite as a by-product.

Bacterial species	References
Bacillus pasteurii	Achal et al. (2013), Mondal and Ghosh (2018)
Bacillus subtilis	Rahaman et al. (2020), Vijay et al. (2017)
Bacillus licheniformis	Rahaman et al. (2020), Vahabi et al. (2015)
Bacillus sphaericus	Wang, Snoeck, et al. (2014)
Bacillus cohinii	Jonkers and Schlangen (2008)
Sporosarcina pasteurii	Chahal et al. (2012)
Bacillus cereus	Rahaman et al. (2022), Tayebani and Mostofinejad (2019)
Bacillus megatarium	Andalib et al. (2016)
Bacillus pseudofirmis	Nežerka et al. (2022)
Bacillus halodurans	Sri Durga et al. (2021)

2021; Kadapure et al., 2020; Nodehi et al., 2022; Smitha et al., 2022). However, there is limited information available on the microstructural characteristics of concrete with bacterial inclusions. Hence, in this chapter, a thorough review of the microstructural characteristics of bacterial concrete is provided with key findings from scanning electron microscope (SEM), energy dispersive X-ray spectroscopy (EDS), X-ray diffraction (XRD), Fourier transform infrared spectroscopy (FTIR), and thermogravimetric analysis (TGA). The next section outlines the flow of this review.

16.2 Methodology adopted for the study

This study is performed by exploring different published articles in reputed journals on different types of bacterial inclusions in concrete. This study also reviews existing literature and summarizes significant results from different microstructural analyses of bacterial concrete. Several relevant technical research articles, theses, book chapters, and conference proceedings are reviewed for this study. These research resources are selected based on title, abstract, keywords, and potential findings related to microstructural analyses. The steps followed in preparing this chapter are presented in Fig. 16.1.

16.3 Background of microstructural and chemical analyses

Stereomicroscopic imaging, scanning electron microscopy with energy dispersive X-ray spectroscopy (SEM-EDS), XRD, FTIR spectroscopy, and TGA are some of the most commonly reported techniques for microstructural, mineralogical, and chemical characterizations of bacterial concrete (Dhami et al., 2012; Jonkers & Schlangen, 2008; Rajczakowska et al., 2019; Ramagiri & Kar, 2019; Vijay &

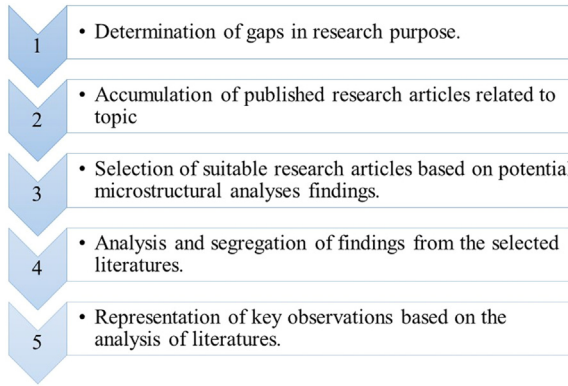

Figure 16.1 Methodology opted for this research article.

Murmu, 2019a). The key findings corresponding to each technique are presented in the following sections.

16.3.1 Stereomicroscopic imaging

A stereomicroscope, also referred to as a binocular inspection microscope, enables the visual inspection of three-dimensional samples at magnifications of up to nearly 150×. This is a low-power consumption compound instrument with magnification that can be varied by changing the resolution of the objective lenses. It is used to observe the surface morphology of homogeneous and heterogeneous materials and to identify different components through shape, size, color, and the formations of voids or potential fracture planes. In a stereomicroscope, illumination is provided on the top of the sample instead of transmitting light through it. A digital stereomicroscope coupled with an inbuilt camera helps to visualize the sample in macro photographic mode with increased resolution provided by the software associated with the camera.

16.3.2 Scanning electron microscope and energy dispersive X-ray spectroscopy

SEM and EDS are used to characterize material morphology and elemental composition. Capturing micrographs at 2500×, 5000×, and 10,000× magnification is commonly reported in the literature on hardened cementitious paste systems. Micrographs captured at 20,000× and higher resolution are reported in case of bacterial inclusions in cementitious samples to capture the development of bacterial colonies and the MICP in the microstructure. Samples of hardened cementitious paste not exceeding 10 mm diameter and 3 mm thickness are preferred for these characterizations. Before performing the SEM-EDS analyses, the samples are oven-dried to make them moisture-free. Subsequently, these samples are coated with a 10 nm thick layer of gold-palladium or, silver or titanium dioxide using a sputter coater to make them electrically conductive. The characterizations are performed under vacuum conditions of $9.6 \times 10{-}5$ Pa or lower (Kar, 2013). The recommended voltage for these characterizations of cementitious samples is 5−15 kV at a working distance of 8−10 mm (Kar, 2013).

16.3.3 X-ray diffraction spectroscopy

XRD is a widely used technique to analyze the crystal structure of solid material by phase identification. The analysis is performed on finely ground, powdered samples. XRD of bacterial concrete is performed over a 2θ range of 5−90 degrees, mostly with a step width of 0.01 or 0.02 degrees at the rate of 2 seconds per step (Kar, 2013). The recommended working conditions to generate the CuKα X-rays are 40 mA current and 40 kV of voltage (Kar, 2013). The minerals are identified by comparing the diffractograms with existing literature.

16.3.4 Fourier transform infrared spectroscopy

FTIR spectroscopy is performed to determine the molecular bonds present in a material. The characterizations are performed by exposing the samples to infrared light in the mid-infrared range (wavenumber of 4000 to 400 cm^{-1}). The absorbed infrared spectra are used to identify the molecular bonds present in the sample. The inclusions of bacteria and nutrients change the molecular bonds in hardened cementitious pastes. The change in the wavenumber of the absorption spectra is referred to as a chemical shift. These chemical shifts are used to determine the progress of chemical reactions and the presence of MICP due to bacterial inclusions. Older FTIR spectroscopy apparatus required powdered samples molded into pellets with KBr. However, modern FTIR spectrometers equipped with attenuated total reflectance attachment can characterize powdered solid samples, making them more user-friendly (Kar, 2013). The molecular bonds are identified by comparing the absorbed wavenumbers from a database provided by MERCK (Merck et al., 2022).

16.3.5 Thermogravimetric analysis

TGA is performed to determine the presence of chemical compounds in a material through mass loss due to increase in temperature. For hardened cementitious pastes, this analysis is performed over a temperature range of 20°C−950°C in air at a heating rate of 10°C per minute. The temperature is increased at a constant rate to measure the gradual mass loss of material. The losses in mass at specific temperatures correspond to the disintegration of particular chemical compounds. The presence of MICP in bacterial concrete can be identified by observing the mass loss corresponding to calcite decomposition at 750°C−780°C.

16.4 Microstructure of bio-concrete

This section presents an extensive review of different works of literature related to bacterial concrete, having adequate information about microstructural analyses. Findings from various experiments of microstructural studies are discussed separately.

16.4.1 Stereomicroscopy of bio-concrete

A study on the inclusions of *B. subtilis*, along with peptone and yeast extract, to enhance the durability of concrete by $CaCO_3$ precipitation concluded that at 44 days of curing, crack width of 400 μm is wholly repaired by MICP (Nguyen et al., 2019). This observation is made through visual inspection in a stereomicroscope. From Fig. 16.2, it is evident that the healing of cracks is gradually increasing over a period of time. From Fig. 16.2C, at the age of 44 days, it can be seen that the cracks are filled with whitish deposition of MICP. The observations from visual inspection are later corroborated through mineralogical and microstructural analyses.

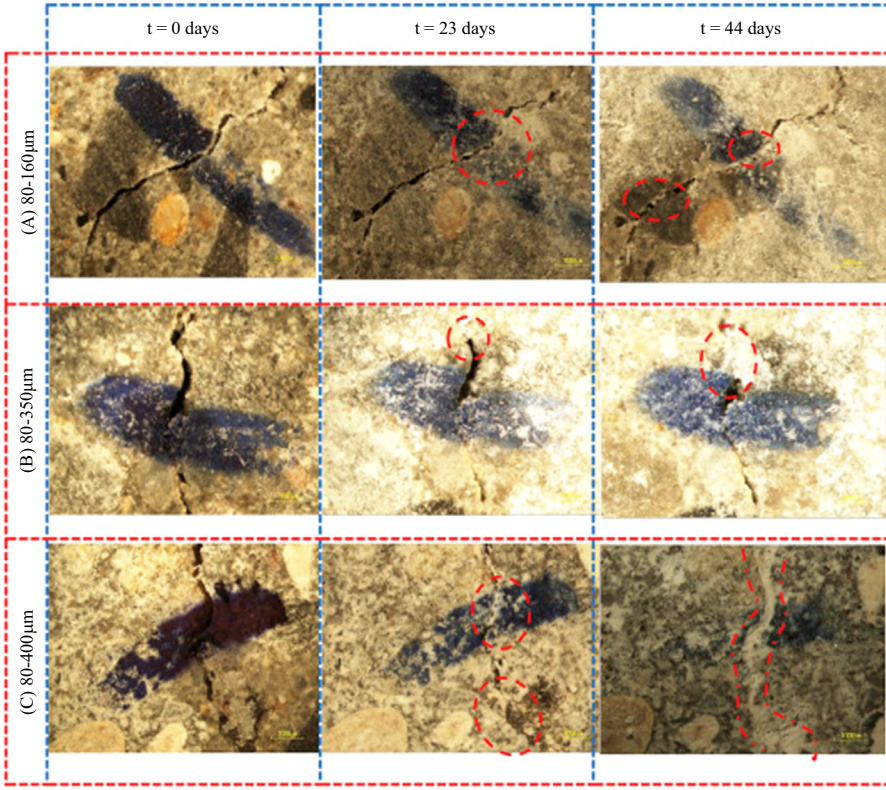

Figure 16.2 Stereomicroscopic image of concrete crack healing after 0, 23, and 44 days of water immersion of specimen prepared (A) without bacteria and nutrient, (B) with nutrient, (C) with bacteria (Nguyen et al., 2019).

It is reported in another study that microencapsulated spores of *Bacillus sphaericus* heal a maximum crack width of 970 μm in concrete (Wang, Soens, et al., 2014). Images captured by stereomicroscope show the gradual decrease in crack width with time and completely healed at three weeks with microbial precipitation (Fig. 16.3).

A study by Esaker et al. (2021) reports that the curing media of cracked mortar specimens with inclusions of *B. subtilis* plays a significant role in the healing process. The study demonstrates that cracks having widths of 280 and 260 μm get completely healed when the specimens are cured in water and pH-neutral soil, respectively. These observations are made through stereomicroscopic analysis. The results are presented in Fig. 16.4.

It is also reported that the white precipitate that heals the cracks is calcium carbonate, as confirmed through stereomicroscopy (Fig. 16.5). The findings from

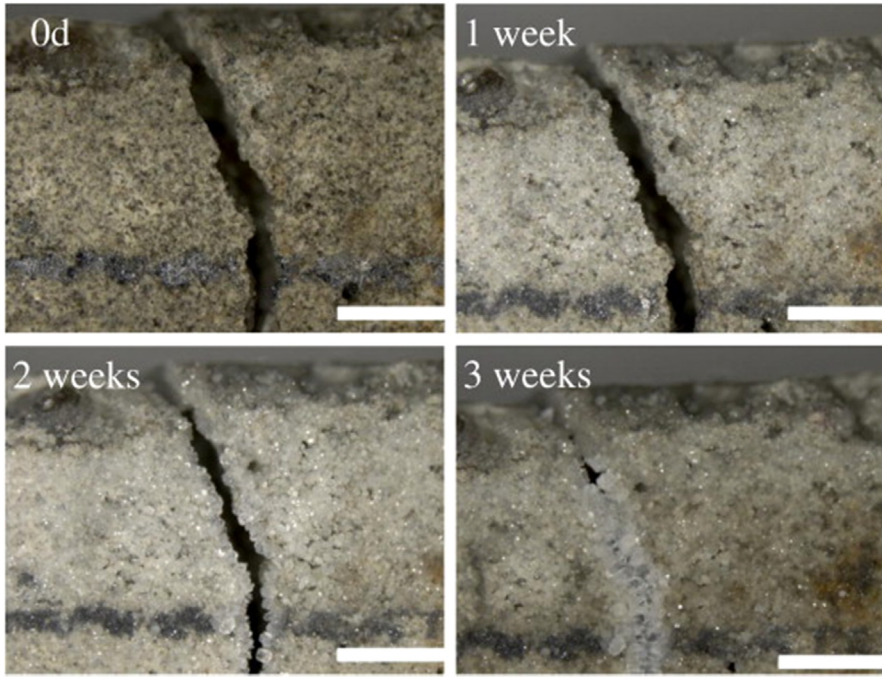

Figure 16.3 Stereomicroscopic image of the concrete crack healing process (Wang, Soens, et al., 2014).

stereomicroscopy are correlated with SEM-EDS in the section scanning electron microscopy of bio-concrete.

A study by Wang, De Belie, et al. (2012) shows that diatomaceous earth (DE) coating can protect bacterial cells from the highly alkaline environment of concrete. The study concluded that the DE encapsulated *B. sphaericus* shows much higher metabolic activity, improving the crack healing efficiency. Cracks of width varied from 0.05 to 1 mm in concrete specimens are healed by bacterial inclusions by three weeks, as visualized through stereomicroscopy in Fig. 16.6.

As stereomicroscopic observations rely mostly on visual inspections by experts and comparisons with existing information, it is essential to conduct SEM-EDS to characterize the morphologies and elemental compositions of the chemical phases present in hardened cementitious paste with bacterial inclusions.

16.4.2 Scanning electron microscopy of bio-concrete

SEM is conducted for hardened cementitious pastes with bacterial inclusions to observe the changes in morphology caused by MICP. The metabolic activity of bacteria inside the cementitious environment precipitates calcite, which occupies the voids and pores in the hydrated paste to improve the resistance to chemical attacks.

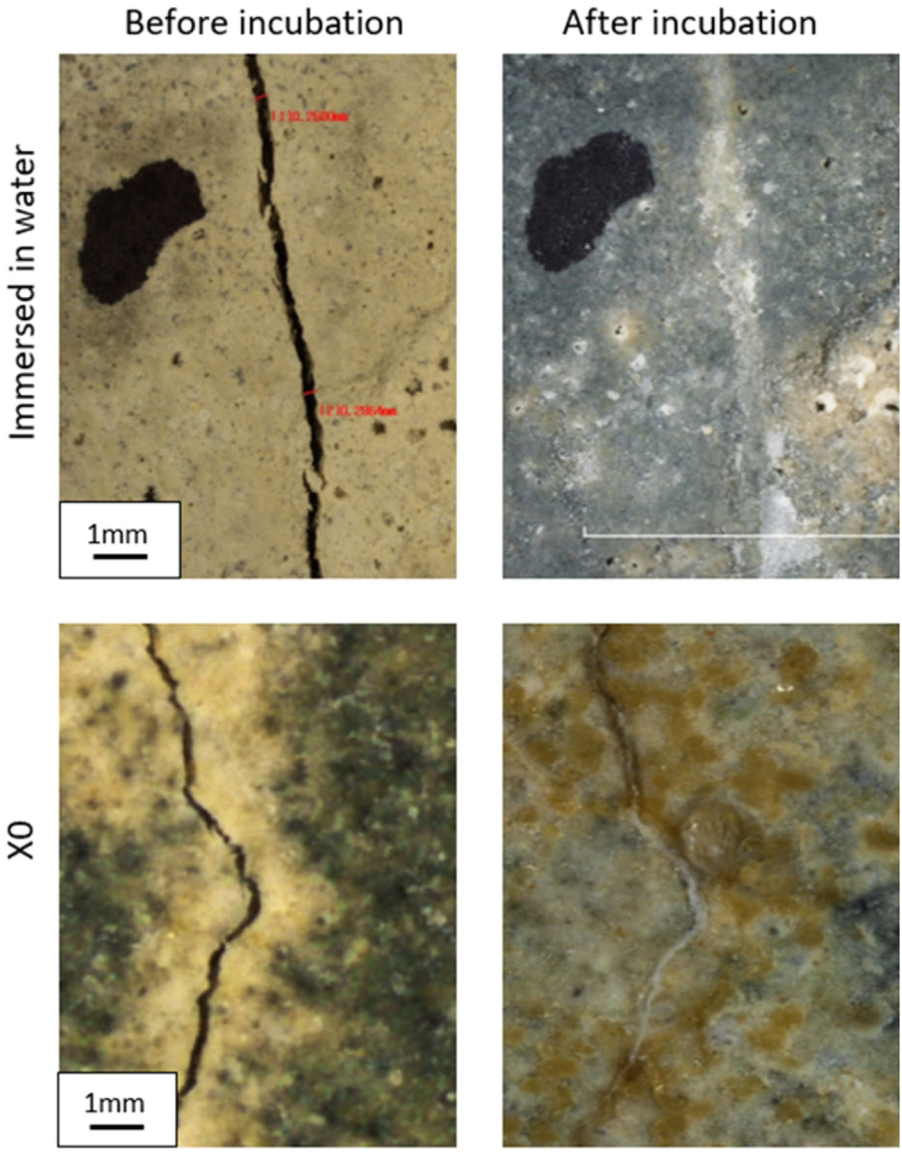

Figure 16.4 Stereomicroscope image of mortar specimen before and after crack healing (Esaker et al., 2021).

Also, to identify the presence of bacterial cells and the additional nutrients, SEM techniques are useful. A rod-shaped morphology is observed in hydrated cement paste with *Bacillus* sp. inclusions (Fig. 16.7). Additionally, the deposition of dense calcite crystals with rod-shaped impressions is observed near the bacterial colonies as precipitation (Achal et al., 2011).

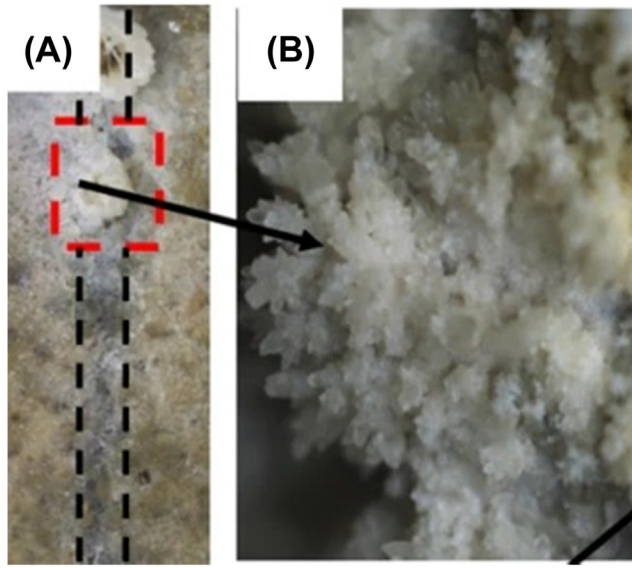

Figure 16.5 Stereomicroscopic image of (A) Calcium carbonate crystal deposited in cracks, (B) magnified image of calcium carbonate as indicated by red square (Esaker et al., 2021).

Another study on the use of *Sporosarcina pasteurii* inclusions shows the deposition of distinct calcite crystals in the pores of the hydrated paste (Nosouhian et al., 2016), as shown in Fig. 16.8. Also, *Bacillus pasteurii* precipitate calcium carbonate in pores in the matrix of the concrete specimen (Yoosathaporn et al., 2016).

Calcite precipitation due to bacterial activity is reported in another study (Luo et al., 2015). The MICP is observed to heal the cracked surface through the deposition of a closely packed lamellar morphology corresponding to crystalline calcite (Fig. 16.9). The elemental compositions of the above systems obtained through EDS spectral analysis revealed that precipitation in the crack surface is essentially a combination of calcium, carbon, and oxygen atoms with a weighted percentage of 47.58%, 27.29%, and 24.93%, respectively. This chemical composition is consistent with that of calcium carbonate, confirming the presence of MICP.

Observations from the stereomicroscopy by Nguyen et al. (2019) demonstrated that the crack is healed with inclusion of *B. sphaericus*. The precipitation inside the microstructure to heal the crack is also analyzed using SEM and EDS (Nguyen et al., 2019). Fig. 16.10A shows the homogeneous dissemination of calcite crystals in different forms. Mostly, the bouquets-needle-like and rhombohedral structure of calcite crystal is observed. EDS findings (Fig. 16.10B) show that precipitation is mainly a combination of three elements: carbon, oxygen, and calcium, and the authors conclude that the precipitated mineral is $CaCO_3$.

It is reported in another study that inclusions of *B. sphaericus* help to self-heal in cementitious concrete systems by the deposition of $CaCO_3$ (Wang, Soens, et al., 2014).

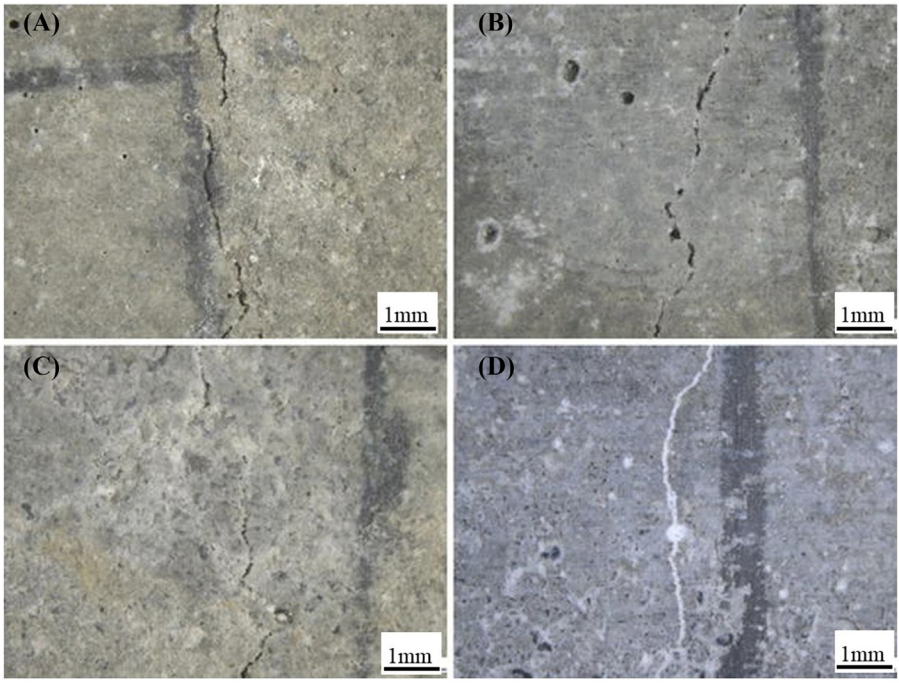

Figure 16.6 Stereomicroscope image of concrete crack healing in different specimens (A) only with DE immersed in water, (B) only with DE immersed in the deposition medium, (C) with DE-immobilized bacteria immersed in water, and (D) with DE-immobilized bacteria immersed deposited media. (Wang, De Belie, et al., 2012).

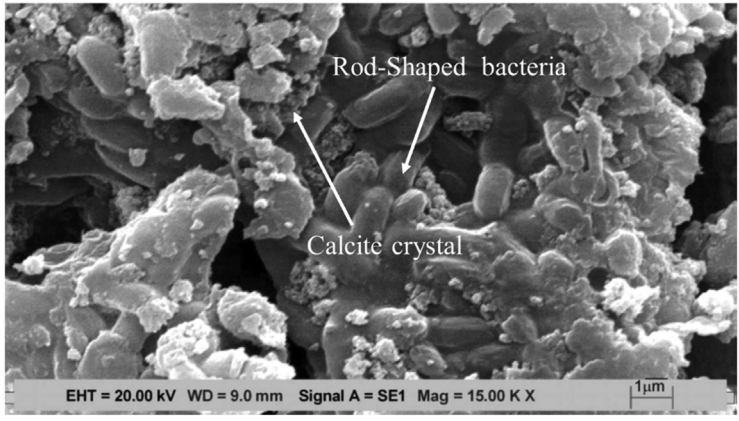

Figure 16.7 Micrographs of *Bacillus* sp. incorporated concrete (Achal et al., 2011).

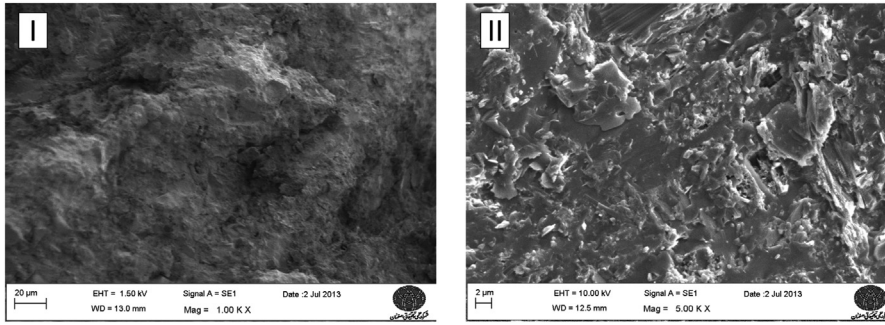

(A)

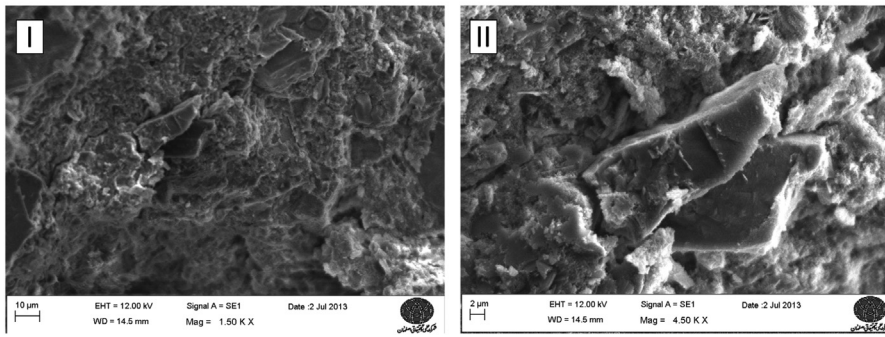

(B)

Figure 16.8 Micrographs of (A) concrete with *Bacillus subtilis* and (B) concrete with *Sporosarcina pasteurii*, including developing calcite crystal (Nosouhian et al., 2016).

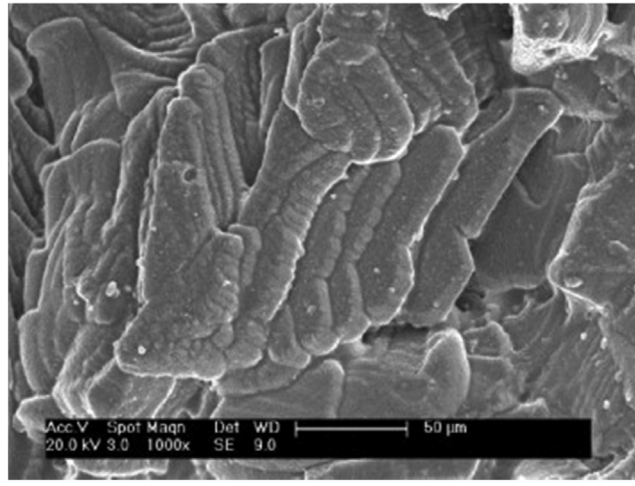

Figure 16.9 Micrographs of calcite precipitation at the crack surface (Luo et al., 2015).

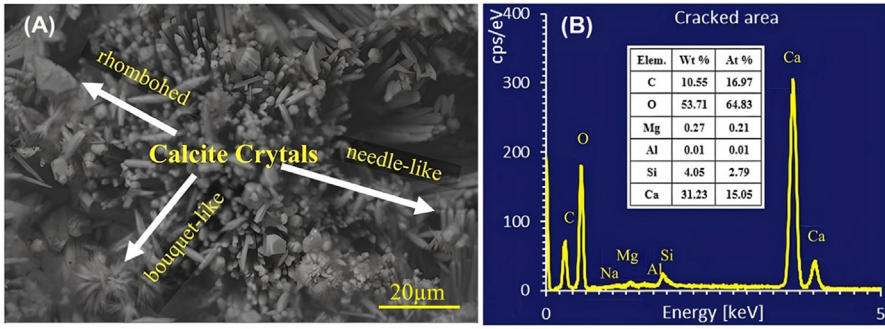

Figure 16.10 (A) Micrograph and (B) Energy dispersion spectra of deposited calcite in the crack (Nguyen et al., 2019).

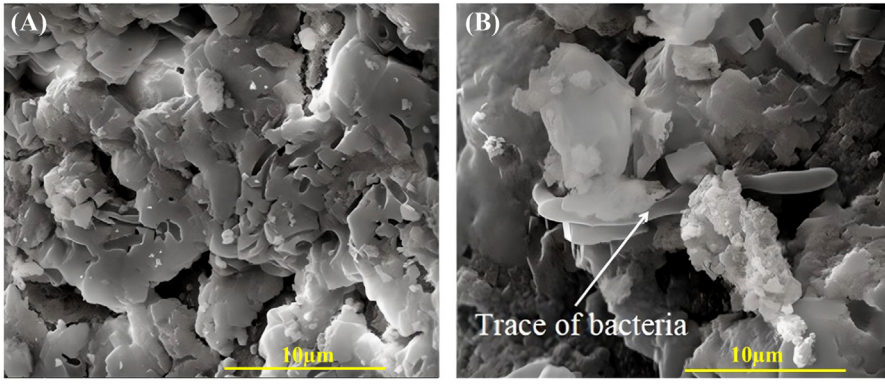

Figure 16.11 Micrographs of (A) $CaCO_3$ precipitation inside the crack. (B) Traces of bacteria inside the concrete (Wang, Soens, et al., 2014).

Fig. 16.11 shows the $CaCO_3$ precipitation and the presence of bacterial cells in the hardened cementitious paste.

Calcium carbonate precipitation observed through stereomicroscopy presented in Fig. 16.5 is validated through SEM imaging. The dense morphology of $CaCO_3$ is presented in Fig. 16.12 (Esaker et al., 2021).

SEM-EDS analysis provides information on the morphology and elemental composition of a material system. Additionally, the findings from XRD analyses are discussed in the following section to determine the crystallinity of any newly formed material due to bacterial inclusions.

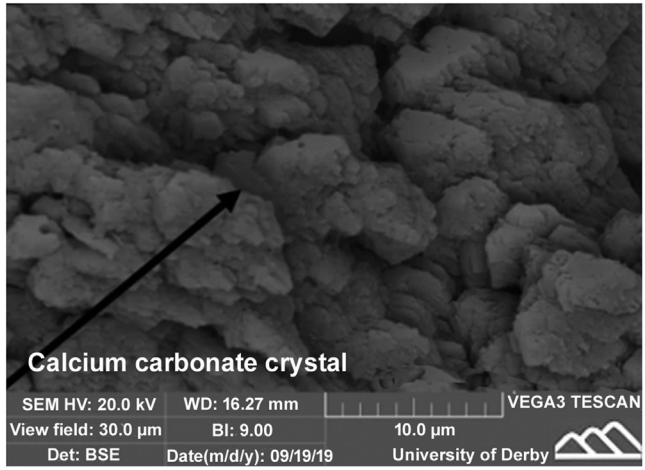

Figure 16.12 Micrographs of the dense structure of calcium carbonate crystal (Esaker et al., 2021).

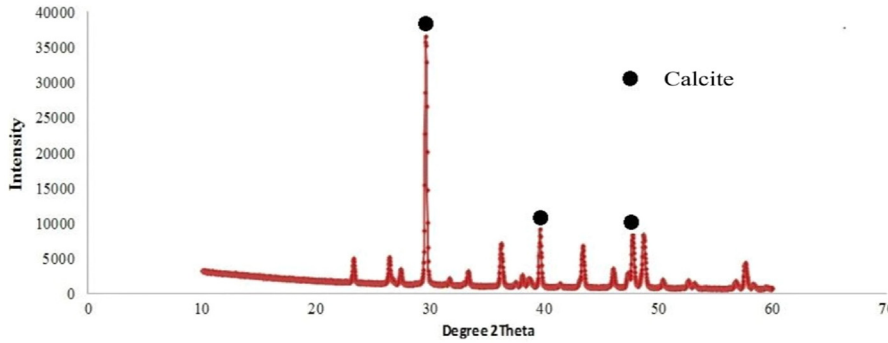

Figure 16.13 XRD pattern of precipitated material inside the crack (Vijay & Murmu, 2019b).

16.4.3 X-ray diffraction of bio-concrete

In a study conducted by Vijay and Murmu (2019b), the use of *B. subtilis* along with basalt fiber and calcium lactate, crack healing is observed along with enhancement in the durability of concrete. XRD analyses are performed to identify the crystallinity of the precipitate from bacterial metabolism. The peaks observed at 2θ angles of 29.6, 36.2, 39, and 47.7 degrees confirm the presence of crystalline calcite. The corresponding XRD pattern is given in Fig. 16.13.

A study on mortar cubes treated with ureolytic mixed culture, calcium chloride, and nutrient broth shows the formation of a precipitate over the surface of the

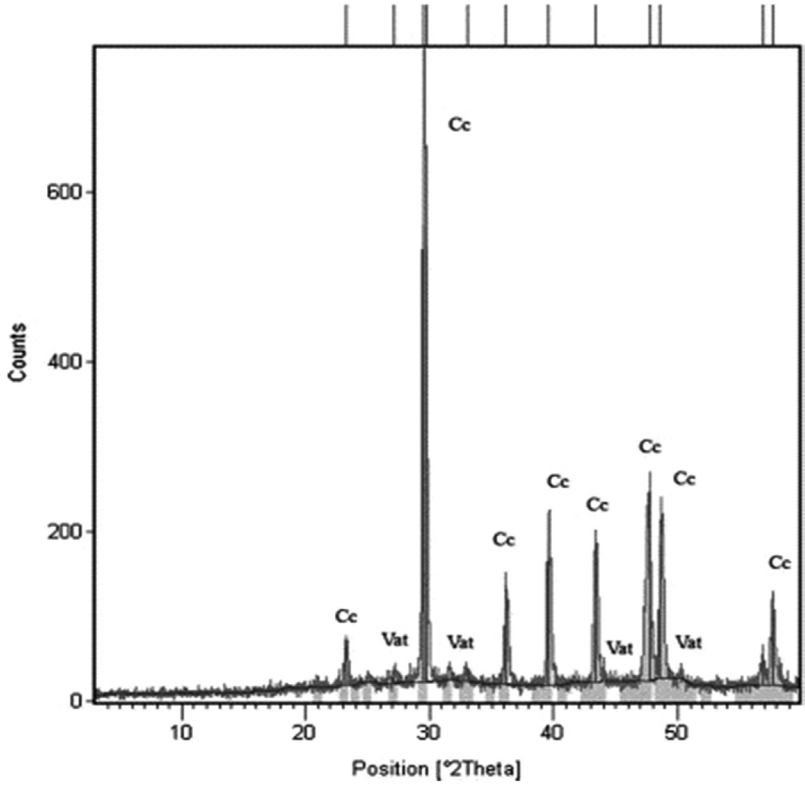

Figure 16.14 XRD pattern of bacterial mortar incorporated with mixed culture, $CaCl_2$, and nutrient broth (De Muynck et al., 2008).

specimens (De Muynck et al., 2008). XRD analyses of the precipitate (Fig. 16.14) confirm the presence of crystalline calcite (Cc) and vaterite (Vt). Furthermore, the addition of nutrient broth and bacteria to the mortar cube also forms the Vt crystal, as observed in Fig. 16.14.

XRD analyses from another study (Fig. 16.15) show that the addition of 10% silica fume, along with *S. pasteurii* (10^5 cell/mL), leads to the formation of more calcite peaks (Cc) peaks (Chahal et al., 2012).

XRD analyses from another study (Sahoo et al., 2016) on the inclusion of *B. sphaericus* in mortar cubes show additional calcite peaks compared to control mortar cubes (Fig. 16.16). These additional peaks of calcite represent the additional calcite deposition due to bacterial inclusions.

16.4.4 Fourier transform infrared spectroscopy of bio-concrete

In a study on *B. subtilis* inclusions in concrete, MICP is observed in the presence of urea nutrients (Huynh & Son, 2017). Absorbance peaks of CO_3^{2-} are observed at a

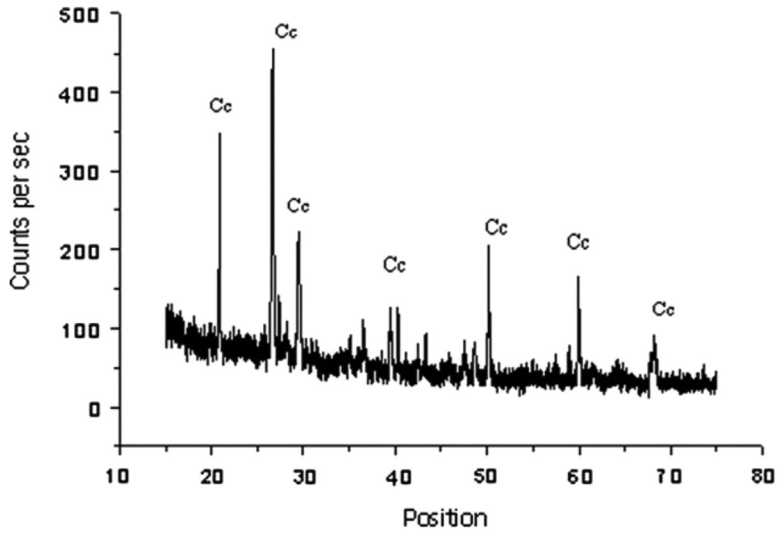

Figure 16.15 XRD patterns of *Sporosarcina pasteurii* and 10% silica fume incorporated cementitious paste (Chahal et al., 2012).

wavenumber of 712, 875, 1459, and 2519 cm^{-1}. Peaks are seen at the wavenumber of 1798, 2880, and 2980 cm^{-1} in tune with the C = O stretching bond of CO_3^{2-}. Also, the absorbance peaks at a wavenumber of 1469 cm^{-1} are consistent with the C-O bond in $CaCO_3$ (Huynh & Son, 2017). Another study concludes that CO_3^{2-} is located at 870 and 1424−1430 cm^{-1} (Chandra Sekhara Reddy & Ravitheja, 2019).

16.4.5 Thermogravimetric analysis of bio-concrete

A study conducted on *B. sphaericus* to identify the ability to precipitate $CaCO_3$ in concrete environment (Van Tittelboom et al., 2010) implements TGA techniques to compare these bacterial cells in active (BS) and autoclaved (autoclaved BS) conditions. Fig. 16.17 shows that at 100°C, the first mass loss is observed due to water evaporation. The second mass loss is observed between 500°C and 800°C due to the decomposition of $CaCO_3$. This loss in mass in the range of 500°C−800°C confirms the formation of calcite due to metabolic activity of the bacterial cells.

Another study using bacterial inclusions reports that the decomposition of $CaCO_3$ happens at a temperature between 650°C and 750°C (Wang, Van Tittelboom, et al., 2012). A recent study on cement paste without bacteria (Control), cement paste with *Bacillus cohnii* (BC), and cement paste with dead bacteria (DBC) reports that the mass loss observed between 760°C−780°C corresponds

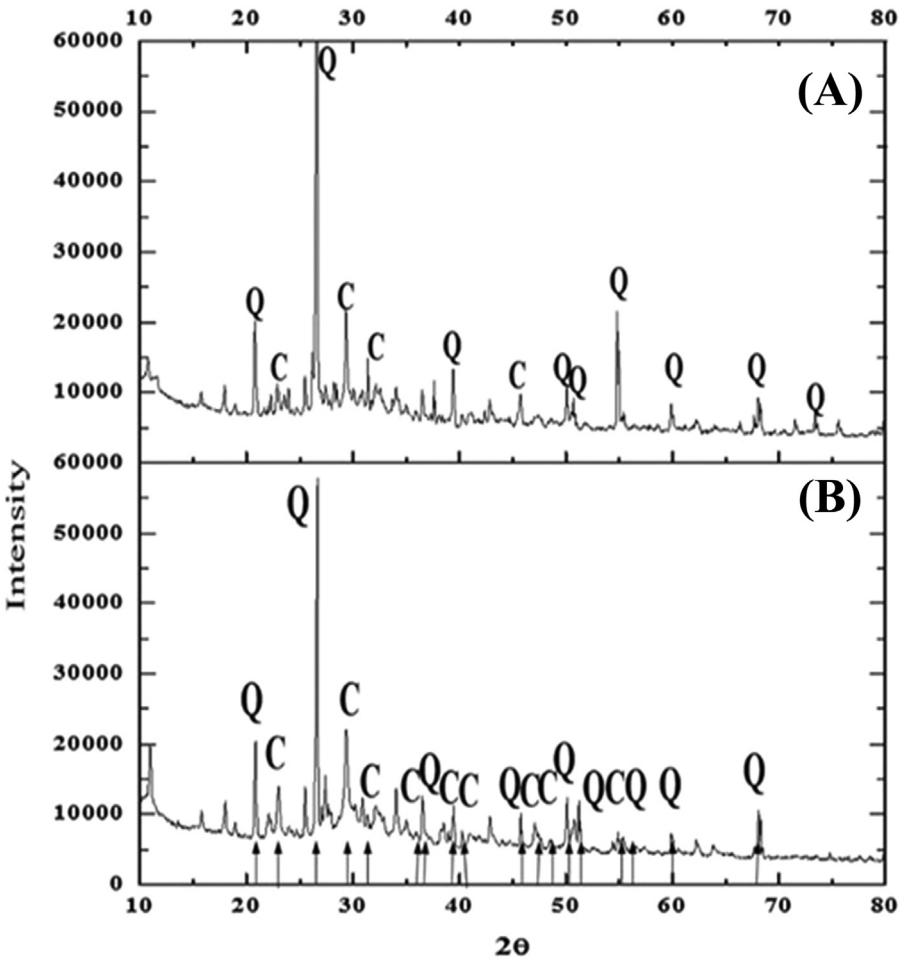

Figure 16.16 XRD patterns of (A) control mortar cube and (B) bacteria incorporated mortar cube sample. *C*, Calcite; *Q*, quartz (Sahoo et al., 2016).

to the decomposition of $CaCO_3$ (Skevi et al., 2021). The corresponding observation is given in Fig. 16.18.

Based on the observations from morphological, elemental, mineralogical, and chemical analyses, MICP in the microstructure of hardened cementitious paste systems is confirmed. The dense crystalline nature of the precipitated calcite aids in filling the voids, thereby resisting the ingress of harmful chemicals and enhancing the durability of concrete with bacterial inclusions. The conclusions from this review are presented below.

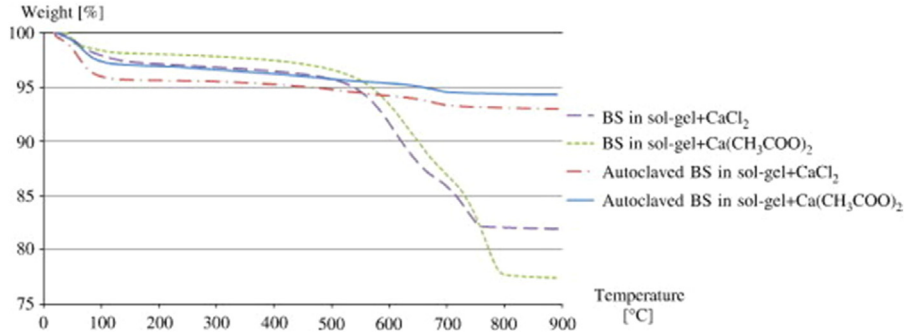

Figure 16.17 TGA results of active and autoclaved bacteria incorporated concrete (Van Tittelboom et al., 2010).

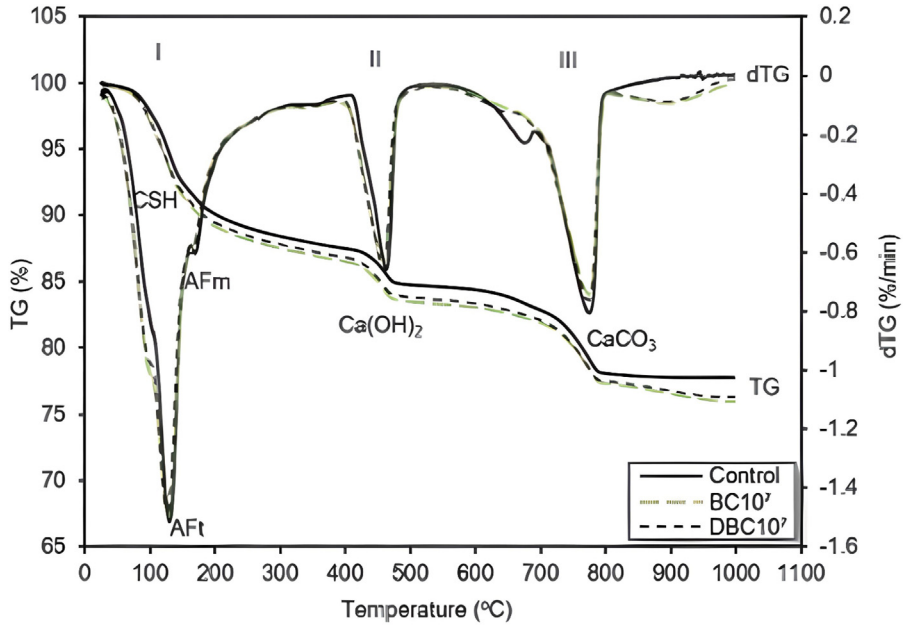

Figure 16.18 TGA of cement pastes without bacteria, with bacteria, and with dead bacteria (Skevi et al., 2021).

16.5 Conclusions

This chapter reviews available studies on the inclusions of different types of bacteria in concrete to improve durability. This study specifically highlights the

morphology, mineralogy, and chemistry changes of cementitious systems containing bacterial inclusions. The key findings from this study are:

1. *Bacillus* strains are found to be the most commonly used bacteria for inclusions in concrete.
2. Stereomicroscopic analyses show that cracks finer than or equal to 1 mm can be healed by the inclusion of Bacillus strains with suitable nutrients. It is found that bacterial cells are more effective when included with encapsulations to protect them in highly alkaline concrete environments.
3. SEM-EDS techniques confirm the deposition of calcite in the hardened cementitious microstructure. The presence of the bacterial cells can be observed at magnifications of 20,000 ×. The presence of calcite crystals can be observed at lower magnifications. The formation of calcite is characterized through its dense morphology and confirmed with elemental analysis using EDS.
4. The crystalline nature of calcite is validated through XRD analysis. The formation of additional peaks of calcite in samples containing bacterial inclusions confirms the deposition.
5. The presence of the calcite precipitate is also confirmed through analysis of the molecular bonds using FTIR spectroscopy.
6. The use of TGA corroborates the findings from the morphological, mineralogical, elemental, and molecular bond characterizations.
7. Finally, this review on microstructural characteristics concludes that the inclusion of bacterial cells in cementitious concrete systems exhibits the potential for further studies at the specimen level in laboratory as well as field conditions. Favorable results from these studies can encourage widespread usage of bacterial inclusions for crack healing in concrete and reduce the need for regular maintenance and repair. This technique can thus be recommended as a sustainable construction practice.

Acknowledgments

This study is performed as a part of a CSIR-sponsored project (CSIREMR- II 22/0770/18). The authors would like to thank BITS-Pilani, Hyderabad Campus, for providing the resources necessary for this study.

References

Achal, V., Mukherjee, A., & Reddy, M. S. (2011). Microbial concrete: Way to enhance the durability of building structures. *Journal of Materials in Civil Engineering*, *23*(6), 730−734.

Achal, V., Mukerjee, A., & Sudhakara Reddy, M. (2013). Biogenic treatment improves the durability and remediates the cracks of concrete structures. *Construction and Building Materials*, *48*, 1−5. Available from https://doi.org/10.1016/j.conbuildmat.2013.06.061.

Andalib, R., Abd Majid, M. Z., Hussin, M. W., Ponraj, M., Keyvanfar, A., Mirza, J., & Lee, H. S. (2016). Optimum concentration of *Bacillus megaterium* for strengthening

structural concrete. *Construction and Building Materials*, *118*, 180−193. Available from https://doi.org/10.1016/j.conbuildmat.2016.04.142.

Buller, A. S., Buller, A. M., Ali, T., Tunio, Z. A., Shabbir, S., & Malik, M. A. (2021). Experimental characterization of bacterial concrete against mechanical and durability performance. *Engineering, Technology & Applied Science Research*, *11*(1), 6703−6707. Available from https://doi.org/10.48084/etasr.3983.

Chahal, N., Siddique, R., & Rajor, A. (2012). Influence of bacteria on the compressive strength, water absorption and rapid chloride permeability of concrete incorporating silica fume. *Construction and Building Materials*, *37*, 645−651. Available from https://doi.org/10.1016/j.conbuildmat.2012.07.029.

Chandra Sekhara Reddy, T., & Ravitheja, A. (2019). Macro mechanical properties of self healing concrete with crystalline admixture under different environments. *Ain Shams Engineering Journal*, *10*(1), 23−32. Available from https://doi.org/10.1016/j.asej.2018.01.005.

De Muynck, W., Cox, K., Belie, N. De, & Verstraete, W. (2008). Bacterial carbonate precipitation as an alternative surface treatment for concrete. *Construction and Building Materials*, *22*(5), 875−885. Available from https://doi.org/10.1016/j.conbuildmat.2006.12.011.

Dhami, N. K., Reddy, M. S., & Mukherjee, A. (2012). Improvement in strength properties of ash bricks by bacterial calcite. *Ecological Engineering*, *39*, 31−35. Available from https://doi.org/10.1016/j.ecoleng.2011.11.011.

Ellis, L. D., Badel, A. F., Chiang, M. L., Park, R. J. Y., & Chiang, Y. M. (2020). Toward electrochemical synthesis of cement—An electrolyzer-based process for decarbonating $CaCO_3$ while producing useful gas streams. *Proceedings of the National Academy of Sciences of the United States of America*, *117*(23), 12584−12591. Available from https://doi.org/10.1073/pnas.1821673116.

Esaker, M., Hamza, O., Souid, A., & Elliott, D. (2021). Self-healing of bio-cementitious mortar incubated within neutral and acidic soil. *Materials and Structures/Materiaux et Constructions*, *54*(2). Available from https://doi.org/10.1617/s11527-021-01690-1.

Fan, L., Tan, X., Zhang, Q., Meng, W., Chen, G., & Bao, Y. (2020). Monitoring corrosion of steel bars in reinforced concrete based on helix strains measured from a distributed fiber optic sensor. *Engineering Structures*, *204*, 110039. Available from https://doi.org/10.1016/j.engstruct.2019.110039.

Garside, M. (2021). *Major countries in worldwide cement production 2010−2020. Statista International*.

Huynh, N. N. T., & Son, N. K. (2017). An investigation on the use of *Bacillus subtilis* Hu58 in cement mortar. *ASEAN Engineering Journal*, *7*(2), 1−8. Available from https://doi.org/10.11113/aej.v7.15489.

Jonkers, H. M., & Schlangen, E. (2008). *Development of a bacteria-based self healing concrete*. *Proceedings of the International FIB Symposium 2008 − Tailor made concrete structures: New solutions for our society* (p. 109) CRC Press/Balkema. Available from https://doi.org/10.1201/9781439828410.ch72.

Kadapure, S. A., Kulkarni, G., Prakash, K. B., & Kadapure, P. S. (2020). Mechanical and durability performance of sustainable bacteria blended fly ash concrete: An experimental study. *International Journal of Sustainable Engineering*, *13*(1), 45−53. Available from https://doi.org/10.1080/19397038.2019.1644386.

Kar, A. (2013). Characterizations of concretes with alkali-activated binder and correlating their properties from micro-to specimen level. West Virginia University.

Luhar, S., Luhar, I., & Shaikh, F. U. A. (2022). A review on the performance evaluation of autonomous self-healing bacterial concrete: Mechanisms, strength, durability, and

microstructural properties. *Journal of Composites Science*, *6*(1), 1−35. Available from https://doi.org/10.3390/jcs6010023.

Luo, M., Qian, C. X., & Li, R. Y. (2015). Factors affecting crack repairing capacity of bacteria-based self-healing concrete. *Construction and Building Materials*, *87*, 1−7. Available from https://doi.org/10.1016/j.conbuildmat.2015.03.117.

Merck KGaA, IR Spectrum Table & Chart, Merck KGaA, Darmstadt, Germany (2022). https://www.sigmaaldrich.com/IN/en/technical-documents/technical-article/analytical-chemistry/photometry-and-reflectometry/ir-spectrum-table. Accessed: 29 June 2022.

Mondal, S., & Ghosh, A. (2018). *Microbial concrete as a sustainable option for infrastructural development in emerging economies. Urbanization challenges in emerging economies: Resilience and sustainability of infrastructure* (pp. 413−423). American Society of Civil Engineers.

Nežerka, V., Demo, P., Schreiberová, H., Ryparová, P., & Bílý, P. (2022). Self-healing concrete: application of monod's approach for modeling *Bacillus pseudofirmus* growth curves. *European Journal of Environmental and Civil Engineering*, 1−13. Available from https://doi.org/10.1080/19648189.2021.2021996.

Nguyen, T. H., Ghorbel, E., Fares, H., & Cousture, A. (2019). Bacterial self-healing of concrete and durability assessment. *Cement and Concrete Composites*, *104*, 103340. Available from https://doi.org/10.1016/j.cemconcomp.2019.103340.

Nodehi, M., Ozbakkaloglu, T., & Gholampour, A. (2022). A systematic review of bacteria-based self-healing concrete: Biomineralization, mechanical, and durability properties. *Journal of Building Engineering*, *49*104038. Available from https://doi.org/10.1016/j.jobe.2022.104038.

Nosouhian, F., Mostofinejad, D., & Hasheminejad, H. (2016). Concrete durability improvement in a sulfate environment using bacteria. *Journal of Materials in Civil Engineering*, *28*(1). Available from https://doi.org/10.1061/(asce)mt.1943-5533.0001337.

Rahaman, S., Dutta, J. R., Bandyopadhyay, M., et al. (2022). Laboratory Investigations to Optimize the Physicochemical Parameters for *Bacillus cereus* Inclusions in Concrete for Enhanced Compressive Strength and Chloride Resistance. *J. Inst. Eng. India Ser. A*, *103*, 1147−1164. Available from https://doi.org/10.1007/s40030-022-00685-7.

Rahaman, S., Dutta, J. R., Kar, A., & Bandyopadhyay, M. (2020). *Investigating the growth of microbial colonies in cement paste to aid in concrete repair*, *Lecture notes in civil engineering* (46, pp. 247−256). Springer. Available from https://doi.org/10.1007/978-3-030-26365-2_24.

Rajczakowska, M., Habermehl-Cwirzen, K., Hedlund, H., & Cwirzen, A. (2019). Autogenous self-healing: A better solution for concrete. *Journal of Materials in Civil Engineering*, *31*(9). Available from https://doi.org/10.1061/(asce)mt.1943-5533.0002764.

Ramagiri, K., & Kar, A. (2019). Effect of precursor combination and elevated temperatures on the microstructure of alkali-activated binder. *Indian Concrete Journal*, *93*(10), 34−43.

Rao, M. V. S., Reddy, V. S., Hafsa, M., Veena, P., & Anusha, P. (2013). Bioengineered concrete − A sustainable self-healing construction material. *Research Journal of Engineering Sciences*, 2.

Sahoo, K. K., Sathyan, A. K., Kumari, C., Sarkar, P., & Davis, R. (2016). Investigation of cement mortar incorporating *Bacillus sphaericus*. *International Journal of Smart and Nano Materials*, *7*(2), 91−105. Available from https://doi.org/10.1080/19475411.2016.1205157.

Skevi, L., Reeksting, B. J., Hoffmann, T. D., Gebhard, S., & Paine, K. (2021). Incorporation of bacteria in concrete: The case against MICP as a means for strength improvement.

Cement and Concrete Composites, 120. Available from https://doi.org/10.1016/j.cemconcomp.2021.104056.

Smitha, M. P., Suji, D., Shanthi, M., & Adesina, A. (2022). Application of bacterial biomass in biocementation process to enhance the mechanical and durability properties of concrete. *Cleaner Materials*, *3*, 100050. Available from https://doi.org/10.1016/j.clema.2022.100050.

Souradeep, G., & Kua, H. W. (2016). Encapsulation technology and techniques in self-healing concrete. *Journal of Materials in Civil Engineering*, *28*(12). Available from https://doi.org/10.1061/(ASCE)MT.1943-5533.

Sri Durga, C. S., Ruben, N., Sri Rama Chand, M., Indira, M., & Venkatesh, C. (2021). Comprehensive microbiological studies on screening bacteria for self-healing concrete. *Materialia*, *15*, 101051. Available from https://doi.org/10.1016/j.mtla.2021.101051.

Tayebani, B., & Mostofinejad, D. (2019). Self-healing bacterial mortar with improved chloride permeability and electrical resistance. *Construction and Building Materials*, *208*, 75−86. Available from https://doi.org/10.1016/j.conbuildmat.2019.02.172.

Tziviloglou, E., Wiktor, V., Jonkers, H. M., & Schlangen, E. (2016). Bacteria-based self-healing concrete to increase liquid tightness of cracks. *Construction and Building Materials*, *122*, 118−125. Available from https://doi.org/10.1016/j.conbuildmat.2016.06.080.

Vahabi, A., Ramezanianpour, A. A., & Akbari Noghabi, K. (2015). A preliminary insight into the revolutionary new line in improving concrete properties using an indigenous bacterial strain *Bacillus licheniformis* AK01, as a healing agent. *European Journal of Environmental and Civil Engineering*, *19*(5), 614−627. Available from https://doi.org/10.1080/19648189.2014.960951.

Van Tittelboom, K., De Belie, N., De Muynck, W., & Verstraete, W. (2010). Use of bacteria to repair cracks in concrete. *Cement and Concrete Research*, *40*(1), 157−166. Available from https://www.sciencedirect.com/science/article/pii/S0008884609002361.

Vijay, K., & Murmu, M. (2019a). Effect of calcium lactate on compressive strength and self-healing of cracks in microbial concrete. *Frontiers of Structural and Civil Engineering*, *13*(3), 515−525. Available from https://doi.org/10.1007/s11709-018-0494-2.

Vijay, K., & Murmu, M. (2019b). Self-repairing of concrete cracks by using bacteria and basalt fiber. *SN Applied Sciences*, *1*(11). Available from https://doi.org/10.1007/s42452-019-1404-5.

Vijay, K., Murmu, M., & Deo, S. V. (2017). Bacteria based self healing concrete − A review. *Construction and Building Materials*, *152*, 1008−1014. Available from https://doi.org/10.1016/j.conbuildmat.2017.07.040.

Wang, J. Y., De Belie, N., & Verstraete, W. (2012). Diatomaceous earth as a protective vehicle for bacteria applied for self-healing concrete. *Journal of Industrial Microbiology and Biotechnology*, *39*(4), 567−577. Available from https://doi.org/10.1007/s10295-011-1037-1.

Wang, J., Van Tittelboom, K., De Belie, N., & Verstraete, W. (2012). Use of silica gel or polyurethane immobilized bacteria for self-healing concrete. *Construction and Building Materials*, *26*(1), 532−540. Available from https://doi.org/10.1016/j.conbuildmat.2011.06.054.

Wang, J. Y., Snoeck, D., Van Vlierberghe, S., Verstraete, W., & De Belie, N. (2014). Application of hydrogel encapsulated carbonate precipitating bacteria for approaching a realistic self-healing in concrete. *Construction and Building Materials*, *68*, 110−119. Available from https://doi.org/10.1016/j.conbuildmat.2014.06.018.

Wang, J. Y., Soens, H., Verstraete, W., & De Belie, N. (2014). Self-healing concrete by use of microencapsulated bacterial spores. *Cement and Concrete Research*, *56*, 139−152. Available from https://doi.org/10.1016/j.cemconres.2013.11.009.

Wiktor, V., & Jonkers, H. M. (2011). Quantification of crack-healing in novel bacteria-based self-healing concrete. *Cement and Concrete Composites*, *33*(7), 763−770. Available from https://doi.org/10.1016/j.cemconcomp.2011.03.012.

Yoosathaporn, S., Tiangburanatham, P., Bovonsombut, S., Chaipanich, A., & Pathom- aree, W. (2016). A cost effective cultivation medium for biocalcification of *Bacillus pasteurii* KCTC 3558 and its effect on cement cubes properties. *Microbiological Research*, *186−187*, 132−138. Available from https://doi.org/10.1016/j.micres.2016.03.010.

Geoenvironmental evaluation on coal gangue: greener alternative to existing fill materials

17

Mohammed Ashfaq[1] *and Arif Ali Baig Moghal*[2]
[1]Osaimi Geotechnic Company, Tabuk, Saudi Arabia, [2]National Institute of Technology Warangal, Warangal, Telangana, India

17.1 Introduction

Sustainable development as a concept promotes economic progress with minimal environmental and societal impacts. However, achieving sustainability goals necessitates a paradigm shift in the existing developmental models. The exhausting resource and their increasing procurement costs have enhanced the focus to utilize alternative raw materials in earthworks. While the constantly growing industrial and construction activities produce subsidiary products which have favorable mechanical properties to facilitate their utilization in civil engineering applications (Ashfaq, Lal, et al., 2020; Hammond et al., 2011). The unscientific disposal of waste generated from mining/industrial activity in loose dumping/littering induces environmental problems and contributes to the wastage of scarce natural resources. Consequently, the approach for waste management has been to mitigate the environmental problems associated with its accumulation and disposal. However, there is growing impetus to reduce waste by adopting technologies that minimize waste generation or valorize the waste into a valuable resource (van Ewijk & Stegemann, 2020). Among the different industrial by-products, coal gangue, the by-product produced during coal excavation in the form of coal gangue (CG) has assumed greater importance. Annually, more than 400 million tons of CG have been generated globally. The utilization of CG in India is lower compared to countries like Australia and China, which have attained 95% recycling of CG (Ashfaq, Heera Lal, et al., 2021; Ashfaq, Heeralal, et al., 2021; Wu et al., 2017). Currently, the CG is disposed as loose dumps which can potentially cause leaching of trace metal elements (TME) into the surrounding environments when subject to runoff water. The utilization of CG can be a prudent solution to the existing environmental and economic costs associated with its disposal (Ashfaq, Moghal & Basha, 2022; Lim & Chu, 2006). The abundant presence of alumina and silica in CG facilitate its wide utilization in the cement and concrete manufacturing industry (Mangi et al., 2019). The volume of CG production is substantially greater than its utilization. In view of this, attempts have been made to find alternative modes for its bulk utilization, including as a fill material in the retaining wall and embankment applications (Ashfaq et al., 2020a;

Green Materials in Civil Engineering. DOI: https://doi.org/10.1016/B978-0-443-19106-0.00017-8

Ashfaq et al., 2020; Ashfaq, Moghal & Basha, 2022) as a subgrade and subbase material in low volume roads pavement. Further, Cao et al. (2011) have established its usage as an alternative fine aggregate in concrete which enhanced the overall workability (Dong et al., 2015; Wang et al., 2016). The primary reason which restricts the bulk application of CG in earthworks is the ambiguity related to potential environmental effects of its utilization. The earlier researchers have evaluated the chemical properties and factors impacting the TME mobilization from CG (Ashfaq et al., 2020b; Chuncai et al., 2014; Zhang & Ouyang, 2014). Traditionally, CG's environmental impact assessment in earthworks primarily focuses on mobilization of TME and other hazardous components. Consequently, for risk assessment, the frameworks were developed with a threshold limit for concentration of TME from CG. However, the attempts to evaluate the influence of pH, method of testing, specimen size, and interaction time on the mobilization of trace metals from CG have not been considered. Roth and Eklund (2003) have affirmed that TME mobilization studies form only the primary stage of environmental impact analysis, which ought to be complemented with a robust assessment of emissions and energy consumption. The application of life cycle assessment (LCA) in construction works is an established approach for estimating the environmental impacts of alternate material utilization. The advent of an efficient LCA instrument in the form of carbon footprint assessment (CFA) with exclusive focus on CO_2 emissions has augmented the greater application of sustainability assessment. The use of CFA simplifies the difficult and intricate process of calculating the main Green House Gas (GHG) emissions. The environmental benefits with the utilization of FA were documented by Olsson et al. (2006) and Ashfaq and Moghal (2022). Similar results for the utilization of CG in earthworks were demonstrated by Ashfaq, Baig Moghal, et al. (2022). Though substantial literature is available on the sustainability benefits of combustion ashes, parallel studies on CG have sparsely been noted. Hence, the current study made efforts to carry out SA based on CG's mechanical properties to confirm its pertinence as fill material in embankment applications. Comprehensive leaching tests were performed on CG by altering various parameters, including the pH, testing method, specimen size, and interaction time. Furthermore, CFA was performed to estimate the emissions at various stages of embankment construction.

17.2 Materials and methods

The CG considered in the present study is sourced from the nearest coal mine (18°23′00.8″N 79°49′33.6″E), which is 100 km away from the proposed embankment (18°38′33.2″N 79° 23′24.6″E).

17.2.1 Geotechnical and leaching characteristics

The mechanical strength characterization studies (unit weight and shear strength) were performed in compliance with the corresponding standards (Standard Test

Methods, 2012, 2011a). The hydraulic conductivity (HC) of CG was evaluated with the help of permeameter (rigid wall) and the test was carried out in the standard procedure (Standard Test Methods, 2015). The compression characteristics were assessed by using edometer setup, and the seating load was varied from 50 to 350 kPa to compute the collapse potential of CG (Standard Test Methods, 2011b). The samples were compacted to 95% of the max density (MDD) and the water content was fixed at optimum moisture content (OMC). In the current study, collapse potential (Cp) was estimated by using Eq. (17.1), wherein e_o represents the initial void ratio value. Similar approach was adopted by Ashfaq et al. (2020a):

$$C_p = \Delta e_o/(1 + e_o) \tag{17.1}$$

The leaching studies were carried out on CG to comprehend the trace metal mobilization characteristics. The four metal elements (Arsenic [As], Chromium [Cr], Manganese [Mn], and Zinc [Zn]) with initial concentrations exceeding US EPA regulatory limits were considered for the leaching studies. The factors influencing leaching, such as pH, testing methodology, interaction time, and size of the specimen, were analyzed to comprehend the mobilization characteristics of selected TME. Firstly, specimens were subjected to acid digestion (hydrochloric acid-nitric acid combinations) in compliance with the standard procedure (United States Environmental Protection Agency EPA, 1996) to identify the initial concentrations of selected TME, followed by static and dynamic leaching studies, which were carried out following Standard Test Methods (2014) and Standard Test Methods (2020), respectively. The concentrations of selected TME was determined from atomic absorption spectroscopy. The solid−liquid ratio of 20 was maintained in comparative leaching studies; the double-distilled water (deionized) and CG samples represent the liquid (L) and solid (S) fractions, and the ratio varied from 5 to 100. For comparative leaching studies (static and dynamic), an L/S ratio of 20 was maintained. After every testing cycle, the pH of the leachates was noted by following the standard procedure (ASTM, n.d.).

17.2.2 The carbon footprint assessment methodology

For the CFA on CG application, an ongoing project by the government of Telangana, which involves the construction of highway embankment, was considered. The geotechnical characterization results have indicated that CG's shear strength and compressibility characteristics are comparable to granular materials.

17.2.2.1 Scope and goal

The methodology adopted for CFA was based on a framework proposed by Shillaber et al. (2016), and the earthwork considered is the construction of a 10,000 m^3 embankment. The emissions from multiple phases of construction were combined for the CO_{2e} assessment. The three stages of CFA include material acquirement and handling, transport, and building/construction.

17.2.2.2 Inventory

For various materials considered in CFA, the embodied carbon (CC-carbon emission coefficient), inventory documented by (2011) was selected. To enable the comparison of emissions, 100 km transport distance was fixed for all the materials which is akin to practical distance (of 94 km) between the mining and proposed construction site. The machinery and vehicle type considered for various transport and site operation were in adherence with the Versions of the Waste Reduction Model (2016). The data on vehicle capacity and engine efficiency was adopted from Shillaber et al. (2016).

17.2.2.3 System boundary

The emissions related to the following works were omitted from CFA: (1) The transportation of human resources (employees/labor) to the construction site. (2) The transport and procurement of fuel consumed by vehicles and machinery. (3) The upkeep of the built structure (embankment). (4) The embodied carbon of machines/vehicles utilized in embankment construction.

The omissions are in line with the guidelines stipulated by International Organization for Standardization ISO14044 (2006). The total carbon emissions for the proposed embankment were projected by using the subsequent equation:

$$T([\![CO]\!]_{2e}) = P(CO_{(2e)}) + H(CO_{(2e)}) + S(CO_{(2e)}) \tag{17.2}$$

A similar approach was adopted by Ashfaq et al. (2020) and Shillaber et al. (2016) to estimate emissions.

17.3 Results and discussion

The results obtained from geotechnical, leaching, carbon footprint, and stability analysis on CG and its application scenario are presented in the following sections.

17.3.1 Geotechnical characteristics of coal gangue

The unit weight of material proportionately influences its mechanical characteristics. The variation in dry density with the corresponding moisture content (10%–24%) for standard compactive effort is presented in Table 17.1. The results presented showed that the OMC and MDD values were 16%, 1740 (kg/m^3). In line with the observations made for other industrial by-products (IBP), the compaction characteristics of CG are relatively higher than cohesive soils. They are akin to silty sands (Ashfaq et al., 2020a). The comparatively lower variation in MDD with the corresponding moisture content can facilitate compaction at site even for dry OMC, owing to its superior drainage characteristics. Further, in Table 17.1, the OMC and MDD values of CG compared with the standard guidelines (Indian Standard IS: 1498, 1970)

Table 17.1 Geotechnical properties of coal gangue (CG) and comparison with design specifications.

Property	Design specification	CG values
	IS 1498	
Maximum dry density (kg/m^3)	1760−2300	1740−1960
Optimum moisture content (%)	Not specified	16−18
Cohesion (kN/m^2)	Negligible	Noncohesive
The angle of international friction (φ)	>25 degrees	39−43 degrees
Hydraulic conductivity (cm/s)	10^{-5}−10^{-3}	10^{-5}−10^{-4}
Coefficient of consolidation (cm^2/s)	–	0.06−0.077
Collapse potential	Not specified	0.11−0.18

confirm its applicability as fill material in an embankment. The shear strength parameters are essential inputs in the design and stability assessment of embankment. The CG fundamentally does not possess cementation characteristics generally noted for calcium-rich IBPs (steel slag, Class C fly ash) and typically derives its strength from frictional components (Ashfaq et al., 2020a). From the results presented in Table 17.1, the slight disparity in the frictional angle of various CG samples (39−43 degrees) is mainly due to the alteration in morphology, which is influenced by its mineralogical composition and geological formation of parental rocks. From comparing with desired specifications (Indian Standard IS:1498, 1970), it is inferred that CG exhibits favorable engineering properties to enable its application in embankment.

The HC and compressibility properties are essential for the design of earth and hydraulic structures. The HC values of CG exhibited substantial variations (Table 17.1) with the gradation, which can be attributed to several factors which include degree of compaction, fines content, and pore spacing and pozzolanic potential. Further, the earlier study by Ashfaq et al. has established that confinement and moisture content significantly influence the HC of CG. The coefficient of consolidation (Cv) values of CG varied from 0.05 to 0.07, which is fairly higher compared to soils with identical gradation characteristics (sand/silty sand). The greater compressibility values of CG may manifest in the form of rapid completion of primary consolidation. Based on the Cv values, it is apparent that primary consolidation is attained during construction with minimal settlements at the end of construction. With the favorable compressibility behavior (Cv values), CG meets the design standards in accordance with Indian Standard IS:1498 (1970), further approving its application as a fill material. Based on the collapse index (Cp value corresponding to vertical stress of 200 kPa) presented in Table 17.1, CG is classified as a slightly collapsible material as per ASTM (2003). The Cp values (0.11−0.18) of CG is relatively lower than values observed for sands (Mangi et al., 2019; Wu et al., 2017) and by virtue of this behavior, the CG utilization can potentially sustain the rapid infiltration of runoff water (Amin et al., 2022).

17.3.2 Leaching studies

TME leaching is a significant environmental problem due to its toxic effects and accumulation throughout the food chain and hence in the human body.

17.3.2.1 Variation in pH and metal extraction with liquid–solid ratio and interaction time

The CG-based embankments also need to be designed with minimal environmental concerns. The main environmental problem is the contamination of surface or subsurface water streams induced due to trace metal leaching. The variation in pH with LSR is shown in Fig. 17.1, and it is noted that CG exhibited mainly acidic behavior with linearly decreasing pH over increment in LSR. The highest fall in pH with the transition from neutral to acidic nature was noted at LSR of 20. The linear decrease is due to the pronounced rise in the attack by hydrogen ions on the mineral phases of selected TME. Similar observations were made for fly ash by Ashfaq and Moghal (2022). The variation in pH with the duration of interaction is presented in Fig. 17.1, and it is noted that the pH exhibited a falling trend with the rise in the duration of the interaction. The rapid fall is recorded for intermediate duration (48 and 72 h), and for the higher duration of interaction (96 and 120 h), the reduction in pH was observed to be minimal. Further, the pH of the leachate was also altered by the variation in the size of the specimen. The lower fraction (0.425 mm passing) exhibited a more significant fall in pH for higher interaction time attributed to their

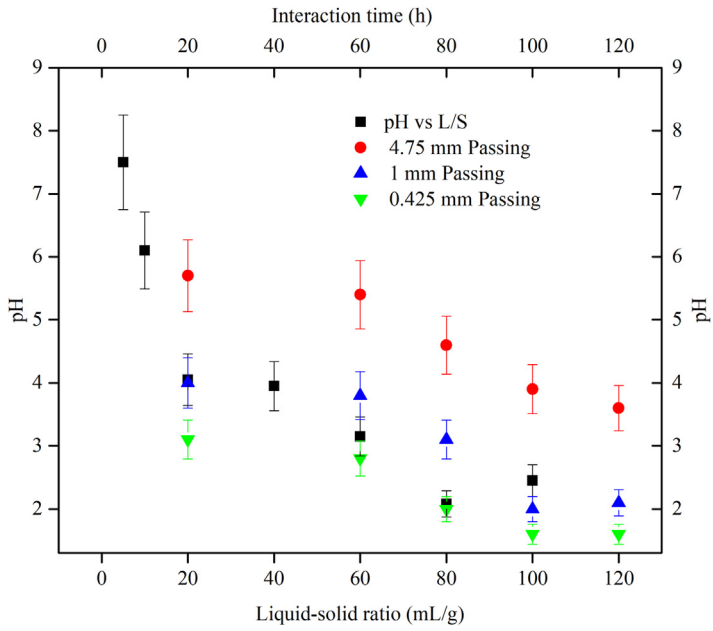

Figure 17.1 pH versus interaction time (h) and liquid–solid ratio (mL/g).

prolonged attack on mineral phases of CG. The finer fraction's substantially higher fall in pH may be attributed to its greater specific surface area than the coarser fraction (Ashfaq et al., 2020b). The initial concentration of selected TME is presented in Table 17.2. The variation in metal extraction (ME) of selected TME with LSR is shown in Fig. 17.2. For a given LSR, the leaching (ME) of selected TME remained constant, which is in the order of As > Zn > Mn > Cr. As exhibited relatively higher mobility with ME (%) of 30, which may be attributed to its inability to form arsenate under a higher acidic medium, it can react with TME to form precipitates (Ashfaq, Heera Lal, et al., 2020; Moghal et al., 2022; Mohammad et al., 2022). The relatively lower mobilization of Cr may be attributed to its feebly lower solubility in the CG matrix. Identical to As, Mn also exhibited pH-sensitive leaching. The higher mobility of Mn can also be due to the absence of carbonate and oxy-hydroxides, which impedes the dissolution of Mn through chemisorption. The leaching characterization of Zn is mainly driven by its potential to react with organic ligands and the subsequent formation of hydration compounds (Ashfaq et al., 2020b). Being oxyanionic in nature, As and Cr exhibited a pH-sensitive leaching pattern with higher mobility with the rise in the L/S ratio. On the other hand, Zn exhibited amphoteric leaching characteristics to mobilize acidic and alkaline conditions.

Table 17.2 Initial concentrations of selected trace metal elements in coal gangue.

Heavy metals	As	Cr	Mn	Zn
Leachate (mg/L)	17.8	1.6	23	32
US EPA regulatory limit (mg/L)	0.01	0.1	0.05	5

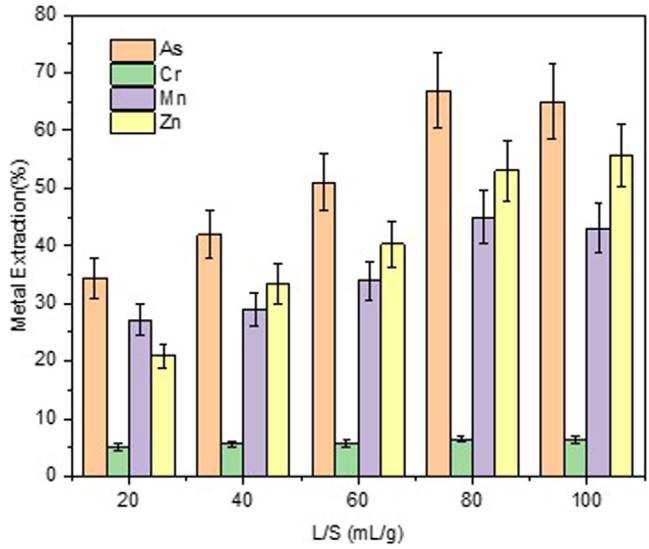

Figure 17.2 The metal extraction versus liquid−solid (mL/g) for selected trace metal elements.

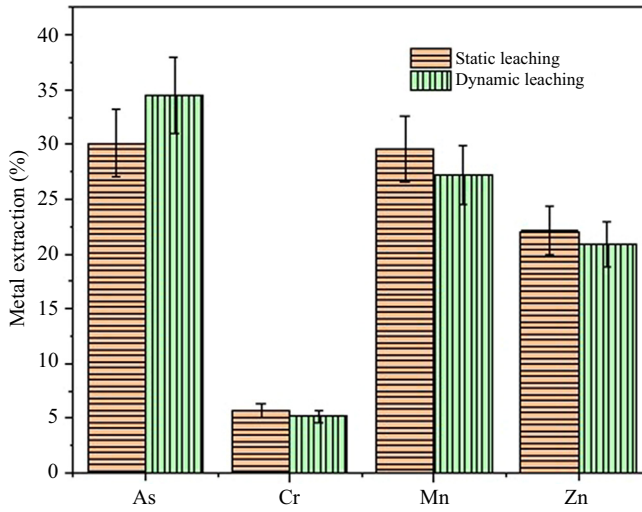

Figure 17.3 The variation in metal extraction of selected trace metal elements with testing condition.

To simulate static leaching observed in excavation mines, column leaching studies were done. Since the maximum spike in leaching with the switch from basic to the acidic medium was noted for an L/S ratio of 20, it was considered for comparative leaching studies. The variation in leaching characteristics of selected TME under static and dynamic conditions is presented in Fig. 17.3.

It can be noted that nonuniform leaching was observed for both testing methods. However, the order of leaching for selected TME remained constant for both the leaching methods; the quantity of metal extracted was observed to be relatively higher in the static leaching method, which can be attributed to its higher interaction time and relatively generous sample dosage (Ashfaq et al., 2020b).

17.3.2.2 Effect of particle size and interaction time on leaching

The CG at the mining site often encounters water logging/submergence situations induced due to the prolonged rainfalls. In submergence conditions, the duration of interaction between the leachate and CG is substantially higher, not represented in standard leaching tests. Earlier research by Cetin and Aydilek (2013) have noted that interaction time influences the leaching characteristics of TME in CG. Thus leaching characteristics of CG under extended interaction time (24−120 h) is studied. The variation in ME (%) with the size of the specimen is shown in Fig. 17.4.

It is apparent from the results that the size of the specimen directly influences the variation in metal extraction (%) of selected TME. The order of mobility (ME) of selected TME is noted as As > Mn > Zn > Cr. The variation in ME (%) of the selected TME with the duration of interaction and specimen size is presented in Fig. 17.5.

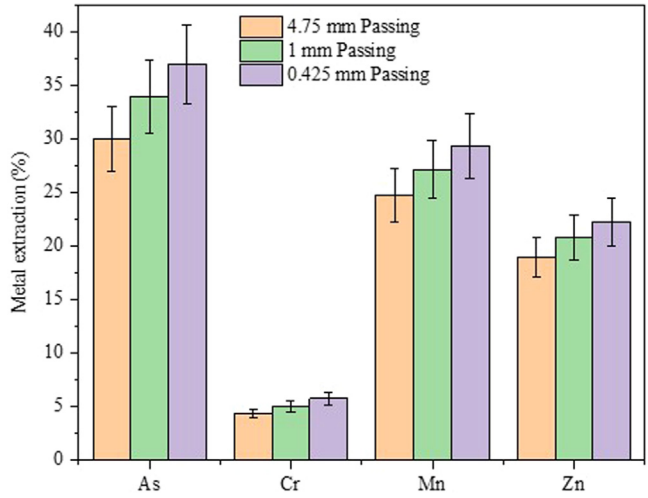

Figure 17.4 The variation in the leaching characteristics with the size of the specimen.

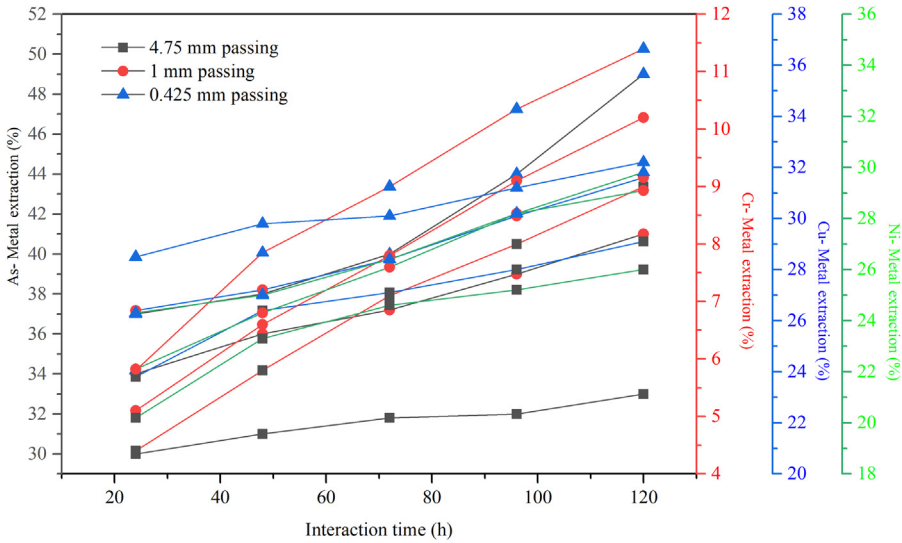

Figure 17.5 The variation in the metal extraction (%) with the size of the specimen and interaction time.

A gradual rise in ME (%) was observed with the duration of interaction from the results. The highest ME (%) was noted for an intermediate duration of 48 and 72 h, followed by a gradual decrease for 96 and 120 h of interaction time. Further, in general, the leaching tendency of the finer specimen is more significant than the

coarser, which further increased with the duration of the interaction. Thus from the leaching studies, it can be inferred that the selected TME have exhibited tendencies to mobilize from the CG, and the observations made are in line with the earlier studies.

17.3.3 Carbon footprint assessment on coal gangue application in earthworks

The CFA evaluated the carbon emissions with the CG utilization in the embankment, and the detailed calculations are presented in Table 17.3. The site operations involved in the construction of embankment include leveling, loading, and compaction of CG fill. The CO_{2e} for each phase of constructing embankment are shown in Fig. 17.6.

It is noted that the CO_{2e} from phase I are considerably more with almost 74% stake in overall emissions. The CO_{2e} concerning site operations phase are minor, reflecting the minuscule volume of operation (Ashfaq, Baig Moghal, et al., 2021). Further, the extent of obtaining construction materials to the site mainly explains the considerably higher CO_{2e} from phase I. The higher CC value of CG also contributes to the CO_{2e}, which in turn is impacted by the enormous consumption of fuel for mining (Ashfaq et al., 2021; Shillaber et al., 2016). It is clear that the CO_{2e} from transport are unavoidable and constant for all material types. However, the effect of CO_{2e} from transport can considerably enhance the overall emissions which is elucidated in Fig. 17.7.

The influence of vehicle category and transport distance on the net emissions is shown in Fig. 17.7, and the vehicles considered are pickup truck (PT) and medium-duty dumper (MD). The stacking capacity and extent of fuel consumption of PT and MD are 1 (tons) and 7.5 (km/L) and 4(tons) and 3.36 (km/L), respectively. The results demonstrate that CO_{2e} are directly impacted by the transport distance, with over 400% rise in emissions for mere increase in transport distance of 75 km.

Table 17.3 Carbon footprint assessment calculations for coal gangue-based embankment.

Process	**Machine/vehicle**	**Fuel (L)**	**CC (kg CO_2/unit)**	**kg CO_{2e}**
Procurement				
Embodied carbon Grinding	Nil Jaw crusher	Nil 17,725	0.07 3.25	1,330,000 57,605
Haulage				
Coal gangue	Medium-duty dumper	143,250	3.25	465,562
Site operation spreading excavation Compaction	*Bulldozer* *Pickup excavator* *Pneumatic roller*	859.5 1591.7 1061	3.25 3.25 3.25	2793 5172 3448

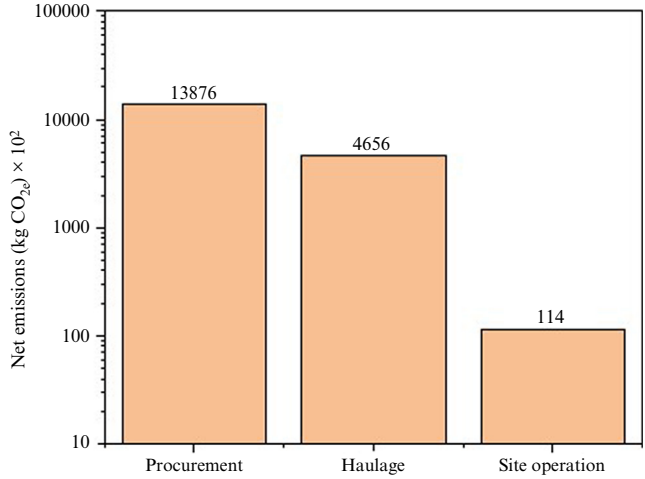

Figure 17.6 The net emissions for each stage of embankment construction.

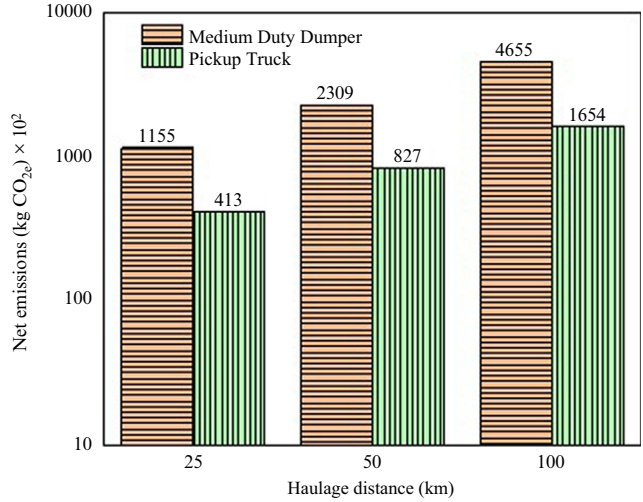

Figure 17.7 The influence of transport distance and vehicle type on the net emissions.

The noted variation is consistent for the vehicle category, and the difference in CO_{2e} hiked from 74,127 to 300,202. Further, it was observed that emissions rose from 46,186 and 16,536 (kg CO_{2e}) for a hike of 10 km in transport distance. The considerably higher CO_{2e} for PT are primarily due to the greater fuel consumption, which is determined by its lower stacking capacity. The CFA results further emphasize the environmental gains of CG utilization in earthworks. The gains rise manifold for the situations with moderately lesser transport distance.

17.4 Conclusions

In the current study, the geotechnical, leaching, and CFA were performed to construct embankment. Based on the findings of the study, the conclusions drawn are presented below:

- The geotechnical characterization results confirmed that CG exhibits favorable engineering properties (IS 1498) for an embankment fill material.
- The leaching tests revealed that selected TME exhibit a higher tendency of leaching under acidic conditions, which is also influenced by the specimen size and interaction time. The highest ME (%) of 45 was noted for most acceptable fraction (0.425 mm passing) for an interaction time of 120 h.
- The CFA revealed that emissions from embodied carbon were highest with a 78% share in overall emissions.
- Overall emissions and the order of emissions from CFA were constant for both the vehicle types, and the order observed was: procurement (embodied carbon) > transport > site operation.
- Based on the observations made from the study, it is understood that the utilization of CG is a sustainable alternative with reduced emissions and more excellent stability.

17.5 Practical relevance of the study

This study reinforces the potential of CG as an alternative fill material in earthworks. The study has established that utilization of CG can substantially reduce carbon emissions. Based on the findings of the study, the authors conclude that CG is a potential green material which can augment sustainable construction.

References

Amin, M. N., Iqbal, M., Ashfaq, M., Salami, B. A., Khan, K., Faraz, M. I., Alabdullah, A. A., & Jalal, F. E. (2022). Prediction of strength and CBR characteristics of chemically stabilized coal gangue: ANN and random forest tree approach. *Materials*, *15*(12). Available from https://doi.org/10.3390/ma15124330, https://www.mdpi.com/1996-1944/15/12/4330/pdf?version = 1655556528.

ASTM. (n.d.) *ASTM D4972-13: Standard test methods for pH of soils*. <https://www.astm.org/d4972-13.html>.

ASTM. (2003) *D5333: Standard test methods for measurement of collapse potential of soils*. ASTM.

Ashfaq, M., Baig Moghal, A. A., & Almajed, A. (2022). *Sustainability benefits of utilizing coal gangue as fill material in earthworks* (2022, pp. 453−462). India: Geotechnical Special Publication, American Society of Civil Engineers (ASCE). Available from https://doi.org/10.1061/9780784484050.047, http://ascelibrary.org/.

Ashfaq, M., Baig Moghal, A. A., & Basha, B. M. (2021). Reliability-based design optimization of chemically stabilized coal gangue. *Journal of Testing and Evaluation*, *51*(1).

Available from https://doi.org/10.1520/JTE20210176, https://www.astm.org/DIGITAL_LIBRARY/JOURNALS/TESTEVAL/jote_issues.html.

Ashfaq, M., Heera Lal, M., & Moghal, A. A. B. (2020). *Static and dynamic leaching studies on coal gangue*. *Lecture notes in civil engineering* (89, pp. 261–270). India: Springer Science and Business Media Deutschland GmbH. Available from https://doi.org/10.1007/978-3-030-51350-4-28, http://www.springer.com/series/15087.

Ashfaq, M., Heera Lal, M., & Moghal, A. A. B. (2021). *Utilization of coal gangue for earthworks: Sustainability perspective*. *Lecture notes in civil engineering* (144, pp. 203–218). Springer Science and Business Media Deutschland GmbH India. Available from https://doi.org/10.1007/978-981-16-0077-7-20, http://www.springer.com/series/15087.

Ashfaq, M., Heeralal, M., Baig Moghal, A. A., & Baig Moghal, A. A. (2021). *Effect of fines content on the shear behavior of coal gangue* (2021, pp. 264–271). India: Geotechnical Special Publication. American Society of Civil Engineers (ASCE). Available from https://doi.org/10.1061/9780784483411.025, http://ascelibrary.org/.

Ashfaq, M., Heeralal, M., & Moghal, A. A. B. (2020a). Characterization studies on coal gangue for sustainable geotechnics. *Innovative Infrastructure Solutions*, *5*(1). Available from https://doi.org/10.1007/s41062-020-0267-3, https://www.springer.com/journal/41062.

Ashfaq, M., Heeralal, M., & Moghal, A. A. B. (2020b). Effect of coal gangue particle size on its leaching characteristics. *Geotechnical Special Publication, American Society of Civil Engineers (ASCE) India*, *2020*(319), 107–114. Available from https://doi.org/10.1061/9780784482827.012, http://ascelibrary.org/.

Ashfaq, M., Lal, M. H., Moghal, A. A. B., & Murthy, V. R. (2020). Carbon footprint analysis of coal gangue in geotechnical engineering applications. *Indian Geotechnical Journal*, *50*(4), 646–654. Available from https://doi.org/10.1007/s40098-019-00389-z, http://www.springer.com/engineering/civil + engineering/journal/40098.

Ashfaq, M., & Moghal, A. A. B. (2022). Cost and carbon footprint analysis of flyash utilization in earthworks. *International Journal of Geosynthetics and Ground Engineering*, *8*(2). Available from https://doi.org/10.1007/s40891-022-00364-4, https://link.springer.com/journal/40891.

Ashfaq, M., Moghal, A. A. B., & Basha, B. M. (2022). The sustainable utilization of coal gangue in geotechnical and geoenvironmental applications. *Journal of Hazardous, Toxic, and Radioactive Waste*, *26*(3). Available from https://doi.org/10.1061/(ASCE)HZ.2153-5515.0000705, http://ascelibrary.org/hzo/.

Cao, D., Ji, J., Liu, Q., He, Z., Wang, H., & You, Z. (2011). Coal gangue applied to low-volume roads in China. *Transportation Research Record* (2204), 258–264. Available from https://doi.org/10.3141/2204-32.

Cetin, B., & Aydilek, A. H. (2013). PH and fly ash type effect on trace metal leaching from embankment soils. *Resources, Conservation and Recycling*, *80*(1), 107–117. Available from https://doi.org/10.1016/j.resconrec.2013.09.006.

Chuncai, Z., Guijian, L., Dun, W., Ting, F., Ruwei, W., & Xiang, F. (2014). Mobility behavior and environmental implications of trace elements associated with coal gangue: A case study at the Huainan Coalfield in China. *Chemosphere*, *95*, 193–199. Available from https://doi.org/10.1016/j.chemosphere.2013.08.065, http://www.elsevier.com/locate/chemosphere.

Dong, Z., Xia, J., Fan, C., & Cao, J. (2015). Activity of calcined coal gangue fine aggregate and its effect on the mechanical behavior of cement mortar. *Construction and Building Materials*, *100*, 63–69. Available from https://doi.org/10.1016/j.conbuildmat.2015.09.050.

Hammond, G., Jones, C., Lowrie, E. F., & Tse, P. (2011). Embodied carbon. *The inventory of carbon and energy*. Available from https://greenbuildingencyclopaedia.uk/wp-content/uploads/2014/07/Full-BSRIA-ICE-guide.pdf.

Indian Standard IS:1498. (1970). *Classification and identification of soils for general engineering purposes. Methods of test for soils.* <https://archive.org/details/gov.in.is.1498.1970>.

International Organization for Standardization ISO14044. (2006). *Environmental management: life cycle assessment; requirements and guidelines*. <https://www.iso.org/standard/38498.html>.

Lim, T. T., & Chu, J. (2006). Assessment of the use of spent copper slag for land reclamation. *Waste Management and Research*, *24*(1), 67−73. Available from https://doi.org/10.1177/0734242X06061769.

Mangi, S. A., Ibrahim, M. H. W., Jamaluddin, N., Arshad, M. F., & Mudjanarko, S. W. (2019). Recycling of coal ash in concrete as a partial cementitious resource. *Resources*, *8*(2). Available from https://doi.org/10.3390/resources8020099, https://res.mdpi.com/resources/resources-08-00099/article_deploy/resources-08-00099.pdf?filename = &attachment = 1.

Moghal, A. A. B., Rasheed, R. M., & Mohammed, S. A. S. (2022). Sorptive and desorptive response of divalent heavy metal ions from EICP-treated plastic fines. *Indian Geotechnical Journal*. Available from https://doi.org/10.1007/s40098-022-00638-8, http://www.springer.com/engineering/civil + engineering/journal/40098.

Mohammad, N., Moghal, A. A. B., Rasheed, R. M., & Almajed, A. (2022). Critical review on the efficacy of electrokinetic techniques in geotechnical and geoenvironmental applications. *Arabian Journal of Geosciences*, *15*(8). Available from https://doi.org/10.1007/s12517-022-10037-1.

Olsson, S., Kärrman, E., & Gustafsson, J. P. (2006). Environmental systems analysis of the use of bottom ash from incineration of municipal waste for road construction. *Resources, Conservation and Recycling*, *48*(1), 26−40. Available from https://doi.org/10.1016/j.resconrec.2005.11.004.

Roth, L., & Eklund, M. (2003). Environmental evaluation of reuse of by-products as road construction materials in Sweden. *Waste Management*, *23*(2), 107−116. Available from https://doi.org/10.1016/S0956-053X(02)00052-1.

Standard Test Methods. (2011a). *Standard test methods for one dimensional consolidation properties of soil under incremental loading*. ASTM.

Standard Test Methods. (2011b). S*tandard test methods for direct shear test of soils under consolidated drained conditions*. ASTM.

Standard Test Methods. (2012). *Standard test methods for laboratory compaction characteristics of soil using standard effort* (12 400 ft-lbf/ft3 (600 kN-m/m3)). ASTM.

Standard Test Methods. (2014). *Standard test methods for leaching solid material in a column apparatus*. ASTM.

Standard Test Methods. (2015). Standard test methods for measurement of hydraulic conductivity of porous material using a rigid-wall, compaction-mold permeameter. ASTM.

Standard Test Methods. (2020). *Standard test methods for shake extraction of solid waste with water*. ASTM.

Shillaber, C. M., Mitchell, J. K., & Dove, J. E. (2016). Energy and carbon assessment of ground improvement works. II: Working model and example. *Journal of Geotechnical and Geoenvironmental Engineering*, *142*(3). Available from https://doi.org/10.1061/(ASCE)GT.1943-5606.0001411, http://ojps.aip.org/gto/.

United States Environmental Protection Agency (EPA). (1996). *United States Environmental Protection Agency (EPA): Method 3050B acid digestion of sediments, sludges, and soils*. <https://www.epa.gov/sites/default/files/2015-06/documents/epa-3050b.pdf>.

van Ewijk, S., & Stegemann, J. A. (2020). Recognising waste use potential to achieve a circular economy. *Waste Management*, *105*, 1−7. Available from https://doi.org/10.1016/j.wasman.2020.01.019, http://www.elsevier.com/locate/wasman.

Versions of the Waste Reduction Model. (2016). *Versions of the waste reduction model (WARM)*, US EPA. <https://www.epa.gov/warm/versions-waste-reduction-model-warm>.

Wang, J., Qin, Q., Hu, S., & Wu, K. (2016). A concrete material with waste coal gangue and fly ash used for farmland drainage in high groundwater level areas. *Journal of Cleaner Production*, *112*, 631−638. Available from https://doi.org/10.1016/j.jclepro.2015.07.138.

Wu, H., Wen, Q., Hu, L., Gong, M., & Tang, Z. (2017). Feasibility study on the application of coal gangue as landfill liner material. *Waste Management*, *63*, 161−171. Available from https://doi.org/10.1016/j.wasman.2017.01.016, http://www.elsevier.com/locate/wasman.

Zhang, H., & Ouyang, S. (2014). Release characteristics of heavy metals from coal gangue under simulation leaching conditions. *Energy Exploration and Exploitation*, *32*(2), 413−422. Available from https://doi.org/10.1260/0144-5987.32.2.413.

Utilization of Sustainable Material: Ferrock for Stabilization of Subgrade Soil

18

Mayuri Makwana Nirav[1] *and Santosh Shah G.*[2]
[1]Civil Engineering Department, Gujarat Technological University, Chandkheda, Gandhinagar, Gujarat, India, [2]Civil Engineering Department, Centre for Research & Innovation, Sankalchand Patel University, Visnagar, Mehsana District, Gujarat, India

18.1 Introduction

Ferrock is different from cement in that it absorbs more CO_2 (a highly hazardous gas) than it produces. Ferrock can endure more compression brought on by seismic activity and is five times stronger than normal Portland cement (a powdered building material comprising chalk, concrete, mortar, and clay) (Das et al., 2014). Many novel materials are emerging as a result of the search for carbon-neutral and sustainable alternatives to the current construction techniques, all of which aim to enhance the environment. Concrete is one of the materials that has been targeted the most in attempts to do so or find a substitute (Garcia et al., 2017).

Currently, 4 billion tonnes of concrete are produced annually, which emits carbon dioxide into the atmosphere and uses mostly nonrenewable raw materials (Graedel and Allenby, 2010). One such substance that has recently emerged and is intended to take its place is ferrock, which aims to replace or reduce the usage of concrete with a carbon-negative and superior material made primarily of recycled resources (David, 2017).

Ferrock is Table 18.1 much less expensive because it is made from waste; it is carbon negative because it absorbs more carbon dioxide than it produces during the hardening process; and it is also relatively chemically inactive, allowing it to be used in environments like salt water without degrading and being strengthened by the salt (Engineering Intro, 2012). Although the use of this material in large projects may not currently be practicable due to the difficulty and unreliability of obtaining huge quantities of waste materials, it has the potential to be very successful in small projects. Although with the current development of construction growth, these resources will probably continue to be easily accessible; if it gets more widely used, the price of these products, which are currently waste materials, may become more coveted and consequently more expensive.

Future research and development must focus on finding new building materials that are more environmentally friendly than the ones we presently use, which have a significant impact on greenhouse gas emissions.

Green Materials in Civil Engineering. DOI: https://doi.org/10.1016/B978-0-443-19106-0.00018-X

Table 18.1 Summary of raw materials required for ferrock manufacturing.

Material	Substantial percent (by weight) (%)	Specification/comments
Steel powder	60	Waste metallic iron powder (19.03 μm)
Glass or fly ash	20	Class F fly ash ground glass particles
Limestone	10	Limestone powder (median particle size of 0.7 μm) IS 2109 : 1982
Metakaolin	8	Al2(OH)4Si2O5
Mediocre organic acid	2	In earlier studies, oxalic acid has been utilized as a catalyst

18.2 An understanding of important technologies

Clay and limestone are both employed in the formulation of ferrock, though in much smaller proportions than in Ordinary portland cement —8% and 10%, respectively—than in Ordinary portland cement (Engineering Intro, 2012). Eighty percent of the combination is made up of low-value waste materials. The primary component is metallic iron powder, a by-product of shot blasting, a finishing process used in the production of steel. The iron powder is ground down to a micro-particle scale (19.03 μm) during the shot blasting process, which causes a significant annoyance to the blasting facility due to its ineffective applicability and the inherent respiratory hazard connected with dealing with such a tiny material (Geiger et al., 2017). These components are mixed dry with a silica source, like fly ash or recycled glass. Oxalic acid is additionally added to speed up the chemical reaction before being combined to produce a consistent mixture.

18.3 Potential applications

1. Ferrock is approved to be utilized in slabs, bricks, sidewalks, paves, breakwaters, and walls; it is economical for small projects.
2. It is suggested to implement it in pilot projects within marine environments.
3. About 95% of the materials used to make ferrock are recycled. It absorbs carbon dioxide during production, which is completely opposite to cement made from chalk and clay.
4. Ferrock is resistant to oxidation, ultraviolet radiation, corrosion, chemicals, rotting, and rust, making it an exceptional material for constructing pipes and tubes (Niveditha et al., 2021).

18.4 Testing procedures

The substance ferrock is utilized as a binder. Iron powder, fly ash, limestone, metakaolin, and oxalic acid are just a few of the ingredients that make up

ferrock. The specific gravity of ferrock is 5.29 of size 90 μm. Based on IS 383, we used locally available Sand (passing through 2.36 mm) with Fineness modulus 4.66 and Specific gravity 2.73 (2002). The amount of ferrock material for soil subgrade is taken in the proportions of 5%, 10%, 15%, and 20% by dry weight of soil. These proportions were used to create mix samples, which were then produced as described below and subjected to a series of laboratory tests to ascertain the index characteristics, swelling, and California bearing ratio (CBR) values of both the Varnama village soil and the mixed proportion samples. The expansive soil which was bought form varnama village subjected to a variety of laboratory testing, including grain size analysis, Atterberg limits, compaction Table 18.14, soaked CBR, and tests for swell potential and swell pressure.

18.4.1 Combination of soil and ferrock material samples

1. Natural soil
2. Soil + 5% ferrock
3. Soil + 10% ferrock
4. Soil + 15% ferrock
5. Soil + 20% ferrock

18.4.2 Lab investigations

Various lab investigations to be carried out on the mix proportion of soil and ferrock material are as follows:

- Sieve analysis
- Atterberg limits
- Proctor compaction test
- CBR test

18.4.3 Analysis of lab investigation

1. Standard Proctor test for soil—ferrock material.
2. Unconfined compressive strength (UCS) test for soil—ferrock material.
3. CBR test for soil—ferrock material.

18.5 Findings and conclusion

The findings of the experiments are given and discussed in this section. The addition of ferrock material for subgrade stability is seen to have the following effects:

18.5.1 Soil stability

The expansive soil treated with ferrock is shown to have different soil consistency qualities, such as liquid limit, plastic limit, and plasticity index. Both the liquid limit and plasticity index are gradually declining. With the inclusion of ferrock material, plastic limit values have been increased.

The swell potential and swelling properties are the soil samples' swell pressure when combined with ferrock material The test results demonstrate that as the fraction of ferrock material grew, the swell potential and swell pressure values considerably decreased, from 18.7% to 4.5% and from 175 to 75 kPa, respectively.

The findings of the experiments are given and discussed in this section. The addition of ferrock material for subgrade stability is seen to have the following effects:

18.5.2 Features of compaction

Maximum dry density (MDD) and optimal moisture content (OMC) measurements of the compaction characteristics of soil samples stabilized with ferrock material show peak values at 5% and 15% ferrock material, respectively. With an increase in ferrock material, MDD has been seen to increase while OMC has reduced. The MDD of untreated soil increased by around 7% at 15% ferrock content, while the OMC fell by about 15% Table 18.2 and 18.3. This finding suggests that the compaction characteristics are significantly impacted by the addition of ferrock material Table 18.4 and 18.5.

18.5.3 Soaked California bearing ratio

The soil exhibits a significant rise in CBR with 5% ferrock material added, and subsequent additions of ferrock material are gradually changing the variation of CBR. This is evident from the variation of soaking CBR of the soil stabilized with ferrock material. When ferrock material was only 5%, CBR significantly improved by nearly 90%. Additionally, it is noted that the CBR value is approximately 17 times higher at 5% ferrock material than it is at untreated soil. Peak CBR values are seen for ferrock materials at 5% and 15% Table 18.10−18.12. After 15% of ferrock material was added to the soil, it stabilized, and the CBR values started to decline. The transition from a dispersed to a flocculate soil structure may be responsible for this improvement in CBR (−).

Table 18.2 Standard Proctor test for expansive soil only.

Mould wt.	**2.5**	**2.5**	**2.5**	**2.5**	**2.5**	**2.5**
Trial	1	2	3	4	5	6
Wt. of water added = ww (mL)	240	300	360	420	480	540
Weight of mould + compacted soil	4.5	4.64	4.69	4.7	4.65	4.6
Weight of compacted soil = w (g)	2.071	2.211	2.261	2.271	2.221	2.171
Average moisture content = w%	8.952058	10.54268	12.14286	13.77826	15.45718	17.40467
Bulk density = w/(mould volume) = (g/cc)	2.071	2.211	2.261	2.271	2.221	2.171
Dry density = bulk density/(1 + w) = (g/cc)	1.900836	2.000132	2.016178	1.995988	1.923657	1.84916

Table 18.3 Standard Proctor test for expansive soil + 5% ferrock material.

Mould wt.	**2.429**	**2.429**	**2.429**	**2.429**	**2.429**	**2.429**
Trial	1	2	3	4	5	6
Wt. of water added = ww (mL)	240	300	360	420	480	540
Weight of mould + compacted soil	4.65	4.67	4.71	4.75	4.72	7.68
Weight of compacted soil = w (g)	2.32	2.38	2.45	2.48	2.39	2.35
Average moisture content = w%	8.952058	10.54268	12.14286	13.77826	15.45718	17.40467
Bulk density = w/(mould volume) = (g/cc)	2.32	2.38	2.45	2.48	2.39	2.35
Dry density = bulk density/(1 + w) = (g/cc)	2.129377	2.153015	2.184713	2.179678	2.070031	2.001624

Table 18.4 Standard Proctor test for expansive soil + 10% ferrock material.

Mould wt.	**2.429**	**2.429**	**2.429**	**2.429**	**2.429**	**2.429**
Trial	1	2	3	4	5	6
Wt. of water added = ww (mL)	240	300	360	420	480	540
Weight of mould + compacted soil	4.67	4.7	4.72	4.75	7.69	4.68
Weight of compacted soil = w (g)	2.33	2.38	2.46	2.49	2.4	2.35
Average moisture content = w%	8.952058	10.54268	12.14286	13.77826	15.45718	17.40467
Bulk density = w/(mould volume) = (g/cc)	2.33	2.38	2.46	2.49	2.4	2.35
Dry density = bulk density/(1 + w) = (g/cc)	2.138555	2.153015	2.193631	2.188467	2.078693	2.001624

Table 18.5 Standard Proctor test for expansive soil + 15% ferrock material.

Mould wt.	**2.429**	**2.429**	**2.429**	**2.429**	**2.429**	**2.429**
Trial	1	2	3	4	5	6
Wt. of water added = ww (mL)	240	300	360	420	480	540
Weight of mould + compacted soil	4.74	4.76	4.78	4.81	4.77	4.71
Weight of compacted soil = w (g)	2.35	2.4	2.42	2.49	2.4	2.35
Average moisture content = w%	8.952058	10.54268	12.14286	13.77826	15.45718	17.40467
Bulk density = w/(mould volume) = (g/cc)	2.35	2.4	2.42	2.49	2.4	2.35
Dry density = bulk density/(1 + w) = (g/cc)	2.156912	2.171107	2.157962	2.188467	2.078693	2.001624

Table 18.6 Standard Proctor test for expansive soil + 20% ferrock material.

Mould wt.	**2.429**	**2.429**	**2.429**	**2.429**	**2.429**	**2.429**
Trial	1	2	3	4	5	6
Wt. of water added = ww (mL)	240	300	360	420	480	540
Weight of mould + compacted soil = w (g)	4.77	4.79	4.8	4.83	4.77	4.74
Weight of compacted soil = w (g)	2.4	2.42	2.46	2.48	2.41	2.38
Average moisture content = w%	8.95	10.54	12.14	13.77	15.45	17.40
Bulk density = w/(mould volume) = (g/cc)	2.4	2.42	2.46	2.48	2.41	2.38
Dry density = bulk density/(1 + w) = (g/cc)	2.20	2.18	2.19	2.17	2.08	2.027

Table 18.7 Unconfined compressive strength test for expansive soil only.

Sl. no.	Dial gauge reading	Deformation (mm)	Proving ring reading	Load (kN)	Strain (%)	Corrected area (mm^2)	Compressive strength (N/mm^2)
1	0	0	0	0	0.000	11.341	0.000
2	50	0.5	12	0.016	0.658	11.416	0.014
3	100	1	33	0.045	1.316	11.492	0.039
4	150	1.5	65	0.098	1.974	11.569	0.085
5	200	2	95	0.144	2.632	11.648	0.124
6	250	2.5	121	0.16	3.289	11.727	0.136
7	300	3	123	0.186	3.947	11.807	0.158
8	350	3.5	148	0.221	4.605	11.889	0.186
9	400	4	160	0.226	5.263	11.971	0.189
10	450	4.5	166	0.245	5.921	12.055	0.203
11	500	5	168	0.246	6.579	12.140	0.203
12	550	5.5	169	0.24	7.237	12.226	0.196
13	600	6	169	0.24	7.895	12.313	0.195
14	650	6.5	168	0.238	8.553	12.402	0.192
15	700	7	168	0.238	9.211	12.492	0.191
16	750	7.5	168	0.238	9.868	12.583	0.189
17	800	8	164	0.235	10.526	12.675	0.185
18	850	8.5	164	0.235	11.184	12.769	0.184
19	900	9	163	0.231	11.842	12.865	0.180
20	950	9.5	161	0.231	12.500	12.961	0.178

Table 18.8 Unconfined compressive strength test for expansive soil + 5% ferrock material.

Sl. no.	Dial gauge reading	Deformation (mm)	Proving ring reading	Load (kN)	Strain (%)	Corrected area (mm^2)	Compressive strength (N/mm^2)
1	0	0	0.000	0.000	0.000	11.341	0.000
2	50	0.5	10.000	0.016	0.658	11.416	0.014
3	100	1	22.000	0.030	1.316	11.492	0.026
4	150	1.5	49.000	0.056	1.974	11.569	0.048
5	200	2	70.000	0.098	2.632	11.648	0.084
6	250	2.5	92.000	0.125	3.289	11.727	0.107
7	300	3	105.000	0.146	3.947	11.807	0.124
8	350	3.5	121.000	0.169	4.605	11.889	0.142
9	400	4	130.000	0.179	5.263	11.971	0.150
10	450	4.5	137.000	0.195	5.921	12.055	0.162
11	500	5	144.000	0.205	6.579	12.140	0.169
12	550	5.5	146.000	0.208	7.237	12.226	0.170
13	600	6	169.000	0.241	7.895	12.313	0.196
14	650	6.5	168.000	0.239	8.553	12.402	0.193
15	700	7	168.000	0.239	9.211	12.492	0.191
16	750	7.5	167.000	0.238	9.868	12.583	0.189
17	800	8	164.000	0.234	10.526	12.675	0.185
18	850	8.5	164.000	0.234	11.184	12.769	0.183

Table 18.9 Unconfined compressive strength test for expansive soil + 10% ferrock material.

Sl. no.	Dial gauge reading	Deformation (mm)	Proving ring reading	Load (kN)	Strain (%)	Corrected area (mm^2)	Compressive strength (N/mm^2)
1	0	0	0	0	0	11.3411	0
2	50	0.5	11	0.015	0.6	11.4163	0.013
3	100	1	35	0.049	1.3	11.4924	0.043
4	150	1.5	71	0.101	1.9	11.5695	0.087
5	200	2	98	0.139	2.6	11.6477	0.119
6	250	2.5	109	0.155	3.3	11.7269	0.132
7	300	3	132	0.188	3.9	11.8072	0.159
8	350	3.5	153	0.218	4.6	11.8887	0.183
9	400	4	164	0.233	5.3	11.9712	0.195
10	450	4.5	170	0.242	5.9	12.0549	0.201
11	500	5	173	0.246	6.6	12.1398	0.203
12	550	5.5	177	0.252	7.2	12.2259	0.206
13	600	6	177	0.252	7.9	12.3132	0.204
14	650	6.5	178	0.253	8.5	12.4018	0.204
15	700	7	176	0.250	9.2	12.4917	0.201
16	750	7.5	175	0.249	9.8	12.5829	0.198
17	800	8	175	0.249	10.5	12.6754	0.196
18	850	8.5	174	0.248	11.2	12.7693	0.194
19	900	9	173	0.246	11.8	12.8646	0.191

Table 18.10 Soaked California bearing ratio (CBR) test for expansive soil.

Sl. no.	Plunger penetration (mm)	Dial gauge readings	Applied load (kg)	CBR stress (kg/cm^2)	Standard load intensity (kg/cm^2)	CBR intensity (% age)
1	0	0	0	0		
2	0.5	3	6.51	0.33		
3	1	9	20.56	1.05		
4	1.5	15	40.25	2.06		
5	2	20	51.02	2.62		
6	2.5	23	55.32	2.84	70	4.057
7	3	26	65.23	3.35		
8	3.5	30	77.23	3.96		
9	4	33	85.56	4.39		
10	4.5	35	88.45	4.54		
11	5	37	95.45	4.89	105	4.657

18.6 Conclusion

A study was conducted experimentally to determine the impact of ferrock material on the expanding soils' geotechnical properties in relation to their application as pavement subgrade. This study examined the effects of different ferrock material percentages (0%, 5%, 10%, 15%, and 20%) on the geotechnical properties of expanding soil Table 18.1−18.14.

The local soil with an increased percentage of ferrock material, result into the swell potential and swell pressure values reduced from 18.7% to 4.5% and from 175 to 75 kPa, respectively. It has been noted that in order to add more ferrock material, the swell potential and swell pressure must first be reduced by around 60% after the addition of 15% ferrock material (Ash Ahmed and James West, 2023).

Most of the strength increases occurred during the soaking phase, indicating that stabilizing reactions and strength increases were continuous.

CBR significantly improved at 5% ferrock material. CBR values are gradually changing as a result of ferrock substance. The soil treated with 15% ferrock material showed less swelling. Therefore 15% ferrock material can be used cost-effectively to stabilize expansive soils for use as road pavement Table 18.11−18.13.

Table 18.11 Soaked California bearing ratio (CBR) test for expansive soil + 5% ferrock material.

Sl. no.	Plunger penetration (mm)	Dial gauge readings	Applied load (kg)	CBR stress (kg/cm^2)	Standard load intensity (kg/cm^2)	CBR intensity (% age)
1	0	2.75	2.85	0.15		
2	0.5	12.25	17.1	0.9		
3	1	23.52	21.47	1.13		
4	1.5	29.65	33.25	1.75		
5	2	39.54	46.55	2.45		
6	2.5	51.89	52.25	2.75	70	3.92
7	3	61.78	76	4		
8	3.5	71.66	81.7	4.3		
9	4	78.56	85.88	4.52		
10	4.5	82.53	92.91	4.89		
11	5	94.56	99.75	5.25	105	5.00

Table 18.12 Soaked California bearing ratio (CBR) test for expansive soil + 10% ferrock material.

Sl. no.	Plunger penetration (mm)	Dial gauge readings	Applied load (kg)	CBR stress (kg/cm^2)	Standard load intensity (kg/cm^2)	CBR intensity (% age)
1	0	1	2.52	0.1326		
2	0.5	10	23.45	1.2342		
3	1	18	43.52	2.2905		
4	1.5	21	53.52	2.8168		
5	2	27	61.78	3.2516		
6	2.5	32	74.52	3.9221	70	5.60
7	3	33	85.52	4.5011		
8	3.5	39	98.52	5.1853		
9	4	40	98.84	5.2021		
10	4.5	44	103.78	5.4621		
11	5	45	110.26	5.8032	105	5.52

Table 18.13 Soaked California bearing ratio (CBR) test for expansive soil + 15% ferrock material.

Sl. no.	Plunger penetration (mm)	Dial gauge readings	Applied load (kg)	CBR stress (kg/cm^2)	Standard load intensity (kg/cm^2)	CBR intensity (% age)
1	0	1	2.47	0.13		
2	0.5	6	14.83	0.76		
3	1	13	32.12	1.64		
4	1.5	20	49.42	2.52		
5	2	26	64.25	3.27		
6	2.5	30	74.13	4.11	70	5.88
7	3	36	88.96	4.53		
8	3.5	40	98.84	5.04		
9	4	42	103.78	5.29		
10	4.5	45	111.20	5.67		
11	5	46	113.67	6.03	105	5.75

Table 18.14 Soaked California bearing ratio (CBR) test for expansive soil + 20% ferrock material.

Sl. no.	Plunger penetration (mm)	Dial gauge readings	Applied load (kg)	CBR stress (kg/cm^2)	Standard load intensity (kg/cm^2)	CBR intensity (% age)
1	0	1	2.47	0.13		
2	0.5	3	7.41	0.38		
3	1	6	14.83	0.76		
4	1.5	10	24.71	1.26		
5	2	15	37.07	1.89		
6	2.5	20	49.42	2.52	70	3.60
7	3	24	59.30	3.02		
8	3.5	28	69.19	3.53		
9	4	30	74.13	3.78		
10	4.5	32	79.07	4.03		
11	5	34	84.01	4.28	105	4.08

References

Ash A. & James W. (2023) (Submitted for publication). Experimental Investigation of Engineering Properties of Iron-Based Binary and Ternary Pozzolanic Supplementary Cementitious Materials. Journal of Materials and Polymer Science, 3(1).

Das, S., et al. (2014). Pore- and micro-structural characterization of a novel structural binder based on iron carbonation. *Science Direct. Materials Characterization*, Web. 27 Feb. 2017.

David S. (2017). *Top ten list of characteristics for ferrock TM—A new green building material*.

Engineering Intro. *Cement manufacturing process*. [ONLINE] Available from <http://www.engineeringintro.com/uncategorized/cement-manufacturing-process/>; 2012 Accessed 02. 04.17.

Garcia, A. L., Achaiah, A. T., Bello, J., & Donovan, T. (2017). Ferrock: A life cycle comparison to ordinary Portland cement. *ISE 576 − Industrial Ecology*, April 24.

Geiger, O., et al. (2017). Ferrock concrete. *Natural Building Blog*, *2021*, Retrieved June 7. Available from http://www.naturalbuildingblog.com/ferrock-concrete/.

Graedel, T. E., & Allenby, B. R. (2010). *Industrial ecology and sustainable engineering*. *Chapter 12: Introduction to life cycle assessment*. Pearsons Education.

Mohanty, M. (2015). Stabilization of Expansive Soil Using Fly Ash. *NIT, Rourkela*, Submitted for publication.

Niveditha, M., Manjunath, Y. M., & Prasanna, S. H. S. (2021). Ferrock: A carbon negative sustainable concrete. *International Journal of Sustainable Construction Engineering and Technology*, *11*, 90−98, 26 July.

Vijayan, D. S., Kumar, D., Aravindan, S., & Janarthanan, T. S. (2019). Evaluation of ferrock: A greener substitute to cement. *Materials Today Proceedings*, *8*, 171−178, October.

Index

Note: Page numbers followed by "*f*" and "*t*" refer to figures and tables, respectively.

A
A/B. *See* Alkaline activator to binder ratio (A/B)
AAC. *See* Alkali-activated cements (AAC)
AAS. *See* Alkali-activated slag (AAS)
Acidification potential (AP), 28
Aerobic decomposition, 231
Aggregates, 15, 56, 99, 113–114
  materials replacing, 125–128
  mixture, 113
Agricultural waste materials, 116
Agricultural/nontraditional waste, 115
Air-dried clayey soil, 86–88
Alkali-activated cements (AAC), 186–188
Alkali-activated slag (AAS), 186
Alkaline activator solution, 15
Alkaline activator to binder ratio (A/B), 20–21
Alkaline activators, 57
Alkaline environment, 232
Alkaline liquid (Na_2SiO_3), 57, 58*t*
Alkaline solid (NaOH), 58
  flakes, 58, 58*t*
Alkalis, 113
Alumina-silicate source materials, 41–42
Aluminum slag, 68
  efficiency of geogrid based on friction embedded in, 76*t*
  experimental program, 70
    geogrid sample connected at interface of upper and lower shear boxes, 70*f*
  interaction coefficients of geogrids embedded in aluminum slag at peak and critical states, 76*t*
  materials used, 68–69
  particles, 70, 72–73
    comparison of interfacial shear strength envelopes with direct shear strength envelopes for, 75*f*
    direct shear strength envelopes of aluminum slag particles at peak and critical states, 72*f*
    used in study, 69*f*
  results, 70–77
    basic characteristics of aluminum slag, 70–71, 71*f*
    direct shear testing, 71–73
    interface direct shear testing, 73–77
Ambient temperature, 58
Anaerobic biostimulation, 231
Anaerobic decomposition, 231
Aquatic plants, 235–237
Artificial seawater, 234
Atomic absorption spectrophotometer, 234
Atomic absorption spectroscopy, 265
Autodesk Revit, 28–29
  LCA, 28–29
  Tally, 28

B
BA. *See* Bagasse ash (BA)
Bacillus
  B. cereus, 241–242
  B. cohnii, 255–256
  B. licheniformis, 241–242
  B. pasteurii, 249
  B. sphaericus, 246
  B. subtilis, 241–242
Bacterial cells, 247–248, 255
Bacterial concrete, 241–242, 244
Bagasse ash (BA), 115
Basalt, 114
BC soil. *See* Black cotton soil (BC soil)
Bentonite, 153–154
Bermuda Triangle, 103
  of concrete, 104*f*
Bi. *See* Binder Index (Bi)

BIM. *See* Building Information Modeling (BIM)
Binary packing densities
  of copper slag, 137*f*
  of ennore sand, 137*f*
Binder Index (Bi), 13, 21–24
  validation of, 21–24
Binocular inspection microscope, 244
Bio-based rejuvenator, 173–175
Bioconcrete
  methodology adopted for study, 243, 243*f*
  microorganisms form spores and use ureolysis to precipitate calcite, 242*t*
  microstructural and chemical analyses, 243–245
  microstructure of bio-concrete, 245–256
Biodegradable polymer, 230
Biomass, 110
Biomediated self-healing ground improvement technology applied to marine environment
  characteristics of microbes, 233*t*
  development of, 233–235
  trend of calcium elution weight and magnesium adsorption weight, 234*f*
  trend of deterioration depth from top of specimens, 235*f*
Biopolymers, 230
Bituminous binder, 170
Bituminous mixture, 165
Black basalt aggregates, 56
Black cotton soil (BC soil), 153–154
Blast furnace slag, 55, 110
Blended cements, 112
Bond stress, 123*t*
Building Information Modeling (BIM), 28

C

Calcareous pulverized fuel FA, 116
Calcite crystal, 249
Calcite precipitation, 249
Calcium aluminate, 202–203
Calcium carbonate, 234–235, 246–247, 249
Calcium hydroxide, 95, 214
Calcium ions, 231
Calcium lactate, 253
Calcium oxide, 41–42
Calcium silicate, 214
Calcium silicate hydrate (CSH), 41–42, 54–55, 202–203
Calcium-magnesium, 231–232
  minerals, 231
  systems, 233
Calcium-rich IBPs, 266–267
Calcium-rich nutrient sources, 241–242
California Bearing Ratio (CBR), 81–82, 280–281
  with and without coir reinforcement, 158*t*
  soaked CBR test for expansive soil, 291*t*
  soaked CBR values at percentages of coir fiber, 160*f*
  test results, 157–159
  unsoaked and soaked CBR values of black cotton soil, 158*f*
  unsoaked CBR values at percentages of coir fiber, 159*f*
Carbon capture and storage (CCS), 189
Carbon dioxide (CO_2), 279–280
  emissions, 219, 263–264
Carbon emissions, 266, 272
Carbon fiber, 221
Carbon fiber-reinforced polymer (CFRP), 220–221
Carbon footprint, 219
Carbon footprint assessment (CFA), 263–264
  on coal gangue application in earthworks, 272–273, 272*t*
  inventory, 266
  methodology, 265–266
  net emissions for each stage of embankment construction, 273*f*
  scope and goal, 265
  system boundary, 266
    geotechnical properties of coal gangue, 267*t*
Carbonization, 109
CBR. *See* California Bearing Ratio (CBR)
CC. *See* Coir composite (CC)
Cc. *See* Crystalline calcite (Cc)
CCS. *See* Carbon capture and storage (CCS)
CE. *See* Constructional energy (CE)
Cement, 38, 97, 153–154, 234
  cement-bonded FA aggregates, 126
  composites, 202
  industry emission, 41
  industry sector, 219

manufacturing industry, 41
materials replacing, 115–128
paste, 201
production, 41
utilization of mineral wastes in cement as in-active fillers, 184–185
Cement kiln dust (CKD), 189–190
Cement replacement materials (CRMs), 115
Cementitious concrete systems, 249–252
Cementitious subbase (CTSB), 82
Cementless geopolymer concrete, 53
CFA. *See* Carbon footprint assessment (CFA)
CFRP. *See* Carbon fiber-reinforced polymer (CFRP)
CG. *See* Coal gangue (CG)
Chemical admixture, 100
Chemical composition
of copper slag, 134, 135*t*
of geopolymer concrete as per mix design, 59
chemical components in fly ash and GGBS-based geopolymer concrete, 61*t*
of GGBS and fly ash, 43*t*
Chlorides, 113, 124
CKD. *See* Cement kiln dust (CKD)
Clay, 280
CMOD. *See* Crack mouth opening displacement (CMOD)
Coal gangue (CG), 263–264
carbon footprint assessment on coal gangue application in earthworks, 272–273, 272*t*
leaching studies, 268–272
effect of particle size and interaction time on leaching, 270–272, 271*f*
variation in pH and metal extraction with liquid–solid ratio and interaction time, 268–270
materials and methods, 264–266
carbon footprint assessment methodology, 265–266
geotechnical and leaching characteristics, 264–265
results, 266–273
geotechnical characteristics of coal gangue, 266–267
Coal refuse, 184
Coarse aggregates, 56, 57*t*, 100, 114, 125
Coir composite (CC), 160–162
Coir fiber, 154, 157–159
Coir geotextile fiber, 155
Coir geotextile mats, 162
Coir mats, 160–162
Collapse potential (Cp), 264–265
Combustion process, 181
Composite technology, 221
Compression testing machine, 207–208
Compressive strength, 54–55
of geopolymer concrete, 17
effect of alkaline activator to binder ratio, 20
effect of ground granulated blast furnace slag to fly ash ratio, 21, 22*f*
effect of molarity/concentration of NaOH solution, 19, 19*f*
of GGBS-based concrete mixtures, 130*t*
of GPM cube, 46, 50*f*, 50*t*
for high performance concrete, 101*t*
of mortar, 43–45
test, 141–142, 207–209
compressive strength of geopolymer concrete, 17
test results on geopolymer concrete cubes, 18*t*
testing procedure for, 17
of UHPC with copper slag, results for, 144*t*
of UHPC with ennore sand, results for, 143*t*
variation of, 23*f*
variation of compressive strength of geopolymer mortar for different water-to-water glass ratios, 46–51
Computational-based models, 224
Concrete, 97, 99, 101, 110–114, 128–129, 203, 219
"Bermuda Triangle" of, 104*f*
curing process, 100
industry, 110
materials forming ternary systems for, 128
mixtures
properties of, 122*t*
proportions, 121*t*
specifications of siliceous fly ash for use in, 120*t*
specimens preparations, 207

Concrete (*Continued*)
utilization of mineral wastes in concrete as in-active fillers, 184−185
Consistency of geopolymer paste, 43, 45−46
Constituency test, 45−46
Construction materials, 109
used for manufacturing of high performance green concrete, 96*f*
Construction products or during manufacture, application for mineral carbon sequestration within, 189−190
Construction techniques, 279
Construction waste materials, 125
Constructional energy (CE), 29−30
Conventional CTSB, 82
Conventional OPCCs, 119−121
Conventional polymeric reinforcements, 82
Conventional stabilization techniques, 153−154
Conventional techniques, 153
Copper slag (CS), 133, 136
binary packing densities of, 137*f*
chemical composition of, 134
physical and chemical properties of, 133−134, 134*t*
results for compressive strength of UHPC with, 144*t*
Corrosion, 280
resistance, 232
Cp. *See* Collapse potential (Cp)
Crack healing, 253
Crack mouth opening displacement (CMOD), 143
Cracking tolerance index (CT_{index}), 171−172
Critical stress intensity factor, 143
CRMs. *See* Cement replacement materials (CRMs)
Crushed glass, 97
Crushed granite, 114
Crystal deposition technologies, 230
Crystal precipitation by microbial functions and engineering applications, mechanisms of, 229−232
Crystalline, 256
Crystalline calcite (Cc), 253−254
Crystalline minerals, 232
Crystallization technologies, 230
CS. *See* Copper slag (CS)
CSH. *See* Calcium silicate hydrate (CSH)
CSIR-SERC. *See* CSIR-Structural Engineering Research Centre (CSIR-SERC)
CSIR-Structural Engineering Research Centre (CSIR-SERC), 119
first fly ash building built in India at, 120*f*
CT_{index}. *See* Cracking tolerance index (CT_{index})
CTSB. *See* Cementitious subbase (CTSB)
Cube compressive strength, 144−145
compression testing of mixes with copper slag and failure pattern, 146*f*
ratio of compressive strength of 7 cm cubes to 10 cm cubes, 145*t*
Curing, 113
alternative cycles of, 113
regime, 141, 142*f*
Cyclic load test, 154

D

DAQ. *See* Data acquisition system (DAQ)
Data acquisition system (DAQ), 86
DBC. *See* Dead bacteria (DBC)
DE. *See* Demolition energy (DE)
DE coating. *See* Diatomaceous earth coating (DE coating)
Dead bacteria (DBC), 255−256
Decision tree, 190−191
Degradation of infrastructure, 109
Demolition energy (DE), 29−30
Denitrification reactions, 236
DGW. *See* Double glass windows (DGW)
Diatomaceous earth coating (DE coating), 247
stereomicroscope image of concrete crack healing using DE encapsulated bacteria, 250*f*
Direct shear parameters, 72−73
Direct shear strength envelopes for aluminum slag particles, comparison of interfacial shear strength envelopes with, 75*f*
Direct shear testing, 71−73
comparison of direct shear parameters from present study with available literature, 75*f*

direct shear strength envelopes of aluminum slag particles at peak and critical states, 72*f*
variation of shear stress of aluminum slag particles, 72*f*
Dolomite precipitation, 232
Double glass windows (DGW), 29–30
Drainage function, 153–154
Durability, 95

E
Earthwork, 265
carbon footprint assessment on coal gangue application in, 272–273
Eco-friendly, 109, 125–126
Economic growth, 201
EDS. *See* Energy dispersive X-ray spectroscopy (EDS)
Efficiency of geogrid, 73
Eklahare Thermal Power Plant, 82
Elastic modulus, 219–220
Elastic response, 173–174
Electrical conductor, 221
Electro-static precipitators (ESPs), 116
Electromagnetic waves, 208
Energy absorption, 223–224
Energy Dispersive X-Ray (EDX) analysis, 212–213
Energy dispersive X-ray spectroscopy (EDS), 242–244
Engineered concretes, 128–149
high-performance concrete, 128–130
mixing of UHPC, 138–149
UHPC, 130–138
Engineering green concrete
materials forming ternary systems for concrete, 128
materials replacing aggregate, 125–128
materials replacing cement, 115–128
FA, 116–123
GGBS, 123–124
silica fume, 124–125
strategies for sustainability, 114–128
for sustainable infrastructure
aggregates, 113–114
coarse aggregates, 114
concrete and green concrete, 110–112
engineered concretes, 128–149
engineering green concrete strategies for sustainability, 114–128
fine aggregates, 114
hydration, 113
key ingredients, 112–113
other ingredients, 113
proportioning, 112
reinforcing bars, 114
Ennore sand (ES), 133
binary packing densities of, 137*f*
results for compressive strength of UHPC with, 143*t*
Environment, 109, 111
Environmental product declaration (EPD), 30
EP. *See* Eutrophication potential (EP)
EPD. *See* Environmental product declaration (EPD)
Epoxy resin, 222–223
EQT. *See* Equitensiometer (EQT)
Equitensiometer (EQT), 1–2
ES. *See* Ennore sand (ES)
ESPs. *See* Electro-static precipitators (ESPs)
Ettringite, 214
Eutrophication potential (EP), 28
Externally bonded fiber polymer reinforcements (FRP EBR), 225

F
FA. *See* Fly ash (FA)
FA-GBFS. *See* Fly ash-granulated blast furnace slag (FA-GBFS)
FAGP. *See* Fly ash-based geopolymer (FAGP)
Ferrock, 279–280
findings, 281–290
features of compaction, 282
soaked California bearing ratio, 282–290
soil stability, 282
material for stabilization of subgrade soil, 280–281
potential applications, 280
testing procedures, 280–281
analysis of lab investigation, 281
combination of soil and ferrock material samples, 281
lab investigations, 281

Ferrock (*Continued*)
understanding of important technologies, 280
Fiber-reinforced nanocomposites, 222
Fiber-reinforced UHPC, 147
Fiber−reinforced polymer (FRP), 220−221
characteristics of, 221
orientation of fibers in carbon fiber-reinforced polymer, 222*f*
nanocomposites, 222−224
CFRP-wrapped beam under test, 224*f*
characteristics of fiber-reinforced polymers, 221
chemical structures of epoxy system, 223*f*
demand of infrastructure material and worldwide production, 220*f*
history, development, and applications of, 221*f*
standard practices and codes involved in fiber-reinforced polymer-structural retrofit, 224−225
Filter paper technique, 2
Filtration function, 153−154
Fine aggregates, 42−43, 56, 57*t*, 99, 114, 125
Flexural strength
of geopolymer concrete, 17, 19
effect of alkaline activator to binder ratio, 20−21, 21*f*
effect of ground granulated blast furnace slag to fly ash ratio, 21, 22*f*
effect of molarity/concentration of NaOH solution, 19
test, 142−143
of ultrahigh performance concrete, 145−147, 147*f*
variation of, 24*f*
Fly ash (FA), 1, 13−14, 27−28, 41−42, 55−57, 81−82, 95, 97, 110, 115−123, 117*f*, 126, 128, 153−154, 280−281
basic properties of, 83*t*
chemical composition, 14*t*, 43*t*
of Class F and Class C type fly ash, 99*t*
of Indian fly ashes, 118*t*
durability properties of fly ash concrete, 119−121
FA-based GPC, 23−24
FA-GBFS mixes, 85
effect of ground granulated blast furnace slag to fly ash ratio, 21
HVFAC, 121−123
major mode of fly ash utilization in India FY2021−22, 119*f*
particle size distribution curves, 83*f*
physical and chemical properties of, 57*t*
properties of, 3*t*, 82
regression models for water retention characteristic curve of, 5−8
specifications of siliceous fly ash for use in concrete, 120*t*
studies on water retention characteristic curve of, 1−2
water retention characteristic curves of, 3−5
Fly Ash Mission, 116−117
Fly ash-based geopolymer (FAGP), 61*t*, 186
Flyash-based high strength geopolymer concrete
experimental program, 56−62
literature study, 54−56
factors influencing geopolymer concrete properties, 55−56
geopolymerization, 54−55
raw materials for geopolymer concrete, 55
materials, 56−58
alkaline liquid, 57
alkaline solid, 58
coarse and fine aggregates, 56, 57*t*
fly ash and GGBS, 56−57
mix design, 58−62
chemical composition of geopolymer concrete as per mix design, 59
geopolymer concrete mix design, 58−59
mean compressive strength results for all mix trials, 62
observations for geopolymer concrete pilot mix revised trial-1, 59−61
objective of study, 53
scope of work, 53
Fly ash-GGBS, consistency of geopolymer paste for different proportions of, 47*t*

Fly ash-granulated blast furnace slag (FA-GBFS), 82
methodology, 85
CBR test results for various fly ash-granulated blast furnace slag mixes, 86*f*
laboratory experimentation, 85
Standard Proctor and CBR tests results, 86*t*
model pavement, 86
properties of materials, 82−85
chemical properties of materials, 84−85, 85*t*
fly ash and granulated blast furnace slag, 82
marine clay, 82−83
reinforcement, 84
results, 90−91
detailed tests and parameters, 90*t*
difference in deformation for unreinforced and reinforced cases, 91*f*
load-deformation curve for reinforced and unreinforced sections, 91*f*
model pavement tests results, 90*t*
sample preparation of model pavement, 86−89
Food chain, 268
Fossil fuels, 184
Fourier transform infrared spectroscopy (FTIR spectroscopy), 242−243, 245
of bio-concrete, 254−255
of dried bacterial solution, 257*f*
Fracture energy (GF), 143
test, 143
of ultrahigh-performance concrete prisms, 147−149
flexural strength of UHPC mixes, 149*t*
load *vs*. CMOD, 148*f*
load *vs*. deflection of notched UHPC specimens, 148*f*
Fredlund & Xing (FX model), 2−4
comparison of FX WRCC regression fit, 9*f*
computed WRCC of, 6*f*
estimated WRCC
of FX model for KTPS fly ash, 6*f*
for RTPS fly ash, 5*f*
FRP. *See* Fiber−reinforced polymer (FRP)
FRP EBR. *See* Externally bonded fiber polymer reinforcements (FRP EBR)
FTIR spectroscopy. *See* Fourier transform infrared spectroscopy (FTIR spectroscopy)
Fuel consumption, 272−273
Functional unit, 32
FX model. *See* Fredlund & Xing (FX model)

G

GBFS. *See* Granulated blast furnace slag (GBFS)
Geogrids, 82
efficiency of geogrid based on friction embedded in aluminum slag, 76*t*
interaction coefficients of geogrids embedded in aluminum slag at peak and critical states, 76*t*
Geopolymer, 41−42, 186−188
mix design, 62
Geopolymer concrete (GPC), 13, 41−42, 111
effect of alkaline activator to binder ratio, 20−21
on compressive strength of geopolymer concrete, 20, 20*f*
on flexural strength of geopolymer concrete, 20−21, 21*f*
cast and curing of geopolymer concrete specimens, 15−17
compressive strength of geopolymer concrete, 17
flexural strength or modulus of rupture of geopolymer concrete, 17
testing procedure for compressive strength test, 17
chemical composition of geopolymer concrete as per mix design, 59
compressive strength of, 50*f*, 50*t*
experimental program, 14−15
materials used, 14−15, 14*t*
mix proportions, 15, 16*t*
schematic diagram of, 14*f*
factors influencing geopolymer concrete properties, 55−56
final setting time of, 49*f*
effect of ground granulated blast furnace slag to fly ash ratio, 21

Geopolymer concrete (GPC) (*Continued*)
on compressive strength of geopolymer concrete, 21
on flexural strength of geopolymer concrete, 21
mix design, 58−59
data for design of low calcium fly ash-based geopolymer concrete, 59*t*
mix design for M70 grade equivalent geopolymer concrete, 60*t*
mix designs with varying water-to-solids and alkaline liquid-to-source-material ratio, 61*t*
mix proportion for geopolymer concrete, 60*t*
effect of molarity/concentration of NaOH solution, 19
on compressive strength of, 19
on flexural strength of, 19
observations for geopolymer concrete pilot mix revised trial-1, 59−61
mean compressive strength result comparison for different trial mixes, 62*f*
raw materials for, 55
test results, 17−24
validation of binder index, 21−24
Geopolymer mortar (GPM), 45
Geopolymer paste, 43
consistency of, 43, 45−46
for different proportions of fly ash-GGBS, 47*t*
initial setting time of, 49*f*
Geopolymerization, 54−55
Geopolymers, 54
Geotechnical engineering, 5−8, 67
development of preservation materials with self-healing and environmental preservation functions based on the microbial functions, 233−237
mechanisms of crystal precipitation by microbial functions and engineering applications, 229−232
GFRP. *See* Glass fiber-reinforced polymer (GFRP)
GGBS. *See* Ground granulated blast furnace slag (GGBS)
GHG. *See* Greenhouse gas (GHG)
GHPC. *See* Green high-performance concrete (GHPC)
Glass fiber-reinforced polymer (GFRP), 220−221
Global CO_2 emissions, 181
Global warming, 189, 241
Global warming potential (GWP), 28
Global waste generation, 181
Gold-palladium, 244
GPC. *See* Geopolymer concrete (GPC)
GPM. *See* Geopolymer mortar (GPM)
Gradation coefficients of AS particles, 71
Grading of aggregates, 113
Granular materials, optimization of, 134−136
Granulated blast furnace slag (GBFS), 81−82
basic properties of, 83*t*
particle size distribution curves, 83*f*
Granules, 237
Green concrete, 95, 109−112, 184
Green high-performance concrete (GHPC), 111
Greenhouse gas (GHG), 111, 202
emissions, 222, 279
Ground granulated blast furnace slag (GGBS), 13−14, 21, 27−28, 41−42, 55−57, 115, 123−124, 123*f*, 184
chemical composition, 14*t*, 43*t*, 124*t*, 130*t*
GGBS-based GPC, 23−24
chemical components in, 61*t*
effect of ground granulated blast furnace slag to fly ash ratio, 21
micro-structure related properties of GGBS-based concrete mixtures, 132*t*
physical and chemical properties of, 57*t*
physical properties of, 124*t*
GWP. *See* Global warming potential (GWP)
Gypsum, 153−154

H

HC. *See* Hydraulic conductivity (HC)
Healing process, 246
Heat treatment of POFA, 116
Hemicellulose, 154
Heterogeneous materials, 244
High performance concrete (HPC), 95
advantages of, 96
applications of, 96

construction materials used for manufacturing of high performance green concrete, 96*f*
curing of high performance green concrete, 104
high performance green concrete, 97−100
mix design of, 96−97
mix proportion, 100−101
strength development, 101−103
"Bermuda Triangle" of concrete, 104*f*
classification of high performance concrete, 103*t*
water to cementitious material ratio and strength of high performance concrete, 104*f*
superplasticizer in high performance green concrete, 100
transporting and placing of high performance green concrete, 103
High performance green concrete, 97−100
cement and supplementary cementitious materials, 97−100
aggregates, 99
coarse aggregate, 100
fine aggregate, 99
fly ash, 97
silica fume, 97−99
curing of, 104
superplasticizer in, 100
transporting and placing of, 103
High range water reducers (HRWR), 136−138
High volume fly ash concrete (HVFAC), 121−123
bond stress, 123*t*
concrete mixture proportions, 121*t*
properties of concrete mixtures, 122*t*
High-performance concrete (HPC), 110, 128−130. *See also* Ultrahigh performance concrete (UHPC)
chemical composition of GGBS, 130*t*
compressive strength of GGBS-based concrete mixtures, 130*t*
cumulative intrusion *vs*. pore size, 131*f*
micro-structure related properties of GGBS-based concrete mixtures, 132*t*
XRD of mix, 131*f*
matrix with and without fly ash, 132*f*
High-range water-reducer (HRWR), 133
High-strength concrete, 56
High-strength geopolymer concrete, 53
Higher energy, 149
Holy grail approach, 223
Homogeneous materials, 244
HPC. *See* High performance concrete (HPC); High-performance concrete (HPC)
HRWR. *See* High range water reducers (HRWR); High-range water-reducer (HRWR)
Human resources, 266
HVFAC. *See* High volume fly ash concrete (HVFAC)
Hydrated paste, 247−248
Hydration, 113
compounds, 268−269
process, 104, 202
Hydraulic conductivity (HC), 264−265
Hydrogen ions, 268−269
Hydrolysis reaction, 231−232

I

IBPs. *See* Industrial by-products (IBPs)
Ideal cracking test (IDEAL-CT test), 171−172, 176
cracking tolerance index results of combinations of mixtures, 177*f*
test setup and load *vs*. displacement curve, 172*f*
IDEAL-CT test. *See* Ideal cracking test (IDEAL-CT test)
Igneous rocks, 114
Indian coal yields, 116
Indian fly ashes, chemical composition of, 118*t*
Indian Road Congress, 85
Indirect tensile strength ratio (ITSR), 175−176
Indirect tensile strength test (ITS test), 171, 175−176
tensile strength ratio values of mixtures, 176*f*
Industrial by-products (IBPs), 126, 130−133, 266−267
Industrial CRMs, 115
Industrial wastes, 67
management, 67
materials, 97, 125
products, 41

Industrial/traditional waste/by-products, 115
Infrastructure, 109, 114–115
Inorganic minerals, 229
Interaction coefficient of geogrids, 76–77
  embedded in aluminum slag at peak and critical states, 76*t*
Interface direct shear testing, 71–77
  breakage of transverse ribs observed during interface, 76*f*
  comparison of interfacial shear strength envelopes with direct shear strength envelopes for aluminum slag particles, 75*f*
  efficiency of geogrid based on friction embedded in aluminum slag, 76*t*
  interaction coefficients of geogrids embedded in aluminum slag at peak and critical states, 76*t*
  variations of interface shear stress, 75*f*
Iron ore, 123–124
Iron powder, 280–281
ITS test. *See* Indirect tensile strength test (ITS test)
ITSR. *See* Indirect tensile strength ratio (ITSR)

K

Kakatiya thermal power station (KTPS), 2
Kerogen, 184
KFA. *See* KTPS fly ash (KFA)
KTPS. *See* Kakatiya thermal power station (KTPS)
KTPS fly ash (KFA), 2, 6*f*
Kyoto Protocol, 111

L

Lab investigations, 281
  analysis of lab investigation, 281
LAS test. *See* Linear amplitude sweep test (LAS test)
LCA. *See* Life cycle assessment (LCA)
LCE. *See* Life cycle energy (LCE)
Life cycle assessment (LCA), 27–29, 263–264
  integrated building information modeling software, 30
Life cycle energy (LCE), 27–28
Life cycle inventory, 32
Lignin, 154
Limestone, 114, 280–281
  fines, 115
Limiting oxygen index (LOI), 116
Linear amplitude sweep test (LAS test), 170, 173–175
  fatigue-life curves, 175*f*
  shear stress *vs*. shear strain of all combinations of binder, 175*f*
Liquid–solid ratio and interaction time
  pH versus interaction time and liquid–solid ratio, 268*f*
  selected trace metal elements in coal gangue, 269*t*
  variation in metal extraction of selected trace metal elements, 270*f*
  variation in pH and metal extraction with, 268–270
Lithium slag, 188
Load-deformation behaviour, 159
Load-deformation curve, 90
  for reinforced and unreinforced sections, 91*f*
LOI. *See* Limiting oxygen index (LOI)
Low calcium fly ash, 42
  data for design of low calcium fly ash-based geopolymer concrete, 59*t*
Low embodied energy, 109
Low-volume roads (LVRs), 153
Lower subbase, 85
LVRs. *See* Low-volume roads (LVRs)

M

Machine learning approaches, 224
Macro photographic mode, 244
Macro plastic fibers, 203
Magnesium hydroxide ($Mg(OH)_2$), 233
Magnesium ions, 231
Manual Series 2 (MS-2), 169
Marine clay, 82–83
  soil sample properties, 84*t*
Marshall method, 169
Marshall mixture design, 169
  Marshall parameters at optimum binder content for specimens, 170*t*
Materials forming ternary systems for concrete, 128
  side effects and interactions of supplementary cementitious materials, 129*f*

Materials replacing aggregate, 125–126
Materials replacing cement, 115–125
  and aggregates, 126–128
Matric potential sensor (MPS), 1–2
Maximum dry density (MDD), 282
MC. *See* Mineral carbonation (MC)
MCS. *See* Mineral carbon sequestration (MCS)
MDD. *See* Maximum dry density (MDD)
ME. *See* Metal extraction (ME)
Mean compressive strength results
  for all mix trials, 62
  comparison for different trial mixes, 62*f*
Mechanical properties of latex-modified high-strength concrete, 202–203
Metakaolin (MK), 111, 115, 280–281
Metal extraction (ME), 268–270
  variation in pH and metal extraction with liquid–solid ratio and interaction time, 268–270
Metallic iron powder, 280
MICP. *See* Microbiologically induced calcite precipitation (MICP)
Microbial crystal precipitation technology, 229
Microbial functions, 235
  development of biomediated self-healing ground improvement technology applied to marine environment, 233–235
  development of preservation materials with self-healing and environmental preservation functions based on, 233–237
  functional granules for sediment conservation at World Natural Heritage site, 235–237
  mechanisms crystal precipitation by of microbial functions and engineering applications, 229–232
    biopolymers, 230
    calcium-magnesium, 231–232
    selection of microbial functions with potential for engineering applications, 232
    silicate, 230–231
    sulfate, 231
  selection of microbial functions with potential for engineering applications, 232, 232*t*
Microbial produced enzyme-based crystal precipitation technologies, 229
Microbiologically induced calcite precipitation (MICP), 241–242
Microstructural analysis, 210–214
  X-ray diffraction analysis for control mix, 213*f*
Microstructural and chemical analyses, 243–245
  Fourier transform infrared spectroscopy, 245
  scanning electron microscope and energy dispersive X-ray spectroscopy, 244
  stereomicroscopic imaging, 244
  thermogravimetric analysis, 245
  X-ray diffraction spectroscopy, 244
Microstructural tests, 208
Microstructures, 204
  of bio-concrete, 245–256
  Fourier transform infrared spectroscopy of bio-concrete, 254–255
  scanning electron microscopy of bioconcrete, 247–252
  stereomicroscopy of bio-concrete, 245–247
  thermogravimetric analysis of bioconcrete, 255–256
  X-ray diffraction of bio-concrete, 253–254
Mill tailings, 183
Mine tailings, 188
Mineral admixture-based concrete, 121–122
Mineral carbon sequestration (MCS), 184
  application for mineral carbon sequestration within construction products or during manufacture, 189–190
Mineral carbonation (MC), 189
Mineral extraction, 181, 184
Mineral fillers, 185
Mineral wastes, 181–184
  mineral waste tailing heap with close-up of material, 183*f*
  optimal utilization of mineral wastes, 190–191

Mineral wastes (*Continued*)
United Kingdom and territory recycling rates for household waste, 182*f*
utilization of mineral wastes, 184−190
application for mineral carbon sequestration within construction products or during manufacture, 189−190
geopolymer and alkali-activated cements, 186−188, 188*f*
mineral wastes for use as supplementary cementitious materials, 185−186
utilization of mineral wastes in cement and concrete as in-active fillers, 184−185
Mineralogy tests, 208
Minerals, 244
Mining, 181
Ministry of Road Transport and Highways (MoRT&H), 166
Mix composition, 136−138
Mix design, 58−62, 112
for M70 grade equivalent geopolymer concrete, 60*t*
mix proportions of tested samples, 207*t*
preparations, 207
Mix proportion, 100−101
of high performance green concrete, 102*t*, 103*t*
water/binder ratio and compressive strength for high performance concrete, 101*t*
MK. *See* Metakaolin (MK)
Model pavement, 86
loading arrangements of model test setup, 87*f*
sample preparation of, 86−89
experimental procedure, 88−89
subbase layer, 88, 89*f*
subgrade, 86−88, 88*f*
systematic sketch of small-scale model pavement, 87*f*
tests, 81−82
Modulus of rupture of geopolymer concrete, 17
Molarity
effect of, 19
of alkaline solution, 55−56
Molybdenum, 185
MoRT&H. *See* Ministry of Road Transport and Highways (MoRT&H)
Mortar
compressive strength of, 43−45
variation of compressive strength of mortar different proportions of water-to-water glass ratio, 46−51
MPS. *See* Matric potential sensor (MPS)
MS-2. *See* Manual Series 2 (MS-2)
MSCR test. *See* Multiple stress creep recovery test (MSCR test)
Multiple stress creep recovery test (MSCR test), 165, 170, 173
J_{nr} value for reclaimed asphalt pavement-blended PMB with different rejuvenators, 174*f*
J_{nr_diff} value for reclaimed asphalt pavement-blended PMB with different rejuvenators, 174*f*

N

Nanoalumina, 223
Nanoclay, 223
Nanocomposites, 222
Nanomaterials, 222
Nanosilica, 223
Natural coir geotextile
materials for study, 155, 157*f*
engineering properties of subgrade black cotton soil, 155*t*
experimental setup, 155−156
experimental setup with fabricated mold, 157*f*
physical properties of coir fiber, 156*t*
results, 157−162
California bearing ratio test results, 157−159
wheel tracking test results, 159−162
Natural resources, 109, 112, 125−126
Natural rubber latex (NRL), 202
hardened concrete properties, 209−214
compressive strengths of concrete, 210*f*
microstructural analysis, 210−214, 211*f*, 212*f*, 213*f*
materials, 204−205, 205*f*
OPC chemical composition, 204*t*
materials and method, 204−214
results, 209

slump test, 209
testing methods, 205−208
Nitrification reactions, 236
Nitrogen gas, 237
Nonlinear equations, 5−8
Nonlinear regression equations, 2
Nonrenewable raw materials, 279
Nontraditional waste materials, 116
Nonwoven geotextile, 84
Normal curing in open bath chamber, 113
Normal strength concrete (NSC), 110
NRL. *See* Natural rubber latex (NRL)
NSC. *See* Normal strength concrete (NSC)
Nutrients, 237

O

OBC. *See* Optimum binder content (OBC)
ODP. *See* Ozone depletion potential (ODP)
OE. *See* Operational energy (OE)
Oil shale, 184
OMC. *See* Optimum moisture content (OMC)
OPC. *See* Ordinary Portland cement (OPC)
OPCCs. *See* Ordinary Portland cement concretes (OPCCs)
Operational energy (OE), 29−30
Optimal compaction method, 136
Optimal utilization of mineral wastes, 190−191
decision tree for optimal mineral waste feedstocks utilization, 190*f*
Optimization of granular materials, 134−136, 136*t*
binary packing densities
of copper slag, 137*f*
of ennore sand, 137*f*
Optimized mix, 138−139
Optimum binder content (OBC), 169
Optimum dosage
rejuvenating agent and process for arriving at, 167
three types of rejuvenators, 168*f*
viscosity and specific gravity of rejuvenators, 168*t*
Optimum moisture content (OMC), 264−265, 282
Ordinary Portland cement (OPC), 41−42, 110, 186, 204
Ordinary Portland cement concretes (OPCCs), 119−121
Organic ligands, 268−269
Organic oil-bearing material, 184
Oxalic acid, 280−281
Oxidation, 280
Ozone depletion potential (ODP), 28

P

Packing density (PD), 136
Packing studies, 136
Palm oil clinker aggregate (POCA), 115
Palm oil fuel ash (POFA), 115
Particle size distribution curves, 83*f*
PC. *See* Portland cement (PC)
PD. *See* Packing density (PD)
Pectin, 154
PED. *See* Primary energy demand (PED)
Performance grade (PG), 167
PET. *See* Polyethylene terephthalate (PET)
PG. *See* Performance grade (PG)
Planetary mixer machine, 138−139
Plastic fibers, 204−205
hardened concrete properties, 209−214
compressive strengths of concrete, 210*f*
microstructural analysis, 210−214, 211*f*, 212*f*, 213*f*
materials, 204−205, 205*f*
and method, 204−214
OPC chemical composition, 204*t*
results, 209
slump test, 209
testing methods, 205−208
Plastic garbage, 203
Plastic waste, 203
Plasticizers, 202
POCA. *See* Palm oil clinker aggregate (POCA)
POFA. *See* Palm oil fuel ash (POFA)
Poly acrylic ester-based high-range water−reducer, 133
Polyester uniaxial geogrids, 68
Polyethylene terephthalate (PET), 203
Polymeric fiber, 202
Polymerization, 41−42, 55
Polymers, 166, 202
Polypropylene, 202
Portland cement (PC), 53, 128, 241

Portland Pozzolana Cement (PPC), 116–117
Pozzolanic materials, 82, 186
  impacts of concrete incorporated with, 34*t*
Pozzolanic waste, 82
PPC. *See* Portland Pozzolana Cement (PPC)
Primary energy demand (PED), 28
Pullout mode of failure, 67–68
Pulverized FA, 115
Q
Quantitative sustainable concrete approach
  Autodesk Revit, 28–29
  case study, 31–32, 32*f*
    functional unit, 32
    life cycle inventory, 32
    system boundaries, 31
  literature review, 29–30
    life cycle assessment integrated building information modeling software, 30
  methodology, 30, 31*f*
  results, 32–38
    A1 to A3 module AP comparison, 35*f*
    A1 to A3 module EP comparison, 36*f*
    A1 to A3 module GWP comparison, 36*f*
    A1 to A3 module PED comparison, 37*f*
    A1 to A3 module SFP comparison, 37*f*
    impacts of concrete incorporated with pozzolanic materials, 34*t*
    impacts of RCC, 33*t*
    transportation module impacts comparison, 38*f*

R
Ramagundam thermal power station (RTPS), 2
RAP material. *See* Reclaimed asphalt pavement material (RAP material)
Raw materials, 241, 263–264
  for geopolymer concrete, 55
RC. *See* Reinforced concrete (RC)
RCA. *See* Recycled concrete aggregates (RCA)
Reclaimed asphalt pavement material (RAP material), 165–166
  Marshall mixture design, 169
  material, 166–169
    aggregate gradation, 167–169, 168*f*
    rejuvenating agent and process for arriving at optimum dosage, 167
    virgin and extracted reclaimed asphalt pavement binder, 166–167
    virgin and reclaimed asphalt pavement aggregate properties, 166, 166*t*
  result, 173–177
    ideal cracking test, 176
    indirect tensile strength test, 175–176
    linear amplitude sweep test, 173–175
    multiple stress creep recovery, 173
    toughness index, 177
  test method, 170–172
Recycled aggregate, 97
Recycled concrete aggregates (RCA), 111, 128
Red mud, 55
Regression analysis, 5–8
Regression equations, 8–9
Regression models for water retention characteristic curve of fly ash, 5–8
  comparison of proposed WRCC regression model with experimental data, 9*f*
Rehabilitation techniques, 241
Reinforced concrete (RC), 219–220
  structures, 109
Reinforced soil structure, 67–68
Reinforcement, 84, 84*f*
  function, 153–154
Reinforcing bars, 114
Rejuvenators, 165, 167
RFA. *See* RTPS fly ash (RFA)
RHA. *See* Rice husk ash (RHA)
Rice husk ash (RHA), 115–116
RTPS. *See* Ramagundam thermal power station (RTPS)
RTPS fly ash (RFA), 2
  estimated WRCC of FX model for, 5*f*
Rutting potential, 155

S
S-type load cell, 88
Sandy gravel soil, 159–160
SBS. *See* Styrene-Butadiene-Styrene (SBS)
Scanning electron microscopy (SEM), 208, 242–244, 246–247
  of *Bacillus* sp. incorporated concrete, 250*f*
  of bioconcrete, 247–252

of calcite precipitation at crack surface, 251*f*
of dense structure of calcium carbonate crystal, 253*f*
and EDS spectra of deposited calcite in the crack, 252*f*
Scanning electron microscopy with energy dispersive X−ray spectroscopy (SEM−EDS), 243−244
SCMs. *See* Supplementary cementitious materials (SCMs)
Sediment conservation at World Natural Heritage site
functional granules for, 235−237
procedure for granular material preparation, 236*f*
Self-healing functions, 233
SEM. *See* Scanning electron microscopy (SEM)
SEM−EDS. *See* Scanning electron microscopy with energy dispersive X−ray spectroscopy (SEM−EDS)
Separation function, 153−154
Sequestration, 189
SERC. *See* Structural Engineering Research Centre (SERC)
Setting time, 43, 44*t*
geopolymer paste, 46, 48*t*
SF. *See* Silica fume (SF)
SFP. *See* Smog formation potential (SFP)
SG. *See* Specific gravity (SG)
Shear stress, 173−174
variation, 72*f*, 73
Shearing process, 73
Shot blasting process, 280
Sieve analysis of copper slag, 134, 135*f*
Silica fume (SF), 97−99, 110, 115, 124−125, 128, 153−154
Silica-based soil improvement technology, 230
Silicate, 230−231
Siliceous FA, 116−119
specifications of siliceous fly ash for use in concrete, 120*t*
Siliceous pulverized fuel FA, 116
Siloxane bonds, 230
Silver dioxide, 244
Sipozz, 115
Slag, 41−42, 97
Slag cement, 128
Slag wastes, 67, 73
Slag-based high strength geopolymer concrete
experimental program, 56−62
literature study, 54−56
factors influencing geopolymer concrete properties, 55−56
geopolymerization, 54−55
raw materials for geopolymer concrete, 55
materials, 56−58
alkaline liquid, 57
alkaline solid, 58
coarse and fine aggregates, 56, 57*t*
fly ash and GGBS, 56−57
mix design, 58−62
chemical composition of geopolymer concrete as per mix design, 59
geopolymer concrete mix design, 58−59
mean compressive strength results for all mix trials, 62
observations for geopolymer concrete pilot mix revised trial-1, 59−61
objective of study, 53
scope of work, 53
Slimes, 184
Slump test, 207, 209
slump result of concrete mixes, 209*f*
Small coarse aggregate, 113
Small-scale model pavement, systematic sketch of, 87*f*
Smog formation potential (SFP), 28
Soaked California bearing ratio, 282−290
raw materials required for ferrock manufacturing, 280*t*
soaked CBR test for expansive soil, 291*t*
soaked CBR test for expansive soil + 10- ferrock material, 292*t*
soaked CBR test for expansive soil + 15- ferrock material, 292*t*
soaked CBR test for expansive soil + 20- ferrock material, 292*t*
soaked CBR test for expansive soil + 5- ferrock material, 292*t*
standard proctor test for expansive soil, 283*t*

Soaked California bearing ratio (*Continued*)
standard proctor test for expansive soil + 10- ferrock material, 285*t*
standard proctor test for expansive soil + 15- ferrock material, 286*t*
standard proctor test for expansive soil + 20- ferrock material, 287*t*
standard proctor test for expansive soil + 5- ferrock material, 284*t*
unconfined compressive strength test for expansive soil, 288*t*
unconfined compressive strength test for expansive soil + 10- ferrock material, 290*t*
unconfined compressive strength test for expansive soil + 5- ferrock material, 289*t*
Sodium hydroxide, 15
Sodium hydroxide solution, 58
concentration, 13, 19
Sodium silicate. *See* Alkaline liquid (Na_2SiO_3)
Soil, 157
combination of soil and ferrock material samples, 281
microorganisms, 229
particles, 230
stability, 282
Soil−geogrid interaction failures, 67−68
Soil−geogrid interface interaction, 67
Solid rubber, 155
Solidification accelerator, 235−236
Sorptivity values for concrete mixtures, 121
Soxhlet extraction apparatus, 166−167
Soxhlet extractor, 166
SP. *See* Superplasticizers (SP)
Specific gravity (SG), 82−83, 205
Sporosarcina
S. aquimarina, 233
S. pasteurii, 233, 249
Stabilization of subgrade soil
findings, 281−290
features of compaction, 282
soaked California bearing ratio, 282−290
soil stability, 282
potential applications, 280
testing procedures, 280−281
analysis of lab investigation, 281
combination of soil and ferrock material samples, 281
lab investigations, 281
understanding of important technologies, 280
Standard Proctor tests results, 86*t*
Static leaching method, 270
Steel, 219−220
plants, 82
Stereomicroscopy
of bio-concrete, 245−247
imaging, 243−244
stereomicroscopic image of concrete crack healing, 246*f*, 247*f*
Strength
development of HPC, 101−103
of geopolymer concrete, 13
Structural Engineering Research Centre (SERC), 119
Structural grade FACC, 119−121
Styrene-Butadiene-Styrene (SBS), 166−167
Subbase layer, 155
Subgrade soil, 155, 157−158
Substantially greener concrete, 56
Suction, measurement of, 2−3
Sugarcane bagasse, 115
Sulfate-reducing bacteria, 231
Sulfates, 113, 124, 231
Superplasticizers (SP), 15, 100, 110
in high performance green concrete, 100
Supplementary cementitious materials (SCMs), 27−28, 97−100, 111, 185
mineral wastes for use as, 185−186
classification of pozzolans, 187*f*
side effects and interactions of, 129*f*
Sustainability, 109, 111
engineering green concrete strategies for, 114−128
Sustainable building materials, 186
Sustainable development, 263−264
Sustainable materials, 53
System boundaries, 31

T

Tally (Autodesk Revit software), 28
Tensile strength ratio (TSR), 171
Tensiometer (TM), 1−2
Ternary combinations, 136
Ternary mixture, 128

Ternary solution, 128
Test(ing) method, 170–172, 205–208
  compressive strength test, 207–208, 208*f*
  IDEAL cracking test, 171–172
  indirect tensile strength test, 171
  linear amplitude sweep test, 170
  microstructural and mineralogy tests, 208
  mix design and concrete specimens preparations, 207
  multiple stress creep recovery, 170
  sieve analysis, 206, 206*f*
  specific gravity and water absorption test, 205
  toughness index, 172
TGA. *See* Thermogravimetric analysis (TGA)
Thermal curing, 113
Thermal insulation (TI), 29–30
Thermogravimetric analysis (TGA), 242–243, 245, 255–256, 257*f*
Three-dimensional geocell, 153–154
Three-dimensional geogrid, 153–154
TI. *See* Thermal insulation (TI); Toughness index (TI)
Titanium dioxide, 244
TM. *See* Tensiometer (TM)
TME. *See* Trace metal elements (TME)
Toughness index (TI), 172, 177
  of for combinations of bituminous mixtures, 177*f*
  normalized indirect tensile strength *vs.* strain, 173*f*
Trace metal elements (TME), 263–264
Transportation module impacts comparison, 38*f*
Transverse ribs observed during interface, breakage of, 76*f*
Trial mix, 139
  preparation of, 138–139
TSR. *See* Tensile strength ratio (TSR)

U

UCS test. *See* Unconfined compressive strength test (UCS test)
UHPC. *See* Ultrahigh performance concrete (UHPC)
UHSC. *See* Ultrahigh-strength concrete (UHSC)
Ultrahigh performance concrete (UHPC), 130–138. *See also* High-performance concrete
  casting of ultrahigh performance concrete specimens, 139
    optimized mix, 139
    trial mix, 139
  chemical composition of copper slag, 134
  constituents, 133
  curing regime, 141
  mix composition, 136–138
  mix proportions
    for optimized mixes, 139*t*
    of trial mixes, 138*t*
  mixing of, 138–149
  optimization of granular materials, 134–136
  optimized mix, 138
  physical and chemical properties of copper slag, 133–134
  preparation of trial mixes, 138–139
  specimen preparation, 140–141, 141*f*
  test results, 143–149
    cube compressive strength, 144–145
    flexural strength of ultrahigh performance concrete, 145–147
    fracture energy of ultrahigh-performance concrete prisms, 147–149
    optimized mix results, 144
    results for compressive strength of UHPC with copper slag, 144*t*
    results for compressive strength of UHPC with ennore sand, 143*t*
    trial mix results, 143–144
  tests on ultrahigh-performance concrete, 141–143
    compressive strength test, 141–142
    flexural strength test, 142–143
    fracture energy test, 143
  trial mixes, 138–139
Ultrahigh-strength concrete (UHSC), 111
Ultraviolet radiation, 280
Unconfined compressive strength test (UCS test), 281
Uniaxial geogrids, 68–69
  experimental program, 70
    geogrid sample connected at interface of upper and lower shear boxes, 70*f*
  materials used, 68–69

Uniaxial geogrids (*Continued*)
properties of geogrids used in present study, 69*t*
results, 70−77
basic characteristics of aluminum slag, 70−71, 71*f*
direct shear testing, 71−73
interface direct shear testing, 73−77
used in present study, 69*f*
Unsaturated behavior, 1
Upper subbase, 85

V
Validation of binder index, 21−24
variation of compressive strength, 23*f*
variation of flexural strength, 24*f*
Vaterite (Vt), 253−254
VFA. *See* VTPS fly ash (VFA)
Vicat apparatus, 43
Vijayawada thermal power station (VTPS), 2
Virgin and extracted reclaimed asphalt pavement binder, 166−167
Virgin and reclaimed asphalt pavement aggregate properties, 166
VTPS. *See* Vijayawada thermal power station (VTPS)
VTPS fly ash (VFA), 2
computed WRCC of FX model for, 6*f*

W
W/b ratio. *See* Water-to-binder ratio (W/b ratio)
w/c ratio. *See* Water-to-cement ratio (w/c ratio)
W/S ratio. *See* Water-to-solids ratio (W/S ratio)
W/WG. *See* Water-to-water glass (W/WG)
Waste, 181
glass, 55
management, 182, 263−264
materials, 279
in concrete, 125
rock, 182−183
waste-derived fuels, 110
Waste engine oil (WEO), 167
Waste vegetable oil (WVO), 167
Water (H_2O), 54
absorption, 211
test, 205
permeability, 210, 229
Water glass, 42−43
experimental program, 43−45
compressive strength of mortar, 43−45
consistency of geopolymer paste, 43
setting time, 43, 44*t*
materials used, 42−43
chemical composition of GGBS and fly ash, 43*t*
results, 45−51
consistency of geopolymer paste, 45−46
final setting time of geopolymer concrete, 49*f*
initial setting time of geopolymer paste, 49*f*
setting time geopolymer paste, 46, 48*t*
variation of compressive strength of mortar different proportions of water-to-water glass ratio, 46−51
Water retention characteristic curve (WRCC), 1
experimental program, 2
particle size distributions, 4*f*
properties of fly ash, 3*t*
measurement of suction, 2−3
objectives of present study, 2
regression model with experimental data, comparison of proposed, 9*f*
results, 3−8
computed WRCC of FX model for VTPS fly ash, 6*f*
estimated WRCC of FX model for KTPS fly ash, 6*f*
estimated WRCC of FX model for RTPS fly ash, 5*f*
of fly ash, 3−5
particle size diameter and WRCC fitting parameters of fly ash samples, 7*t*
regression models for water retention characteristic curve of fly ash, 5−8
WRCCs, 7*f*
studies on water retention characteristic curve of fly ash, 1−2
validation with published study, 8−9
comparison of proposed FX WRCC regression fit, 9*f*
Water-to-binder ratio (W/b ratio), 186
for high performance concrete, 101*t*

Water-to-cement ratio (w/c ratio), 100−101, 112, 136−138
Water-to-solids ratio (W/S ratio), 59
Water-to-water glass (W/WG), 43
  variation of compressive strength of mortar different proportions of, 46−51
WEO. *See* Waste engine oil (WEO)
Wheel tracking test (WTT), 154−155, 159−160
  results, 159−162
  wheel passes with respective rut depth at H/3 position of coir geotextiles, 161*f*
Workability, 96−97
WRCC. *See* Water retention characteristic curve (WRCC)
WTT. *See* Wheel tracking test (WTT)
WVO. *See* Waste vegetable oil (WVO)

X
X-ray diffractometer, 208
X-ray fluorescence spectrometry test, 84
X−ray diffraction (XRD), 214, 242−243
  of bio-concrete, 253−254
  of mix, 131*f*
    matrix with and without fly ash, 132*f*
  pattern of precipitated material inside crack, 253*f*
  patterns of *Sporosarcina pasteurii* and 10-silica fume, 255*f*
  spectroscopy, 244
XRD. *See* X−ray diffraction (XRD)